MICROSTRUCTURAL AND MECHANICAL CHARACTERISATION OF CAST FE-AL-MO-TI-B ALLOYS

Zur Erlangung des akademischen Grades eines

DOKTORS DER INGENIEURWISSENSCHAFTEN (Dr.-Ing.)

von der KIT-Fakultät für Maschinenbau des
Karlsruher Instituts für Technologie (KIT)
angenommene

DISSERTATION

von

M.Sc. Andreas Abel

Tag der mündlichen Prüfung: 09.04.2025

Hauptreferent*in: Prof. Dr.-Ing. Martin Heilmaier
Korreferent*in: Prof. Dr.-Ing. Birgit Skrotzki

This document is licensed under a Creative Commons
Attribution-ShareAlike 4.0 International License (CC BY-SA 4.0):
https://creativecommons.org/licenses/by-sa/4.0/deed.en

Disclaimer:
Parts of this dissertation including text, data, tables and figures were reproduced and adapted from a final report of the publicly funded AiF project "Werkstoffanwendung FeAl (WAFEAL)" (FKZ: IGF 20965 N). Figures and tables from the report are additionally cited when appearing. Other reproduced and modified parts falling under different licence agreements are cited at relevant positions of this dissertation.

Abstract

With the advent of variable renewable energies, long-term energy storage capacities and flexible power generation technologies will be required for reliable grid stability. Hence, power plant technologies and turbomachinery components will continue to be developed and employed for efficient re-conversion of stored energy. With the introduction of new working fluids for higher thermal efficiencies, the working conditions of exposed components and materials will require higher corrosion resistance, but with the same mechanical performance, manufacturability and cost. Intermetallic iron aluminide alloys with their outstanding oxidation and corrosion resistance and good high-temperature properties depict a possible candidate for use in high-temperature structural applications. A quinary Fe-26Al-4Mo-0.5Ti-1B solid-solution alloy with eutectic particle hardening particularly demonstrated competitive mechanical properties compared to high-alloy P92 steels in previous studies. To derive standard material specifications with industrially relevant casting strategies, centrifugal investment-cast Fe-25Al-3.7Mo-0.4Ti-1B was characterised with respect to microstructure, thermophysical properties and mechanical properties under quasi-static tensile and creep loading up to 700 °C. Compared to P92 steel, the alloy demonstrated superior tensile strength above 550 °C and lower creep rates at 650 °C if stresses increase above 170 MPa. At lower temperatures though, the mechanical properties were inferior to P92 steel and related Fe-Al-Mo-Ti-B alloys, which was correlated to large grain sizes, a high tendency to surface and bulk cracking and a pronounced effect of tension-compression asymmetry. In further studies on alloy composition with varying Al, Mo and B concentration, a non-linear relationship of solid-solution hardening with solute Mo concentration was found. In this regard, halving Mo was the most effective measure for reducing brittleness without decreasing strength at room and elevated temperatures. Higher solidification rates and grain refinement down to 30 µm by die casting had a positive effect on ambient tensile strength, but were not achievable by investment casting. Dilatometry and hardness measurements indicated a low thermal vacancy hardening effect which was less sensitive to low-temperature annealing than in B2 FeAl alloys. Although mechanical properties up to 550 °C could be considerably improved by alloy development and processing, ductility at room temperature generally remained below 1%, necessitating substantial design margins for components from Fe-Al-Mo-Ti-B alloys. Despite the inherent limitations of alloy and casting process, the gained insights will help to prioritise future areas of research to mature cost-effective higher-order Fe_3Al alloys for high-temperature structural applications.

Kurzfassung

Mit dem verstärkten Einsatz erneuerbarer Energien werden weiterhin Kraftwerkstechnologien und Turbomaschinenkomponenten für eine effiziente Rückwandlung von Energie aus Langzeitspeichern benötigt. Die Erhöhung der thermischen Effizienz durch neue Arbeitsmedien erfordern zukünftig eine höhere Korrosionsbeständigkeit der eingesetzten Werkstoffe bei gleicher mechanischer Leistung, Verarbeitbarkeit und Kosten. Intermetallische Eisenaluminid-Legierungen mit hervorragender Oxidations- und Korrosionsbeständigkeit und guten Hochtemperatureigenschaften sind mögliche Alternativen zu hochlegierten P92-Stählen für den Einsatz in strukturellen Hochtemperaturanwendungen. Zur Ableitung von genormten Werkstoffdaten wurde eine im Schleudergussverfahren hergestellte Fe-25Al-3,7Mo-0,4Ti-1B-Mischkristalllegierung mit eutektischer Partikelhärtung hinsichtlich Mikrostruktur, thermophysikalischer und mechanischer Eigenschaften unter quasistatischer Zug- und Kriechbeanspruchung bis 700 °C charakterisiert. Im Vergleich zu P92-Stahl zeigte die Legierung eine höhere Zugfestigkeit über 550 °C und geringere Kriechraten bei 650 °C, wenn die Spannungen 170 MPa übersteigen. Bei niedrigeren Temperaturen waren die mechanischen Eigenschaften jedoch gegenüber P92-Stahl und verwandten Fe-Al-Mo-Ti-B-Legierungen unterlegen, was mit hohen Korngrößen, einer hohen Neigung zu Oberflächen- und Volumenrissen und einem starken Einfluss der Zug-Druck-Asymmetrie in Verbindung gebracht wurde. In weiteren Untersuchungen zur Legierungszusammensetzung mit unterschiedlichen Al-, Mo- und B-Konzentrationen wurde eine nicht-lineare Beziehung zwischen der Mischkristallhärtung und der gelösten Mo-Konzentration festgestellt. In diesem Zusammenhang war die Halbierung der Mo-Konzentration die wirksamste Maßnahme zur Verringerung der Sprödigkeit ohne Verringerung der Festigkeit bei Raum- und erhöhten Temperaturen. Höhere Erstarrungsgeschwindigkeiten und Kornfeinung wirkten sich positiv auf die Zugfestigkeit bei Raumtemperatur aus, konnten aber im Feinguss nicht erreicht werden. Dilatometrie- und Härtemessungen deuteten auf eine geringe thermische Leerstellenhärtung hin, die weniger empfindlich auf das Niedertemperaturglühen reagierte als bei B2-FeAl-Legierungen. Obwohl die mechanischen Eigenschaften bis 550 °C durch Anpassung der Zusammensetzung und der Prozessparameter erheblich verbessert werden konnten, blieb die Duktilität bei Raumtemperatur grundsätzlich unter 1 %, was erhebliche Konstruktionsmargen für Bauteile aus Fe-Al-Mo-Ti-B-Legierungen bedingt. Trotz der Grenzen von Legierung und Gießverfahren werden die gewonnenen Erkenntnisse dazu beitragen, künftige Forschungsschwerpunkte zu setzen, um kostengünstige, mehrkomponentige Fe_3Al-Legierungen für strukturelle Hochtemperaturanwendungen zu entwickeln.

Danksagung

Mein erster und größter Dank gilt meiner Wegbegleiterin zum Doktor, Frau Prof. Dr.-Ing. Birgit Skrotzki, für eine Betreuung, die sich jede Doktorand*in wünschen würde, und das Vertrauen, das zusammen mit ihrer Geduld eine feste Säule für mich war. Auch möchte ich mich bei Herrn Prof. Dr.-Ing. Martin Heilmaier für seine Betreuung und stete Bereitschaft für fachliche Austausche herzlich bedanken. Für wertvolle wissenschaftliche Diskussionen möchte ich auch Herrn Dr. Martin Palm (ehemals Max-Planck-Institut für Eisenforschung) und Prof. Dr. Easo P. George (ehemals Oak Ridge National Laboratory, USA) danken.

Diese Arbeit ist entstanden während der Duchführung des IGF/AiF-Forschungsvorhabens „Werkstoffanwendung FeAl (WAFEAL)“. Hierzu möchte ich meinen Dank an den Fördergeber, das Bundesministerium für Wirtschaft und Klimaschutz (BMWK), und insbesondere Herrn Dirk Bösel von der Forschungsvereinigung Verbrennungskraftmaschinen e.V. (FVV) für das Vertrauen und die gute Betreuung während der Projektzeit aussprechen. Auch möchte ich Herrn Dr. Dan Roth-Fagaraseanu und Frau Susanne Mosler von Rolls-Royce Deutschland Ltd & Co KG für ihr fortwährendes Interesse und ihre Ideen danken, die sie uns in vielen Arbeitskreissitzungen entgegengebracht haben. An dieser Stelle möchte ich mich insbesondere auch bei unseren beiden Projektpartnern, Herrn Heiner Michels und Herrn Pawel Zapala von Access e.V., und ihren Kolleg*innen bedanken, die für die Probenfertigung geackert haben und mit denen stets eine gute Zusammenarbeit gelungen ist.

Außerdem ist diese Dissertation noch vielen weiteren Personen zu verdanken, die mich vor allem experimentell und mit ihrer Expertise, aber auch menschlich unterstützt haben: Ich danke der Fa. Henschel GmbH und der Feinwerkstatt der BAM für die herausfordernde und doch zuverlässige Bearbeitung und Kontrolle von mechanischen und thermophysikalischen Proben. Ich danke außerdem Herrn Dr. Sebastian Recknagel und Frau Janina Roik für die nasschemischen Untersuchungen sowie Herrn Dr.-Ing. Tobias Mente und Herrn Jörg Schlischka für die Funken-OES Messungen. Großen Dank gilt Herrn Andreas Grunewald, der mich nicht nur bei den Probeninspektionen tatkräftig unterstützt hatte, sondern auch mit Rat und Tat zur Seite stand, um geeignete metallographische Ätzungen zu finden. Ich möchte mich auch bei Herrn Hennig Goldbeck, der die Röntgenfeinstrukturanalyse übernahm, sowie Herrn Romeo Saliwan Neumann und Frau Gabriele Oder, die die EBSD-Messungen und die Elektronenstrahlmikroanalysen durchführten und zudem allen Fragen Rede und Antwort standen, ganz herzlich bedanken. Frau Evgenia Bajer bin ich dankbar für die immer sehr schnelle und zuverlässige Messung von Dichtewerten. Mein Dank gilt außerdem Herrn Dr. Julian Rosalie und Dr. Anna Manzoni für die TEM-Messungen und die großartige fachliche Unterstützung. Großer Dank gilt auch Herrn Steffen Thärig, dem Alleskönner, der mich bei der Durchführung von Härtemessungen, Standard-Zug- und Druckversuchen sowie bei der Präparation und Aufnahme von metallographischen Schliffen tatkräftig unterstützt hat. Auch möchte ich Frau Christine Krimmling für weitere Härtemessungen sowie Herrn Patrick Uhlemann sowie Frau Kathrin Matzak für weitere Zugversuche und ihre immer engagierte und hilfsbereite Arbeitsweise danken. Für die Umsetzung der Kriechversuche möchte ich mich ganz herzlich bei Frau Sina Schriever bedanken, die mit größter Sorgfalt und Hilfsbereitschaft an den monatelangen Auftrag herangegangen ist. Zudem bedanke ich mich bei Herrn Peter Löwe für die Durchführung der Miniatur-Zugversuche und seine immer spannenden, technischen Geschichtsstunden. Auch möchte ich großen Dank an Frau Elke Sonnenburg für die gesonderten Wärmebehandlungen, die vielen Fraktographie-Aufnahmen am REM und ihre stets hilfsbereite Unterstützung im Labor aussprechen. Dank gilt auch meinem Masteranden Amir Parizad für die etlichen optischen Fraktographie-Bilder und sein Vertrauen in mich als wissenschaftlicher Betreuer. Herrn Faruk Bayram und Frau Michelle Fiebig möchte ich für die dynamischen Resonanzmethodenmessungen herzlich danken. Für die zahlreichen Dilatometrie-Messungen richte ich großen Dank an Herrn Christian Meyer, der äußerst zuverlässig, engagiert und motiviert mich unterstützt hat. Außerdem bedanke ich mich bei Herrn Dr.-Ing. Stefan Reinsch für die vielen Differenz-Thermoanalysen und seinen stets kollegialen und freundlichen Umgang. Auch möchte ich vielen bereits genannten und weiteren Kollegen in- und außerhalb meines Fachbereich danken, dass sie mich stets im Labor- und Arbeitsalltag unterstützt haben, sei es mit technischer Ausstattung oder Ratschlägen.

Auch möchte ich mich an dieser Stelle bei den zahlreichen Doktoranden-Mitstreitern während meiner Zeit an der BAM bedanken, egal ob im gleichen Büro, im Abteilungsseminar oder beim AK-PhD-Meeting. Jeder Austausch und jede Kaffeerunde war eine bereichernde und wertvolle Pause zum Alltag, insbesondere nach mehreren Monaten Kontaktbeschränkungen.

Nicht zuletzt gilt mein immerwährender, unerschöpflicher Dank an meine direkte und erweitere Familie, meine Freunde und alten Weggefährten, die mir immer Halt, Wertschätzung und Mitgefühl gegeben haben, auf dem Weg hierher und hoffentlich darüber hinaus. Und an Khanh-Ly, wegen der ich dieses wissenschaftliche Kapitel in meinem Leben doch noch schreiben konnte und mit der ich erst den Mut, es zu beginnen, und dann den Stolz, es zu vollenden, gefunden habe.

Contents

List of Publications **XI**

List of Figures **XX**

List of Tables **XXII**

List of Acronyms **XXIII**

List of Symbols **XXV**

1. Introduction and motivation **1**

2. Literature review **5**

2.1. Binary Fe-Al alloy system 5

2.2. Thermophysical properties 7

2.3. Mechanical properties 7

2.3.1. Yield strength and strengthening mechanisms 7

2.3.2. Creep behaviour 11

2.3.3. Ductility 13

2.4. The Fe-Al-Mo-Ti-B system 14

3. Materials and methods **17**

3.1. Processing 17

3.1.1. Fe-Al-Mo-Ti-B alloys 18

3.1.2. Quasi-binary Fe-Al alloys 19

3.2. Post-processing 19

3.2.1. Heat treatments 20

3.2.2. Sample manufacture and quality control 20

3.3. Chemical analysis 22

3.3.1. Inductively coupled plasma - optical emission spectrometry (ICP-OES) . . . 23

3.3.2. Single element trace analyses 23

3.3.3. X-ray fluorescence (XRF) spectroscopy and spark optical emission spectrometry (S-OES) 24

3.4. Thermophysical characterisation 25

3.4.1. Gas pycnometry 25

3.4.2. Dynamic resonance method 26
3.4.3. Differential thermal analysis (DTA) 27
3.4.4. Dilatometry 27
3.5. Microstructural characterisation 30
3.5.1. X-ray diffraction (XRD) 30
3.5.2. Optical microscopy (OM) 31
3.5.3. Scanning electron microscopy (SEM) 33
3.5.4. Electron backscatter diffraction (EBSD) 34
3.5.5. Electron probe microanalysis (EPMA) 35
3.5.6. Transmission electron microscopy (TEM) 35
3.6. Mechanical testing 36
3.6.1. Hardness measurement 36
3.6.2. Compression testing 37
3.6.3. Quasi-static tensile testing 37
3.6.4. Creep testing 40

4. Characterisation of investment-cast Fe-26Al-4Mo-0.5Ti-1B 43

4.1. Microstructure and phase evolution 43
4.2. Thermophysical properties 51
4.2.1. Phase transitions 51
4.2.2. Coefficient of thermal expansion (CTE) 52
4.2.3. Young’s modulus, shear modulus and Poisson’s ratio 54
4.3. Mechanical properties 56
4.3.1. Compressive and indentation properties 56
4.3.2. Quasi-static tensile properties 58
4.3.3. Creep properties 66
4.4. Tension-compression asymmetry 84

5. Effect of alloy composition 89

5.1. Microstructure and phase evolution 90
5.2. Hardness and tensile properties 96
5.3. Solid-solution hardening by Mo in near-Fe_3Al alloys 99

6. Casting-induced microstructural variations: Implications for tensile properties 103

7. Effect of cooling rate and heat treatments on room temperature properties **113**
7.1. Processing-microstructure-property correlation 113
7.2. Vacancy hardening in quinary and binary Fe-Al alloys 119
7.3. Effects of grain refinement on tensile behaviour 127

8. Conclusions and outlook **135**

A. Drawings **145**

B. Further investigations **151**

References **179**

List of Publications

Peer-reviewed journals

A. Abel, J. M. Rosalie, S. Reinsch, P. Zapala, H. Michels, B. Skrotzki, "Influence of Mo and B additions in intermetallic near-Fe_3Al alloys on microstructure and mechanical properties", Intermetallics 163 (2023) 108074.
Contributions: Conceptualisation, Methodology, Validation, Formal analysis, Investigation (OM), Data curation, Writing – Original draft, Writing – Review & Editing, Visualisation, Project administration

Further contributions

A. Abel, P. Zapala, H. Michels, B. Skrotzki, *Microstructure-Property-Correlation of a Mo-Ti-B alloyed iron aluminide*, in: *Proceedings Intermetallics*, ed. by M. Heilmaier, M. Krüger, M. Palm, F. Stein, Conventus Congressmanagement & Marketing GmbH, Jena, 2021: 119–120.
Contributions: Conceptualisation, Methodology, Validation, Formal analysis, Investigation (OM), Data curation, Writing – Original draft, Visualisation, Project administration

P. Zapala, **A. Abel**, H. Michels, B. Skrotzki, *Werkstoffanwendung FeAl (WAFEAL)*, FVV final report H1322, Frankfurt a. M., 2023.
Contributions: Conceptualisation, Methodology, Validation, Formal analysis, Investigation (OM), Data curation, Writing – Original draft, Writing – Review & Editing, Visualisation, Project administration

P. Zapala, **A. Abel**, H. Michels, B. Skrotzki, *Werkstoffanwendung FeAl (WAFEAL)*, in: *Conference transcript*, FVV Spring Networking Event, Heft R604, Wuerzburg, 2023.
Contributions: Conceptualisation, Methodology, Validation, Formal analysis, Investigation (OM), Data curation, Writing – Original draft, Visualisation, Project administration

List of Figures

1.1. Global share of technologies for electricity generation from 2000 to 2028 reprinted from IEA [1] under the CC BY 4.0 licence. 2

2.1. (a) Phase diagram of binary Fe-Al reproduced from Zamanzade et al. [43] under the CC BY 4.0 licence, (b) dominant crystal structures of Fe-Al alloys up to an Al content of 50 at% (created by Vesta ver. 3.5.7) [44]. 6

2.2. (a) Compressive and tensile 0.2% proof strength of Fe-(26-28)Al either processed by laser metal deposition (LMD) [24] or casting as a function of temperature. Castings are either in as-cast condition or were annealed at 400 °C/672 h. The red arrow indicates an estimate of thermal vacancy hardening and the red area depicts the influenced temperature range. The blue area encloses the temperature range of the YSA peak, with the blue arrow indicating the strain rate dependency of strength. Reprinted with permission from [18]. 8

2.3. 0.2% proof strength of iron aluminides as a function of Al concentration at 100, 500 and 700 °C. Phase boundaries at the respective temperatures are marked by arrows. Reprinted with permission from [18]. 10

3.1. X-ray scans of cracks (i) observed in investment castings of Fe-26Al-4Mo-0.5Ti-1B (a) and investment castings of Fe-23.5Al-4Mo-0.5Ti-1B (b). Tensile blank sections (ii) appear crack-free in both cases. Adapted from [143] 19

3.2. Dye penetrant inspection (a) and magnetic particle inspection (b) of a reference sample with surface cracks. Adapted from [143]. 22

3.3. Schematic representation of thermal vacancy annihilation processes in dilatometric measurements with different temperature programs [143] (solid line: thermal vacancy-free material behaviour; dashed line: thermal vacancy-hardened material behaviour): (a) ideal thermal expansion versus thermal expansion with an irreversible contraction due to annihilation of mobile thermal vacancies, (b) differential dilatometry method with repeated heating and cooling cycles at constant temperature rates, (c) time-dependent dilatometry method at constant temperature. 29

3.4. Schematic illustration of determining average grain diameter via Heyn lineal intercept method in horizontal (t(0°)) and vertical (t(90°)) direction. Adapted from [143]. 32

3.5. Comparison of a microsection image before (a) and after (b) segmentation of secondary phase fractions (highlighted in red) via image editing and automatic image thresholding. Adapted from [143]. 33

4.1. SEM microsections of investment-cast Fe-25Al-3.7Mo-0.4Ti-1B: (a) as-cast condition, (b) after homogenisation treatment HT2 (1000 °C/100 h/FC). Adapted from [143]. 44

4.2. X-ray diffractograms of investment-cast Fe-25Al-3.7Al-0.4Ti-1B: (a) as-cast condition, (b) after HT2. Adapted from [143]. 47

4.3. Transmission Electron Microscopy (TEM) analysis of the alloyed Fe_3Al matrix (a,c,e) and the eutectic boride (Mo_2FeB_2) phase (b,d,f): (a,b) Bright-field (BF) images. (c,d) Inverted selected area electron diffraction (SAD) patterns generated from the areas indicated by dashed circles in a and b. Zone axes are [011] for Fe_3Al and [235] for Mo_2FeB_2. Image d is a superposition pattern of the matrix (blue circles) and the eutectic boride phase (red ovals). (e,f) Simulated diffraction patterns of the crystal structures of binary Fe_3Al (dark spots) and Mo_2FeB_2 (bright spots) corresponding to the same zone axes and scale as in images c and d. Indexed reflections from experimental patterns in c and d are superimposed for comparison. Reproduced from Abel et al. [191] under the CC BY 4.0 licence. 48

4.4. OM images of tensile specimen cross-sections (a,b) and magnifications (c,d) of investment-cast Fe-25Al-3.7Mo-0.4Ti-1B after HT2 with (a,c) grain contrast after Adler etching and (b,d) phase contrast after OP-S polishing. 49

4.5. Histogram and possible log-normal grain size distributions of investment-cast as-cast Fe-25Al-3.7Mo-0.4Ti-1B (casting wall thickness: 10 mm) taken from Feret diameters of manually segmented grains. The as-received mean grain diameter is contrasted to d_{gs} from lineal intercept method in an inset graph. 50

4.6. DTA heating and cooling curves at $\pm 10\,\mathrm{Kmin}^{-1}$ of as-cast Fe-25Al-3.7Mo-0.4Ti-1B. Baselines were subtracted for better visualisation of peaks. Adapted from [143]. . 52

4.7. Relative length change $\Delta L/L_0$ of as-cast Fe-25Al-3.7Mo-0.4Ti-1B in dilatometric measurements and resulting technical $\bar{\alpha}(T_0, T)$ and physical CTE $\alpha(T)$. Adapted from [143]. 53

4.8. Temperature dependent (a) Young's modulus E (reproduced from [143]), (b) shear modulus G and (c) Poisson's ratio υ of as-cast Fe-25Al-3.7Mo-0.4Ti-1B. Data on binary Fe_3Al is given for reference [58, 146]. 55

4.9. Compressive room temperature stress-strain curves of investment-cast Fe-25Al-3.7Mo-0.4Ti-1B after casting and after homogenisation (HT2). 57
4.10. Engineering stress-strain curves of investment-cast Fe-25Al-3.7Al-0.4Ti-1B alloys (in as-cast condition below 400 °C, otherwise homogenised at HT2) representative for various temperatures up to 650 °C under tensile loading. The abscissa is cut off and does not show the fracture point at 650 °C. Reproduced and adapted from [143]. 58
4.11. Tensile properties of investment-cast Fe-25Al-3.7Al-0.4Ti-1B dependent on temperature: (a) $R_{p0.2}$ and R_m, (b) A and Z. Reproduced and adapted from [143]. . . 60
4.12. Fracture surfaces of the Fe-25Al-3.7Mo-0.4Ti-1B alloy following tensile tests at room temperature (a), 550 °C (b) and 650 °C (c). The fracture surfaces from stereographic imaging are shown on the left, while magnified SEM images are presented on the right. Reproduced and adapted from [143]. 61
4.13. Comparison of temperature dependence of 0.2% proof strength $R_{p0.2}$ (a) and elongation after fracture A (b) of investment-cast Fe-25Al-3.7Mo-0.4Ti-1B from tensile tests with literature data [18, 38, 99, 115, 127, 131]. P92 represents minimum values defined by DIN EN 10216-2 [13]. Adapted from [143]. 64
4.14. True creep strain e_{ft} over time t of Fe-25Al-3.7Mo-0.4Ti-1B (in HT2 state) tested at temperatures between 600 and 700 °C and various constant loads translated as initial stresses σ_0. (a) Full view of all graphs (reproduced from [143]), (b) magnified view of selected graphs. 67
4.15. Half-logarithmic plot of true creep rate $\dot{e}_{ft}$ over time t of homogenised Fe-25Al-3.7Mo-0.4Ti-1B tested at temperatures between 600 and 700 °C and various initial stresses σ_0. (a) Full view of all graphs cut off after $e_{ft} = 15\%$ (reproduced and adapted from [143]), (b) magnified view on primary creep stage of all graphs. . . 68
4.16. Half-logarithmic plot of true creep rate $\dot{e}_{ft}$ over true creep strain e_{ft} of Fe-25Al-3.7Mo-0.4Ti-1B creep tested at temperatures between 600 and 700 °C and various initial stresses σ_0. (a) Full view of all graphs (b) magnified view on primary creep stage of all graphs. Reproduced and adapted from [143]. 69
4.17. Arrhenius plot of Fe-25Al-3.7Al-0.4Ti-1B for the determination of the creep activation energy Q_c based on the true constant creep rates $\dot{e}_{ft,ss}$ at $e_{ft} = 2\%$ and an initial stress of 120 MPa. 71

4.18. Norton plot of Fe-25Al-3.7Al-0.4Ti-1B for temperatures between 600 to 700 °C based on true minimum creep rates $\dot{e}_{ft,min}$ and true constant creep rates $\dot{e}_{ft,ss}$ locally determined at different creep strains e_{ft}. Stress exponents n are given in the legend. 73

4.19. Norton plot of investment-cast Fe-25Al-3.7Al-0.4Ti-1B at 650 °C in comparison to related ternary and multicomponent Fe_3Al alloys and P92 steel from literature [11, 38, 99, 234, 241]. Alloy types are distinguished by line colour, alloying additions by symbols and creep testing methods by line style. Stress exponents n are given in the legend. 76

4.20. Creep plots of homogenised Fe-25Al-3.7Al-0.4Ti-1B tested under stepwise load increase at 650 °C: (a) Half-logarithmic plot of true creep rate $\dot{e}_{ft}$ over time t, (b) Half-logarithmic plot of true creep rate $\dot{e}_{ft}$ over true creep strain e_{ft} (data from single load tests are given for comparison), (c) Norton plot based on $\dot{e}_{ft,min}$ for creep tests under stepwise load increase and single loads. 78

4.21. Optical micrographs of pristine (a) and creep tested samples (b-d) from longitudinal cross-sections (loading direction is horizontal). (b) 600 °C/120 MPa, (c) 650 °C/200 MPa, (d) 700 °C/120 MPa. 80

4.22. Illustration of local creep cavitation quantification within Fe-25Al-3.7Al-0.4Ti-1B (shown example: 650 °C/200 MPa) dependent on the distance to the fractured surface by division of longitudinal macrosections into finite measurement sections. Cavities, as identified by segmentation, are exemplarily shown in a magnified view. 81

4.23. Feret diameter of cavities, cavity fraction, cavity density and specimen diameter over distance from fracture surface of Fe-25Al-3.7Al-0.4Ti-1B creep tested at 650 and 700 °C and two initial stresses σ_0 each. Mean values and standard deviations of the original homogenised state are additionally displayed in the plots. Mean cavity parameters and given creep results of investigated specimens are given in the legends. 82

4.24. $R_{p0.2}$ and $R_{dp0.2}$ as a function of T for different Fe-Al alloys: (a) Fe_3Al-4Mo-TiB_2-type [38], (b) Fe_3Al-2Mo-TiB_2-type [38, 127], (c) Fe_3Al-TiB_2-type [99, 131] and (d) binary Fe_3Al [34, 88]. 86

4.25. Engineering stress-strain curves at room temperature under compressive and tensile loading for differently processed Fe-25Al-3.7Al-0.4Ti-1B alloys: (a) die-cast and homogenised (HT2), (b) investment-cast in as-cast state. 88

5.1. SEM-BSE micrographs of as-cast Fe–26Al-yMo-0.5Ti-zB alloys (26-y-z). Reproduced from Abel et al. [191] under the CC BY 4.0 licence. 92

5.2. SEM-BSE micrographs of as-cast Fe-23.5Al-yMo-0.5Ti-zB alloys (23.5-y-z). Reproduced from Abel et al. [191] under the CC BY 4.0 licence. 92

5.3. Secondary phase fractions f_p including both Mo_2FeB_2 and TiB_2-type particles in as-cast Fe-xAl-yMo-0.5Ti-zB alloys. Adapted from Abel et al. [191] under the CC BY 4.0 licence. 93

5.4. DTA heating curves of as-cast Fe-xAl-yMo-0.5Ti-zB alloys with a constant heating rate of 10 K/min: (a) solid-state transformation range and (b) melting transition range. Reproduced from Abel et al. [191] under the CC BY 4.0 licence. 95

5.5. Mean HV10 macrohardness (a) and mean HV0.01 microhardness in the Fe_3Al matrix phase (b) of as-cast Fe-xAl-yMo-0.5Ti-zB alloys. Adapted from Abel et al. [191] under the CC BY 4.0 licence. 96

5.6. Average 0.2% proof strength $R_{p0.2}$ and ultimate tensile strength R_m at room temperature (a) and 550 °C (b) in Fe-xAl-yMo-0.5Ti-zB alloys. Specimens at 550 °C were homogenised at HT2 before testing. Adapted from Abel et al. [191] under the CC BY 4.0 licence. 97

6.1. True stress-strain curves of two investment-cast Fe-23.5Al-4Mo-0.5Ti-0.5B specimens at 550 °C with equal processing conditions and test parameters. 103

6.2. Inverse pole figures measured by EBSD along the tensile axis (X-direction) of investment-cast 23.5-4-0.5 alloys in HT2 state after tensile testing at 550 °C: Comparison of gauge sections (a,c) and threading sections (b,d) in specimens A and B respectively. 104

6.3. EBSD grain size distributions of investment-cast 23.5-4-0.5 alloys in HT2 state after tensile testing at 550 °C: Comparison of gauge sections (a,b) and threading sections (c,d) in specimens A and B respectively. 106

6.4. EBSD local misorientation maps and normalised frequency distributions below <5° in investment-cast 23.5-4-0.5 alloys in HT2 state after tensile testing at 550 °C: Comparison of gauge sections (a,b) and threading sections (c,d) in specimens A and B respectively, (e) magnification of local misorientation map close to the fracture surface of specimen B. 108

6.5. Overview and magnified SEM images of the fracture surfaces of specimens A (a-c) and B (d-f) in investment-cast 23.5-4-0.5 alloys in HT2 state after tensile testing at 550 °C. 109

7.1. Optical microsections from edge to centre of Fe-25Al-3.7Mo-0.4Ti-1B step samples after die casting (a) and investment casting (b) as a function of wall thickness. Reproduced from [143]. 114

7.2. Average grain diameter d_{gs} and mean Vickers macrohardness H of die-cast and investment-cast samples of as-cast Fe-25Al-3.7Mo-0.4Ti-1B over solidification rate dT/dt. Regression lines of both datasets are displayed as dashed lines. Reproduced and adapted from [143]. 115

7.3. SEM microsections of die-cast Fe-25Al-3.7Mo-0.4Ti-1B: (a) as-cast condition, (b) after homogenisation treatment HT2 (1000 °C/100 h/FC). Adapted from [143]. . 116

7.4. Comparison of average grain diameters d_{gs} (a) and mean macrohardness H (b) of Fe-25Al-3.7Mo-0.4Ti-1B step samples with different wall thicknesses (2.5/20 mm), casting methods (DC/IC) and heat treatments (AC/HT1/HT2). (b) adapted from [143]. 117

7.5. Comparison of average secondary phase fractions f_p of Mo_2FeB_2 particles (a) and mean HV0.01 microhardness H of matrix and eutectic phase (b) in Fe-25Al-3.7Mo-0.4Ti-1B step samples with different wall thicknesses (2.5/20 mm), casting methods (DC/IC) and heat treatments (AC/HT2 in (a) or AC/HT1/HT2 in (b)). (a) adapted from [143]. 119

7.6. Relative length changes $\Delta L/L_0$ measured at an annealing temperature of 400 °C over time for various quinary and binary alloys with different prior processing history. Experimental and smoothed curves are displayed. Literature data on a water-quenched Fe-45Al alloy is given for comparison [296]. 120

7.7. Juxtaposition of three different methods to investigate retained thermal vacancies in various quinary (i.e. die-cast (a,e,i) and investment-cast (b,f,j) Fe-25Al-3.7Mo-0.4Ti-1B) and binary alloys (i.e. Fe-27Al (c,g,k) and Fe-37Al (d,h,l)) after quenching from 700 (OQ1) or 1000 °C (OQ2) and after subsequent vacancy annealing (HT1: 400 °C/168 h/FC): (a-d) differential dilatometry recording the relative length changes $\Delta L/L_0$ over temperature during two heating cycles at 6 Kmin^{-1}, (e-h) true density ρ_t measurements, (i-l) HV0.1 microhardness H measured in the Fe_3Al matrix. 122

7.8. HV0.1 microhardness and 95% CI measured in the Fe_3Al matrix of quinary and binary alloys after quenching from 700 °C (OQ1) or 1000 °C (OQ2) and after subsequent vacancy annealing (HT1: 400 °C/168 h/FC). 125

7.9. Engineering stress-strain curves of small and miniature tensile specimens of Fe-25Al-3.7Mo-0.4Ti-1B with different average grain diameters d_{gs} at room temperature. Information on processing condition, specimen specification and strain rate during testing is given in the legend. 129
7.10. (a) Stress-strain curve of an as-cast Fe-25Al-3.7Mo-0.4Ti-1B miniature tensile specimen, (b) 2D colour plot of local strain e_x measured and analysed by DIC line scanning on the flat gauge section as a function of line position x and the applied strain e, (c) DIC 2D maps of the flat gauge section and magnifications of the maximum strain peak at x = ∼2.5 mm at distinct applied strains e. 132
7.11. Optical images of the die-cast Fe-25Al-3.7Mo-0.4Ti-1B miniature tensile specimen (a) before tensile testing and (b) after fracture, (c) inclined view and magnification of the maximum strain peak at x = ∼2.5 mm after fracture by SEM. 133

A.1. Drawing (a) and 3D rendering (b) of Fe-26Al-4Mo-0.5Ti-1B investment castings for the processing of tensile and creep specimens (extraction location indicated in grey). Adapted from [143]. 145
A.2. Drawing (a) and 3D rendering (b) of Fe-xAl-yMo-Ti-zB investment castings with different alloy concentrations. Locations for extraction of tensile blanks (grey) and metallographic samples (green) are indicated by colours. Adapted from [143]. . . 146
A.3. Drawing (a) and 3D rendering (b) of Fe-26AlMo-0.5Ti-1B die castings for the processing of tensile specimens (extraction location indicated in grey). Adapted from [143]. 147
A.4. Drawing (a) and 3D rendering (b) of Fe-26Al-4Mo-0.5Ti-1B step samples cast into both copper dies and ceramic moulds. Locations for extraction of metallographic samples at different wall thicknesses are indicated in green. Adapted from [143]. 148
A.5. Drawings of tensile specimen geometries: (a) standard geometry with cylindrical gauge section, a diameter of 10 mm and L_c = 60 mm [143], (b) reduced cylindrical gauge section, a diameter of 5 mm and L_c = 30 mm, (c) miniature geometry with flat gauge section, a thickness of 1 mm thickness, a width of 2.5 mm and L_c = 15 mm. 149
A.6. Drawing of creep specimen geometry with cylindrical gauge section, a diameter of 8 mm and L_c = 60 mm [143]. 149
A.7. Drawing of compression specimen geometry with cylindrical gauge section and a diameter of 10 mm. 149

B.1. Engineering and true stress-strain curves of investment-cast Fe-25Al-3.7Al-0.4Ti-1B homogenised at HT2 during tensile testing at 650 °C. 151

B.2. SEM images of fracture surfaces of Fe-25Al-3.7Mo-0.4Ti-1B after creep testing at 650 °C/160 MPa. 151

B.3. Comparison of the creep specimen geometry before and after the creep test of Fe-25Al-3.7Mo-0.4Ti-1B [143]. The images compare the maximum and minimum stress levels tested at the three test temperatures 600 °C (a,b), 650 °C (c,d) and 700 °C (e,f). 152

B.4. Optical microsections of cross-sectional areas of Fe-27Al (a,b) and Fe-37Al (c,d) at two magnifications. Images were taken after oil-quenching from 700 °C followed by HT1. 153

B.5. Hall-Petch regression applied to macrohardness HV10 over ${d_{gs}}^{-1/2}$ of Fe-25Al-3.7Mo-0.4Ti-1B step samples. Only die-cast and investment-cast samples with different wall thicknesses and subsequent homogenisation treatment (HT2) were considered. 154

List of Tables

4.1. Measured composition of the Fe-26Al-4Mo-0.5Ti-1B base alloy after casting. Concentrations were determined by ICP-OES except for C (IR absorption), Si (Reduced Molybdosilicate Spectrophotometric Method) and H (CGHE). 44

4.2. Microstructural parameters of investment-cast Fe-25Al-3.7Mo-0.4Ti-1B in the as-cast and HT2 state (1000 °C/100 h/FC). Data reproduced from [143]. 45

4.3. WDS elemental composition of Fe_3Al (matrix) and Mo_2FeB_2 (secondary boride phase) in investment-cast Fe-25Al-3.7Mo-0.4Ti-1B. Li et al.'s elemental compositions of an Fe-25.4-4.2Mo-0.5Ti-1.2B alloy are given for reference [38]. Reproduced and amended from Abel et al. [191] under the CC BY 4.0 licence. 46

4.4. Mean macrohardness HV10, mean microhardness HV0.01 and 95% CI of phases in investment-cast Fe-25Al-3.7Mo-0.4Ti-1B tested in as-cast and homogenised (HT2) state. Data reproduced from [143]. 56

4.5. Mean tensile properties and 95% CI of investment-cast Fe-25Al-3.7Mo-0.4Ti-1B at ambient and elevated temperatures. Reproduced from [143]. 60

5.1. Nominal and actual composition of as-cast Fe-xAl-yMo-0.5Ti-zB alloys (measured by XRF spectroscopy and S-OES*). Reproduced from Abel et al. [191] under the CC BY 4.0 licence. 90

5.2. Average grain diameters d_{gs} and 95% confidence intervals of investment-cast Fe-xAl-yMo-0.5Ti-zB in as-cast condition according to Heyn lineal intercept method. Reproduced from Abel et al. [191] under the CC BY 4.0 licence. 91

5.3. WDS elemental composition of Fe_3Al matrix and Mo_2FeB_2 secondary phase in investment-cast Fe-xAl-yMo-0.5Ti-zB alloys in as-cast condition. Reproduced from Abel et al. [191] under the CC BY 4.0 licence. 91

5.4. Phase transition temperatures of as-cast Fe-xAl-yMo-0.5Ti-zB alloys according to DTA analysis. Reproduced from Abel et al. [191] under the CC BY 4.0 licence. . . 95

7.1. Mean tensile properties and 95% CI (if applicable) at room temperature of several Fe-25Al-3.7Mo-0.4Ti-1B alloys with different average grain diameters d_{gs}. 130

B.1. XRF compositions of quasi-binary Fe-Al alloys after induction melting. 153

B.2. Mean microhardness HV0.1 and 95% CI of Fe_3Al phase in Fe-25Al-3.7Mo-0.4Ti-1B, Fe-27Al and Fe-37Al alloys after oil-quenching (OQ) from different temperatures (OQ1: 700 °C/100 h/OQ, OQ2: 1000 °C/100 h/OQ) as well as after subsequent vacancy annealing at HT1 (400 °C/168 h/FC). 154

List of Acronyms

A2	disordered body-centered cubic crystal structure
AC	as-cast
Al	aluminium
APB	anti-phase boundary
APD	anti-phase domain
Ar	argon
at%	atomic percent, unit of concentration
AWJ	abrasive water jet
B	boron
b.c.c.	body-centered cubic
B2	ordered body-centered cubic crystal structure
BDT	brittle-to-ductile transition
BF	bright-field
BSE	backscattered electron
C	carbon
CGHE	carrier gas hot extraction
CI	confidence interval
Co	cobalt
COD	Crystallography Open Database
Cr	chromium
CTE	coefficient of thermal expansion
Cu	copper
$D0_3$	ordered face-centered cubic crystal structure
DC	die casting, die-cast
dDRX	discontinuous dynamic recrystallisation processes
DIC	digital image correlation
DTA	differential thermal analysis
EBSD	electron backscatter diffraction
EDS	energy-dispersive x-ray spectroscopy
EELS	energy electron loss spectroscopy
f.c.c.	face-centered cubic
FC	furnace-cooled
Fe	iron
Fe-Al	iron aluminide
H	hydrogen
h.c.p.	hexagonal closed packed
HAGB	high-angle grain boundary
HT1	heat treatment 1 (400 °C/168 h/FC)
HT2	heat treatment 2 (1000 °C/100 h/FC)
IC	investment casting, investment-cast
ICP-OES	inductively coupled plasma assisted optical emission spectrometry
ICSD	Inorganic Crystal Structure Database
IPF	inverse pole figure
IR	infrared
LAGB	low-angle grain boundary
LRO	long-range order
Mn	manganese
Mo	molybdenum
mud	multiples of uniform density
Nb	niobium
Ni	nickel
O	oxygen

OM	optical microscopy
OP-S	oxide polishing suspension
OQ	oil-quenched
OQ1	oil-quenching treatment 1 (700 °C/100 h/OQ)
OQ2	oil-quenching treatment 2 (1000 °C/100 h/OQ)
PLB	power law breakdown (referring to Norton law)
ppm	parts per million, unit of concentration
px	pixel
rpm	rounds per minute
S-OES	spark optical emission spectrometry
SAD	selected area electron diffraction
SE	secondary electrons
SEM	scanning electron microscopy
Si	silicon
SSH	solid-solution hardening
STEM	scanning transmission electron microscopy
t(x°)	transversal plane (orientation on this plane)
TCA	tension-compression asymmetry
TEM	transmission electron microscopy
TG	transgranular
Ti	titanium
VRE	variable renewable energies
WDS	wavelength-dispersive x-ray spectroscopy
wt%	weight percent, unit of concentration
XRD	x-ray diffraction
XRF	x-ray fluorescence (spectroscopy)
YSA	yield stress anomaly
Zr	zirconium

List of Symbols

Notation	Unit	Description
$\alpha(T)$	10^{-5} K^{-1}	physical coefficient of thermal expansion (CTE)
$\bar{\alpha}(T_0, T)$	10^{-5} K^{-1}	technical coefficient of thermal expansion (CTE)
θ	°	diffracted angle
λ	Å	x-ray wavelength
λ_p	µm	average particle distance
ρ_t	g·cm^{-3}	true density
σ_0	MPa	initial stress
σ_{eng}	MPa	engineering stress
$\sigma_{lattice}$	MPa	lattice resistance
σ_{orowan}	MPa	Orowan looping stress
σ_t	MPa	true stress
σ_y	MPa	yield stress
υ	–	Poisson's ratio
A	%	elongation after fracture
A_{gs}	m	grain area
A_{per}	%	permanent creep elongation
A_u	%	elongation after creep fracture
B	GPa	bulk modulus
b	Å	Burgers vector
$CRSS$	MPa	critical resolved shear stress

Notation	Unit	Description
C_0	-	refinement factor (Orowan looping stress)
c	wt% or at% or ppm	concentration
d	mm	thickness
d_0	mm	original diameter of gauge sections in compression/tensile tests
d_{gs}	m	average grain diameter
d_{hkl}	nm	lattice plane spacing
d_{HV}	mm^2	mean diagonal length of a Vickers indent
d_p	µm	average particle size
E	GPa	Young's modulus
e	%	strain
$\dot{e}_f$	s^{-1}	creep rate
e_e	%	elastic strain during initial creep loading
$\dot{e}_{ft}$	s^{-1}	true creep rate
$\dot{e}_{ft,min}$	s^{-1}	true minimum creep rate
$\dot{e}_{ft,ss}$	s^{-1}	true constant creep rate
e_f	%	creep strain
e_{ft}	%	true creep strain
e_i	%	strain during initial creep loading
e_p	%	plastic strain during initial creep loading
e_t	%	true strain
e_x	%	local strain along the specimen axis
F	N	force

Notation	Unit	Description
$f_{f,w}$ or $f_{f,h}$	s^{-1}	fundamental resonant frequency of a bar in flexure along width or height
f_t	s^{-1}	fundamental resonant frequency of a bar in torsion
f_m	vol% or -	average matrix fraction
f_p	vol% or -	average secondary phase fraction
G	GPa	shear modulus
H	HV10 or HV0.1 or HV0.01	Vickers hardness
h	mm	height
k	MPa·µm$^{0.5}$	Hall-Petch constant
$\Delta L/L_0$	-	relative length change
ΔL	µm	absolute length change
L_0	mm	initial gauge length, sample length at reference temperature
L_c	mm	parallel gauge length
L_e	mm	extensometer gauge length
L_T	mm	sample length at temperature T
L_u	mm	final gauge length after fracture
l	mm	length
m_E	GPa	slope of the elastic stress-elongation curve
m_s	mg	sample mass
m_T	-	Taylor factor
n	-	Norton stress exponent

Notation	**Unit**	**Description**
n_{total} or n_{gs}	-	total count of grains or count below a specific grain size
p_1	Pa	cell chamber pressure
p_2	Pa	cell chamber pressure after pressure drop
Q_c	$kJ \cdot mol^{-1}$	activation energy of creep
$R_{dp0.2}$	MPa	proof strength at 0.2 % plastic compression
R_m	MPa	ultimate tensile strength
$R_{p0.2}$	MPa	proof strength at 0.2 % plastic elongation
Rz	µm	average maximum surface height
$Rz1_{max}$	µm	maximum surface height
r	-	Feltham's nucleation exponent
S_0	mm^2	original cross-sectional area of gauge sections in compression/tensile tests
S_u	mm^2	minimum cross-sectional area after fracture
ΔT	°C	temperature difference
dT/dt	$K \cdot s^{-1}$	solidification rate
T	°C	test temperature
T_0	°C	reference temperature (20 °C)
T_{BDT}	°C	brittle-to-ductile transition temperature
$T_c^{B2\leftrightarrow A2}$	°C	solid-state transformation temperature from B2 to A2 structure
$T_c^{D0_3\leftrightarrow B2}$	°C	solid-state transformation temperature from $D0_3$ to B2 structure
$T_{liquidus}$	°C	liquidus temperature
$T_{solidus}$	°C	solidus temperature

Notation	**Unit**	**Description**
T_{YSA}	°C	temperature of yield stress anomaly
t	s or min or h	time
t_u	h	time to rupture
V_{cell}	cm^3	cell chamber volume
V_{exp}	cm^3	expansion chamber volume
V_s	cm^3	skeletal volume
w	mm	width
x	at%	Al concentration
y	at%	Mo concentration
Z	%	percentage reduction of area
z	at%	B concentration

Chapter

1

Introduction and motivation

Variable renewable energies (VRE) such as solar photovoltaics and wind power continue to globally merge onto the market for electricity generation (see Figure 1.1). Due to their low cost of energy generation and more benevolent national policies initiated to enforce their roll-out, forecasts see them surpassing conventional and other renewable technologies such as hydropower in the upcoming years [1]. However, VREs pose significant challenges and risks to grid stability due to their environmental fluctuations and difficulty of predicting total power output [1, 2]. The consequences are both economic and security related: imbalances between supply and demand for energy can lead to curtailment measures in the event of grid congestion or even blackouts of critical infrastructure in the event of power shortages. Therefore, electrical energy storages and flexible power generation methods are indispensable parts of our future VRE infrastructure [3–5]. Thermomechanical and chemical energy storages such as compressed or liquid air energy storage, pumped thermal energy storage and Power-to-Gas (methane, H_2) technologies provide the highest capacities for long-term storage and will therefore majorly contribute to the energy supply [6–8]. Complementary to these energy storage units, power plant systems will be required for efficient energy re-conversion and electricity generation. They will also offer the required flexibility for grid stability due to their inherent grid inertia and black start capability [5].

The working conditions for the required turbomachinery components in power plants, which mainly depict compressors, turbines and heat exchangers, are particularly demanding. Besides high pressures of several 100 bars and corrosive environments by exposure to steam, air or working fluids, wide temperature ranges of 300–800 °C are possible [4]. New requirements on the corrosion, oxidation and wear resistance could arise for the new generation of power cycles featuring the use of supercritical CO_2 as working fluids [9, 10]. It offers both the perspective to further boost thermal efficiency and to downsize power plant components. Casting processes, which are often required for the manufacture of parts with intricate geometrical features such as turbine wheels, would also largely benefit from downsizing.

Materials which are handled as potential candidates for the use in supercritical CO_2 power plants

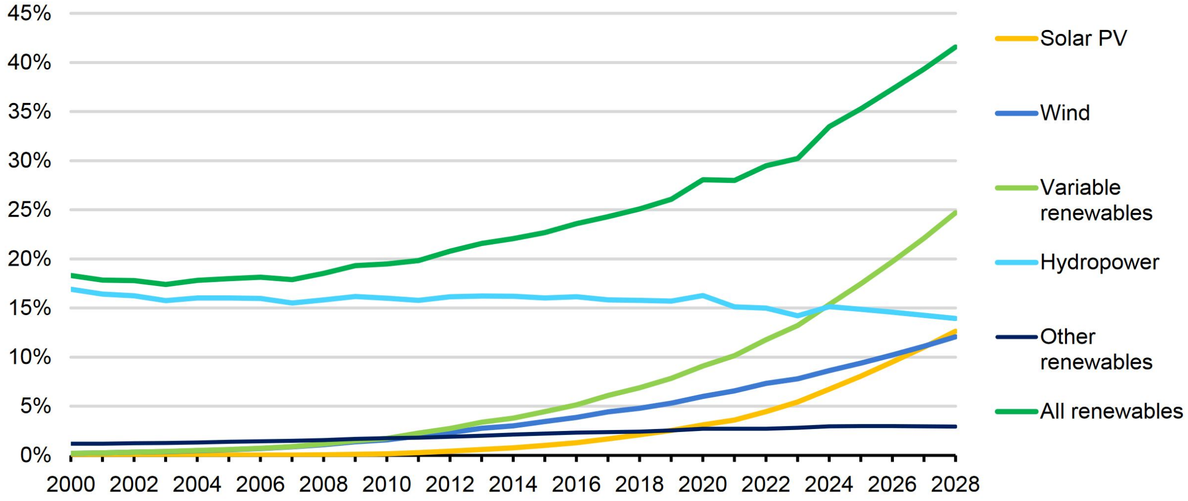

Figure 1.1.: Global share of technologies for electricity generation from 2000 to 2028 reprinted from IEA [1] under the CC BY 4.0 licence.

are commercial P91, P92 and P911 grade ferritic-martensitic steels with 9–12 wt% Cr which represent the group of advanced high-strength steels and belong to the class of heat-resistant stainless steels [11–13]. Especially P92 grade steels (No. 1.4901, DIN/EN designation: X10CrWMoVNb9-2) stand out for their good high-temperature strength, creep resistance and satisfactory corrosion resistance [11, 14, 15]. However, mechanical properties and corrosion resistance decrease significantly above 550 °C, and the high content of expensive transition metal elements makes it a less economically viable solution [13, 16].

A possible substitute for these alloys and the subject of this thesis depict the group of iron aluminides (Fe-Al) which count into the class of ordered intermetallics. They are characterised by good high-temperature strength, high wear resistance, excellent oxidation and corrosion resistance and cost-efficient supply of precursor elements [17, 18]. Due to their low density and hence high-specific strength up to 800 °C, they are able to outcompete heat-resistant steels in these temperature ranges from a mechanical and economical point of view [18]. Due to the potential for weight reduction, they are also handled for structural applications in mobility sectors (e.g. automotive, aeronautics) and more [19, 20].

Iron aluminide alloys were already successfully processed by many manufacturing routes including rolling, forging, casting, powder metallurgy, and additive manufacturing [21–24]. For the production of complex components, casting techniques like investment casting and centrifugal casting are often necessary. These methods proved effective for casting Fe-Al parts on an industrial scale [22, 25]. However, only a limited number of applications have been implemented to date [26–30]. The primary challenges are the generally low ductility at room temperature and the insufficient strength above 600 °C [31, 32]. Measures to tackle the lack of mechanical strength at higher temperatures mainly focussed on alloy development. These aimed at introducing additional strengthening by solutes in ternary Fe-Al-X alloys, by particles and by ordering [33–36]. This is driven by the increasing interest of researchers in ternary and higher-order multicomponent alloy design which often solidify by an eutectic reaction to create complex microstructures with superior mechanical properties [37]. In the past years, a promising new quinary Fe-26Al-4Mo-0.5Ti-1B alloy gained more attention as the mechanical performance under quasi-static compressive and creep loading was comparable or even surpassed the properties of P92 steel [38]. However, application-relevant data such as thermophyiscal properties and mechanical properties under tensile loading up to high temperatures were not determined yet. Besides, several strengthening contributions induced by grain refinement, solid-solution hardening, particle hardening and thermal vacancy hardening were not yet addressed separately or in co-dependency. Due to the complexity of the alloy system, their contributions could be greatly influenced by processing parameters and alloy composition. Based on these knowledge gaps, two main goals were defined for this dissertation: i) to assess the suitability of Fe-26Al-4Mo-0.5Ti-1B alloys from industrially relevant casting processes for structural high-temperature applications and ii) to advance the development of quinary Fe_3Al-Mo-Ti-B alloy systems by fostering an understanding of processing and its impact on microstructure and mechanical properties.

To this end, centrifugal investment castings of Fe-26-4Mo-0.5Ti-1B were characterised with emphasis on microstructural evolution, thermophysical properties and mechanical properties, mainly under quasi-static tensile and creep loading up to 700 °C. Selected mechanical specimens were re-examined by fractographic analysis to assess damage mechanisms in the loading scenarios tested. For alloy development, selected steps along the casting process chain were investigated to derive their potential for optimising mechanical performance. Starting with the choice of alloy composition, the influence of small changes in the concentrations of Al, Mo and B was systematically investigated with respect to microstructure and tensile strength at room and elevated (550 °C) temperatures. The effect of microstructural variations induced by the centrifugal investment casting process was investigated by way of example for its effect on hot tensile properties. In addition, castings with different cooling rates and two subsequent heat treatments were investigated for grain size, secondary phase volume fraction and hardness to assess the relationship between processing, microstructure and properties at room temperature. The effect of thermal vacancy hardening and grain refinement on mechanical properties of quinary Fe_3Al-Mo-Ti-B alloys was evaluated by more in-depth investigations. Thermal vacancy hardening was studied by quenching experiments of quinary and binary Fe-Al alloys with different Al concentrations and a cross-correlation approach of several indirect measurement techniques such as isothermal and differential dilatometry, density and hardness measurements. In turn, the effect of grain refinement on ambient tensile strength and ductility was examined on the base of miniature tensile tests paired with digital image correlation.

Chapter

2 Literature review

Intermetallic iron aluminides (Fe-Al) have been subject to extensive investigation as early as the end of the 19th century [39]. Due to the scarcity of resources in the initial decades of the 20th century, Fe-Al compounds became the focus of scientific attention. The increasing interest of iron aluminides was attributed to their favourable characteristics, including outstanding oxidation and corrosion resistance, high wear resistance and good high-temperature strength [17, 18]. Nowadays, the interest still persists as current environmental policy goals aim for the development and application of high-performance materials with reduced environmental footprint [40]. The following sections will briefly introduce important principles and theories on binary and higher-order Fe-Al alloys with a focus on mechanical properties to put quinary Fe-Al-Mo-Ti-B alloys into context. Multiple reviews on the current knowledge of Fe-Al alloys including detailed descriptions of phases, properties, mechanistics and applications have been also published and are recommended for further reading [18, 41–43].

2.1. Binary Fe-Al alloy system

As the name implies, iron aluminides are primarily composed of iron (Fe) and aluminium (Al).The most relevant and most cited phases lie in the Al concentration range up to 50 at%. Figure 2.1a and b illustrates the respective phase diagram of iron aluminides and the crystal structures that exist in equilibrium [43]. At an Al concentration below 19 at% at 300 °C, Fe-Al is present as a disordered body-centred cubic (b.c.c.) A2 structure (or α-Fe) at room temperature, i.e. Fe builds a solid solution with Al on randomly occupied lattice sites. At concentrations above 19 at% Al, an ordered intermetallic phase with a face-centred cubic (f.c.c.) $D0_3$ structure and Fe_3Al stoichiometry can occur in chemical equilibrium. This phase is constructed as a supercell comprising eight individual b.c.c. unit cells and three sublattices (α, β and γ). In contrast, above approximately 35 at%, an ordered intermetallic phase with a b.c.c. B2 structure and equiatomic FeAl stoichiometry is formed. This phase is characterised by a regular unit cell with Fe at the corner lattice sites and Al in the centre position. Both Fe_3Al and FeAl belong to the class of non-stoichiometric intermetallics as they build an ordered phase in a range of compositions [45]. The deviation to actual

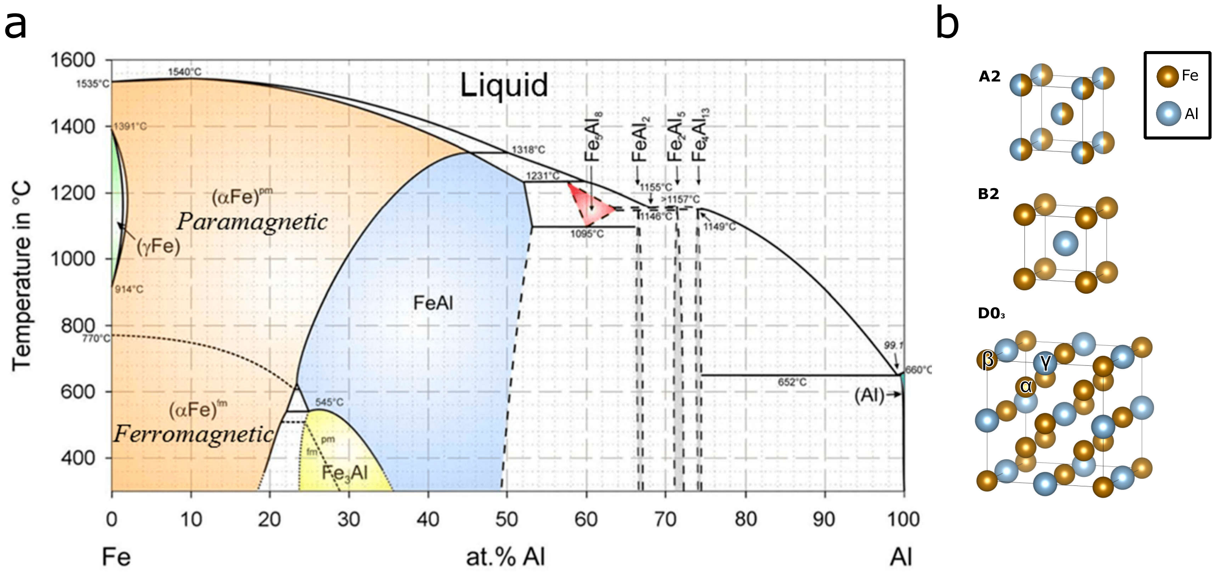

Figure 2.1.: (a) Phase diagram of binary Fe-Al reproduced from Zamanzade et al. [43] under the CC BY 4.0 licence, (b) dominant crystal structures of Fe-Al alloys up to an Al content of 50 at% (created by Vesta ver. 3.5.7) [44].

composition is balanced by constitutional vacancies. A complete $D0_3$ Fe_3Al order is observed to exist within an Al range of approximately 24–35 at% at ambient conditions. Close to ideal Fe_3Al stoichiometry, the thermal stability of the $D0_3$ phase extends to a maximum of 545 °C. At this temperature, the $D0_3$ structure undergoes an order-order transition to form the B2 structure. At 821 °C, an order-disorder transition from B2 to A2 structure takes place.

Both solid-state transformations mark second order transitions according to the Ehrenfest classification [46]. Hence, for the reverse case of cooling from higher temperatures, ordering of a disordered state cannot be fully suppressed even by high cooling rates (e.g. by quenching) [47]. Thereby, ordering proceeds by growing of individual ordered nuclei which eventually become anti-phase domains (APD) [48]. They are usually in the sub-µm range and their name comes from the formation of anti-phase boundaries (APB). These depict thin disordered regions in wavy shapes when resolved by TEM and remain between adjacent ordered domains [48, 49]. Besides ordering, APBs can also originate from dislocation motion which is locally disrupting the ordered lattice structure [50, 51]. These are formed in-between the $D0_3$-type or B_2-type perfect superdislocations which were described to dissociate into coupled four-fold or two-fold partials in $D0_3$ or B2 lattices respectively [52]. Dislocations were mostly seen to move as screw dislocations on {110} slip planes with a primary <111> slip direction [53]. However, multiple studies found and discussed that B2-type superdislocations are mostly present in $D0_3$ ordered Fe-Al alloys at room temperature [54–56]. These imperfect $D0_3$ superdislocations produce trailing APBs which change the local order and deformation behaviour [50, 56].

2.2. Thermophysical properties

The physical properties of Fe-Al alloys are largely determined by the Al concentration and the ordered state, and thus exhibit considerable variation. The addition of aluminium can result in a reduction of the density to 6.72 gcm^{-3} for Fe_3Al or 5.56 gcm^{-3} for FeAl [57]. Similarly, the Young's modulus can be modified from 121 GPa for hyperstoichiometric Fe_3Al to 173 GPa for FeAl [58]. The substitution of Fe atoms as in ternary Fe_3Al-X alloys was also demonstrated to lead to a considerable increases of Young's modulus if large solute concentrations were chosen [59]. The coefficients of thermal expansion (CTE) are particularly dependent on order and magnetic state. To illustrate, the physical coefficients of thermal expansion $\alpha(T)$ with Al concentrations up to 25 at% Al are between 1.3 and $1.4 \cdot 10^{-5}\ \text{K}^{-1}$ at 200 °C, while at temperatures around 550 °C they can vary from $1.4 \cdot 10^{-4}$ to $4.0 \cdot 10^{-5}\ \text{K}^{-1}$ [60].

2.3. Mechanical properties

The mechanical properties of intermetallic Fe-Al alloys are unique compared to their metallic competitors. As for other intermetallic aluminides including Ni-Al and Ti-Al alloys, their strength comes from their strong chemical bonding of unequal metal atom species and the long-range order of lattices [45, 61–63]. Both aspects indirectly determine their distinctive properties such as high melting points, high disordering temperatures and low diffusivities. These are usually good indicators for high yield strength and high creep resistance which are required for high-temperature and structural applications [64, 65]. However, these properties usually come at the expense of poor ductility and fracture toughness at low temperatures [66, 67].

2.3.1. Yield strength and strengthening mechanisms

The low density and high yield strengths of Fe-Al based alloys make for competitive specific strengths compared to Co- and Ni-based alloys and steels [20, 29]. However, the yield strength which defines the onset of plastic deformation is more variable and subject to multiple effects in

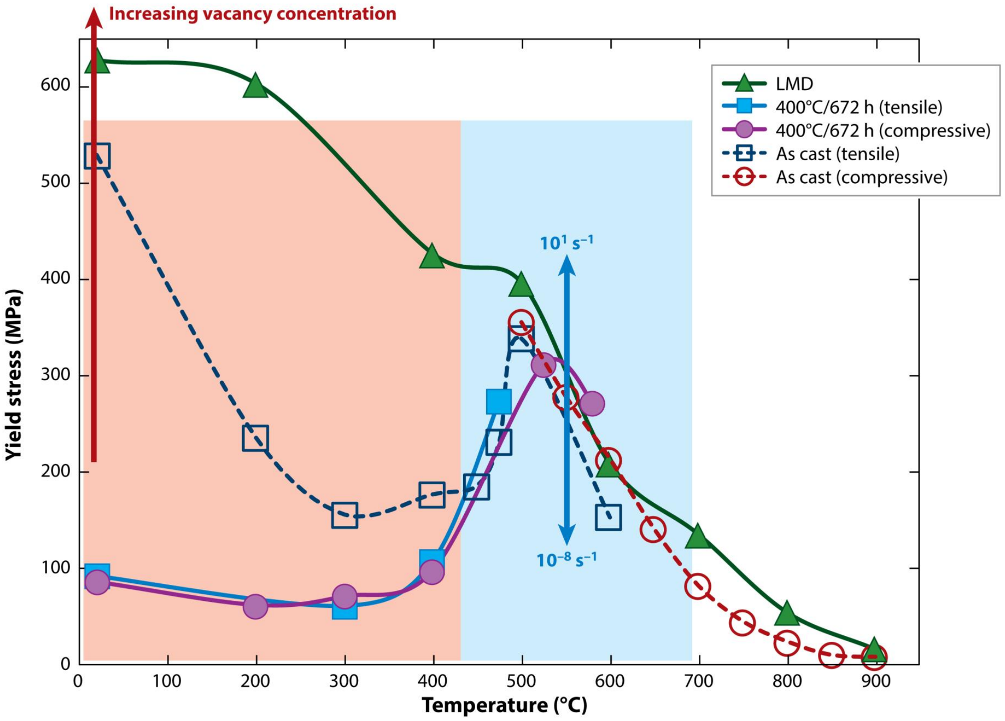

Figure 2.2.: (a) Compressive and tensile 0.2% proof strength of Fe-(26-28)Al either processed by laser metal deposition (LMD) [24] or casting as a function of temperature. Castings are either in as-cast condition or were annealed at 400 °C/672 h. The red arrow indicates an estimate of thermal vacancy hardening and the red area depicts the influenced temperature range. The blue area encloses the temperature range of the YSA peak, with the blue arrow indicating the strain rate dependency of strength. Reprinted with permission from [18].

Fe-Al alloys at different temperatures.

At temperatures below about 400 °C (see red area in Figure 2.2), thermal vacancies were shown to contribute to yield strength in many Fe-Al alloys [68–71]. In demarcation to constitutional vacancies, thermal vacancies easily form at elevated temperatures, especially due to low formation enthalpies in Fe-Al alloys, and can be retained to room temperature by high cooling rates [72]. The strengthening effect as for constitutional vacancies is induced by the interaction of dislocations with the modified elastic field of point defects [73]. In turn, subsequent annealing at temperatures sufficient to activate vacancy migration (≥ 400 °C) can annihilate frozen-in thermal vacancies and revoke the strengthening effect after a sufficient holding time (e.g. one week) [74]. The yield strength increase was mostly proposed to follow a square root dependency on concentration [69]. A variety of methods were used to relate the thermal vacancy concentration to x-ray and bulk density, hardness, macroscopic length change and positron lifetime [69, 75–78]. Furthermore, the effect of thermal vacancy hardening was shown to increase with Al concentration and quenching temperature [69, 73]. Therefore, the maximum yield strength increase induced by thermal vacancies was shown to considerably vary, from only 30 rel% in binary $D0_3$ Fe-26Al up to 500 rel% in B2 Fe-40Al [70, 71]. The addition of Ni solutes in ternary B2 Fe-Al-X alloys had anomalous effects on the thermal vacancy hardening effect, with specific solute concentrations reducing the hardening effect compared to unalloyed Fe-Al [79, 80]. Studies on other solutes concluded a lower thermal vacancy contribution due to higher equilibrium strengths after low-temperature annealing [81].

Above 400 °C, thermal vacancy hardening is overlapped by multiple hardening mechanisms and a local maximum in strength becomes apparent between 400–600 °C (see blue area in Figure 2.2). This maximum is referred to as the yield stress anomaly (YSA) whose origin is a matter of debate since a few decades. Several strengthening models were suggested to explain the causes of the anomalous peak of yield strength [82–87]. A link between the YSA and the $D0_3 \leftrightarrow B2$ phase transformation was disproved in a study [88]. Today, the most widely accepted theory is the vacancy hardening model [86] which suggests that the formation of thermal vacancies is drastically enhanced below the YSA while mobility is still constraint. Hence, the strength increases with increasing thermal vacancy concentration until sufficient vacancy migration occurs to enable dislocation climb, resulting in a decrease in strength. Still, there are more active mechanisms which govern strengthening and softening behaviour in this temperature range. Yoshimi et al. [85] connected the stress increase before reaching the YSA temperature T_{YSA} to the decomposition of <111> superdislocations to <100> partials which are less mobile at this temperature or get pinned by thermal vacancies. Against this, Saka et al. [83] explained the stress increase with increasing dissociation and locking of <111> superdislocations by climb. Another pinning mechanism to dislocations was connected to the relaxation and thickening of APBs [84]. All these pinning mechanisms are potentially responsible for the reported strain rate dependency of the YSA whose range of strength is depicted in Figure 2.3 by a blue arrow [89]. All pinning phenomena disappear as soon as the preferred slip direction transitions from <111> to <001> at T_{YSA} and deformation is governed by single dislocations [90, 91].

Above T_{YSA}, the yield strength in binary Fe-Al alloys falls even more rapidly with temperature than in conventional alloys like P92 steel [13, 88]. For this reason, strength improvement is still regarded as the main priority for alloy development. One parameter affecting strength over temperature is a sensible adjustment of Al content, as the yield stress of binary Fe-Al varies sensitively

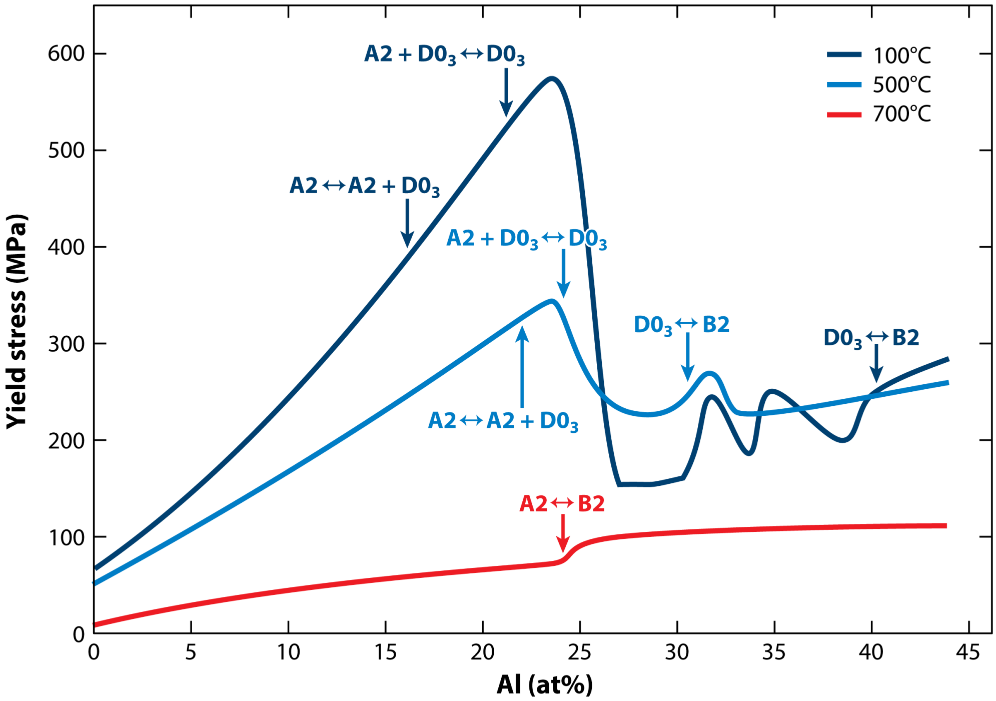

Figure 2.3.: 0.2% proof strength of iron aluminides as a function of Al concentration at 100, 500 and 700 °C. Phase boundaries at the respective temperatures are marked by arrows. Reprinted with permission from [18].

with Al concentration (see Figure 2.3). Yield strength experiences a maximum near the stoichiometric Fe_3Al composition for temperatures up to 500 °C [92]. Hypostoichiometric compositions with A2 + $D0_3$ phase mixtures usually have a lower strength in comparison, but are stronger than hyperstoichiometric compositions with $D0_3$ or B2 structure. Only above the YSA, when the ordered $D0_3$ phase vanishes, hyperstoichiometric compositions with B2 structure maintain slightly higher strengths than compositions with disordered A2 structure. The superior strength in stoichiometric Fe_3Al alloys with $D0_3$ structure is also related to the high degree of long-range order, which mainly reduces dislocation mobility [63, 93].

Further strengthening was therefore achieved by solid solution alloying as the $D0_3$ phase area can be extended to higher temperatures. Multiple solutes such as Ti, Mo, W, Si, V and Nb proved linear increases of $T_c^{D0_3 \leftrightarrow B2}$ with concentration in ternary and higher-order alloys compared to the binary system [38, 88, 94, 95]. Moreover, a few solutes were demonstrated to provide additional strengthening at temperatures beyond T_{YSA} by solid-solution hardening [34]. However, the advantages of solid solution alloying are curtailed by the solubility limit of solutes and the increasing brittleness (see next paragraph).

Adjustment of microstructural features is also able to substantially contribute to increased yield strength. The yield strength of multiple binary Fe-Al alloys between 34–50 at% Al was roughly shown to follow a square root dependency on grain size which suggests contributions by Hall-Petch strengthening [96]. Similarly, it was stated that the factor of grain refinement in Fe-40Al may be translated to a similar factor increase of yield strength [97]. However, grain coarsening at higher temperatures limits the strengthening contribution to lower temperatures.

Besides grain size, particle hardening is another viable solution to increase strength across low and elevated temperatures. Independent of lattice mismatch, both coherent and incoherent particles were shown to have positive effects on mechanical properties. Incoherent secondary phases such as carbides provide increased strength up to 600 °C. However, they can lose their strengthening effect at higher temperatures due to coarsening and be detrimental to ductility due to often observed acicular morphologies [35]. The latter argument also applies to Laves phase particles which depict another option, but are usually difficult to control in their precipitation kinetics [35]. The better option are borides which normally form by a eutectic reaction and, like this, can be distributed along the grain boundaries to prevent grain coarsening of the Fe-Al phase [18]. Therefore, grain boundary-strengthened microstructures can be achieved by conventional casting methods without further heat treatments. In addition, borides provide similar strengthening than carbides and only show slight coarsening after homogenisation treatments [98, 99].

2.3.2. Creep behaviour

Fundamentals of creep

Creep describes the time-dependent plastic deformation behaviour at temperatures higher than $0.4T_{liquidus}$, the absolute melting temperature, under sustained loading [100]. This loading scenario is both interesting from an application-based and scientific point of view. Application-wise, these conditions are critical test scenarios for most structural applications in the aerospace and power plant industries as the yield point is lowered in low strain rate cases. Scientifically speaking, most materials, despite many different characteristics, may be roughly described by the same three stages with respect to creep time and strain [101]. In pure metals, the primary creep stage is marked by a fast increase of creep strain e_f after initial loading with a subsequently declining creep rate $\dot{e}_f$. In some materials, primary creep may be inverted in that creep rate may shortly increase [102]. It is followed by a regime of constant creep rate which characterises the secondary creep stage. As soon as $\dot{e}_f$ slowly, but exponentially increases, tertiary creep is sustained until failure. The evolution of creep rate with time or strain is a result of dynamic dislocation processes and reactions, partially with a formation of subgrain structures [103]. The secondary creep stage which allows for easier comparison of creep properties of different materials defines a unique stage of dynamic equilibrium between nucleation and annihilation of dislocations or a balance between hardening and softening mechanisms [100]. It is described until today by Norton's law according to equation (2.1)

$$\dot{e}_f = A \cdot \left(\frac{\sigma}{E(T)}\right)^n \cdot exp\left(-\frac{Q_c}{k_B T}\right) \tag{2.1}$$

where A defines a material-specific constant, σ the applied stress, E the Young's modulus, n Norton's stress exponent, Q_c the creep activation energy, k_b the Boltzmann constant and T the temperature [101]. The stress exponent n and the activation energy Q_c determine the dependency of creep rate on stress and temperature respectively and were early on recognised, especially n, as an indicator for possible rate-controlling deformation mechanisms [104]. The most frequent were related to diffusional dislocation climb-controlled ($4 \leq n \leq 7$ [105]) and viscous glide-controlled ($n \approx 3$ [106]) deformation mechanisms although they also depend on stress regimes. These are also used to categorise creep data to a class I or class M (metal-type) or a class II or class A (alloy-type) behaviour [101]. Much higher stress exponents ($n \geq 7$) are either related to a power law breakdown (PLB) or to particle hardening, if applicable [100].

Tertiary creep is especially characterised by homogenenously distributed cavitation events which involve the nucleation and growth of nm-sized or micro-cavities [107]. Their formation is mainly triggered by grain boundary sliding, especially in coarse-grained microstructures, by vacancy condensation at particles or by dislocation pile-ups at phase boundaries [101].

Creep in Fe-Al alloys

Although most of the analogies of creep were derived from disordered metals and alloys, creep rates of ordered Fe-Al alloys were found to have similar stress dependencies. Stress exponents n of both binary and higher-order iron aluminides were mostly ranging between 3–5 which was often associated to viscous drag and dislocation climb as rate-controlling mechanisms [102]. However, the influence of order is not yet well understood. Early findings concluded a sharp decrease in creep strength with the transition from $D0_3$ to B2 structure which is connected to the loss of long-range order and the increase of dislocation mobility with less APB drag [18, 93]. Against this, others reported no change in creep mechanism and similar values for n and Q_c [108, 109]. Generalisation of mechanisms is complicated as stress exponents were often reported to vary with temperature and the presence of truly constant creep rates is frequently missing [101]. Furthermore, the strain rate dependency of the YSA could contribute to a distortion of creep data. The insufficient creep strength of binary Fe-Al alloys can be tackled by the same high-temperature strengthening mechanisms presented in subsection 2.3.1. Mostly, increasing ordering temperature with solutes, solid-solution hardening amplifying solute drag and particle hardening by increasing the Orowan looping stress were shown to considerably enhance creep performance [18, 35, 101]. A combination of strengthening strategies was deemed beneficial for achieving good high-temperature strength with acceptable ductility [38].

2.3.3. Ductility

The major cause which is related to poor ductilities with less than 2–4% at room temperature in $D0_3$ and B2 structured Fe-Al alloys is environmental embrittlement [18, 110, 111]. This phenomenon is attributed to the spontaneous reaction of water vapour from atmospheric humidity with aluminium on the surface. This reaction yields the formation of oxides while releasing atomic hydrogen [110, 112]. Hydrogen itself is highly mobile and can ease crack initation and propagation at defects and stress concentrations on the surface or in the volume. This is also attributed to the mainly transgranular cleavage fracture in air [113]. Apart from lower mechanical performance and higher notch sensitivity, difficulties in forming, machining and welding are the consequences [17, 114].

With higher temperatures, binary Fe-Al up to 42 at% Al become gradually more ductile above 200 °C [115]. This is surprising compared to other intermetallics which show a sharp brittle-to-ductile transition (BDT) at much higher temperatures within a short temperature interval (< 100 K) [116, 117]. Only by alloying with transition metal elements, a classical BDT evolves as in ordinary intermetallics and at much higher temperatures [18]. The BDT is usually associated with a sudden increase of fracture toughness or elongation after fracture and sometimes with a change of fracture mode with temperature [117]. However, the temperature of the BDT T_{BDT} is not well defined to this day as different experimental methods are employed and T_{BDT} was shown to be strain rate sensitive [118].

Several ways of increasing the ductility of Fe-Al alloys have been demonstrated, in particular at room temperature. With respect to alloying, only Cr solute additions were found to significantly enhance room temperature ductility, even in combination with other solutes [97, 119]. Minor additions of B also exhibited beneficial effects on ductility and BDT through segregation to grain boundaries where it is thought to increase cohesion [120]. Against this, impurity concentrations of C and Si were recommended to be kept low to avoid precipitation of Fe_3AlC which were discussed to potentially enhance embrittlement [121, 122].

Concerning processing, reduction of thermal vacancies either by slow cooling processes or subsequent low-temperature annealing was shown to recover ductility in Fe-45Al alloys [123]. As described in the previous subsection, thermal vacancies may potentially contribute to hardening at temperatures below 400 °C. Morris and Morris-Muñoz [97] generalised this approach and claimed that the yield strength set by its thermal condition determines the achievable ductility independent of hardening mechanism. Furthermore, processing strategies for grain refinement below 100 µm revealed great potential to increase ductility, particularly with grain sizes below 10 µm [124]. However, this might not always be applicable as others only reported marginal difference in ductility if tested with different grain sizes [125, 126].

With respect to testing, the surface condition of specimens can sensitively affect ductility in analogy to the environmental embrittlement effect. Pre-oxidation by high-temperature annealing or testing in dry, oxygen or vacuum conditions yielded higher ductilities accordingly [111]. Also increased strain rates were shown to affect fracture strains positively [111].

2.4. The Fe-Al-Mo-Ti-B system

With the aim of achieving high-temperature strength with moderate ductility, the quinary Fe_3Al-Mo-Ti-B alloy system has emerged as a promising candidate in previous publications [18, 38, 127]. The main purpose of the alloying elements is to incorporate Mo and Ti solutes into the matrix and to form boride particles. In particular, the addition of Mo provides several areas of improvement. Aqueous corrosion resistance in chloridic and acidic environments as well as the salt spray resistance have been greatly improved by Mo additions [128–130]. Furthermore, Mo has a high solubility of about 6 at% in the Fe_3Al matrix, making it an ideal candidate for solid-solution hardening [131]. The hardening mechanism was mainly attributed to the atomic size misfit generated by Mo with higher metallic radius by substituting for Fe on β-sublattice positions

[88, 132, 133]. At the same time, Mo was measured to increase the D0_3-B2 order transformation by 25–35 $K \cdot (at\%\ Mo)^{-1}$ [88, 134]. In studies by Palm et al. [34], the compressive 0.2% proof strength of a ternary Fe-26Al-4Mo alloy was still 200 MPa at 700 °C and 100 MPa at 800 °C [34]. Positive effects on creep resistance were also observed with Mo additions.

Ti additions have similar effects to Mo as Ti is also likely to sit on Fe β-sublattice sites [133]. It was shown to provide similar strengthening by solid-solution hardening as Mo and had an even greater effect on the shift of the order-order reaction per solute concentration (60 $K \cdot (at\%\ Ti)^{-1}$) [88]. However, larger solute concentrations of > 5 at% revealed a tremendous increase of T_{BDT} to above 600 °C [20].

The addition of minor concentrations of B without further alloying was particularly beneficial in improving ductility at room temperature. B was shown to segregate in minute amounts at the grain boundaries which had a positive effect on grain boundary cohesion [135]. This was later associated to a transition from intercrystalline to transcrystalline fracture and an increase in strength [120]. The segregation and strengthening of grain boundaries by B has also been proposed to mitigate environmental embrittlement in B2 FeAl alloys and thereby increase the achievable ductilities [111, 136]. Once other alloying elements are added, boron has a high tendency to form incoherent particles so that the beneficial effects of B on ductility disappear [18]. In combination with Ti, they build TiB_2 borides along grain boundaries by a eutectic reaction [98, 99]. Due to the pinning of grain boundaries, grain coarsening could be inhibited during homogenisation treatments at 1100–1200 °C for several hours [98, 99]. A fine network of boride particles was most effective in reducing creep rates at relatively high stresses [32, 99].

In combination with Mo, however, it should be mentioned that the ductility of boride-strengthened Fe_3Al alloys was surprisingly maintained at relatively low temperatures as suggested by few recent reports [38, 127]. The BDT of a Fe-25.4Al-4.2Mo-0.5Ti-1.2B alloy was found to be > 250 °C in the polished state, the same alloy with only half the Mo concentration even 100 °C [38]. In addition, the alloys exhibited high compressive strength at temperatures near and above the YSA and particularly low creep rates when compared to high-alloy steels such as P92 [38]. However, mechanical strength was only determined under compressive loading. In addition, the tensile ductility of quinary Fe_3Al-xMo-Ti-B alloys has been reported to be significantly reduced at room temperature and above when Mo concentrations are > 0.5 at% [131].

Chapter

3 Materials and methods

3.1. Processing

Processing of samples for the investigations in this thesis was conducted at the research institute Access e.V. (Aachen, Germany). Fe-26Al-4Mo-0.5Ti-1B (at%) was chosen as a base alloy composition. Seven more quinary alloy compositions with different nominal concentrations of Al (23.5 or 26 at%), Mo (2 or 4 at%) and B (0.5 or 1 at%) were selected for studying the effects on microstructure and mechanical properties (see chapter 5). Quasi-binary Fe-Al alloys with minor additions of Nb, Zr, C and B were used to investigate vacancy hardening in iron aluminide solid solutions (see section 7.2). The base alloy as well as alloy variations (from here on denoted as Fe-xAl-yMo-0.5Ti-zB alloys) were cast by the investment casting (IC) method into preheated ceramic moulds. This process is an important technique to the industry as it allows for the manufacture of complex and thin parts needed for implants, jewellery, turbocharger wheels and more [137, 138]. Ceramic moulds with an inner layer of Al_2O_3 and additional insulation were fabricated based on wax models injected into machined aluminium moulds. Wax models were designed according to their requirements for final specimen dimensions and optimal melt flow behaviour. The basic casting systems were also simulated by MAGMASOFT® at Access e.V. to optimise mould filling and solidification and to reduce porosity. For the filling of ceramic moulds, the centrifugal casting method was employed. It is often paired with investment casting due to its excellent form-filling behaviour, low porosity and improved mechanical properties [139]. Moreover, Fe-Al alloys were already successfully cast with the described techniques on an industrial scale [22, 25]. To examine the effect of cooling rate on the properties of the base alloy (see chapter 7), die casting (DC) was additionally employed. Permanent copper dies offer a much faster solidification and cooling of casts due to the high thermal conductivity and excellent heat transfer capabilities of copper [140]. Copper dies were machined from two halves enclosing the melt and equipped with a quick-release mechanism for rapid extraction. The following sections and subsections will guide the reader through the specifics of the casting processes, post-processing steps and sample manufacture.

3.1.1. Fe-Al-Mo-Ti-B alloys

Quinary iron aluminide alloys with varying Mo, Ti and B additions were produced from commercially available pure elements and commissioned master alloys with an improved melting range. Pure elements consisted of pure Fe (99.8 wt%, PURON Metals, Germany) and high-purity Al (99.998 wt%, Norsk Hydro ASA, Norway). Pure Al was selected as it can build a protective oxide scale on top of the melt before casting [141, 142]. Master alloys in the shape of lose granules were Fe-36.4Mo (wt%, IME RWTH Aachen, Germany), Fe-72.2Ti (wt%, Otto Junker GmbH, Germany) and Fe-19.6B (wt%, Otto Junker GmbH, Germany). Precursor materials were melted and cast into shape in a SuperCast SC centrifugal casting system (LINN High Therm GmbH, Germany). Pellets and granules were sandblasted, cleaned in ethanol and dried before placing them in the crucible. Casting moulds and dies were preheated to a minimum of 100 °C to evaporate residual hydrogen from the inner surfaces. In addition, ceramic moulds were preheated to around 1200 °C in an external furnace. This strategy aims to reduce stresses in the casting by decreasing the thermal gradient in contact with the mould. The casting chamber was flushed with Ar before evacuating to a medium vacuum to avoid incorporating gases or contaminants. Inductive coils provide heating and the resulting melt is homogenised for 120 s. An overheat of 100 to 150 K above the liquidus temperature is set before casting. The melt is injected into the sprue with a rotational speed of 200 rpm for at least 60 s. After casting, ceramic moulds including their castings are transferred to a furnace preheated to at least 1000 °C for slow cooling to ambient temperature ($\sim$3 Kmin^{-1}). In contrast, die castings were cooled in air after removal from the casting chamber (from $\sim$250 °C).

Different mould designs were cast with the methods described above depending on the casting method and the required sample dimensions for characterisation. Those included various designs for the extraction of mechanical test blanks (see Figures A.1, A.2 and A.3 in the appendix) and a step geometry comprising wall thicknesses of 2.5 to 20 mm (see Figure A.4).

Castings were examined for potential cracking both visually and by X-ray radiography [143]. Cracks appeared in the yellow tapered region in Figure A.1b and in the central runner system originating from macroporosities (blue sections wrapped between green slabs in Figures A.2b and A.3b). Exemplary X-ray scans of such cracks are depicted in Figures 3.1a and b and highlighted as (i). Still, most casting sections where mechanical blanks were extracted (indicated as (ii)) appear without cracks. Only crack-free blanks were further processed into mechanical specimens.

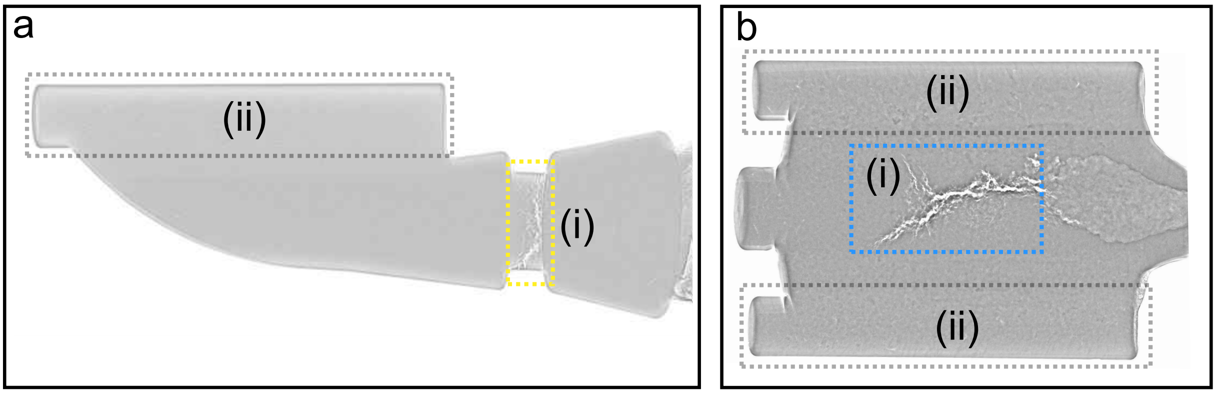

Figure 3.1.: X-ray scans of cracks (i) observed in investment castings of Fe-26Al-4Mo-0.5Ti-1B (a) and investment castings of Fe-23.5Al-4Mo-0.5Ti-1B (b). Tensile blank sections (ii) appear crack-free in both cases. Adapted from [143]

Additional measures such as non-destructive tests were implemented to verify the integrity of specimens before mechanical testing (see subsection 3.2.2).

3.1.2. Quasi-binary Fe-Al alloys

The examination of vacancy hardening in Fe-26Al-4Mo-0.5Ti-1B (see section 7.2) was supported by measurements of quasi-binary Fe-Al alloys with three different nominal Al concentrations (27, 33 and 39 at%), only minor alloy additions (< 0.5 at%) of Nb and Zr and trace amounts of B and C [144, 145]. This comparison allowed for validation of the test setup due to reduced complexity and referencing to literature data. Alloys were fabricated by induction melting at Max-Planck-Institut fuer Eisenforschung GmbH (Duesseldorf, Germany). A furnace with a maximum capacity of 50 kg was used and each alloy was melted from high-purity raw materials in a vacuum. Induction melt products were cut into circular blanks by water-cooled sawing. Alloys originate from a doctoral study by Janda published in 2015 [146]. Further information on cast products is given in his thesis.

3.2. Post-processing

The post-processing steps mainly consisted of extracting casting blanks, applying heat treatments if applicable and contouring to the required specimen dimensions for investigations. Besides the as-cast (AC) state, annealed conditions were also examined. Heat treatments were applied before sample manufacture to avoid the formation of thick oxide scales which would superimpose the annealed condition.

The following subsections only provide general information on used techniques and devices. For more details on specimen geometries and conditions, the reader is advised to refer to the specific subsections on characterisation and mechanical test methods.

3.2.1. Heat treatments

As the effect of thermal vacancy hardening in Fe-Al-Mo-Ti-B alloys was unknown, a comparison to a supposed thermal vacancy-free condition was established by heat treatment. For this purpose, annealing to 400 °C for 168 h in air followed by furnace cooling (heat treatment 1 - HT1) was conducted. Furnace cooling (FC) is necessary to reach an equilibrium state of thermal vacancies at room temperature. In contrast, increased thermal vacancy concentrations were induced by sufficiently long annealing (100 h) at one of two different temperatures (700 °C/1000 °C) in air followed by oil-quenching (OQ).

As the microstructure in Fe-Al-Mo-Ti-B alloys is expected to change at higher temperatures [38], a homogenisation treatment was especially considered for high-temperature tests above 400 °C. Accordingly, samples were annealed to 1000 °C for 100 h in air with subsequent slow cooling in a switched-off furnace (heat treatment 2 - HT2).

Heat treatments (HT1 and HT2) of step samples and mechanical test blanks were conducted at Access e.V. in a Carbolite 13131 furnace (Carbolite Gero GmbH & Co. KG, Germany). Temperatures were monitored by type K thermocouples. Furnace cooling was measured to an average of 0.5 $\mathrm{Kmin^{-1}}$.

Quenching experiments and vacancy removal treatments for dilatometric studies (see subsection 3.4.4 and section 7.2) were conducted at the Federal Institute for Materials Research and Testing (BAM) Berlin. Annealing at 700 °C or HT1 was carried out in a Nabertherm NA 60/85 furnace (Nabertherm GmbH, Germany) with temperature control by type K thermocouples. Samples requiring annealing at 1000 °C were heated in a Nabertherm N 41/H equipped with type S thermocouples.

3.2.2. Sample manufacture and quality control

Mechanical test blanks (grey sections in Figures A.1b, A.2b and A.3b) as well as slabs or cuboids for metallographic investigations (green sections in Figures A.2b and A.4b) were first cut by abrasive water jet (AWJ) machining. With this technique, a part is cut by local abrasion via the impact of a high-pressure water jet which is a mixture of water, air and abrasives. Accordingly, it offers minimum heat generation within thick parts while keeping cutting forces low [147]. Works were performed at Access e.V. with an OMAX 55100 precision jetmachining centre (OMAX Corporation, USA).

Cylindrical specimens for tensile, compressive and creep testing as well as a few samples for thermophysical characterisations were manufactured by turning at Henschel GmbH Germany and at the mechanical workshop of BAM. Gauge sections of tensile specimens were additionally longitudinally polished (i.e. along the gauge section axis) to minimise the risk of notch sensitivity and environmental embrittlement influencing mechanical test results at temperatures below the BDTT. Surfaces were ground to a target average maximum surface height Rz and a maximum surface height $Rz1_{max}$ of < 2 µm. The surface roughness parameters were randomly tested by profilometry with a Hommel-Etamic W20 measuring device (JENOPTIK Industrial Metrology GmbH, Germany) according to DIN EN ISO 4287 [148] and DIN EN ISO 4288 [149] respectively. Two line scans were performed on each tested specimen.

More intricate specimen processing required electrical discharge machining, also known as wire cutting. Such processing was used for the extraction of dilatometer samples from casting or induction melt blanks and for the manufacture of die-cast miniature tensile specimens. Thereby, a cutting wire connected as the cathode is constantly fed from a spool close to the workpiece acting as an anode. The applied voltage under running water leads to frequent current discharges leading to continuous erosion at the workpiece [150]. The works were carried out at the mechanical workshop at BAM.

Due to the observed brittleness and the risk of cracks propagating during further processing (see Figures 3.1a and b), finished specimens were examined on surface cracking before mechanical testing. Non-destructive testing methods were applied including camera-based inspection as well as dye penetrant inspection or magnetic particle inspection. Dye penetrant inspection (see Figure 3.2a) was conducted according to DIN EN ISO 3452-1 [151] applying first a red dye penetrant and second a white developer (Helling GmbH, Germany) on gauge sections to uncover present cracks. Magnetic particle inspection (see Figure 3.2b) was employed on a complementary or alternative basis. Specimens were simultaneously wetted with a suspension of ferromagnetic powder and fluorescing particles (Super Magna LY 2500-MP wb) and magnetised in a Hellmag 1100 standard high-current device (Helling GmbH, Germany) with a magnetic field strength of

20–40 $\mathrm{Acm^{-1}}$ along its sample radius. In this manner, present cracks can be made visible under UV light as they produce a stray field which will accumulate the powdered suspension. Only specimens without detected cracks were approved for mechanical testing.

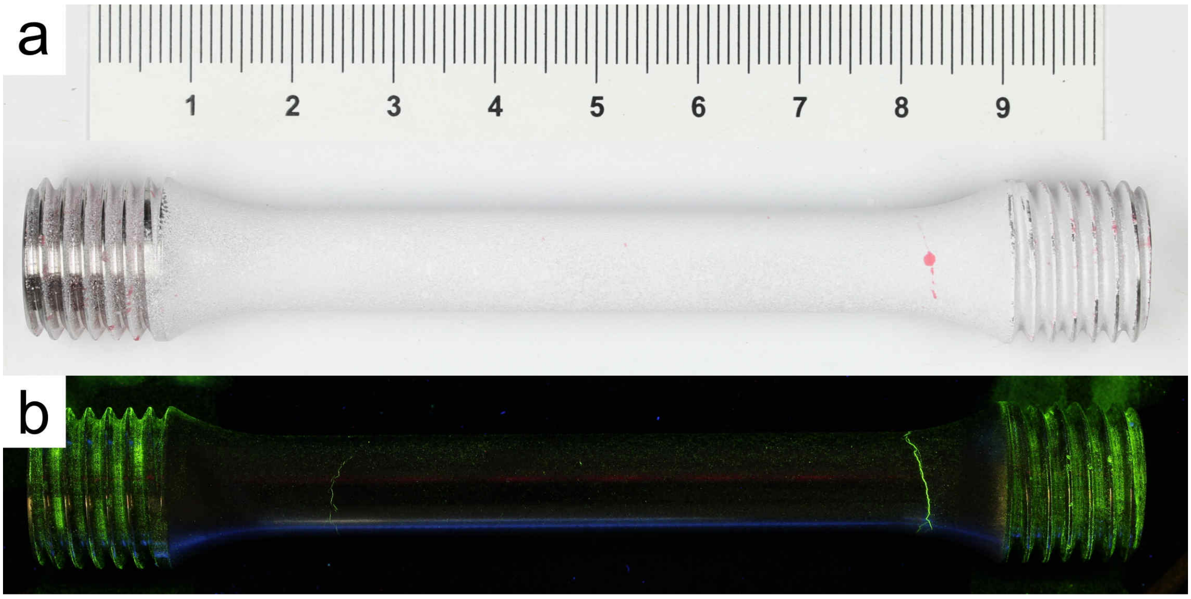

Figure 3.2.: Dye penetrant inspection (a) and magnetic particle inspection (b) of a reference sample with surface cracks. Adapted from [143].

3.3. Chemical analysis

The actual composition of all alloys after casting was determined and compared to the nominal concentrations. For an accurate characterisation of the base alloy (Fe-26Al-4Mo-0.5Ti-1B), inductively coupled plasma assisted optical emission spectrometry (ICP-OES) was used for all expected elements as well as minor or trace elements. Special focus was placed on silicon and hydrogen impurities as both were shown to cause brittleness in Fe-Al alloys [111, 152–154]. For accurate quantification of trace concentrations, Si was measured by reduced molybdosilicate spectrophotometric method and H by carrier gas hot extraction. Due to a higher count of Fe-xAl-yMo-0.5Ti-zB alloy variations to be measured, actual Fe, Al, Mo and Ti concentrations were analysed by X-ray fluorescence (XRF) spectroscopy. Boron concentrations specifically were quantified by spark optical emission spectrometry (S-OES). The composition in quasi-binary Fe-Al samples was also verified by XRF spectroscopy.

All measurements werden conducted at BAM. Measured compositions can be found in the respective results sections. Below, the methods' basics are briefly explained.

3.3.1. Inductively coupled plasma - optical emission spectrometry (ICP-OES)

For ICP-OES, cut sample of 0.5 g representative of the bulk volume in as-cast base alloys from die casting was dissolved by microwave-assisted acid digestion in a solution of 15 ml aqua regia and 1 ml mannitol solution [155]. The acid digestion was then analysed in a SPECTRO ARCOS spectrometer (SPECTRO Analytical Instruments GmbH, Germany). An inductively coupled plasma discharge is generated by flowing argon (Ar) gas through a torch into a high-power radio frequency electromagnetic field where Ar atoms get ionised by a spark. A stable plasma is formed by a cascade reaction of RF-accelerated electrons ionising more Ar atoms and by high temperatures. The acid digestion is nebulised as a sample aerosol and gets injected into the plasma. In there, analytes get excited to emit characteristic radiation of the present elements. The wavelengths and intensities are detected and used against standard solutions to identify and quantify the concentrations of the analytes. For more information, the reader is referred to specialised literature [156, 157].

3.3.2. Single element trace analyses

Reduced molybdosilicate spectrophotometric method

From the used educts and their measured impurities, a Si content of around 0.02 at% was expected. For this reason, the reduced molybdosilicate spectrophotometric method for Si concentrations of 0.01 to 0.05 wt% was applied. The sample material was dissolved in aqua regia and sodium peroxide to receive a molybdosilicate complex. After reduction with ascorbic acid, the analyte was measured in an Evolution 350 UV-Vis spectrophotometer (Thermo Fischer Scientifc Inc., USA) at a wavelength of 810 nm. For more information, the reader is referred to the procedure described in DIN EN ISO 4829-2 [158].

Infrared (IR) absorption spectroscopy

For the determination of carbon content, IR absorption spectroscopy was employed. Around 1 g of the analyte was combusted and measured in an ELEMENTRAC CS-i analyser (Eltra GmbH, Germany) according to DIN EN ISO 9556 [159]. The combustion takes place in an induction furnace under pure oxygen flux and is accelerated by the addition of selected chemicals. Products like CO_2 or CO are then quantified by IR absorption intensities.

Carrier gas hot extraction (CGHE)

The hydrogen content was determined by CGHE in a G8 Galileo analyser (Bruker AXS GmbH, Germany) [160]. A few grams of the alloy material were heated by an external infrared furnace to effuse and desorb hydrogen. A continuous carrier gas stream of nitrogen transports recombined molecular hydrogen to a thermal conductivity detector where a differential signal is measured. The difference to the thermal conductivity of the reference gas can be used to derive a hydrogen concentration.

3.3.3. X-ray fluorescence (XRF) spectroscopy and spark optical emission spectrometry (S-OES)

Metallographic slabs of each as-cast alloy variant (green sections in Figure A.2b) were cut with a distance of at least 10 mm to the edge to retrieve flat surfaces representative of the bulk volume. Induction-melt blanks of quasi-binary Fe-Al alloys were analysed on their front surfaces. Surfaces to be measured by XRF spectroscopy were additionally milled and cleaned before analysis. Relative concentrations of expected elements were determined in air by a calibrated Niton™XL3t GOLDD+ XRF analyser (Thermo Fischer Scientifc Inc., USA). In general, primary x-rays from an Ag source excite analyte atoms ejecting electrons from low-orbital states according to the photoelectric effect. For energetic reasons, electrons from higher-orbital states fall into the empty states while emitting secondary x-ray fluorescence radiation. This radiation is characteristic of the energy transition between the atom's electron energy levels. The emitted wavelengths and their intensities are detected with a large-area silicon drift detector. This technique allows for fast and reliable quantification of elements heavier than Mg and the device showed good results on a range of certified reference materials [161]. More information on XRF principles and instrumentation is given in [162]. To ensure that the device works properly, sample material which was previously analysed by ICP-OES was measured by XRF analysis. An average deviation of < 3 rel% (for Al) was found. Measurements on Fe-xAl-yMo-0.5Ti-zB alloys were performed multiple times to verify the repeatability of results.

As the quantification of light elements such as boron (B) is difficult with XRF spectroscopy, S-OES was used. For this purpose, a SPECTROTEST TXC35 Mobile Metal Analyser (SPECTRO Analytical Instruments GmbH, Germany) was employed. The measurement technique is based on the principles of optical emission spectrometry as explained before, but a spark is used for local evaporation of the sample material. For this reason, bulk material with a flat surface can be analysed. The spark evaporates surface material in a radius of up to 8 mm. Samples surfaces were prepared by grinding with corundum paper. The instrument's measuring chambers were flushed by Ar 5.0 for 15 min before starting the measurements. Concentrations were quantified based on self-calibrated reference materials of as-cast base alloys whose compositions were determined by ICP-OES. Measurements of alloy variants were repeated up to six times and an average value of the B content (in wt%) was determined.

3.4. Thermophysical characterisation

3.4.1. Gas pycnometry

Apart from a general thermophysical characterisation of the base alloy, density was also measured to qualitatively compare the vacancy hardening effect in differently processed and annealed Fe-Al samples. Density was determined as the skeletal density of a compact sample using gas pycnometry according to DIN 66137-2 [163]. This requires both the measurement of the mass m_s with a high-precision balance and the skeletal volume V_s with a pycnometer. Cylindrical samples with a diameter of 5 mm and a length of 25 mm were carefully cleaned by ethanol and dried prior to measurements. Samples were weighed by a calibrated BP 210 D analytical balance (Sartorius AG, Germany) with a certified measurement uncertainty of $6 \cdot 10^{-5}$ g. After weighing, samples were transferred into an AccuPyc 1330 gas displacement pycnometer (Micromeritics Instrument Corp., USA) which was run with Helium 6.0 gas. Helium is injected into a cell chamber with a calibrated cell volume V_{cell} and with the sample loaded until reaching equilibrium pressure p_1. Afterwards, a valve to an expansion chamber with a calibrated expansion volume V_{exp} is opened leading to a pressure drop in the cell chamber to p_2. The skeletal volume V_s then can be calculated according to equation (3.1) to

$$V_s = V_{cell} - \frac{p_2}{p_1 - p_2} \cdot V_{exp} \tag{3.1}$$

An average value of V_s was determined from a series of five measurements. The skeletal density was finally calculated as the division of m_s and the average of V_s. Under the assumption of neither internal porosity nor internal cracks in samples, the skeletal density was equated to the true density ρ_t.

3.4.2. Dynamic resonance method

The temperature-dependent Young's modulus E as well as shear modulus G and Poisson's ratio υ of Fe-26Al-4Mo-0.5Ti-1B were determined by the dynamic resonance method according to DIN EN 820-5 [164] and ASTM E1875 [165]. The principle of this method is to excite flexural and torsional resonance mode frequencies by external force. With the knowledge of sample specifications, the measured quantities can be directly used to calculate the dynamic moduli. Three rectangular bars, each with a length l of 100 mm, a width w of 9 mm and a height h of 3 mm, were extracted from as-cast metallographic slabs of investment castings (Figure A.2b) by wire cutting. The requirements for plane parallelism by DIN EN 843-2 [166] and by ASTM E1875 were checked after processing. Two samples served for the determination of Young's modulus in a temperature range of 20 to 1000 °C in steps of 100 K above 100 °C. The remaining sample was used for calibration of the temperature distribution along the sample length prior to measurements. The exact specimen mass m_s and dimensions l, b and h were measured and documented for later calculations. Measurements were taken in a calibrated Elastotron 2000 (HTM Reetz, Germany) equipped with a vacuum furnace. Measurement equipment and software used for data analysis were developed together with the University of Vienna (Austria). Specimens were hung inside the chamber using Al_2O_3 fibre threads. The threads were connected to two transducers, one acting as a transmitter and one detecting vibrations as a receiver. Under a sweeping spectrum of excited frequencies, the frequency and amplitude of resonance modes of the specimens were recorded by an oscilloscope. The fundamental resonant frequencies of a bar in flexure were measured in two directions, namely along the width $f_{f,w}$ and along the height $f_{f,h}$. From each of the fundamental resonant frequencies, Young's modulus can be calculated according to equation (3.2) [164]. The coefficient of thermal expansion (see subsection 4.2.2) was used for the correction of specimen dimensions over temperature. The elastic moduli along the width and height were compared to discuss any inherent anisotropy of the material.

$$E = 0.946 \cdot \left(\frac{m_s f_f^2}{w}\right) \cdot \left(\frac{l}{h}\right)^3 \cdot \left[1 + 6.585 \cdot \left(\frac{h}{l}\right)^2\right] \tag{3.2}$$

The dynamic shear modulus G can be calculated with the identified fundamental resonant frequency of a bar in torsion f_t according to equation (3.3) [164].

$$G = \left(\frac{4 l m_s f_t^2}{wh}\right) \cdot \frac{(h/w) + (w/h)}{4(h/w) - 2.52(h/w)^2 + 0.21(h/w)^6} \tag{3.3}$$

Poisson's ratio υ then becomes accessible using both dynamic moduli according to equation (3.4) [164].

$$\upsilon = \frac{E}{2G} - 1 \tag{3.4}$$

3.4.3. Differential thermal analysis (DTA)

Differential thermal analysis (DTA) was employed to determine phase transitions and melting temperatures of as-cast Fe-Al-Mo-Ti-B alloys. The procedure described in DIN 51007 was followed [167]. Cubic samples with a mass of < 0.2 g were cut by a water-cooled Accutom-10 cut-off machine (Struers GmbH, Germany). Samples originate from investment-cast step samples (Figure A.4b) in the case of Fe-26Al-4Mo-0.5Ti-1B and from metallographic slabs of investment castings (Figure A.2b) for all other alloy variants. The measurements were conducted using a Setaram TAG24 thermobalance (KEP Technologies Inc., USA), which was equipped with a DTA measuring head. The experiments were performed in a flowing argon environment (approximately $35 \cdot 10^{-5}$ $\mathrm{ls^{-1}}$) after repeated evacuation, utilizing covered alumina crucibles. The samples were heated at a rate of 10 $\mathrm{Kmin^{-1}}$ until reaching a maximum temperature of 1600 °C. Subsequent cooling to room temperature was set to a rate of -10 $\mathrm{Kmin^{-1}}$. The heating and cooling cycles were repeated twice to identify irreversible transformations and validate transition temperatures.

3.4.4. Dilatometry

Dilatometric investigations were conducted to assess length variations with temperature for two purposes: determining the coefficient of thermal expansion (CTE) of Fe-26Al-4Mo-0.5Ti-1B and understanding the impact of thermal vacancies in the Fe-Al-Mo-Ti-B alloy system.

To determine the technical and physical CTEs of the base alloy per DIN 51045-1 [168], relative length changes were measured at a constant heating rate of 5 $\mathrm{K min^{-1}}$ up to 1000 °C. Samples were obtained from as-cast metallographic slabs from investment castings (see Figure A.2b). They were cut into cylinders with an initial specimen length L_0 of 25 mm length and a diameter of 5 mm by electric discharge machining. Measurements were conducted using a TMA 801 Type S thermomechanical analyser (Texas Instruments Inc., USA) inside corundum crucibles without a protective gas environment. Relative length changes $\Delta L/L_0$ were monitored via a connecting push rod and processed within the TMA 801 Win TA V.10.0 (2012) software. The temperature accuracy was tested to be at least 5 K and the measurement uncertainty of the $\Delta L/L_0$ signal was calculated to be less than $5 \cdot 10^{-5}$ for the used samples geometries depending on the temperature. The device was calibrated with a certified platinum sample before any dilatometric measurement. The technical CTE $\bar{\alpha}(T_0, T)$ is then calculated based on a reference temperature T_0 (usually 20 °C) according to equation (3.5) and includes the specimen length L_T at temperature T and the corresponding specimen length change ΔL. The physical CTE $\alpha(T)$ corresponds to the slope of the expansion curve at a given temperature T and is derived by local differentiation according to equation (3.6). Two heating cycles were performed which allowed for an assessment of the repeatability of results and the calculation of average CTE values [168].

$$\bar{\alpha}(T_0, T) = \frac{L_T - L_0}{L_0 \cdot (T - T_0)} = \frac{\Delta L}{L_0 \cdot \Delta T} \tag{3.5}$$

$$\alpha(T) = \frac{1}{L_0} \cdot \frac{\delta L}{\delta T} \tag{3.6}$$

Likewise, the effect of thermal vacancies was investigated by dilatometric experiments. In general, these involved the observation of relative length changes in samples with different processing or thermal histories while being exposed to a temperature program. The investigated sample condition is evaluated on its own or compared to a reference state which represents a thermal vacancy-free state. Such a thermal vacancy-free state was usually acquired by an additional heat treatment at 400 °C for 168 h in air followed by slow furnace cooling (HT1, see subsection 3.2.1). Figure 3.3a schematically illustrates the visible difference in relative length changes of samples without and with a pronounced thermal vacancy concentration during constant heating. Thermal

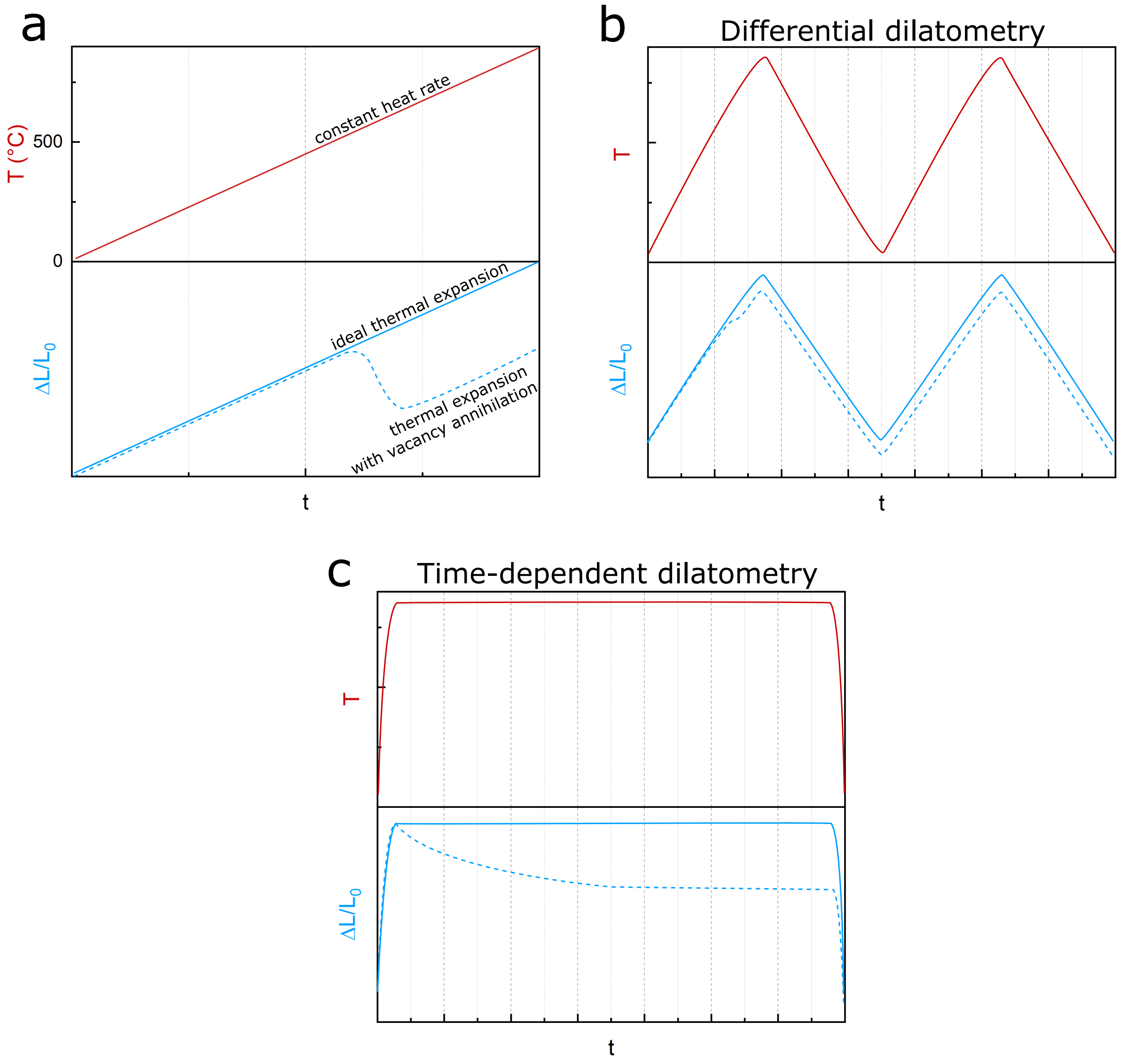

Figure 3.3.: Schematic representation of thermal vacancy annihilation processes in dilatometric measurements with different temperature programs [143] (solid line: thermal vacancy-free material behaviour; dashed line: thermal vacancy-hardened material behaviour): (a) ideal thermal expansion versus thermal expansion with an irreversible contraction due to annihilation of mobile thermal vacancies, (b) differential dilatometry method with repeated heating and cooling cycles at constant temperature rates, (c) time-dependent dilatometry method at constant temperature.

expansion superimposes the measurements, but a retained quantity of thermal vacancies leads to an irreversible contraction (i.e. a negative relative length change) above a temperature where thermal vacancies become mobile [169]. This phenomenon was exploited in two dilatometry methods employed.

In differential dilatometry, two heating and cooling cycles with fixed heating/cooling rates and holding times were run to compare a sample condition to be investigated with a vacancy-free reference condition (see Figure 3.3b). One thermal cycle included heating with a constant heating rate of 6 $\mathrm{Kmin^{-1}}$ up to 700 °C, holding for 10 min followed by cooling at -6 $\mathrm{Kmin^{-1}}$ and a waiting time of 3 h until reaching room temperature. Relative length changes were corrected based on the calibration curve of a platinum reference sample.

The second dilatometry method used was time-dependent dilatometry which measures the relative length changes during annealing at a constant temperature (see Figure 3.3c). The temperature was chosen to 400 °C to investigate the thermal vacancy processes during HT1. For this purpose, samples were rapidly heated at a rate of 20 $\mathrm{Kmin^{-1}}$ to the target temperature which was held for at least 24 h.

3.5. Microstructural characterisation

3.5.1. X-ray diffraction (XRD)

X-ray diffraction (XRD) was used to verify expected phases in Fe-26Al-4Mo-0.5Ti-1B alloys and calculate lattice parameters in selected samples. Bulk volume samples were irradiated by a Co-Kα radiation source in a Seifert PTS 3000 diffractometer (GE Inspection Technologies GmbH, Germany) working in Bragg-Brentano geometry. The diffracted beam intensity and the 2θ angle were recorded with a step size of 0.02°. By Bragg's law, the spacing between diffracting planes d_{hkl}, which is a multitude n of the incident wavelength λ ($\lambda_{Co,K\alpha1} = 1.789007$ Å), is calculated according to equation (3.7).

$$2 \cdot d_{hkl} \cdot sin(\theta) = n \cdot \lambda \tag{3.7}$$

Phases and associated hkl-planes can then be identified by matching d_{hkl}-spacings and intensities with experimentally reported data. Data entries within the Crystallography Open Database (COD) and the Inorganic Crystal Structure Database (ICSD) were utilised for reference. Experimental and reference data were compared within PowderCell 2.4 software [170].

3.5.2. Optical microscopy (OM)

Optical microscopy (OM) was primarily focused on the determination and comparison of microstructural quantities in Fe-Al-Mo-Ti-B alloys which were affected by different cooling rates during processing and the homogenisation treatment HT2. The investigations included measurements of average grain sizes and the secondary phase fractions. Microsections were created by cutting out samples with an Accutom-10 cut-off machine (Struers GmbH, Germany) under water cooling followed by cold mounting. Sample microsections were generally ground with SiC paper down to a grit size of P1200. Polishing and etching strategies as well as the choice of microscope differed by the type of investigations performed afterwards.

Average grain diameter

Grain sizes from two casting strategies (investment casting, die casting), three conditions (as-cast, HT1, HT2) and five wall thicknesses (2.5, 5, 10, 15, 20 mm) were compared. Samples were extracted from step sample castings from the centre of steps as shown in Figure A.4b. Microsections were oriented in the transverse direction to the melt flow. In addition, grain sizes of investment-cast Fe-xAl-yMo-0.5Ti-zB alloy variants were determined in the as-cast condition. Samples were taken from metallographic slabs (see Figure A.2b) at 2 cm distance from the edge. Microsection surfaces were oriented parallel to the cross-section of neighbouring mechanical blanks. For a distinct grain area contrast, microsections were polished with 3 µm diamond paste and etched by immersion into an Adler solution at room temperature for 6 s. The Adler etching solution was prepared with a composition of 100 ml water, 200 ml hydrochloric acid, 60 g iron(III)-chloride and 12 g copper ammonium chloride. Bright-field images were taken by a Zeiss Axiotech 100 HD light microscope equipped with a Zeiss Axiocam 503. Grain sizes were manually determined by Heyn lineal intercept method modified from ASTM E112 [171]. Due to a high scattering range of grain sizes in the order of 10^3 µm, single composite images were stitched from multiple microsection images. Due to an irregular grain morphology, grain boundary intersections were counted in two directions: along (t(0°)) and perpendicular (t(90°)) to the minimum wall thickness (see Figure 3.4). Secondary phase boundaries were ignored during counting. As the available measurement area varied for different wall thicknesses and casting strategies, the test line lengths varied in t(0°) and t(90°) direction. To avoid unequal weighing, the sum of the test line lengths in one direction was balanced for both test directions. A minimum of 200 intersections was collected for statistical significance. The mean intercept lengths of directed test lines were converted into average grain diameters using Tables 3 and 4 from ASTM E112 [171]. An average grain diameter of both directions d_{gs} was calculated following the pooled average concept which is explained in ASTM E1382 [172] and also used in ASTM E112 [171]. The calculation formula is given in equation (3.8).

$$d_{gs} = \sqrt{d_{gs,t(0°)} \cdot d_{gs,t(90°})} \tag{3.8}$$

Results from lineal intercept method were partially compared to measurements after manual segmentation, which depicts a more accurate, but also less efficient approach. Grains were manually segmented at visible grain boundaries and analysed using the analyze particles tool in FIJI V1.53c software [173]. Grains touching the test area border were not included. The Feret diameter which spans the maximum distance within a grain was used as conservative measurand of the grain size d_{gs}.

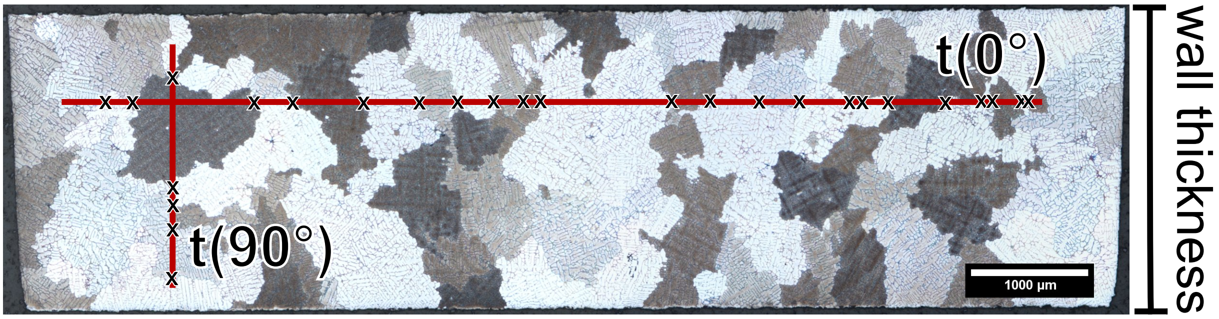

Figure 3.4.: Schematic illustration of determining average grain diameter via Heyn lineal intercept method in horizontal (t(0°)) and vertical (t(90°)) direction. Adapted from [143].

Secondary phase parameters

To differentiate between matrix and secondary phase fractions, microsections were polished down to 1 µm with subsequent polishing in 0.25 µm OP-S NonDry oxide suspension (Struers GmbH, Germany). Fe-xAl-yMo-0.5Ti-zB alloy variants showed poorer phase contrast with oxide polishing suspensions. Therefore, microsections of alloy variants were polished down to 1 µm followed by immersion etching at room temperature in an alkaline etching solution (50 ml distilled water, 2 g NaOH, 1 g KOH) for 30 s. Bright-field mode images were captured using a Zeiss Axioscope 5/7/Vario optical microscope (Carl Zeiss Microscopy, GmbH) with a Zeiss Axiocam 506 with constant image illumination conditions. Secondary phase fractions were obtained by automated image segmentation within FIJI software (Version 1.53c) [173]. Images were converted to 8-bit greyscale followed by auto thresholding using the Otsu or Yen method. In addition, microsection images of Fe-26Al-4Mo-0.5Ti-1B were uniformly edited before auto thresholding. Image editing aimed at enhancing contrast and excluding phases other than the lamellar eutectic phase. The accuracy of the segmentation algorithms was qualitatively evaluated as overlays of the original image (see Figures 3.5a and b). A minimum of eight images for the base alloys and 25 images for the alloy variants (each 519 x 408 μm^2) were analysed and an average area fraction of secondary phases was calculated.

Particle size and distance were also compared for investment-cast Fe-26Al-4Mo-0.5Ti-1B in the as-cast and homogenised state. Particle sizes were analysed with the FIJI “Analyse Particles” tool. Particle distances were estimated by Delaunay Triangulation in FIJI. This algorithm connects the centroids of particles to triangles in a way that minimum angles inside each triangle are maximised. All generated triangle lengths are then averaged for each analysed image.

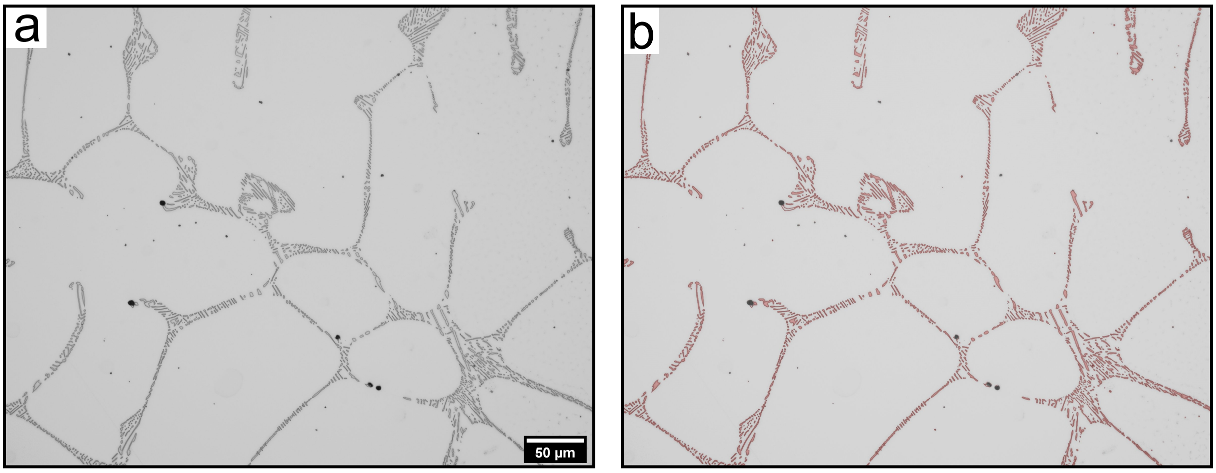

Figure 3.5.: Comparison of a microsection image before (a) and after (b) segmentation of secondary phase fractions (highlighted in red) via image editing and automatic image thresholding. Adapted from [143].

3.5.3. Scanning electron microscopy (SEM)

Scanning electron microscopy (SEM) was employed for both imaging of microstructures and investigating fractured surfaces. Samples were embedded within Technotherm 3000 conductive resin (Kulzer GmbH, Germany) by hot mounting. Microsections were polished down to a 1 µm grain size with a final polishing step using Struers oxide polishing suspension. Microstructural imaging was performed in a LEO Gemini 1530 VP scanning electron microscope (Carl Zeiss SMT

AG, Germany) equipped with a field emission gun usually working at a voltage of 15 kV. Microsections were mainly investigated by backscattered electron (BSE) signals to enhance phase contrast. Fractography was conducted at a Vega 3 SEM (Tescan GmbH, Germany) with a tungsten emitter. Images were recorded at a voltage of 15 kV with a single or combined use of secondary electrons (SE) and BSEs.

3.5.4. Electron backscatter diffraction (EBSD)

Selected hot tensile specimens of alloy variants were investigated post-mortem by electron backscatter diffraction (EBSD). The method is used in an SEM setup with a sample tilted to 70° with respect to the electron beam. In this way, Kossel cones resulting from the diffraction of backscattered electrons in the sample lattices can be recorded in an active-pixel sensor. Due to the limited dimension of the detector, Kossel cones appear as so-called Kikuchi lines originating from a specific lattice plane. The recorded patterns can be indexed according to their position and interplanar angles of present Kikuchi lines. Indexed patterns then can be used to derive locally resolved crystallographic information [174]. Samples were carefully polished at their final step with a MasterMet 0.06 µm colloidal silica suspension (Buehler GmbH, Germany) at low forces to minimise surface damage. Measurements were conducted in the Tescan Vega 3 SEM at a voltage of 20 kV. Microsection areas between 269 and 333 mm^2 were scanned within multiple fields of view with a step size of 5.38 µm. Patterns were acquired with a Symmetry S3 EBSD CMOS detector (Oxford Instruments PLC., UK) with an angular precision below 0.05° at a count time of 0.5 ms/px. Orientation data was processed and stitched by AZtecHKL software (Oxford Instruments PLC, UK). Stitched orientation data was then analysed in HKL Channel 5 Suite (Oxford Instruments PLC, UK) concerning texture, grain orientations, local misorientations and grain sizes (i.e. circle equivalent diameters). As a part of standard noise reduction, only wild spikes extrapolation was performed to correct isolated points with a misorientation $> 2°$ than its surrounding which likely depict misindexings. For grain detection, grain boundaries with a critical misorientation above 10° and boundary completion down to 5° were selected. This corresponds to the minimum angle separating high-angle grain boundaries (HAGBs) from low-angle grain boundaries (LAGBs) [175]. Grains not touching the sample boundary and above a minimum area of 30 px (i.e. a minimum circle equivalent diameter of 33 µm) were considered to ensure reliable grain analysis. Texture was investigated by inverse pole figures (IPF) displayed as contour plots with a half width of 5° and a cluster size of 3°. Orientation intensities of the scanned sample areas are displayed as stereographic projections with respect to the normal of the specimen cross-section (i.e. tensile axis, X). Furthermore, local misorientation maps highlighting local deformations were acquired with a filter size of 5 x 5 px^2 and below a critical angle of 5°.

3.5.5. Electron probe microanalysis (EPMA)

Electron probe microanalysis (EPMA) in combination with wavelength-dispersive x-ray spectroscopy (WDS) was applied to determine the elemental compositions of the matrix and secondary phases. With this technique, characteristic x-rays are emitted by electron bombardment, which are then reflected and detected in a crystal Bragg spectrometer. For more details on the method, the reader is referred to current literature [176]. A JEOL JXA-8900 RL electron probe microanalyzer (JEOL GmbH, Germany), operating at 12 kV and 20 nA, was employed. Multiple spot measurements were conducted to convert element count signals to weight percentages through linear regression. Concentrations were calibrated against pure element standards (except for boron). Mean matrix compositions and boride concentrations were derived from both multispot analysis. Matrix compositions were also compared to areal measurements.

3.5.6. Transmission electron microscopy (TEM)

The main phases as well as the type of ordering in Fe-Al were identified using conventional transmission electron microscopy (TEM). In contrast to SEM, a high-voltage electron beam is focused on an even tinier spot on a sample, thin enough to transmit the incoming electrons. Both high-resolution images and diffraction information on a nm scale can be obtained. A detailed description of the scope of this method can be found in textbooks, e.g. from Williams and Carter [177]. Samples were cut to around 1 mm in thickness and ground to reduce the thickness to 150 µm. Small disks with 3 mm in diameter were punched from the ground slices and electropolished with a Tenupol-3 electropolishing unit (Struers GmbH, Germany) using an electrolyte solution of perchloric acid (6%), 2-butoxyethanol (35%), and methanol (59%) at 50 V and -4 °C. Experiments were conducted on a JEM-2200FS transmission electron microscope (JEOL GmbH, Germany) with a field emission gun running at 200 kV. BF images and selected area electron diffraction (SAD) patterns were acquired. Lattice spacings d_{hkl} were derived from the inverse distance of diffraction spots to the centre beam position. Indexing of lattice planes and verification of phases was performed by comparison to expected lattice spacings under consideration of the applicable selection rules [178]. Expected diffraction patterns were also simulated using JEMS electron microscopy simulation software (2018, 21st build) [179] and compared with experimental patterns. To analyse elemental compositions, transmission electron microscopy was employed in scanning mode (STEM). Energy-dispersive x-ray spectroscopy (EDS) and Cliff-Lorimer method were employed to determine Fe, Al, Mo and Ti concentrations. For light elements, energy electron loss spectroscopy (EELS) was used. The presence of boron was proven by the existence of K-edges at 188 eV [180].

3.6. Mechanical testing

3.6.1. Hardness measurement

Both the general materials hardness (i.e. macrohardness) and the specific hardness of the Fe-Al matrix (i.e. microhardness) were investigated in various combinations of alloy composition, casting strategy and heat treatment. Hardness is generally determined by measuring the residual area of a geometrically defined indenter loaded with a constant force F onto the specimen surface. The use of a Vickers diamond pyramid with an angle of 136° of its opposite faces leaves a square-like indent behind whose diagonals can be measured with an optical microscope. With a mean diagonal length of the Vickers indent d, the Vickers hardness H can then be calculated according to equation (3.9) [181].

$$H = 0.1891 \cdot \frac{F}{d^2} \tag{3.9}$$

Mounted microsections were polished to a minimum of 1 µm grain size. Measurements were conducted on both a KB 30 SR FA Basic hardness tester (KB Prueftechnik GmbH, Germany) and a Qness 60 A+ EVO hardness tester (ATM Qness GmbH, Germany). Procedures complying to DIN EN ISO 6507-1 were followed [181]. For this purpose, lens optics and hardness outputs were verified against a standardized test block preceding the actual testing. Macrohardness was determined with a Vickers indenter under a sustained load of 10 kg for 12 s. Ten indentations were performed per alloy to acquire an average hardness value. Likewise, microhardness was measured with a Vickers indenter applying a load of 0.1 or 0.01 kg for at least 12 s. Due to the higher scattering of results at lower loads, a minimum of 15 indents were executed per alloy.

3.6.2. Compression testing

For compression tests at room temperature, cylinders with a diameter of 10 mm according to Figure A.7 were turned from tested investment-cast and die-cast tensile specimens with different heat treatments. As compression specimens were extracted from threading heads after tensile testing at room temperature, an unaltered thermal history without remaining deformation could be assumed. Actual diameters of test cylinders d_0 were measured in multiple orientations with a dial gauge micrometre (Mitutoyo Corp., Japan) to calculate a mean original cross-sectional area S_0. The engineering stress σ_{eng} under a loading force F can be calculated according to equation (3.10). Tests were conducted according to DIN 50106 [182] to determine the proof strength at 0.2% plastic compression $R_{dp0.2}$. Cylindrical samples were tested in an Instron model 4505 electromechanical universal testing machine (Instron GmbH, Germany) with a calibrated 100 kN load cell and flat compression platens. Contact areas of platens were lubricated with Molykote DX paste (Dow Corning Inc., USA) before sample insertion. The strain was controlled and measured by a two-sided axial extensometer (MTS Systems Corp., USA) with a gauge length of $L_e = 8$ mm attached to the cylindrical specimen. The compression range up to -5% was calibrated to class 0.2 with a dummy steel sample. An increasing compression load was applied at a constant strain rate of $2.5 \cdot 10^{-4}\ \mathrm{s}^{-1}$. Experimental data was processed within the Instron Bluehill 2 Software.

$$\sigma_{eng} = \frac{F}{S_0} \tag{3.10}$$

3.6.3. Quasi-static tensile testing

Standard tensile tests

Standard tensile tests were conducted at ambient and higher temperatures up to 650 °C according to applicable standards DIN EN ISO 6892-1 and -2 [183, 184]. Specimens are exposed, similar to compression tests, with an increasing load until fracture. Tensile curves are usually displayed as engineering stress σ_{eng} over strain e. To account for reductions in cross-section with increasing strain, true stress σ_t and true strain e_t can be deducted from analytical equations (3.11) and (3.12) under the assumption of constant volume. Stress and elongation-related mechanical properties can be derived from an engineering tensile curve. Besides the tensile proof strength at 0.2% plastic elongation $R_{p0.2}$, other parameters were determined such as the slope of the elastic stress-elongation curve m_E, the ultimate tensile strength R_m, elongation after fracture A and the percentage reduction of area in the necked region Z. Thereby, elongation after fracture is calculated by equation (3.13) after measurement of the final gauge length after fracture. Moreover, the percentage reduction of area can be obtained by measuring the minimum cross-sectional area after fracture S_u and calculating the ratio according to equation (3.14).

$$\sigma_t = \sigma_{eng}(1 + e) \tag{3.11}$$

$$e_t = ln(1 + e) \tag{3.12}$$

$$A = \frac{L_u - L_0}{L_0} \cdot 100 \tag{3.13}$$

$$Z = \frac{S_0 - S_u}{S_0} \cdot 100 \tag{3.14}$$

Tensile blanks of die-cast Fe-26Al-4Mo-0.5Ti-1B (Figure A.3b) and investment-cast alloy variations (Figure A.2b) were turned to tensile specimens at Henschel GmbH Germany. Likewise, tensile blanks of investment-cast Fe-26Al-4Mo-0.5Ti-1B (Figure A.1b) were turned into final contour at the mechanical workshop at BAM. The standard geometry was chosen to be a cylindrical gauge section with a diameter d_0 of 10 mm and a parallel gauge length L_c of 60 mm (see Figure A.5a). With a larger grain size anticipated in slowly cooled investment castings, the geometry was aimed at having a minimum quantity of grains (> 100) present in the cross-sectional area to mitigate size effects [185, 186]. A limited set of specimens was also manufactured with a reduced cylindrical gauge section volume ($d_0 = 5$ mm, $L_c = 30$ mm, see Figure A.5b) to prove this effect. A homogenisation treatment HT2 was applied to tensile blanks before turning if tested above 400 °C.

Average original gauge diameters d_0 were determined by a dial gauge micrometre with multiple measurements in different orientations before testing. A calibrated electromechanical C45.105 tensile testing machine (MTS Systems Corp., USA) equipped with a calibrated 100 kN load cell was utilized. Both room and high-temperature tests were conducted with a constant strain rate of $2.5 \cdot 10^{-4}$ s^{-1}. Test data was logged and stored within the MTS Insight Plus and Testsuite TW Elite 4.4.1.525 (2019) softwares.

Room temperature tests were only conducted by strain control with a two-sided DD1 axial extensometer of $L_e = 50$ mm (Hottinger Bruel & Kjar GmbH, Germany). Elongations up to 2% were calibrated to class 0.2. At high-temperature tests above 2.5% elongation, strain control was switched to a constant crosshead speed. This was reasoned with a safe run of the test until fracture as elongations partially exceeded the calibrated interval of extensometers at elevated temperatures. The crosshead speed with the targeted strain rate was estimated to 0.016 $\text{mm}\cdot\text{s}^{-1}$ from pretests of the investment-cast base alloy at 550 °C. Elongations at high-temperature tests were logged with a one-sided MTS 632.51F-03 axial extensometer with a nominal extensometer gauge length of 50 mm and a calibrated elongation range of ±10% of class 0.5. For a larger measurement range of extensions at elevated test temperatures, extensometers were compressed to an initial gauge length of $L_e = 45$ mm effectively corresponding to -10% compression. For the determination of A, two fine marks were placed on the gauge section at a distance of L_0 before testing. After fracture, specimen halves were carefully assembled to measure the mark distance L_u with a Zeiss Axiotech 100 HD microscope equipped with a calibrated TM 321 x-y table (Mitutoyo Corp., Japan).

The heating of tensile specimens was controlled by a three-zone furnace model 3210 (Applied Test Systems Inc., USA). Temperatures T between 250 and 650 °C were selected and monitored by calibrated type S thermocouples spot-welded to the ends of the gauge length. A uniform temperature distribution across the sample was once verified at 650 °C with an additional thermocouple spot-welded to the centre of the gauge length. Test temperature T was held for at least 0.5 h before loading to reach equilibrium temperature in the specimen.

Miniature tensile tests

Tensile tests at room temperature were also conducted on miniature specimens as only thin processing geometries with large cooling rates could produce test specimens with small grain sizes. For this purpose, flat miniature specimens with a cross-sectional area of $S_0 = 1 \text{ x } 2.5 \text{ mm}^2$ and a parallel length of $L_c = 15$ mm (see Figure A.5c) were extracted from die-cast step samples (see Figure A.4b) with a wall thickness of 2.5 mm. Note that the required original gauge length $L_0 = 10$ mm to respect the proportionality law of $L_0 = 5.65 \sqrt{S_0}$ is below the minimum value of 15 mm given by the DIN EN ISO 6892-1 standard [183]. Step samples were cut in halves, ground to a target thickness of 1 mm and then wire-cut to the desired contour at the BAM workshop. Average dimensions were measured with a Mitutoyo dial gauge micrometre. Experiments were conducted in the same tensile testing machine as standard specimens, with a few alterations to the test setup. A calibrated load cell of maximal 10 kN was used and specimens were gripped by pins pressed through its boreholes. A preload of 10 N was applied to miniature samples. Elongations were derived by the Digital Image Correlation (DIC) method. This method displays an optical non-contact technique which enables the visualisation of full-field deformation [187]. A dual-camera system tracks displacements of distinctive points on a sample surface in three dimensions during straining. Displacement fields are correlated to a reference image by cross-correlation functions and differentiated to obtain the local strain fields [188]. In preparation, a fine speckle pattern was sprayed onto one side of the wide and narrow gauge section area. An Aramis system (Carl Zeiss GOM Metrology, Germany) was employed for the DIC method. Two 12 MP monochrome cameras were positioned at an angle of ± 23–25° to the sample surface. The coincidence of pixel locations of both cameras was verified under blue-light illumination on a calibrated object. Images were acquired at a rate of 10 Hz during loading. Image and test data were logged and saved within the ARAMIS Professional 2020 software (Version: 2020 Hotfix 6, Rev. 144376, Build 2021-12-03). Correlations of strain fields were calculated and visualised in the GOM Correlate Professional 2020 software. For a target strain rate of $2.5 \cdot 10^{-4}\ \mathrm{s}^{-1}$ on a virtual gauge length of $L_0 = 10$ mm at $R_{p0.2}$, a constant crosshead speed of $0.00635\ \mathrm{mm{\cdot}s^{-1}}$ was set. Force and crosshead distance data of the tensile testing machine and elongations derived by the DIC method were merged based on the respective time counts.

3.6.4. Creep testing

The creep behaviour of Fe-26Al-4Mo-0.5Ti-1B was investigated to derive creep-related parameters describing the dependency on stress or temperature under constant loading. Creep tests were conducted according to DIN EN ISO 204 [189] in a temperature range of 600 to 700 °C. Individual specimens were tested under constant tensile load, with an overall initial stress range of $40 \leq \sigma_0 \leq 240$ MPa. Tested materials were homogenised at 1000 °C for 100 h (HT2) prior to specimen contouring. This step was aimed at instating a thermodynamically stable microstructure. Creep blanks were taken from investment-cast Fe-26Al-4Mo-0.5Ti-1B (see Figure A.1b) and turned to the target geometry (see Figure A.6) at the mechanical workshop at BAM. Creep specimens were not further polished as test temperatures are within the ductile regime for non-polished surfaces where notch sensitivity should be negligible [38]. The average maximum surface height of creep specimens was measured to $Rz < 5$ µm. Experiments were carried out in two custom-built 20 kN creep testing machines (Mohr & Federhaff AG, Germany) calibrated to class 1 according to DIN EN ISO 7500-2 [190]. Load strings were aligned by applying a preload of 1 kg corresponding to less than 10% of the smallest stress level (40 MPa). A custom-built three-zone furnace (Heraeus GmbH, Germany) heats the specimens whose temperature is monitored by three type-S thermocouples spot-welded across the gauge section. Both thermocouples and temperature data logging were calibrated according to respectively EURAMET/cg-08 and EURAMET/cg-11. Preloaded specimens were heated for 1.5 h after reaching the test temperature. Test loads were applied manually and shock-free leading to an initial strain e_i which can be composed of an elastic component e_e and a plastic component e_p according to equation (3.15). The initial strain e_i can then be subtracted from the total strain e to receive the creep strain e_f according to equation (3.16). The total strain e was directly measured by a one-sided water-cooled extensometer by MTS (model 831 or 833) with a nominal extensometer gauge length of 51 or 52 mm. Extensometers were calibrated to class 1 in a range of ±10%. As with high-temperature tensile tests, extensometers were compressed to -10% at room temperature to extend the calibrated range of measurable strains. Tests were run until creep fracture or at least 500 h. Correspondingly, the creep elongation after fracture A_u or the permanent creep elongation A_{per} was determined according to equation (3.13) by measuring L_u with calipers after cooling to room temperature.

$$e_i = e_e + e_p \tag{3.15}$$

$$e_f = e - e_i \tag{3.16}$$

Chapter 4

Characterisation of investment-cast Fe-26Al-4Mo-0.5Ti-1B

4.1. Microstructure and phase evolution

Parts of this section including figures, tables and results were reproduced and adapted from Abel et al. [191] under the CC BY 4.0 licence.

Due to its high industrial relevance, investment casting was selected as the main processing route of quinary alloys with nominally Fe-26Al-4Mo-0.5Ti-1B (in at%) and its characterisation of major mechanical properties (see section 3.6). To verify its final composition and level of contamination after casting, chemical analysis was performed. Table 4.1 summarises the measured composition of major and trace elements in both at% and wt%. Major elements including trace amounts of transition metal elements (Mn, Cr, Ni) were determined by ICP-OES. Critical trace elements such as C, Si and H, which are reported to influence microstructural evolution and brittleness [111, 192, 193], were measured otherwise (see subsection 3.3.2). Major element concentrations mostly fit the nominal composition. Actual Al concentration is reduced by 1 at% compared to the nominally employed quantity, which is expected to arise from Al evaporation during the melting process before casting. Only minor contents of Mn, Cr and Ni with < 0.02 at% were found. Hydrogen incorporation was limited to 2.1 ± 0.3 ppm (wt) after processing of specimens. Carbon contents (60 ppm (wt)) are fairly low, but do not exclude potential formation of Fe_3AlC carbides which was even reported for concentrations as low as 50 ppm (wt) [122]. Besides that, the measured fraction of Si (190 ppm (wt)) could have an enhancing effect on carbide precipitation dynamics as was suspected by Herrmann et al. [192].

SEM-BSE images of the microstructures from two conditions, i.e. i) as-cast and homogenised at 1000 °C for 100 h followed by furnace cooling (HT2), which were later investigated by mechanical tests are contrasted in Figures 4.1a and b. In general, the microstructure consists of a grey

Table 4.1.: Measured composition of the Fe-26Al-4Mo-0.5Ti-1B base alloy after casting. Concentrations were determined by ICP-OES except for C (IR absorption), Si (Reduced Molybdosilicate Spectrophotometric Method) and H (CGHE).

	Measured composition										
	Fe	Al	Mo	Ti	B	Mn	Cr	Ni	C	Si	H
at%	bal.	25.0	3.7	0.4	1.0	0.01	0.01	< 0.01	0.025	0.034	0.010
wt%	bal.	13.6	7.2	0.4	0.2	0.02	0.01	0.01	0.006	0.019	< 0.001

matrix phase and eutectic phase areas and seams consisting of the matrix phase and a bright secondary phase with mostly lamellar shape. Occasionally, black particles are visible which amount to less than 1 vol%. After HT2, lamellar phases appear to have partially coarsened. To verify potential growth of bright particles after homogenisation treatment, average values of secondary phase fractions f_p, particle size d_p and distance λ_p were measured from multiple micrographs. Under the assumption of random orientation of secondary phases, area fractions in images were taken as volume fractions according to the Delesse principle [194]. The particle distance was determined by Delaunay Triangulation. The microstructural parameters for both conditions are summarised in Table 4.2. It can be confirmed that average particle sizes d_p slightly increase after HT2. By tendency, volume fractions f_p appear constant whereas particle distance λ_p increases after homogenisation treatment. In total, the results indicate that the lamellar phase is not thermodynamically stable and that slight coarsening is taking place during high temperature

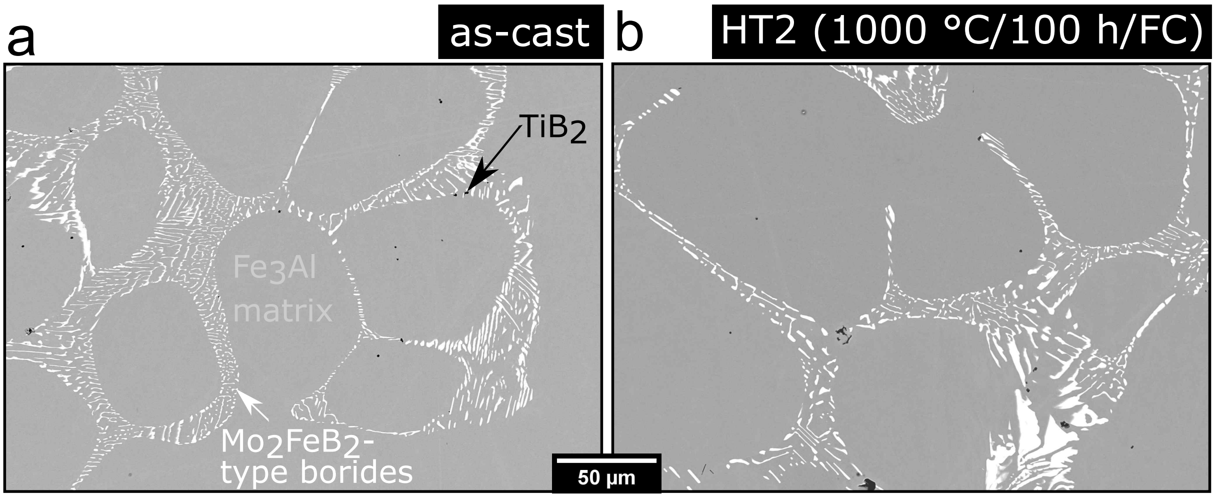

Figure 4.1.: SEM microsections of investment-cast Fe-25Al-3.7Mo-0.4Ti-1B: (a) as-cast condition, (b) after homogenisation treatment HT2 (1000 °C/100 h/FC). Adapted from [143].

Table 4.2.: Microstructural parameters of investment-cast Fe-25Al-3.7Mo-0.4Ti-1B in the as-cast and HT2 state (1000 °C/100 h/FC). Data reproduced from [143].

	as-cast	**1000 °C/100 h/FC**
Average grain diameter d_{gs} (µm)	660 ± 93	795 ± 111
Average secondary phase fraction f_p (vol%)	4.1 ± 0.2	3.9 ± 0.3
Average secondary phase particle size d_p (µm)	4.5 ± 0.4	5.6 ± 0.6
Average secondary phase particle distance λ_p (µm)	11.5	13.7

annealing. This is in contrast to TiB_2 particles, which Doucakis and Kumar [98] reported to not coarsen during annealing at 1100 °C. Thus, lamellar particles appear to be a different phase.

To identify the phases, elemental compositions were first determined by WDS-EPMA. An overview of the WDS results is given in Table 4.3. The grey matrix phase in as-cast condition was measured to a hyperstoichiometric Fe_3Al phase. The iron aluminide matrix builds a solid solution with Mo and Ti. The solute concentrations measured by multispot analysis (3.2 at% Mo, 0.4 at% Ti) differ considerably from averaging over a mapped area (2.4 at% Mo, 0.7 at% Ti). This observation could indicate that solutes are not well homogenised after casting. To verify this assumption, solute concentrations were also measured after homogenisation treatment (HT2) by both methods. However, the difference between multispot analysis (2.9 at% Mo, 0.4 at% Ti) and averaged mappings (2.2 at% Mo, 0.7 at% Ti) is still significant, but both follow a trend of decreasing Mo content. It therefore appears that different values rather arise from different WDS calculation methods, but a higher accuracy should be expected from mappings. Elemental compositions of a similar alloy (Fe-25.4Al-4.2Mo-0.5Ti-1.2B [38]) determined by WDS multispot analysis are comparable to this work, but Mo solute concentrations are slightly higher, probably due to an overall higher Mo content than in this alloy.

The elemental composition of the bright lamellae is only reliably accessible by multispot analysis due to its small dimensions. It was identified as a complex boride phase with high amounts of Mo and Fe and minor amounts of Ti and Al (< 10 at%). Li et al. [38] assigned the secondary phase to a Mo_2FeB_2-type structure evolving in an eutectic reaction. Still, similar to their work, the measured Mo:Fe ratio clearly deviates from the ideal 2:1 ratio, with a lack of Mo or a surplus of Fe even indicating a 1:1 ratio in HT2 state. The increased Fe concentration in borides was assumed to originate from the surrounding Fe_3Al phase as the x-ray excitation volume from the incident electron beam could often be larger than the available boride volume [191]. The dark round phase as occasionally visible in Figure 4.1 was mostly identified as TiB_2 particles with minor additions of Mo, Fe and Al by WDS point analysis. Yet, compositions fluctuated and sometimes included significant carbon contents instead of boron. This aligns with investigations by Moszner et al. [127] on Fe-Al-Mo-Ti-B alloys with lower Mo contents.

Table 4.3.: WDS elemental composition of Fe_3Al (matrix) and Mo_2FeB_2 (secondary boride phase) in investment-cast Fe-25Al-3.7Mo-0.4Ti-1B. Li et al.'s elemental compositions of an Fe-25.4-4.2Mo-0.5Ti-1.2B alloy are given for reference [38]. Reproduced and amended from Abel et al. [191] under the CC BY 4.0 licence.

				Elemental composition (at%)				
Phase	Condition	WDS method	Reference	Fe	Al	Mo	Ti	B
Fe_3Al	as-cast	mapping	this work [191]	70.3	26.6	2.4	0.7	-
	as-cast	multispot	this work [143]	69.3	27.1	3.2	0.4	-
	HT2	mapping	this work	70.4	26.7	2.2	0.7	-
	HT2	multispot	this work [143]	69.5	27.2	2.9	0.4	-
	HT2	multispot	Li et al. [38]	69.6	26.9	3.2	0.34	
Mo_2FeB_2	as-cast	multispot	this work [191]	23.7	1.4	29.7	6.7	38.5
	HT2	multispot	this work [143]	20.0	0.8	21.8	5.1	52.2
	HT2	multispot	Li et al. [38]	25.2	0.5	36.8	8.3	29.2

The crystallography of present phases was investigated by XRD. Figure 4.2 depicts the diffractograms of as-cast and homogenised Fe-25Al-3.7Al-0.4Ti-1B. The $D0_3$ superstructure of Fe_3Al can be usually differentiated from ordered B2 or disordered A2 structures by the presence of superreflections with odd indices only [178]. In as-cast alloys, the $D0_3$ structure could be verified by a distinct (111) reflection alongside other high-intensity reflections such as (220). Surprisingly, neither (111) nor (311) could be detected in HT2 state despite being the highest intensities among $D0_3$ reflections. Instead, the low-intensity (331) plane was visible. Due to the extremely large grain sizes and the consequently lower sampling count of grains, lower stastistics of grain orientations are to be expected and given surface textures might be visible. The (220) reflection which is quite strong due to a preferred orientation at the measurement area might cause the absence of other reflections.

Most expected reflections of tetragonal Mo_2FeB_2 according to Gladyshevskii et al. [195] appear in the two recorded diffractograms. However, an additional single peak at 46° appears which cannot be assigned to another phase possible by present elements or instrumental errors. Minor phases such as Fe_3AlC, TiB_2 or TiC which were mentioned before could not be identified in the

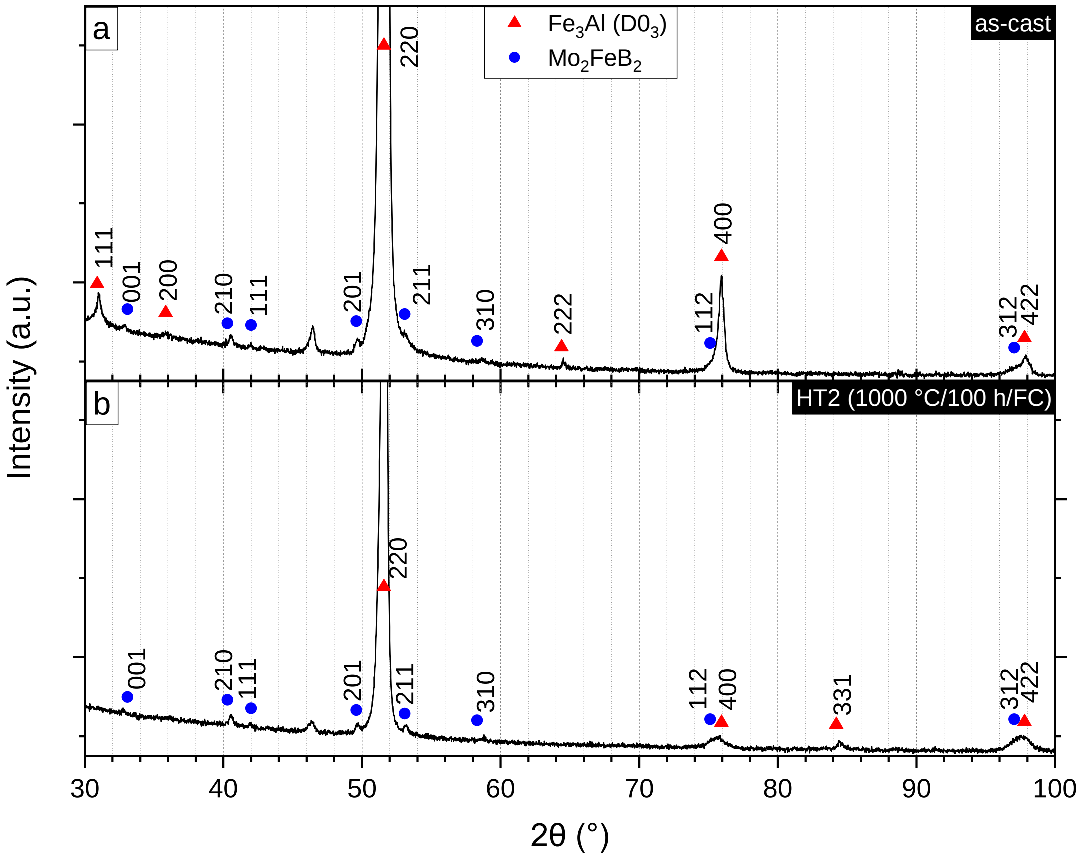

Figure 4.2.: X-ray diffractograms of investment-cast Fe-25Al-3.7Al-0.4Ti-1B: (a) as-cast condition, (b) after HT2. Adapted from [143].

diffractograms. Besides, some peaks of the Mo_2FeB_2 phase (e.g. (001), (210) and (310)) seem to be slightly displaced compared to their theoretical angular positions.

To elucidate the discrepancies, SAD was performed on Fe_3Al and Mo_2FeB_2-type phases within conventional TEM [191]. Investigated areas as defined by electron apertures are illustrated by grey dashed circles in Figures 4.3a and b in bright-field (BF) images. One area confined to the matrix and one containing a lamellar particle were selected. STEM-EDS and STEM-EELS verified the elemental composition of a Mo_2FeB_2-type particle. Measurements on some particles even pointed towards a 2:1 elemental ratio of Mo:Fe. The diffracted SAD patterns of both beam positions are displayed in Figures 4.3c and d with inverted contrast. Indexing was performed using the ordered cubic $D0_3$ structure (Fm-3m, space group 225) [196]. The corresponding SAD pattern in Figure 4.3c unambiguously matches the [011] zone axis of the $D0_3$ Fe_3Al phase. The higher order is given by the presence of $D0_3$ superlattice reflections (111) and (311) (highlighted by blue circles), which exclude the B2 phase by implication [178]. The $D0_3$ order is also confirmed by good coincidence of the simulated diffraction pattern of binary Fe_3Al reproduced by JEMS with the experimental pattern as shown in Figure 4.3e.

For the boride phase, the tetragonal crystal structure for Mo_2FeB_2 proposed by Gladyshevskii et al. (P 4/m b m, space group 127) [195] was assumed. The investigated boride lamella was located at a grain boundary (see Figure 4.3b). Figure 4.3d exhibits the respective SAD pattern, which was found to be a superposition of $D0_3$ Fe_3Al in the [011] zone and the boride. Reflections of the boride phase which fit the Mo_2FeB_2 structure are highlighted by red ovals. The

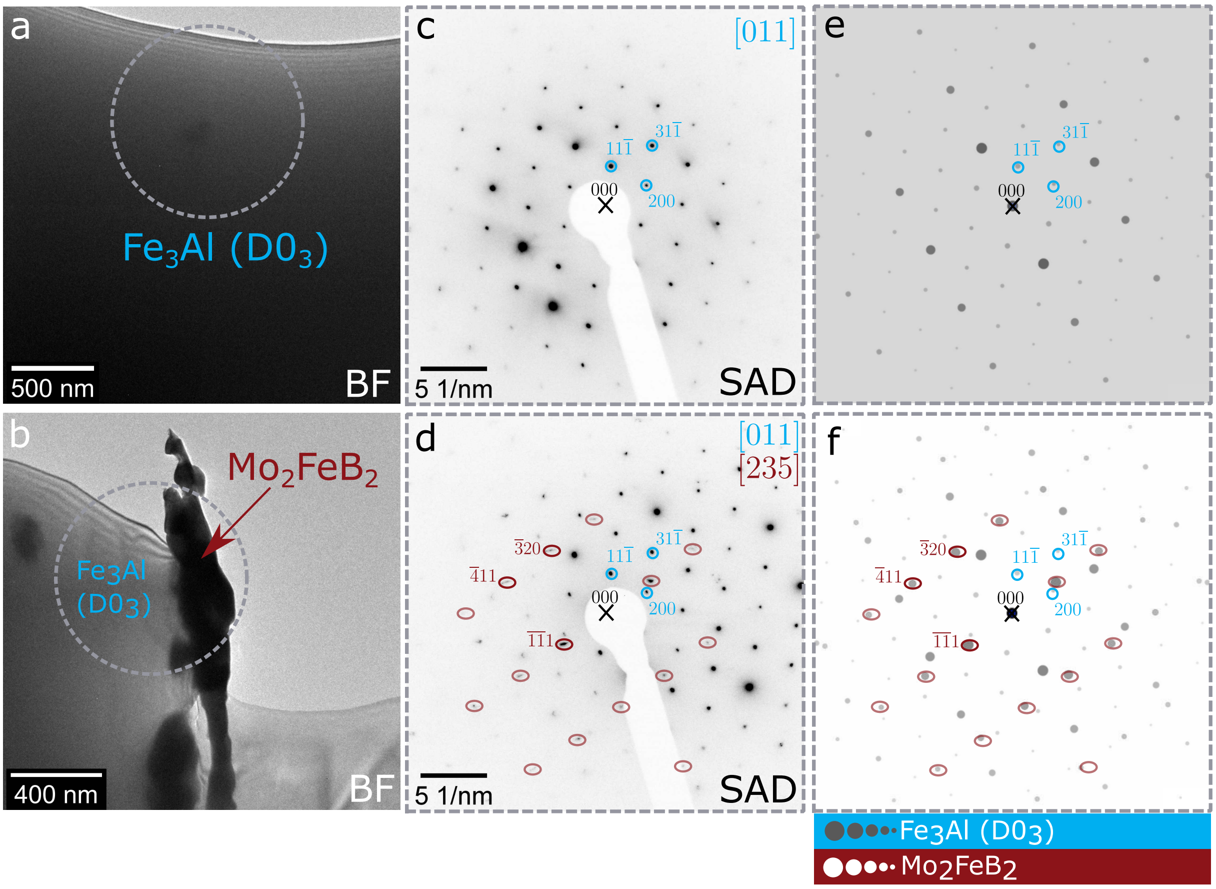
a
Fe3Al (D03)
500 nm
BF
b
Mo2FeB2
Fe3Al (D03)
400 nm
BF
c
[011]
31$\bar{1}$
11$\bar{1}$
000
200
5 1/nm
SAD
d
[011]
[235]
320
$\bar{4}$11
$\bar{1}\bar{1}$1
31$\bar{1}$
11$\bar{1}$
000
200
5 1/nm
SAD
e
31$\bar{1}$
11$\bar{1}$
000
200
f
320
$\bar{4}$11
$\bar{1}\bar{1}$1
31$\bar{1}$
11$\bar{1}$
000
200
Fe3Al (D03)
Mo2FeB2

Figure 4.3.: Transmission Electron Microscopy (TEM) analysis of the alloyed Fe_3Al matrix (a,c,e) and the eutectic boride (Mo_2FeB_2) phase (b,d,f): (a,b) Bright-field (BF) images. (c,d) Inverted selected area electron diffraction (SAD) patterns generated from the areas indicated by dashed circles in a and b. Zone axes are [011] for Fe_3Al and [235] for Mo_2FeB_2. Image d is a superposition pattern of the matrix (blue circles) and the eutectic boride phase (red ovals). (e,f) Simulated diffraction patterns of the crystal structures of binary Fe_3Al (dark spots) and Mo_2FeB_2 (bright spots) corresponding to the same zone axes and scale as in images c and d. Indexed reflections from experimental patterns in c and d are superimposed for comparison. Reproduced from Abel et al. [191] under the CC BY 4.0 licence.

reflections found suggest an orientation close to the [235] zone axis. Figure 4.3f displays the simulation of both patterns in the respective zone axes. The overlayed indexed positions of the boride from experiments fairly fit the theoretical positions of Mo_2FeB_2. In sum, it can be confirmed that secondary phase particles possess a tetragonal crystal structure as for Mo_2FeB_2 even though significant compositional fluctuations can be witnessed.

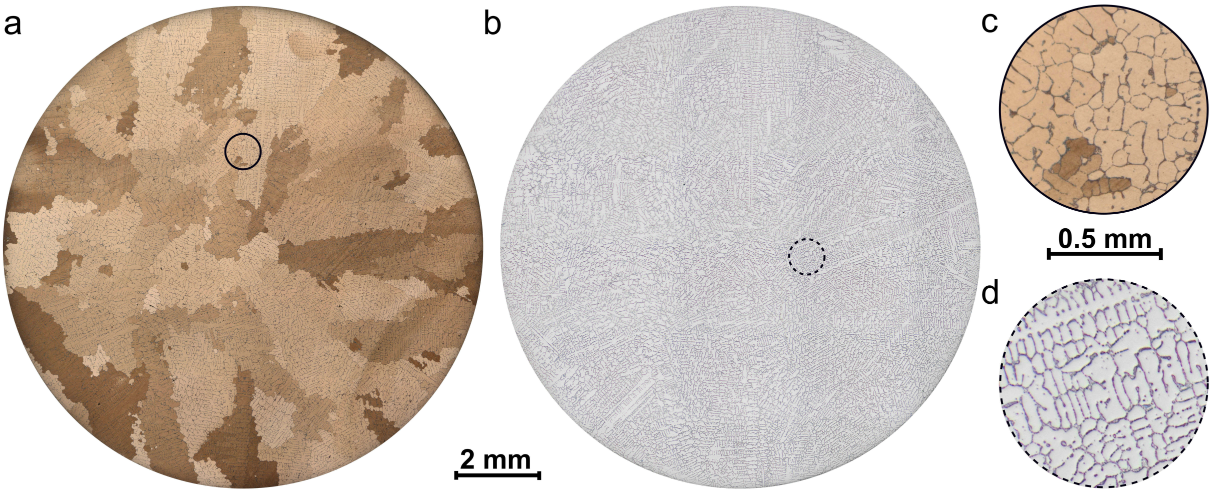

Figure 4.4.: OM images of tensile specimen cross-sections (a,b) and magnifications (c,d) of investment-cast Fe-25Al-3.7Mo-0.4Ti-1B after HT2 with (a,c) grain contrast after Adler etching and (b,d) phase contrast after OP-S polishing.

OM images of the complete cross-section of an investment-cast tensile specimen with an initial wall thickness of around 20 mm and after homogenisation treatment are depicted in Figures 4.4a and b with grain and phase contrast, respectively. Higher magnified sections are also shown (see Figures 4.4c and d). Microsections with phase contrast enable the view of the dendritic solidification structure of the Fe_3Al matrix phase (see Figure 4.4b and d). The eutectic phase with its dark appearing borides is arranged in the interdendritic spacings. The orientation of dendrites changes across the cross-section, but appears constant within grains. The majority of the cross-section is occupied by large grains, but a higher count of smaller grains < 200 µm can be also observed (see Figure 4.4c). Large grains with low aspect ratios appear to be oriented towards the centre (see Figure 4.4a). The loose directionality of grains and dendrites is probably connected to the thermal gradient during casting aligning solidification from the mould walls to the interior of castings. Accordingly, the grain morphology is mainly non-equiaxed and irregular, with grain boundaries usually coinciding with the eutectic seams and boride phase boundaries. The average grain diameter d_{gs} (i.e. a mean value) of as-cast products with a casting wall thickness of around 20 mm was measured to 660 ± 93 µm per lineal intercept method in two directions.

After homogenisation treatment HT2 (1000 °C/100 h/FC), which was applied for mechanical tests above 400 °C, an average grain diameter of 795 ± 111 µm was measured (see Table 4.2). The 95% confidence interval (CI) of values overlaps so that no significant grain growth could be proven after homogenisation. Hence, the expectation could be valid that boride phases inhibit grain growth as was seen with various boride strengthened iron aluminide alloys [99]. Still, the large confidence interval also results from a large scatter of grain sizes, which could distort the interpretation and comparison of mean values. The distribution of grain sizes was exemplarily investigated by manual segmentation of an investment-cast as-cast sample with a wall thickness of 10 mm. Due to the lower wall thickness and higher solidification rates, different grain statistics result. Figure 4.5 shows the histogram of grain sizes determined from maximum Feret diameters.

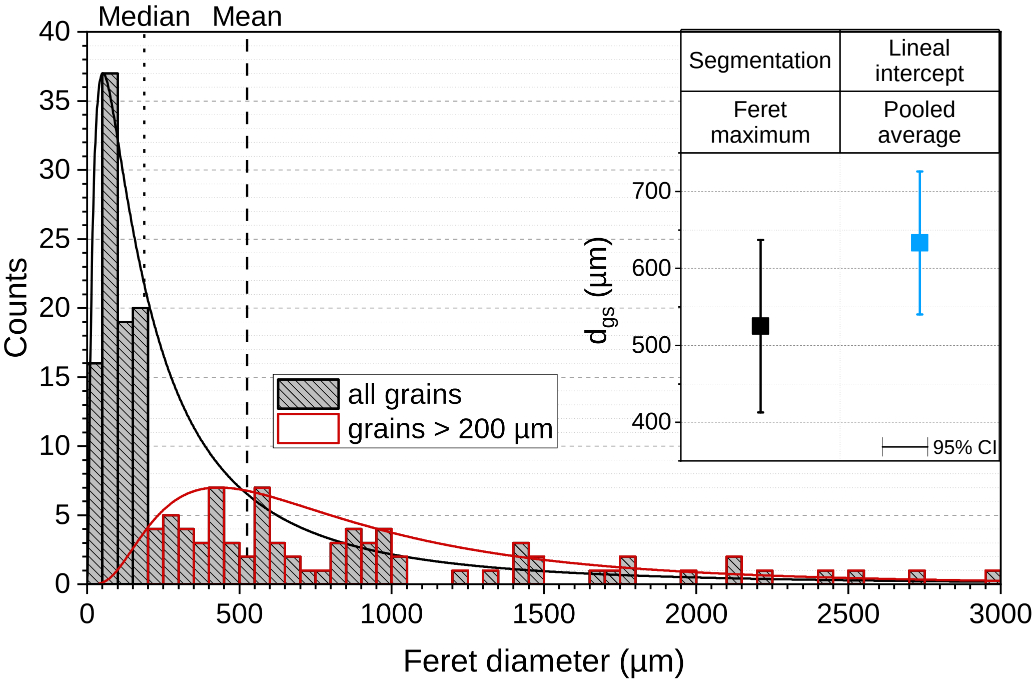

Figure 4.5.: Histogram and possible log-normal grain size distributions of investment-cast as-cast Fe-25Al-3.7Mo-0.4Ti-1B (casting wall thickness: 10 mm) taken from Feret diameters of manually segmented grains. The as-received mean grain diameter is contrasted to d_{gs} from lineal intercept method in an inset graph.

Grain sizes are spread in a log-normal distribution ranging from a few µm up to nearly 3 mm, with the highest count for grains between 50 an 100 µm. Accordingly, the median (188 µm) of the complete grain size distribution fundamentally differs from the mean value (525 µm) so that the average grain diameter d_{gs} represents a very conservative estimate. In addition, a local maximum of counts can be witnessed around the mean value, which could even point towards a duplex distribution of grains. Despite the complexity of results, the use of the mean value as estimate for d_{gs} appears appropriate as larger grain sizes > 500 µm make up for the largest area fraction in cross-sections. Comparison of average grain sizes by manual segmentation and lineal intercept method can only be based on mean values because meaningful median values are not available by lineal intercept method. A good agreement between the mean values d_{gs} calculated from maximum Feret diameters by manual segmentation (525 µm) and from pooled averages of lineal intercepts in two directions (633 µm) was verified as the inset in Figure 4.5 shows. In summary, lineal intercept method should serve as a good, conservative estimate of average grain sizes despite the large scatter.

4.2. Thermophysical properties

4.2.1. Phase transitions

Solid-state transformations and melting transitions of as-cast Fe-25Al-3.7Mo-0.4Ti-1B are illustrated in Figure 4.6 as determined by DTA. The heating (red) and cooling (blue) curves of the second cycle at ±10 $\mathrm{Kmin^{-1}}$ are displayed. The baselines of the temperature difference signal were subtracted to highlight local deflections. In accordance with Li et al. [38], two reversible solid-state transformations and two melting transitions can be detected.

At 662 °C, the transition from ordered $D0_3$ to ordered B2 structure $T_c^{D0_3 \leftrightarrow B2}$ can be found. Likewise, the transition from ordered B2 to disordered A2 $T_c^{B2 \leftrightarrow A2}$ is located at 921 °C. As they represent second-order transitions, they are defined at the local minima of endothermic peaks in the heating curves. A good agreement of the minima in heating curves and the onsets of cooling curves is given. Besides, comparison to DTA heating curves recorded at 5 $\mathrm{Kmin^{-1}}$ (not shown here) only deviated by a few Kelvin verifying the results. Both phase transformation temperatures are shifted to higher temperatures compared to binary Fe_3Al (542 °C ($T_c^{D0_3 \leftrightarrow B2}$) and 753 °C ($T_c^{B2 \leftrightarrow A2}$) [197]). This effect can be deduced from the solid-solution additions of Mo and Ti, which was already observed in multiple studies [38, 95, 131]. The most accepted explanation is connected to the atomic size misfit solutes create and whose induced strain energy is balanced by ordering [132].

The two large deflections at higher temperatures can be assigned to the extended melting range of the alloy which is likely a result of the eutectic boride phase. It spans from the onset of the

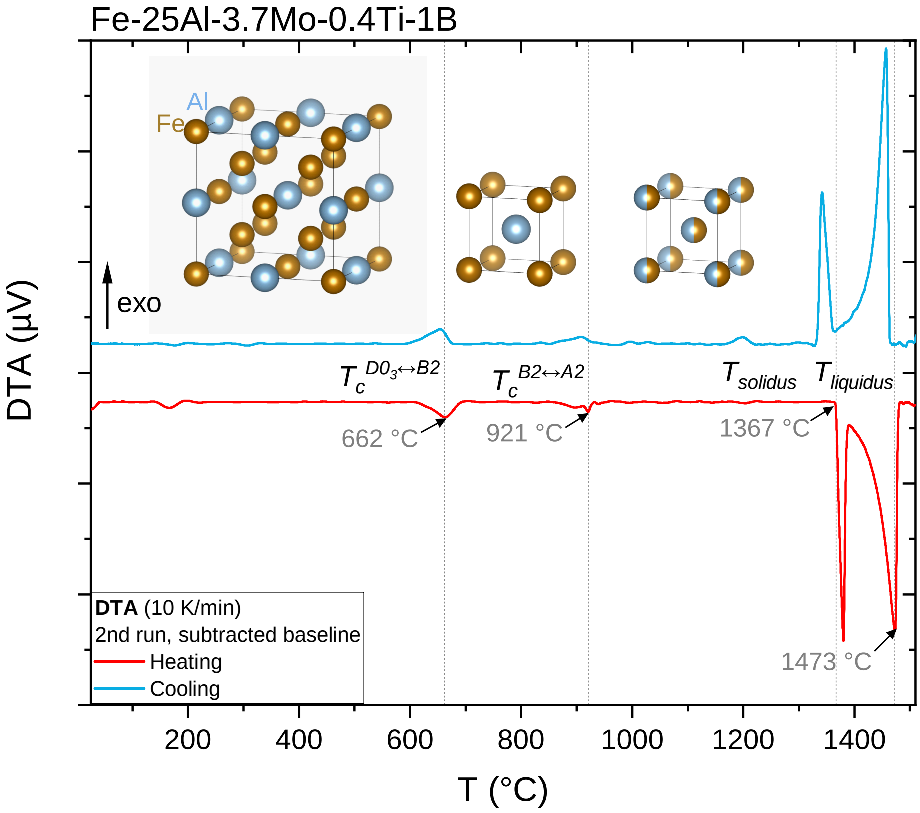

Figure 4.6.: DTA heating and cooling curves at ±10 Kmin^{-1} of as-cast Fe-25Al-3.7Mo-0.4Ti-1B. Baselines were subtracted for better visualisation of peaks. Adapted from [143].

first peak of the heating curve at 1367 °C ($T_{solidus}$) to the minima of the second peak at 1473 °C ($T_{liquidus}$). Values agree well with the onsets of the cooling curve and the data reported by Li et al. [38].

4.2.2. Coefficient of thermal expansion (CTE)

Figure 4.7 exhibits the technical and physical CTEs, $\bar{\alpha}(T_0, T)$ (grey triangles) and $\alpha(T)$ (grey solid line), obtained from the relative length change $\Delta L/L_0$ (red solid line) during sample heating up to 1000 °C. The reference temperature T_0 is usually 20 °C. The technical CTEs appear to be relatively stable over temperature and only vary between $1.28 \cdot 10^{-5}$ and $2.14 \cdot 10^{-5}$ K^{-1}. Against this, the physical CTE curve ranges between $1.8 \cdot 10^{-5}$ and $3.25 \cdot 10^{-5}$ K^{-1}.

Notably, there are two apparent major deflections at similar temperatures as the two solid-state transformations of Fe-25Al-3.7Mo-0.4Ti-1B. These coincide with points of inflections in the plot

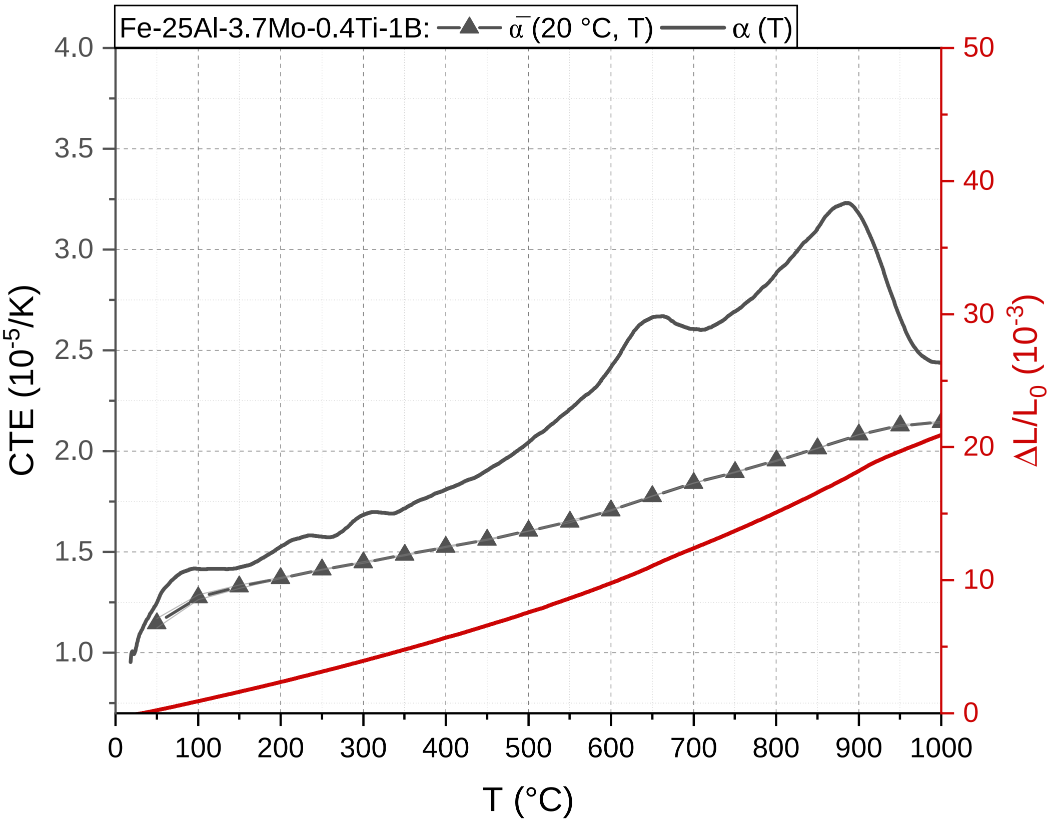

Figure 4.7.: Relative length change $\Delta L/L_0$ of as-cast Fe-25Al-3.7Mo-0.4Ti-1B in dilatometric measurements and resulting technical $\bar{\alpha}(T_0, T)$ and physical CTE $\alpha(T)$. Adapted from [143].

of $\Delta L/L_0$ over temperature. According to the Ehrenfest classification of phase transitions, a mere change in the slope of volume corresponds to a second order phase transition and therefore proves its origin from solid-state transformations [198]. The deviation of $T_c^{B2\leftrightarrow A2}$ derived from the physical CTEs' maximum (890 °C) compared to the value from DTA (921 °C) could originate from differentiation and smoothing, but also different heating rates involved.

Technical CTEs $\bar{\alpha}(T_0, T)$ of Fe-25Al-3.7Mo-0.4Ti-1B are comparable to available data on binary Fe-30Al above 500 °C [199]. In comparison to physical CTEs of binary Fe_3Al [200] though, $\alpha(T)$ of the investigated alloy is higher at most temperatures. The difference between physical CTEs of binary Fe-25Al and Fe-25Al-3.7Mo-0.4Ti-1B might arise from boride particles which are known to alter the elastic response of particulate composites (c) [201]. Their impact can be estimated e.g. by Turner's analytical model [202] which considers a rule of mixture of the technical CTE, the bulk modulus B and the volume fraction f_m or f_p of matrix (m) and particle (p) phase (see equation (4.1)).

$$\bar{\alpha}_c = \frac{\bar{\alpha}_m B_m f_m + \bar{\alpha}_p B_p f_p}{f_m B_m + f_p B_p} \tag{4.1}$$

With equation (4.1), the theoretical value of $\bar{\alpha}_c$ for Fe-25Al-3.7Mo-0.4Ti-1B can be calculated to examine whether the boride phase fraction could significantly increase the technical CTE compared to binary Fe-Al alloys. A minimum temperature of $T = 100$ °C is selected to be able to use reference data on bulk modulus B which was only available for room temperature. An experimental value of binary Fe_3Al (147 GPa [203]) and one from ab-initio calculations for Mo_2FeB_2 (310 GPa [204]) were taken. With respect to technical CTEs $\bar{\alpha}(T_0, 100\ °C)$, similar experimental values were found for binary Fe_3Al ($1.1 \cdot 10^{-5}$ K^{-1}, extrapolated from [199]) and Mo_2FeB_2 borides ($1.0 \cdot 10^{-5}$ K^{-1} [205]). With the average boride phase volume fraction of 0.04 from Table 4.2, a technical CTE of $1.09 \cdot 10^{-5}$ K^{-1} can be determined from the rule of mixture. Due to the low particle fraction, the calculated value of the particulate composite does not significantly differ from the binary Fe-Al alloy, but clearly deviates from the experimental value of Fe-25Al-3.7Mo-0.4Ti-1B ($1.28 \cdot 10^{-5}$ K^{-1}) at 100 °C. Therefore, boride particles can hardly explain the different physical CTEs of Fe-25Al and the investigated alloy.

Another possibility for an increased CTE is the influence of solute additions in the Fe-Al matrix. No data on technical CTEs of specifically Mo alloyed Fe-Al solid solutions was found. However, a study on ternary Fe-26Al-2X alloys by Švec and Kejzlar [206] suggests that these differences could arise from specific solute elements. Solute additions are therefore the likeliest contributor to increased physical CTEs.

4.2.3. Young's modulus, shear modulus and Poisson's ratio

Figures 4.8a and b depict the temperature profile of the Young's modulus E and the shear modulus G of as-cast Fe-25Al-3.7Mo-0.4Ti-1B (black squares) measured and calculated by Dynamic Resonance Method. In addition, both moduli were taken for calculating the Poisson's ratios υ at various temperatures according to equation (3.4). Values are illustrated in Figure 4.8c. Both E and G show a near-linear decline over temperature, with the Young's modulus ranging from 173 GPa (20 °C) to 99 GPa (1000 °C) and the shear modulus decreasing from 69 GPa (20 °C) to 38 GPa (1000 °C). Similar to the dilatometric measurements, slope changes are visible close to $T_c^{D0_3 \leftrightarrow B2}$ and $T_c^{B2 \leftrightarrow A2}$. This correlation is also apparent in the plot of Poisson's ratio (Figure 4.8c) whose values only vary little from 0.26 (20 °C) to 0.29 (1000 °C). Data on Young's modulus [58] and shear modulus [146] of binary D0_3 iron aluminides reveals that the studied quinary alloys have significantly increased elastic properties, although the difference decreases with temperature. Young's moduli *E* of Fe-25Al-3.7Mo-0.4Ti-1B are between 35% (20 °C) and 10% (800 °C) higher and shear moduli *G* between 25% (20 °C) and 12% (900 °C) higher compared to binary Fe_3Al.

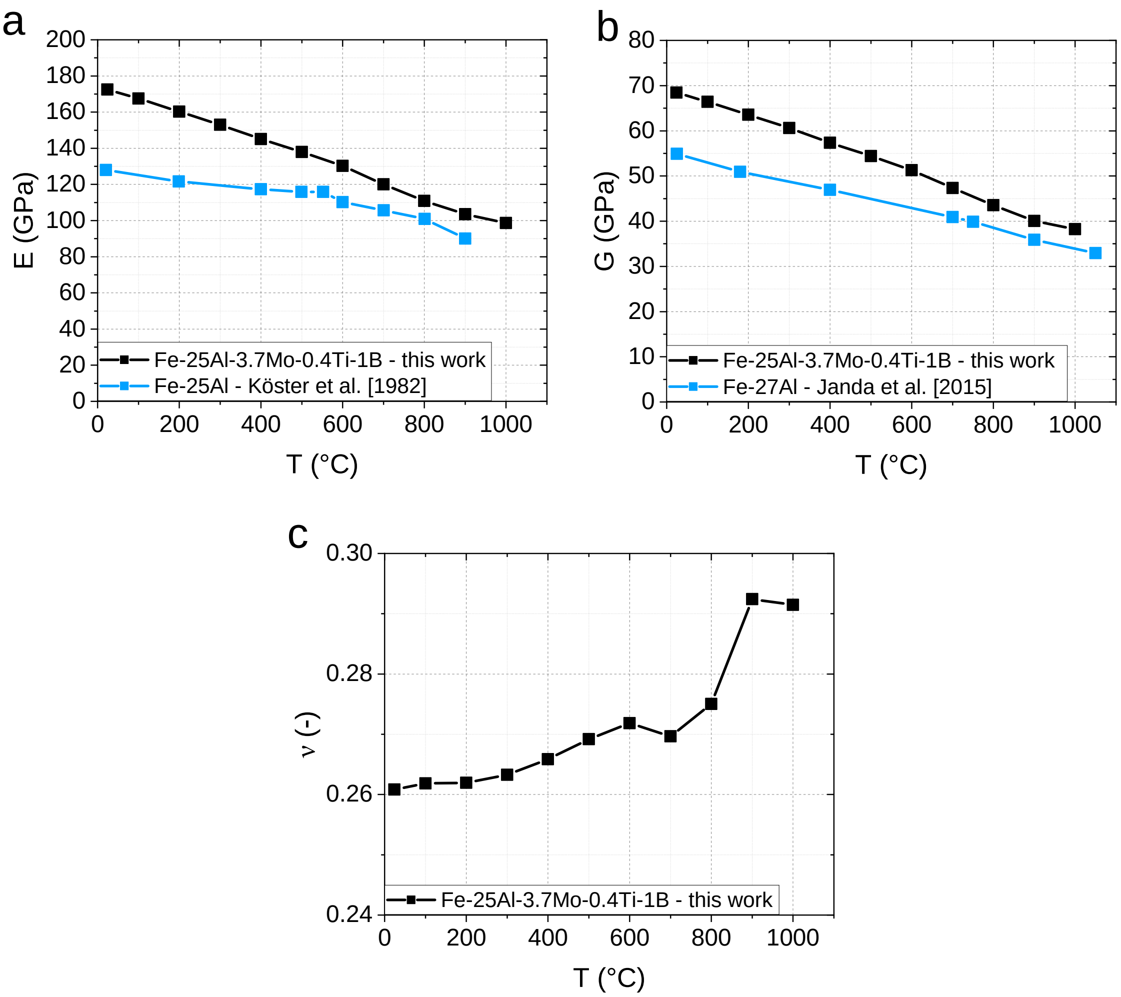

Figure 4.8.: Temperature dependent (a) Young's modulus *E* (reproduced from [143]), (b) shear modulus *G* and (c) Poisson's ratio υ of as-cast Fe-25Al-3.7Mo-0.4Ti-1B. Data on binary Fe_3Al is given for reference [58, 146].

The increases in elastic properties can potentially originate from the solutes in the Fe-Al matrix and the secondary phase particles. The change of elastic properties in Fe_3Al solid solutions with solute concentration was already investigated in experiments at room temperature by Friák and co-workers [59]. Low solute concentrations as for the case of Ti (< 1 at%) did not yield any increase in Young's modulus, but even lowered it slightly. Against this, additions of tungsten with a similar atomic radius as molybdenum increased Young's modulus by nearly 50% (estimated for 3 at% solute concentration). The stiffening effect of Mo_2FeB_2 particles inside the Fe-Al matrix can be estimated by the Voigt-Reuss-Hill (VRH) average analytical model in equation (4.2) [207]. Although it does not capture microstructural details about shape, orientation and distribution of particles, it provides an average of the higher and lower bounds estimated from Voigt and Reuss approximations respectively [208, 209].

$$E_{VRH} = \frac{\bar{E}_V + \bar{E}_R}{2} = \frac{1}{2} \cdot \left(\left[f_m E_m + f_p E_p \right] + \frac{E_m E_p}{f_m E_p + f_p E_m} \right) \tag{4.2}$$

Ab-initio calculations estimated the Young's modulus of non-magnetic Mo_2FeB_2 at room temperature to 378 GPa [204] which agrees well with experimental findings from nanoindentation [210]. Taking the average secondary phase volume fraction of 0.04 from own results, Young's modulus at room temperature could be increased by only 5% to 135 GPa. Therefore, the stiffening effect by eutectic boride particles is probably subordinated to the increase by Mo solute additions in the matrix.

4.3. Mechanical properties

4.3.1. Compressive and indentation properties

Figure 4.9 exhibits the engineering stress-strain curves of as-cast and homogenised Fe-25Al-3.7Mo-0.4Ti-1B alloys during compression tests at room temperature. In as-cast condition, the alloy's proof strength at 0.2% plastic compression $R_{dp0.2}$ is 425 ± 6 MPa and decreases to 339 ± 5 MPa after annealing at 1000 °C for 100 h followed by furnace cooling (HT2).

Table 4.4.: Mean macrohardness HV10, mean microhardness HV0.01 and 95% CI of phases in investment-cast Fe-25Al-3.7Mo-0.4Ti-1B tested in as-cast and homogenised (HT2) state. Data reproduced from [143].

	Vickers test	**as-cast**	**1000 °C/100 h/FC**
Fe-25Al-3.7Mo-0.4Ti-1B	HV10	290 ± 3	284 ± 7
Matrix phase	HV0.01	371 ± 5	379 ± 5
Eutectic phase	HV0.01	580 ± 64	620 ± 89

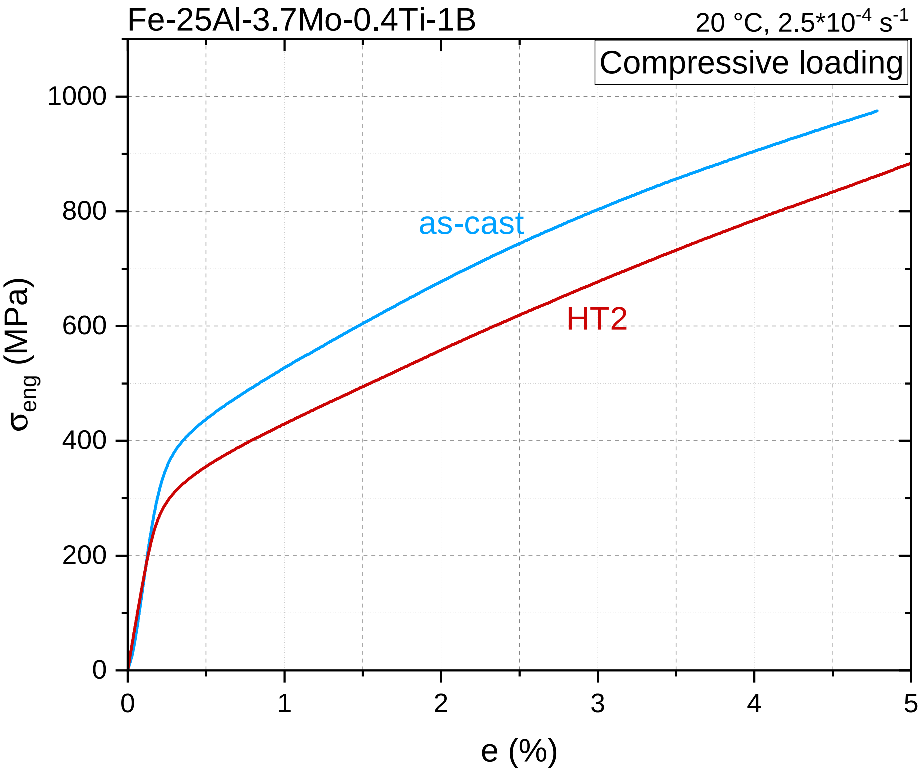

Figure 4.9.: Compressive room temperature stress-strain curves of investment-cast Fe-25Al-3.7Mo-0.4Ti-1B after casting and after homogenisation (HT2).

This significant drop was not observed in measurements of the Vickers macrohardness (see Table 4.4). There, the HV10 values only showed an insignificant decrease from 290 ± 3 HV10 (as-cast) to 284 ± 7 HV10 (HT2). Due to the presence of different phases with differing strengths, lower indentation sizes were also applied to quantify the contributions by matrix and eutectic phase regions. The microhardness of $D0_3$ Fe_3Al with Mo and Ti solutes are fairly similar in as-cast condition (371 ± 5 HV0.01) and after homogenisation (379 ± 5 HV0.01). Values are increased compared to data by Li et al. [38] due to the indentation size effect [211] as Vickers indentation diagonals go down to 7 µm. Likewise, their data suggested no effect of homogenisation treatment on the solid-solution matrix. With regard to the eutectic phase area, microhardness is substantially increased compared to the matrix (as-cast: 580 ± 64 HV0.01) and did not significantly change after HT2 (620 ± 89 HV0.01).

4.3.2. Quasi-static tensile properties

Figure 4.10 plots representative engineering stress-strain curves during tensile loading at temperatures up to 650 °C in air. An inlet depicts a zoomed-in section of the stress-strain curves at room temperature and at 250 °C. The average elastic slope during tensile tests room temperature is 170 ± 8 GPa and agrees well with results from resonance measurements (173 GPa) although the uncertainty is usually expected to be larger [212]. Tensile specimens tested at ambient conditions already fail before reaching the 0.2% proof strength $R_{p0.2}$ with an average ultimate tensile strength of $R_m = 252 \pm 15$ MPa (averaged from five measurements).

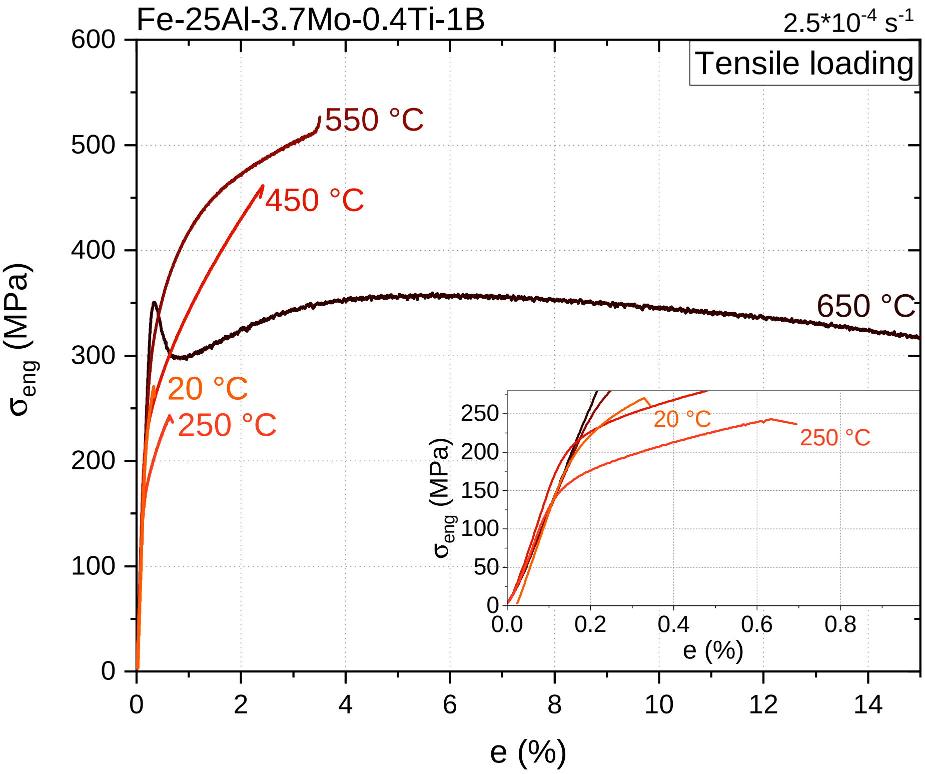

Figure 4.10.: Engineering stress-strain curves of investment-cast Fe-25Al-3.7Al-0.4Ti-1B alloys (in as-cast condition below 400 °C, otherwise homogenised at HT2) representative for various temperatures up to 650 °C under tensile loading. The abscissa is cut off and does not show the fracture point at 650 °C. Reproduced and adapted from [143].

With increasing temperature, ductility of investment-cast Fe-25Al-3.7Mo-0.4Ti-1B only slowly recovers (see Figure 4.10). At 250 °C, only a minor increase in elongation after fracture A is notable. At 450 and 550 °C, ductility increments are also accompanied by increasing work hardening rates below $e = 1\%$ and increasing ulitmate tensile strengths. At 650 °C, discontinuous yielding can be observed featuring an upper and lower yield strength with a yield drop of 40–50 MPa. $R_{p0.2}$ was determined close to the upper yield strength level. R_m was reached after the lower yield point and after deformation with decreasing work hardening rate which is accompanied by faint, but observable stress serrations. Continuing from there, specimens further elongated under decreasing stress reaching elongations after fracture of around 30%. Plotting the curve with true stress σ_t and true strain e_t according to the analytical equations (3.12) and (3.11), two deformation types can be identified (see Figure B.1): i) an extensive region of ideal plastic deformation followed by ii) deformation under continuous necking. The yielding behaviour with limited work softening is a typical deformation mechanism known in solid-solution alloys. First published as high temperature yield point phenomenon [213], it describes the pinning of dislocations by solutes forming so-called Cottrell atmospheres [214]. Especially at higher temperatures, substitutional solute diffusion become fast enough to migrate towards dislocations where they get pinned. The stress needed to overcome the pinning effect is visible in the stress-strain curve as steep work hardening towards the upper yield point. As soon as dislocations are able to break free from the solute pinning centres, free dislocation movement leads to a decrease of the stress until further work hardening processes set in. This yielding behaviour is usually a function of temperature and strain rate and therefore might have not been visible at 550 °C and below. A contribution by excess thermal vacancies or vacancy aggregates can be excluded. According to Morris et al. [215], they were found to already cause mild yield discontinuities at intermediate temperatures (300-500 °C), which could not be observed here. Thus, the likeliest origin of pinning centres are Mo and Ti solutes, which proves their solid-solution hardening effect at higher temperatures. The faint stress serrations following the yield discontinuity might be connected to dynamic strain ageing mechanisms such as the Portevin-Le Chatelier effect [216]. It describes continuous plastic flow instabilities caused by solutes, which lead to local formation of fine deformation bands [217]. Still, a further investigation was not pursued in this case.

Figure 4.11 plots the mean tensile properties at the tested temperatures and their 95% CI. Values are also summarised in Table 4.5. Note that $R_{p0.2}$ could be not established for investment-cast specimens at room temperature. Both 0.2% proof strength $R_{p0.2}$ and ultimate tensile strength R_m show a local maximum at 550 °C. Therefore, the temperature of the maximum of $R_{p0.2}$ (347 MPa) can be estimated as the peak temperature of the yield stress anomaly T_{YSA}. Above this temperature, R_m is drastically reduced, whereas the onset of plastic deformation is only slightly reduced.

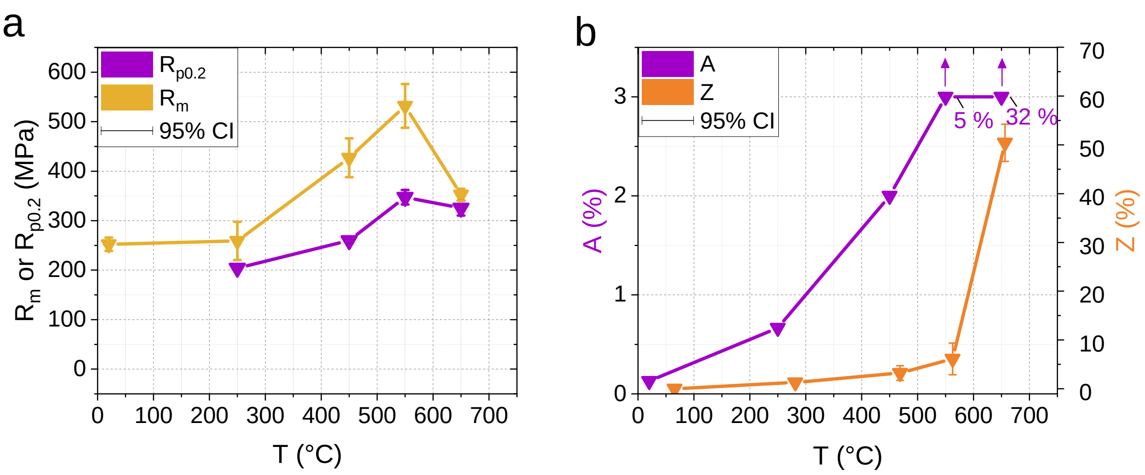

Figure 4.11.: Tensile properties of investment-cast Fe-25Al-3.7Al-0.4Ti-1B dependent on temperature: (a) $R_{p0.2}$ and R_m, (b) A and Z. Reproduced and adapted from [143].

Table 4.5.: Mean tensile properties and 95% CI of investment-cast Fe-25Al-3.7Mo-0.4Ti-1B at ambient and elevated temperatures. Reproduced from [143].

T (°C)	Condition	$R_{p0.2}$ (MPa)	R_m (MPa)	A (%)	Z (%)
20	AC	-	252 ± 14	0.10 ± 0.04	-
250	AC	204 ± 4	259 ± 38	0.7 ± 0.3	1.3 ± 0.5
450	HT2	260 ± 2	427 ± 39	2.0 ± 0.6	3.2 ± 1.5
550	HT2	347 ± 15	532 ± 44	5.0 ± 2.9	6.1 ± 3.2
650	HT2	326 ± 15	353 ± 12	32 ± 2	50 ± 4

Looking at the course of elongation after fracture A over temperature, a significant increase in ductility can only be observed above 550 °C. The classical definition of BDTT which states that ductility transitions from $< 1\%$ to $> 3\%$ within a temperature range of less than 100 K is not met here. Instead, the alloy shows a mild gradual rise of ductility from 250 °C to 550 °C, with the average elongation after fracture increasing from 0.7% to 5%. As the average elongation after fracture at 450 °C is already $2.0 \pm 0.5\%$, the BDT is expected to be above this temperature. A drastic increase in elongation after fracture to over 30% at 650 °C is also accompanied by a large increase of the percentage reduction of area Z from 6% to 50% within 100 K. This indicates a strong correlation between elongation after fracture and necking behaviour.

Results on tensile strength at room temperature appear rather low considering a reported yield strength of as-cast binary Fe_3Al of 529 MPa [18] and the expected strengthening contributions by solid-solution strengthening from Mo and Ti and particle strengthening by borides. To rule

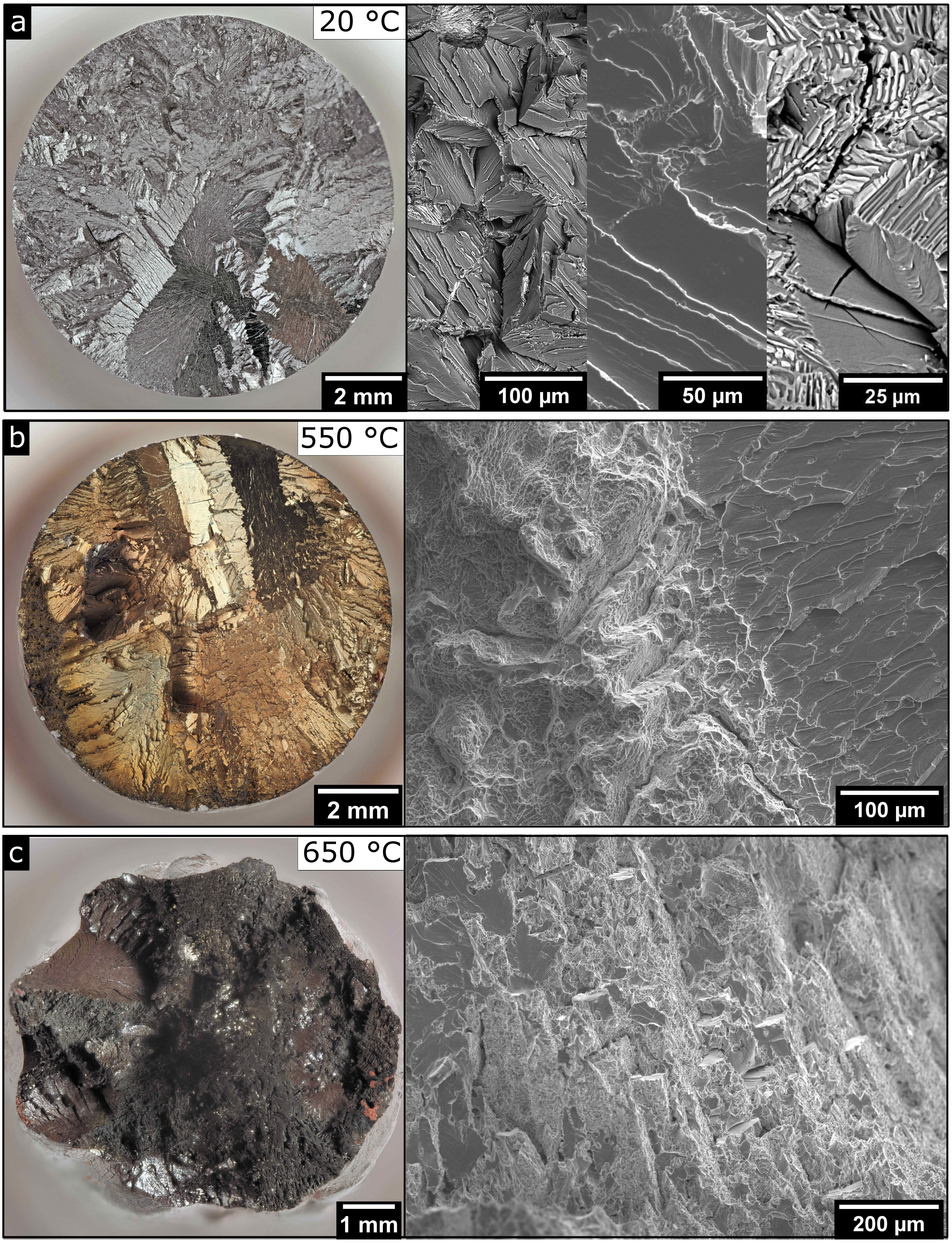
a
20 °C
2 mm
100 µm
50 µm
25 µm
b
550 °C
2 mm
100 µm
c
650 °C
1 mm
200 µm

Figure 4.12.: Fracture surfaces of the Fe-25Al-3.7Mo-0.4Ti-1B alloy following tensile tests at room temperature (a), 550 °C (b) and 650 °C (c). The fracture surfaces from stereographic imaging are shown on the left, while magnified SEM images are presented on the right. Reproduced and adapted from [143].

out premature failure caused by e.g. defects, fractography was performed. Stereographic and SEM images of a fracture surface are shown in Figure 4.12a. It was not possible to identify crack initiation points or to draw a direct conclusion from present defects on specimen fracture. Essentially, fracture surfaces can be described as brittle cleavage areas with no deformation of the outer contour which fits the low ductility in tensile tests. Different repetitive features were observed: i) zigzag-like contours or steps of cleavage planes which illustrate favoured fracture progression along certain orientations, ii) cleavage lines which are characteristic for brittle materials with large grains [218], iii) partial crack deflection at boride phase boundaries (although cracks also progress through boride lamellae). Fracture does not appear to follow grain contours and corresponds to a typically transgranular fracture. Therefore, it is likely that boron did not segregate to the grain boundaries where they could increase grain boundary cohesion, but was fully transformed by the eutectic phase reaction.

Besides, this fracture behaviour is not consistent with a study by McKamey et al. [131] on similar $D0_3$ Fe-Al-Mo-Ti-B alloys with lower Mo solute concentrations (2 at%). They reported a mixed intergranular-transgranular fracture mode which they connected to the presence of borides at the grain boundaries. As for binary alloys, iron aluminides between 25–28 at% were observed to fail intergranularly [219]. There, the change from intergranular to transgranular fracture at lower Al concentrations was attributed to an increase of mechanically induced APBs. The most probable explanation why the investigated alloy exhibits transgranular cleavage instead is an effect by Mo solutes with concentrations above 2 at%. Indeed, McKamey et al. [131] corroborated high brittleness in Fe-Al-Mo-Ti-B alloys with high nominal Mo concentrations (> 2 at%) during sample production. An explanation on the embrittlement effect or the reduced cleavage strength was not given. A possible hypothesis could be potentially linked to the mentioned APB quantities. Within a study on melt-spun $D0_3$ and B2 Fe-Al-Mo alloys, it was shown that with increasing Mo solute concentration, the thermally induced APD sizes could be reduced (i.e. APBs are increased) [220]. This was explained by segregation of Mo solutes to the APBs lowering their mobility. Still, the authors also emphasized in another study that only small APDs are insufficient to reduce plasticity to an extent of transgranular cleavage [221]. In addition, high APB energy is necessary to increase the dislocation-APB interaction (i.e. the resistance of APBs to dislocation motion). Only few experimental data with calculated APB energies is available on ternary alloys. One example is the Fe-Al-Cr system. However, many scientists reported ambiguous data on how Cr additions influence the APB energies [43]. More recent calculation data by CALPHAD method suggests that APB energies have a non-linear correlation with solute concentration in ternary Fe-Al-X alloys and can largely vary in small compositional ranges and depending on the solute species [222]. Thus, more experimental investigations of dislocation spacings and derived APB energies are necessary to conclude this hypothesis.

Further reasons for the observed transgranular fracture can be also linked to the large grain size, which, according to the analytical model by Cottrell et al. [223], is one of the drivers for brittle fracture. Furthermore, the extended network of eutectic boride phases could act as potential high-energy crack paths. As borides are not confined to grain boundaries, but spread across grains (see Figure 4.4a), they could enable transgranular crack propagation. Still, this mechanism should only play a minor role as cleavage lines and planes (without any visible borides adjacent to them) occcupy a higher proportion of the fracture surface.

The fracture behaviour observed following tensile tests at 250 °C and 450 °C is very similar to the fracture mechanisms described at room temperature. Only at 550 °C, a small proportion of dimple fracture becomes discernible on the left side in Figure 4.12b. The ductile region was estimated to be less than 5% of the fracture surface. The remaining specimen cross-section still consists of transgranular cleavage fracture areas. The transition region is given in the magnified SEM image. Only after tensile testing at 650 °C (Figure 4.12c), the fracture mode changes. Clear tapering of the cross-section is evident as well as selective elongation of individual grains in the edge area, which results in an irregular contour. At higher magnifications, larger proportions of ductile honeycomb fracture can be observed, with smaller cleavage planes in-between. In conclusion, at a temperature of 650 °C, a mixed fracture mode with transgranular cleavage and predominantly ductile fracture is established. The results from fractography indicate that the brittle-to-ductile transition temperature T_{BDT} should be rather situated to above 550 °C as only few ductile portions appeared. This also implies that T_{BDT} cannot be understood as a sharp transition here. Instead, the temperature transition range might be even more extended to achieve a mainly ductile fracture. For complex alloys as the one inspected, the classical definition of T_{BDT} is thus a rather non-conservative measure to mark the transition to ductile fracture.

The values of $R_{p0.2}$ and A with respect to temperature are presented in the context of existing literature data in Figures 4.13a and b (data taken from [18, 38, 99, 115, 127, 131]. Minimum values defined for P92 steel according to DIN EN 10216-2 are displayed in pale yellow [13]. The 0.2% proof strength data from tensile tests are displayed as inverted triangles with solid lines as a guide to the eye. In contrast, compressive testing data is marked by squares with dashed lines.

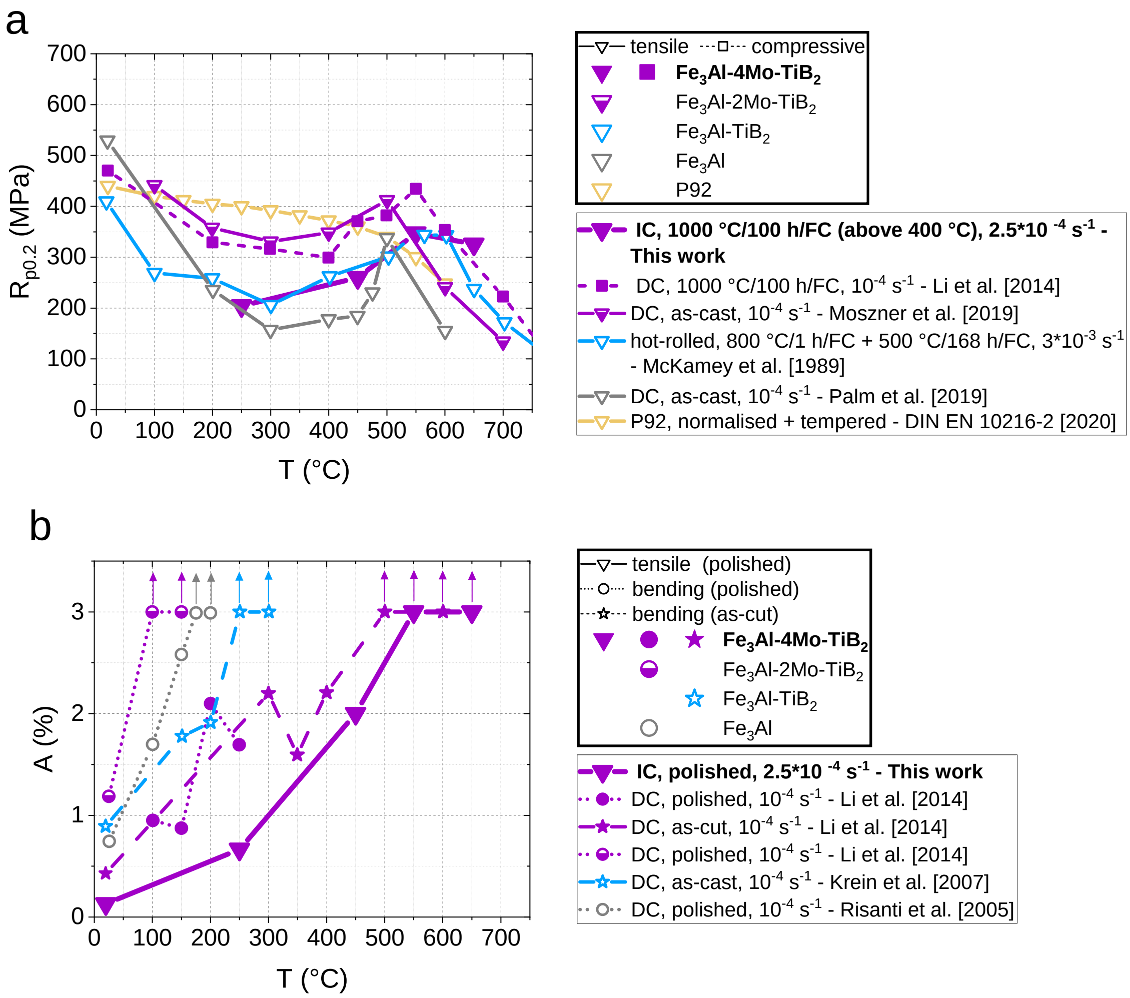

Figure 4.13.: Comparison of temperature dependence of 0.2% proof strength $R_{p0.2}$ (a) and elongation after fracture A (b) of investment-cast Fe-25Al-3.7Mo-0.4Ti-1B from tensile tests with literature data [18, 38, 99, 115, 127, 131]. P92 represents minimum values defined by DIN EN 10216-2 [13]. Adapted from [143].

Li et al. [38] investigated a die-cast alloy with similar composition (4 at% Mo) by compressive testing (purple solid squares). Their peak temperature T_{YSA} agrees well with this study (purple solid triangles). However, $R_{p0.2}$ below 550 °C is by average 105 MPa higher in Li et al.'s data. Two aspects which could contribute to this considerable difference is the loading direction and the grain size. Above T_{YSA}, $R_{p0.2}$ of this study appears to be superior or both data sets approach each other. This circumstance especially hints at an influence of grain size. No explicit specification of grain sizes is given by Li et al., but classical water-cooled die casting, as they used, can easily achieve grain sizes of 50 to 100 µm, which would be considerably lower than investment-cast grain sizes (660 µm). The effect of decreasing grain size on strength and ductility will be further investigated and discussed in 7.2. The possible flow stress differences due to different loading directions will be also later discussed in section 4.4 which also considers compressive and creep data.

Tensile tested Fe_3Al-2Mo-TiB_2 (purple half-solid triangles [127]) even exhibits a higher difference to the investigated alloy (by average 124 MPa below 500 °C). With respect to TiB_2 particle hardened Fe_3Al without solutes (blue open triangles [131]) and binary Fe_3Al (grey open triangles [18]), investment-cast Fe-25Al-3.7Mo-0.4Ti-1B appears to have comparable or slightly higher 0.2% proof strength at intermediate temperatures. The generally low strength below T_{YSA} is most likely a result of the brittle nature which is backed by the dominant cleavage fracture mode up to high temperatures. However, above T_{YSA}, the yield strengths of alloys with 2 at% Mo as well as considered alloys without solutes drop significantly compared to alloys with 4 at% Mo. Thus, it can be concluded that higher incorporation of Mo is especially effective in increasing strength above T_{YSA} for this alloy system. Accordingly, the investigated Fe-Al alloy only surpasses the mechanical strength of P92 steel at 550 °C and above.

A literature comparison of A with emphasis on the BDT is given in Figure 4.13b. Note that referenced alloys were processed by die casting with different final surface conditions and fracture strains were exclusively measured by 4-point bending tests at comparable strain rates. It is evident that the elongations after fracture of the polished investment-cast alloy (purple solid triangles) fall short of the achievable fracture strains of die-cast alloys with similiar composition from 4-point bending tests [38]. This applies to both as-cut (purple solid stars) and polished (purple solid circles) specimens. The absolute differences range from 0.3% at room temperature to ∼1% at 250 °C. The comparably low ductility points at the assumption that the polishing strategy was not sufficient or polishing, generally speaking, not as effective as expected under tensile loading to limit notch sensitivity and environmental embrittlement effects. Still, as no further tests were conducted with differently post-treated surfaces, a final conclusion on the environmental embrittlement effect and its reduction by polishing could not be made. In general, the experimental comparability of tensile strains from bending and tensile tests is described as very good [224, 225], which is also backed by theoretical considerations [226, 227]. At the same time, the applicability is limited in brittle materials and fracture strains achieved by bending tests are often reported to surpass those in uniaxial tensile tests [227, 228]. In consideration of the brittle behaviour exposed by fractography, this could give evidence on a lesser comparability of elongations after fracture of Fe_3Al-4Mo-TiB_2-type alloys by different mechanical tests.

Still, higher grain refinement which can be achieved by die-casting methods (see section 7.1) could also point towards higher ductilities as referenced by Li and co-workers. About the brittle-to-ductile transition, T_{BDT} from bending tests (> 500 °C) [38] almost agrees with the transition temperature determined in tensile tests (> 550 °C). These transition temperatures are significantly higher than T_{YSA} of binary Fe_3Al alloys (> 175 °C, grey open circles) [115]. In contrast, the earlier presented alloys with only TiB_2 particles (> 250 °C, blue open stars) [99] and with TiB_2 + 2 at% Mo additions (> 100 °C, purple half-solid circles) [38] exhibit comparable or even lower values of T_{YSA}. From this comparison, it can be inferred that exceeding a nominal Mo concentration of 2 at% is considerably shifting T_{YSA} to higher temperatures.

4.3.3. Creep properties

The creep behaviour of investment-cast Fe-25Al-3.7Mo-0.4Ti-1B was studied by determining the creep strain under simultaneous constant load and temperature exposure. Based on the DTA results (see subsection 4.2.1), the three investigated temperatures (600, 650, 700 °C) span a homologous temperature range of 0.5–0.56$T_{liquidus}$. The two lower temperatures lie in the $D0_3$ phase field, whereas the higher one can be assigned to the B2 phase field. In contrast, the loads were selected according to reference data on technical competitors such as P92 steel [11]. These stresses thereby yield a σ_0/G ratio range of $9 \cdot 10^{-4}$ to $5 \cdot 10^{-3}$ at the investigated temperatures.

Figure 4.14a plots all curves of true creep strain e_{ft} over time t for the investigated temperature-stress pairs. True creep strains as derived by equation (3.12) were selected to take large reductions of specimen cross-sections into account. Tests without rupture are labelled with a black cross at the last data record. Different temperatures are illustrated by different symbols and colours. Applied loads are displayed as initial stress σ_0 acting at the start of creep tests. All stress levels were below the hot 0.2% proof strength and therefore exhibited no plastic deformation during initial loading. All ruptured specimens achieved creep strains above the calibrated range with 40% and more. Measurements outside the calibrated range showed frequent drops in strain when extensometer probes temporarily rebounded on the specimen. These were manually corrected during data processing to recreate the true strain progression as displayed in Figure 4.14. When reliable strain monitoring was no longer possible due to extensive creep times and strains, curves were extrapolated to the creep strain at fracture which was estimated from the last extensometer signal. Elongations after creep fracture A_u which were measured after cooling to room

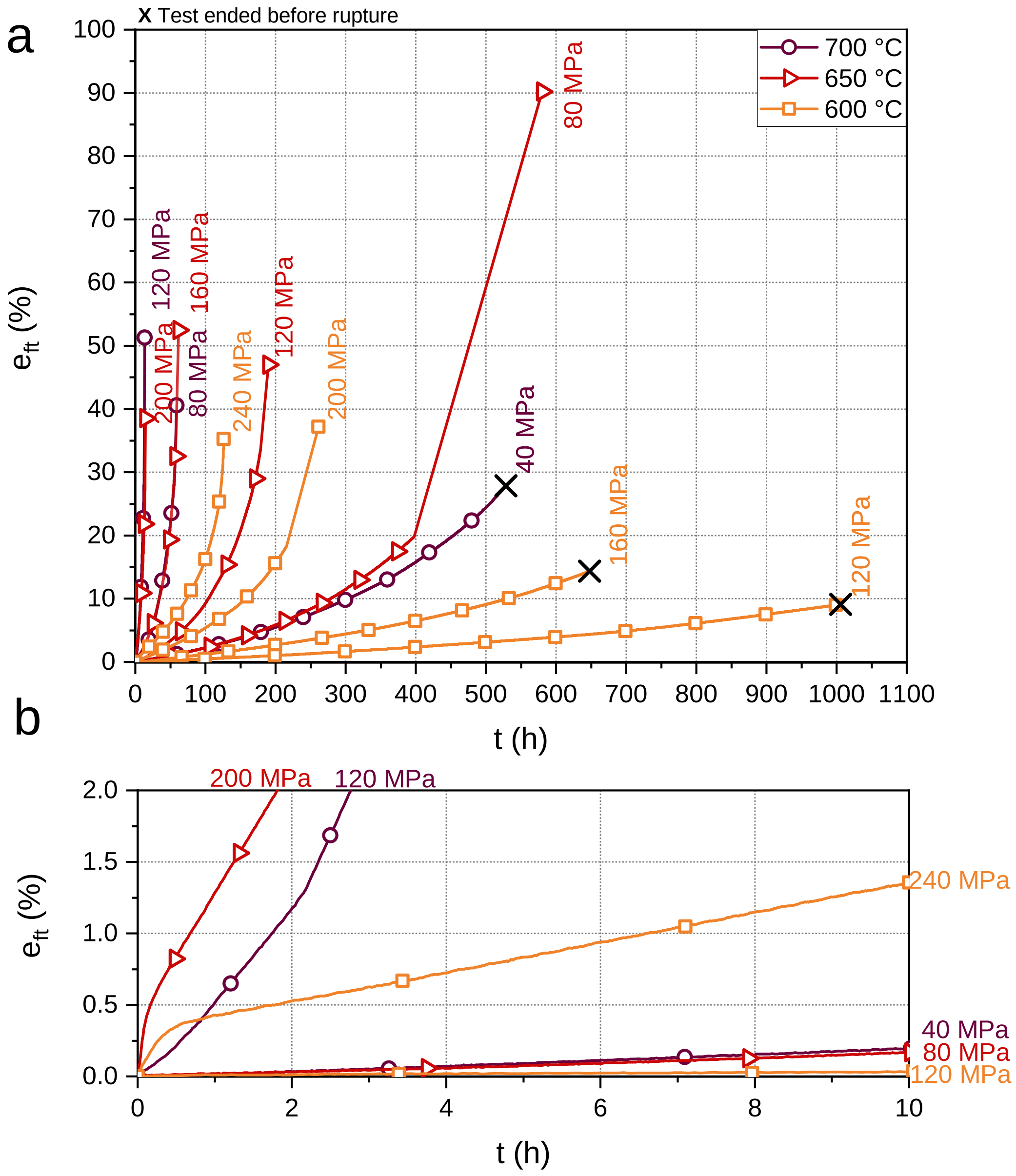

Figure 4.14.: True creep strain e_{ft} over time t of Fe-25Al-3.7Mo-0.4Ti-1B (in HT2 state) tested at temperatures between 600 and 700 °C and various constant loads translated as initial stresses σ_0. (a) Full view of all graphs (reproduced from [143]), (b) magnified view of selected graphs.

temperature ranged from 40% (600 °C/240 MPa) to 92% (650 °C/80 MPa). The lowest creep strains were attained at 600 °C and creep lifes easily extended beyond 500 h under 160 MPa. Figure 4.14a shows the general trend that under constant temperature, the time to rupture t_u usually decreases with increasing stress. This is accompanied by an increasing slope representing the true creep rate $\dot{e}_{ft}$.

A magnified view of true creep strain e_{ft} during the first hours of creep loading is given in Figure 4.14b. Only creep strain graphs of minimum and maximum stress for each temperature are displayed. Most specimens show a continuous increase of true creep strain and only a few (600 °C/240 MPa, 650 °C/200 MPa) exhibit a temporary change from high to low slope within less than an hour. This inflection point can be interpreted as the transition from primary to secondary creep stage. The absence of primary creep or the rapid occurrence of secondary creep indicates that the homogenisation treatment (HT2) was effective in transferring the microstructure closer to thermal equilibrium. Similar conclusions were drawn from creep tests of as-cast and pre-annealed Fe-27Al and Fe-39Al alloys at 650 °C [146]. To study the regions of primary and secondary creep in more detail, a view on the progression of true creep rate $\dot{e}_{ft}$ over time t and true creep strain e_{ft} is worthwhile.

Primary creep

Figures 4.15 and 4.16 depict semi-logarithmic plots with the smoothed curves of true creep rate $\dot{e}_{ft}$ over time t and over true creep strain e_{ft} respectively. Next to them, a magnified view on the first hours (Figure 4.15a) and up to 2% true creep strain (Figure 4.16a) is displayed. With two exceptions (650 °C/200 MPa; 600 °C/240 MPa), the course of $\dot{e}_{ft}$ over t and e_{ft} is as follows:

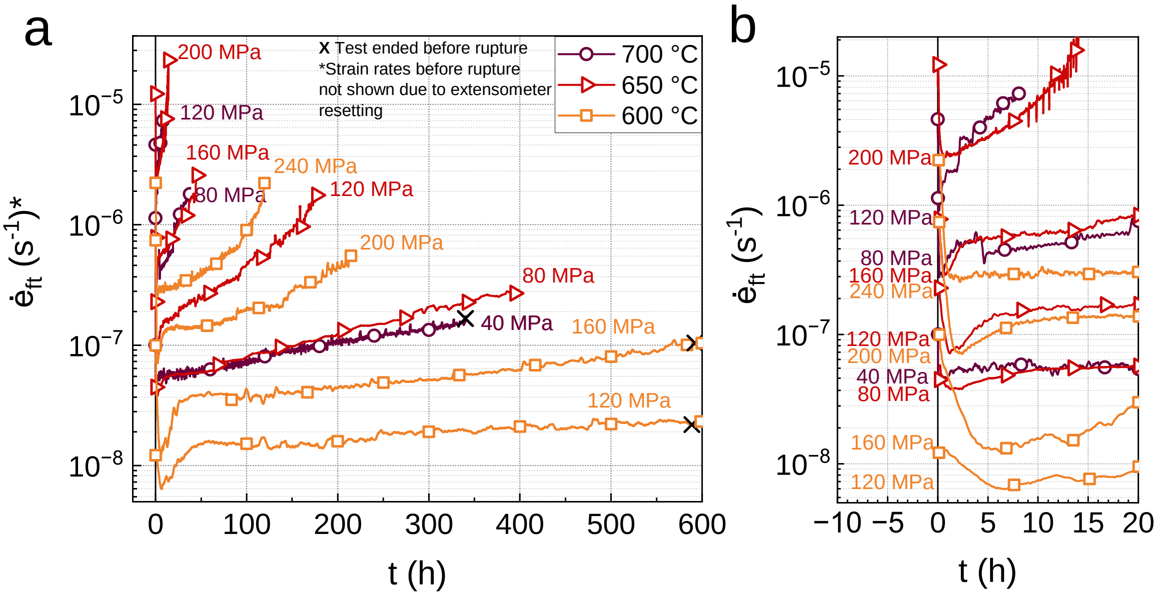

Figure 4.15.: Half-logarithmic plot of true creep rate $\dot{e}_{ft}$ over time t of homogenised Fe-25Al-3.7Mo-0.4Ti-1B tested at temperatures between 600 and 700 °C and various initial stresses σ_0. (a) Full view of all graphs cut off after $e_{ft} = 15\%$ (reproduced and adapted from [143]), (b) magnified view on primary creep stage of all graphs.

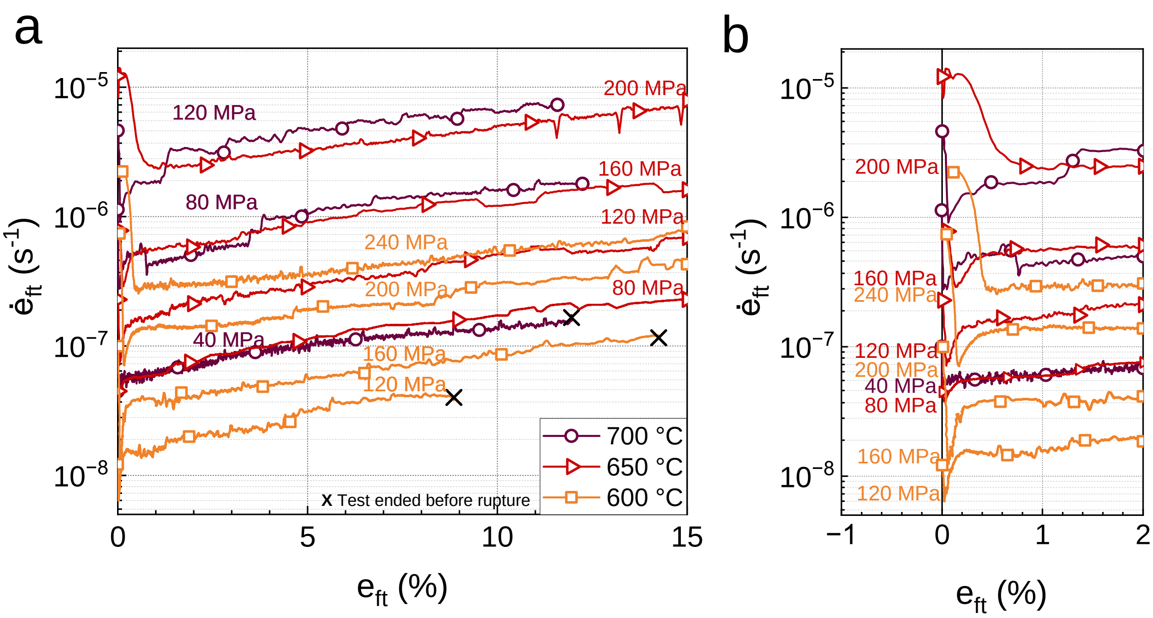

Figure 4.16.: Half-logarithmic plot of true creep rate $\dot{e}_{ft}$ over true creep strain e_{ft} of Fe-25Al-3.7Mo-0.4Ti-1B creep tested at temperatures between 600 and 700 °C and various initial stresses σ_0. (a) Full view of all graphs (b) magnified view on primary creep stage of all graphs. Reproduced and adapted from [143].

$\dot{e}_{ft}$ initially falls to a minimum creep rate $\dot{e}_{ft,min}$ and then gradually rises to an intermediate level where a limited regime of constant creep rate $\dot{e}_{ft,ss}$ is entered. This progression of $\dot{e}_{ft}$ is known in the community as inverse transient behaviour which is usually categorised as class A (alloy-type) creep [229, 230]. It is usually connected to the viscous glide of dislocations being dragged by solute clouds [101]. This mechanism competes with the diffusion-controlled climb of dislocations, which is usually the rate-controlling mechanism [103, 231, 232]. The onset of constant creep rate $\dot{e}_{ft,ss}$ of specimens showing an inverse transient behaviour can be up to half an order of magnitude higher than the determined $\dot{e}_{ft,min}$, especially at lower temperatures and stresses. The impact of this difference on creep mechanism interpretation will be discussed later. The minimum creep rate $\dot{e}_{ft,min}$, if applicable, is reached after several minutes to a few hours, but limited to $t < 8$ h or $e_{ft} < 1\%$. The time t or creep strain e_{ft} associated to $\dot{e}_{ft,min}$ apparently depends on the initial stress σ_0 and temperature T. For constant temperature, it shifts to shorter times and higher creep rates the higher the stresses. For constant stress (i.e. 120 MPa), similar observations can be made for increasing temperatures. Against this, the onset of constant creep rate $\dot{e}_{ft,ss}$ and the end of primary creep is usually reached for $t < 50$ h or $e_{ft} < 1.5\%$. Likewise, it takes less time or higher strains to reach the constant creep rate regime with increasing stress.

The described correlations are as expected for creep experiments at different temperatures and stresses [233]. Rather unexpected is the absence of transient behaviour at the highest stresses at 600 and 650 °C as mentioned previously. Against other experiments, $\dot{e}_{ft,min}$ coincides with $\dot{e}_{ft,ss}$ here. This creep behaviour usually corresponds to normal transient creep which is categorised as class M (metal-type) behaviour [229, 230]. Both creep stresses may mark the onsets of a power law breakdown (PLB) at the respective temperatures, but this will be more thoroughly investigated within the Norton plots later. Although the experiment at 700 °C/120 MPa exhibited an even higher value of $\dot{e}_{ft,min}$ than 600 °C/240 MPa, inverse transient creep is maintained as for lower stresses. Following, specimens show consistent behaviour during primary creep at 700 °C. It can also be implied that a possible transition to PLB is not necessarily connected to surpassing a threshold creep rate.

Secondary creep

After passing the primary creep stage, it is evident from Figures 4.15a and 4.16a that creep rates clearly scale with temperature and stress. The curves regularly depict local variations of $\dot{e}_{ft}$ with time and strain which could point to temporary microstructural softening and hardening processes. As expected from constant loading, which leads to a continuous decrease of the gauge cross-section as the specimen elongates, $\dot{e}_{ft}$ of all specimens is steadily increasing as a function of t and e_{ft} due to the stress increase. This is in contrast to constant stress creep experiments on model alloys where a constant creep rate is theoretically possible. At lower temperatures (i.e. 600 °C), longer constant creep rate regimes below 200 h can be observed (Figure 4.15a), but these regimes get shorter the higher the initial stress. Therefore, it shall be stressed that the secondary creep stage of all here presented creep tests does not illustrate explicit steady-state creep deformation, but only temporary constant creep rate regimes.

As for the temperature dependency of creep, creep rates at 120 MPa were selected to create an Arrhenius plot as in Figure 4.17. By plotting the logarithm of $\dot{e}_{ft,ss}$ at $e_{ft} = 2\%$ (from where a temporarily constant creep rate is maintained) over the inverse temperature, a linear fit can be performed on the data to deduce the Arrhenius exponent in equation (2.1) from the slope $\frac{Q_c}{k_B}$. Rearrangement of the exponent and substitution of the Boltzmann constant k_B with the gas constant R leads to an expression for the activation energy for creep Q_c according to equation (4.3) [100].

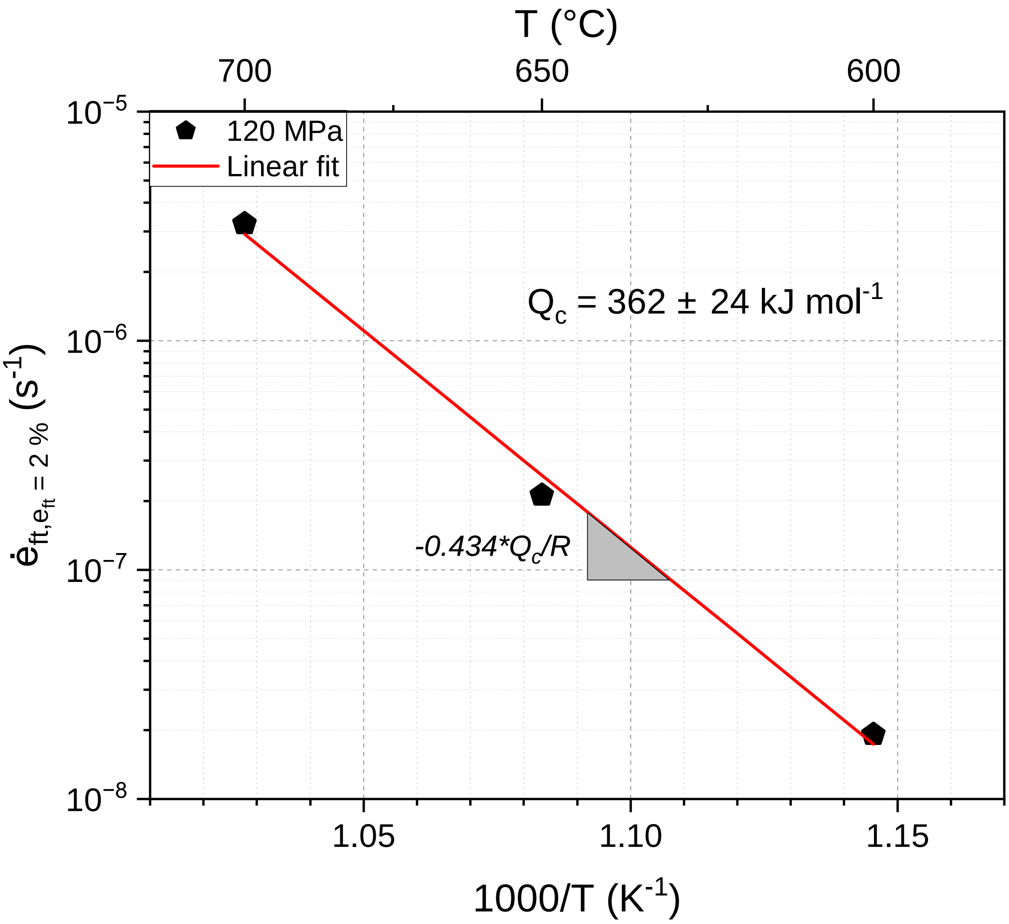

Figure 4.17.: Arrhenius plot of Fe-25Al-3.7Al-0.4Ti-1B for the determination of the creep activation energy Q_c based on the true constant creep rates $\dot{e}_{ft,ss}$ at e_{ft} = 2% and an initial stress of 120 MPa.

$$Q_c = -2.304 \cdot R \cdot \frac{d(log\ \dot{e}_f)}{1/T} \tag{4.3}$$

An activation energy of 362 ± 24 kJ·mol^{-1} (uncertainty is given as the standard error of the linear fit) can be determined. Similar values were generally reported for near-Fe_3Al alloys in the range of 500-700 °C [102] and in particular for iron aluminide solid solutions with Mo (335 kJ·mol^{-1} [234]). It was often observed by researchers that Q_c is similar to the activation energy for self-diffusion [232], but the range of activation energy for Al or Fe self-diffusion in $D0_3$ Fe_3Al (250-280 kJ·mol^{-1} [235, 236]) is clearly smaller than Q_c of Fe-25Al-3.7Mo-0.4Ti-1B. Multiple arguments could contribute to the observed difference. Foremost, the low quantity of test results certainly adds significant uncertainty to the calculations. Furthermore, the calculation of the creep activation energy usually disregards the temperature dependency of Young's modulus E

which affects the stress term in equation (2.1) [100]. Therefore, another temperature dependency term usually needs to be considered. Computation of this correction leads to a reduction of the creep activation energy by 21 kJ·mol^{-1}. Another reason for the difference may be the solid-solution character of the alloy which increases the lattice friction and, in turn, slows down the diffusion kinetics [100]. In literature, the simultaneous activation of multiple creep mechanisms was also suggested to lead to this discrepancy of activation energies [232]. Multiple creep mechanisms were often hypothesized for iron aluminides in general [102] and could be additionally forced by multiple phases present [232].

To analyse the stress dependency of creep rates, both $\dot{e}_{ft,min}$ and $\dot{e}_{ft,ss}$ at different creep strains were selected and plotted over stress. Values for $\dot{e}_{ft,ss}$ were determined at three different creep strains (1, 2 and 3%) as creep rates of a few specimens were not fully constant in this strain range (see Figure 4.16b). The value pairs of in total four creep rates between 600 and 700 °C are displayed in Figure 4.18 in a so-called Norton plot. It foresees a double-logarithmic plot of creep rate over stress to derive the Norton stress exponent n according to equation (2.1) from the slope of the linear fit. Linear fits of minimum creep rates are displayed by solid lines and those of constant creep rates at various creep strains by dashed lines. The stress exponents for $\dot{e}_{ft,min}$ evolve from a higher n at 600 °C (5.6) to a lower value at 700 °C (2.7). At 650 °C, the stress exponent lies in between (4.4). Concerning $\dot{e}_{ft,ss}$ at specific creep strains e_{ft}, stress exponents at 600 °C are especially lower (3.9-4.3) than for $\dot{e}_{ft,min}$ due to a pronounced inverse transient creep behaviour at lower stresses. Considering all tests, values of $\dot{e}_{ft,ss}$ at $e_{ft} = 2\%$ appear most reliable as true secondary creep rates because all specimens entered a temporarily constant creep rate regime and stress exponents n stabilize. The evolution of n concerning $\dot{e}_{ft,min}$ could indicate a transition from climb-controlled creep ($\sim$5) to viscous glide-controlled creep ($\sim$3) [101]. However, considering the constant creep rates at various creep strains, the differences between stress exponents at different temperatures are smaller than assumed by minimum creep rates. At $e_{ft} = 2\%$, values for n only vary between 4.1 (600 °C) and 3.4 (700 °C). Still, a certain trend of changing stress dependency with temperature can be stated, but it remains uncertain whether a shift to a more dominant creep mechanism takes place.

At intermediate temperatures and stresses, publications on near-Fe_3Al alloys mostly reported viscous drag or diffusion-controlled climb of dislocations as possible creep mechanisms [102]. Viscous glide is likely to play a major role in the investigated alloy. Both the inverse transient creep behaviour and the stress exponent give evidence for a class A material [101, 229, 230].

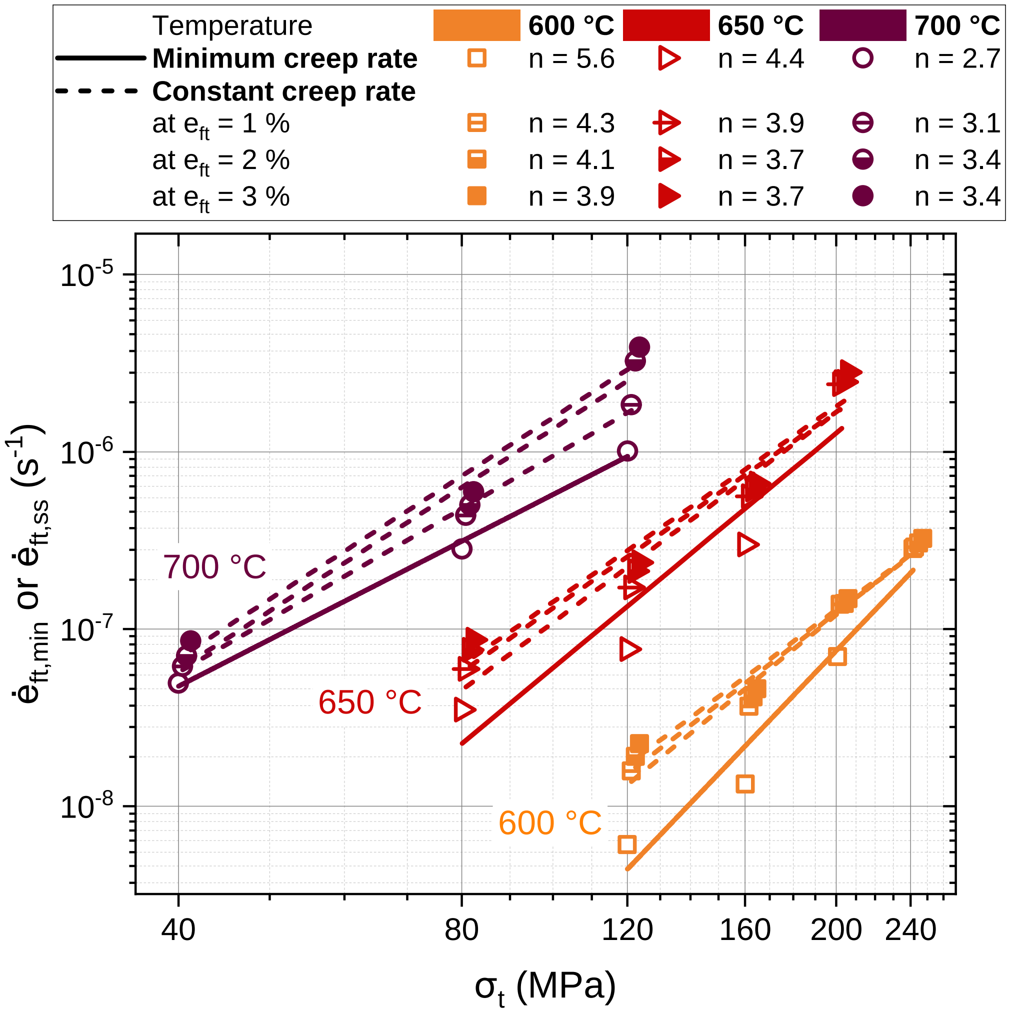

Figure 4.18.: Norton plot of Fe-25Al-3.7Al-0.4Ti-1B for temperatures between 600 to 700 °C based on true minimum creep rates $\dot{e}_{ft,min}$ and true constant creep rates $\dot{e}_{ft,ss}$ locally determined at different creep strains e_{ft}. Stress exponents n are given in the legend.

This is consistent with the larger solute concentrations of Mo and Ti which are present in the matrix.

Besides the effect of solutes, the change of long-range order could impact the resulting creep rates and affect the viscous glide mechanism of dislocations. As exemplarily shown in Figure 4.17 for 120 MPa, the secondary creep rate uniformly increases around one order of magnitude when temperature increases by 50 K. This also applies for the transition from 650 °C to 700 °C during which the order-order transition from $D0_3$ to B2 takes place as measured by DTA (see Figure 4.6). The decreasing creep strength in ordered iron aluminides is generally reasoned with the loss of $D0_3$ order which is connected to a higher mobility of dislocations due to less lattice friction and interaction with APBs [18, 93, 109]. Others especially emphasized lower diffusivities in $D0_3$ structured Fe_3Al compared to B2 structures [237]. First reports by Lawley et al. [93] stated a sharp increase of creep rate when reaching $T_c^{D0_3 \leftrightarrow B2}$. In contrast, the investigated alloy rather exhibits a linear increase of creep rates below and above $T_c^{D0_3 \leftrightarrow B2}$ and no sharp transition can be recognised. For this reason and due to only slightly differing stress exponents n, a change of creep mechanism might not be evident, as was stated by other authors [108, 109]. However, one possible explanation could be that solutes delay the completion of order-order transformation even beyond the measured $T_c^{D0_3 \leftrightarrow B2}$. Morris et al. [238] found indications in in-situ TEM studies that within especially complex $D0_3$ Fe_3Al alloys with multiple solute additions, $D0_3$ ordered domains were still present 100–150 K above the order-order transition temperature measured by calorimetry and x-ray diffraction. This observation was accompanied by a thickening of APB boundaries, which was estimated to be supported by solute segregation there. The mechanism is also known as APB relaxation which is usually associated with the YSA as one possible explanation for the yield strength increase [239]. Hence, a similar phenomenon could be active in Fe-25Al-3.7Mo-0.4Ti-1B and partially and locally suppress the reordering process. Other phenomena related to ordering could also be applicable in the investigated alloy, such as i) anti-site defect strengthening due to off-stoichiometry of B2 structures with near-Fe_3Al composition or ii) decreasing APB production (i.e. disordering) during dislocation glide when <111> superdislocations are increasingly substituted by <100> single dislocations [62]. No further investigations of these mechanisms could be pursued in the time frame though.

Moreover, the investigated alloy may also be markedly influenced by particle strengthening due to the presence of incoherent complex borides. Generally speaking, secondary phase particles mainly contribute to strengthening at lower stresses or higher temperatures and generate a stress exponent which is often notably higher than 5 [101]. Particle strengthening by incoherent particles is usually attributed to either dislocation climb or dislocation looping depending on particle size [100]. Dislocation looping prevails for larger particle sizes. Its strengthening is generated by the additional force needed by dislocations to bow and loop around particles which act as obstacles to dislocation motion. This critical stress is known as Orowan looping stress σ_{Orowan}. The Orowan looping stress can be empirically determined by equation (4.4) [230]

$$\sigma_{Orowan} = \frac{m_T C_0 G b}{\frac{d_p}{2}\left(\frac{2\pi}{3 f_p}\right)^{0.5}} \tag{4.4}$$

where m_T is the Taylor factor (3.1 for untextured fcc polycrystals [233]), C_0 is a refinement factor of 0.8 [240], G is the shear modulus and b is the Burgers vector. The denominator depicts the planar lattice square spacing. With the mean values of particle size d_p (5.6 µm) and phase volume fraction f_p (3.9 vol%) as determined in the homogenised state (see Table 4.2), an Orowan stress of $\sigma_{Orowan} = 1.5$ MPa can be calculated. Although this mechanism is not dependent on time or temperature, increasing diffusion coefficients increasingly enable dislocation climb over particles rendering the Orowan strengthening mechanism weaker with temperature [101]. Morris et al. [35] also estimated this level of particle strengthening as only a minor contribution. In addition, the inhomogeneous distribution of borides as eutectic phase areas led to a larger average particle distance λ_p (13.7 µm, see Table 4.2), which is usually not ideal for effective particle strengthening. Further investigations of crept microstructures (e.g. by TEM) would be necessary to prove this mechanism but were not possible within the scope of the project.

To gain further insights on contributing strengthening mechanisms and, more generally, the effectiveness of alloying additions on creep properties, the secondary creep rates of Fe-25Al-3.7Mo-0.4Ti-1B at 650 °C (black thick solid line) are plotted with reference data on comparable or related alloy compositions in Figure 4.19 (data taken from [11, 38, 99, 234, 241]). Fe_3Al alloys can be differentiated by order state at 650 °C ($D0_3$: black line, B2: grey line) and alloy additions (Mo: purple rhombus (4 at%: solid, 2 at%: half-solid), 1 at% TiB_2: blue open rhombus, 3.5 at% Ti: brown open hexagon, no alloying: grey open circle). Furthermore, experimental details are illustrated such as loading direction (tensile loading: solid lines, compressive loading: dashed lines, indentation loading: dash-dotted lines) and load levels per specimen (single loads: single lines, stepwise load increase: double lines). In addition to creep data on Fe-Al alloys, creep data on P92 steel (pale yellow solid line) is displayed as a benchmark. P92 steel has higher creep strength than Fe-25Al-3.7Mo-0.4Ti-1B at lower stresses but suffers from a large stress dependency ($n = 16$) above 115 MPa. As the low stress dependency of the investigated alloy does not change at higher stresses, Fe-25Al-3.7Mo-0.4Ti-1B is more creep-resistant above 170 MPa than P92.

Most near-Fe_3Al alloys exhibit a similar stress dependency as the base alloy ($3 < n < 4.5$), which indicates viscous glide as the rate-controlling mechanism. Still, this comprises both binary alloys as well as solid solutions, TiB_2 particle-strengthened alloys or the combination of both. So it appears that the rate-controlling creep mechanism is foremost inherent to the ordered state of iron aluminides with this Al concentration and less affected by additional alloying. An exception

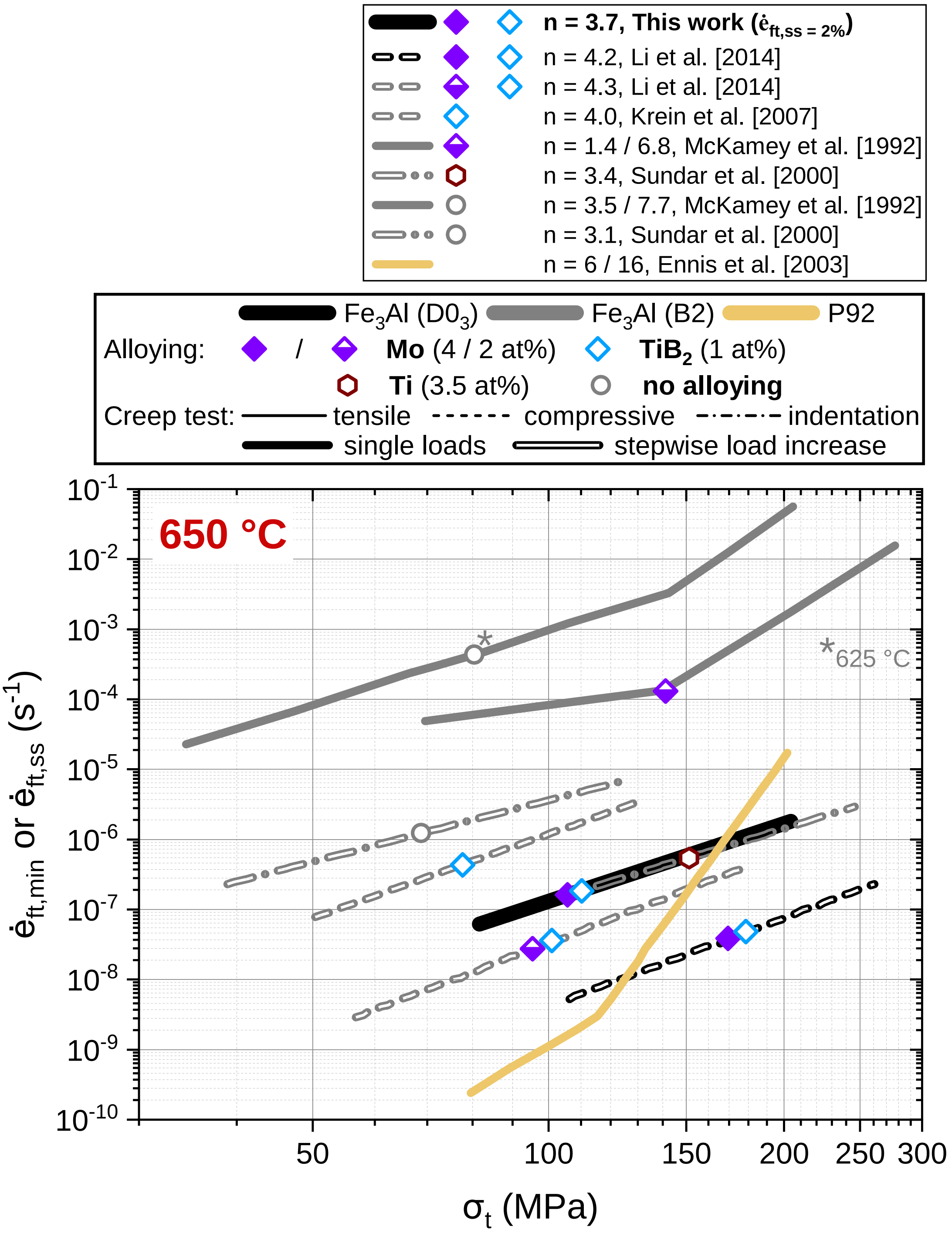

Figure 4.19.: Norton plot of investment-cast Fe-25Al-3.7Al-0.4Ti-1B at 650 °C in comparison to related ternary and multicomponent Fe$_3$Al alloys and P92 steel from literature [11, 38, 99, 234, 241]. Alloy types are distinguished by line colour, alloying additions by symbols and creep testing methods by line style. Stress exponents n are given in the legend.

is the related Fe_3Al-2Mo alloy [234] which appears to be governed by diffusional creep at lower stresses and experiences a PLB above 150 MPa.

Despite the marginal differences in stress dependency, alloying additions notably affect the secondary creep rates. Compared to binary B2 Fe_3Al [234], adding 2 at% Mo for solid solution hardening reduces creep rates by one order of magnitude [234], whereas TiB_2 additions for particle strengthening even lower them by more than two magnitudes of order [99]. Accordingly, the investigated alloy appears to be creep-strengthened by the sum of both contributions, although particle strengthening was believed to contribute less given the explanations above.

Still, secondary creep rates of the investigated alloy are more than one order of magnitude higher than a comparable $D0_3$ Fe_3Al-4Mo-1TiB_2 alloy [38]. Even the same alloy with only 2 at% Mo, which approximately halves the Mo solute concentration in the matrix, still exhibits lower secondary creep rates than the investigated alloy [38]. Low deviations in solute concentration can therefore not be decisive. The most mentionable difference between both sets of specimens was the faster solidification rate inherent to die-casting processes and the potential effects on microstructure. Despite higher cooling rates, eutectic borides did not spread more homogeneously within grain interiors. Consequently, lower particle sizes should not have a higher particle strengthening effect either. According to observations in literature, the estimated difference in grain size (see subsection 4.3.2) should not have any impact on creep if the rate-controlling mechanisms are based on dislocation glide or climb (which appears to be the case) [100, 101].

As no obvious microstructural differences may explain the deviating secondary creep rates, experimental details could become relevant. Creep rate measurements in referenced Fe_3Al-Mo-TiB_2 alloys and others were conducted on a single specimen while the load is incrementally increased (double lines) under compressive loading. This method usually saves time and resources, but it also implies that especially creep rates at higher stresses are a result of their prior loading history. In turn, this affects prior dislocation arrangements and cavitation processes, which could particularly overestimate stress exponents. In addition, shorter loading times per stress level could risk underestimating true constant creep rates. For this reason, the effect of stepwise load increase was reassessed at 650 °C under tensile loading on a single specimen. Equal load levels were selected as in creep tests under a single load. The dwell time at each load level was aimed at only reaching the minimum creep rate and keeping creep strains and thus creep damage as low as possible as they could affect $\dot{e}_{ft,min}$. Figure 4.20a displays the progression of true creep rate $\dot{e}_{ft}$ over time t when stress levels are incrementally increased. A direct comparison of $\dot{e}_{ft}$

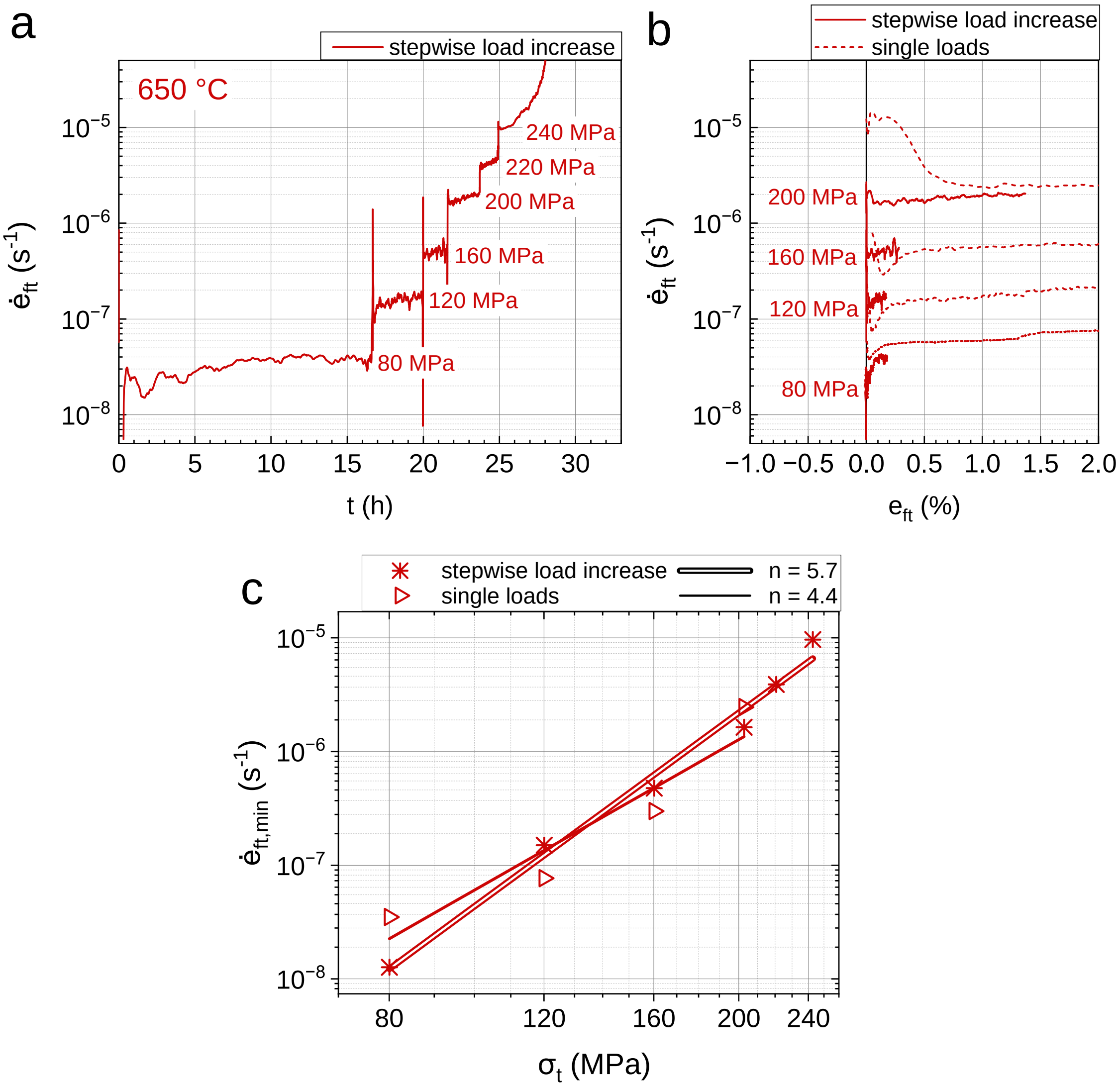

Figure 4.20.: Creep plots of homogenised Fe-25Al-3.7Al-0.4Ti-1B tested under stepwise load increase at 650 °C: (a) Half-logarithmic plot of true creep rate $\dot{e}_{ft}$ over time t, (b) Half-logarithmic plot of true creep rate $\dot{e}_{ft}$ over true creep strain e_{ft} (data from single load tests are given for comparison), (c) Norton plot based on $\dot{e}_{ft,min}$ for creep tests under stepwise load increase and single loads.

- e_{ft} curves of stepwise increasing loads (solid lines) and single loads (dotted lines) is given in Figure 4.20b. From this plot, it is evident that classical primary creep is absent after the first load increase. Instead, an at least temporarily constant creep stage is reached shortly after the load increase. Accordingly, minimum creep rates will be overestimated with increasing stress. This is also reflected in the Norton plot in Figure 4.20c where the regression of $\dot{e}_{ft,min}$ of the stepwise load increase creep test points at an even higher stress exponent of 5.7. Due to the short dwell times at each load level, $\dot{e}_{ft,ss}$ could not be determined at creep strains between 1 and 3% as before. However, an extrapolation of creep curves hints at similar $\dot{\epsilon}_{ft,ss}$ and n values as for single load creep tests (not shown in Figure 4.20b and c). In summary, creep tests under stepwise load increase should yield similar results as creep tests under single loads if secondary creep rates beyond any transient creep stage are considered.

Another experimental setting which varies among the referenced curves in Figure 4.19 (also between the investigated alloy and the data from Li et al. [38]) is the loading direction. Most of the reference data was generated by compressive creep testing (dashed lines) in contrast to indentation creep (dash-dotted lines) and classical tensile creep methods (solid lines). The loading scenario is especially relevant considering creep damaging mechanisms (see next paragraph), but also for the overall creep performance. The extent is illustrated in Figure 4.19 when comparing the Norton plots of the two binary Fe_3Al alloys measured by different creep tests [234, 241]. Secondary creep rates of indentation loaded Fe_3Al alloys are two magnitudes of orders lower than those determined under tensile loading even though the latter were even measured at lower temperatures (625 °C). A potential effect of loading direction will be further discussed in section 4.4.

Tertiary creep

Due to the constant loading mode and the difficulty of probing larger strains during creep testing, a transition to tertiary creep was not clearly definable from Figures 4.14 to 4.16. Anyhow, post-investigations on a macro and micro level revealed differences in creep damages depending on initial stress σ_0, temperature T, final creep elongation and necking behaviour.

A clear necking region was mostly visible after creep testing if temperatures or stresses were sufficiently high. A comparison of creep specimens before and after creep testing is given in Figure B.3 in the appendix. Pronounced necking is normally observed at stresses close to the hot ultimate tensile strength up to $0.7T_{liquidus}$ [100]. The occurrence of necking at lower stresses (e.g. Figure B.3d at 650 °C/80 MPa) is surprising as maximum true stresses (∼155 MPa) are still far below R_m at this temperature (353 MPa). The creep fracture surface at 650 °C/160 MPa (see Figures B.2a-c) appears to correlate to a ductile transgranular fracture with visible dimples. At higher magnifications though (see Figure B.2c), signs of cavity chain formation can be also seen, which leaves an ambiguous impression of the fracture behaviour.

To gain a better understanding on cavity formation and growth, longitudinal cross-sections were investigated by optical microscopy after creep tests. Figures 4.21b-d depict the microstructures

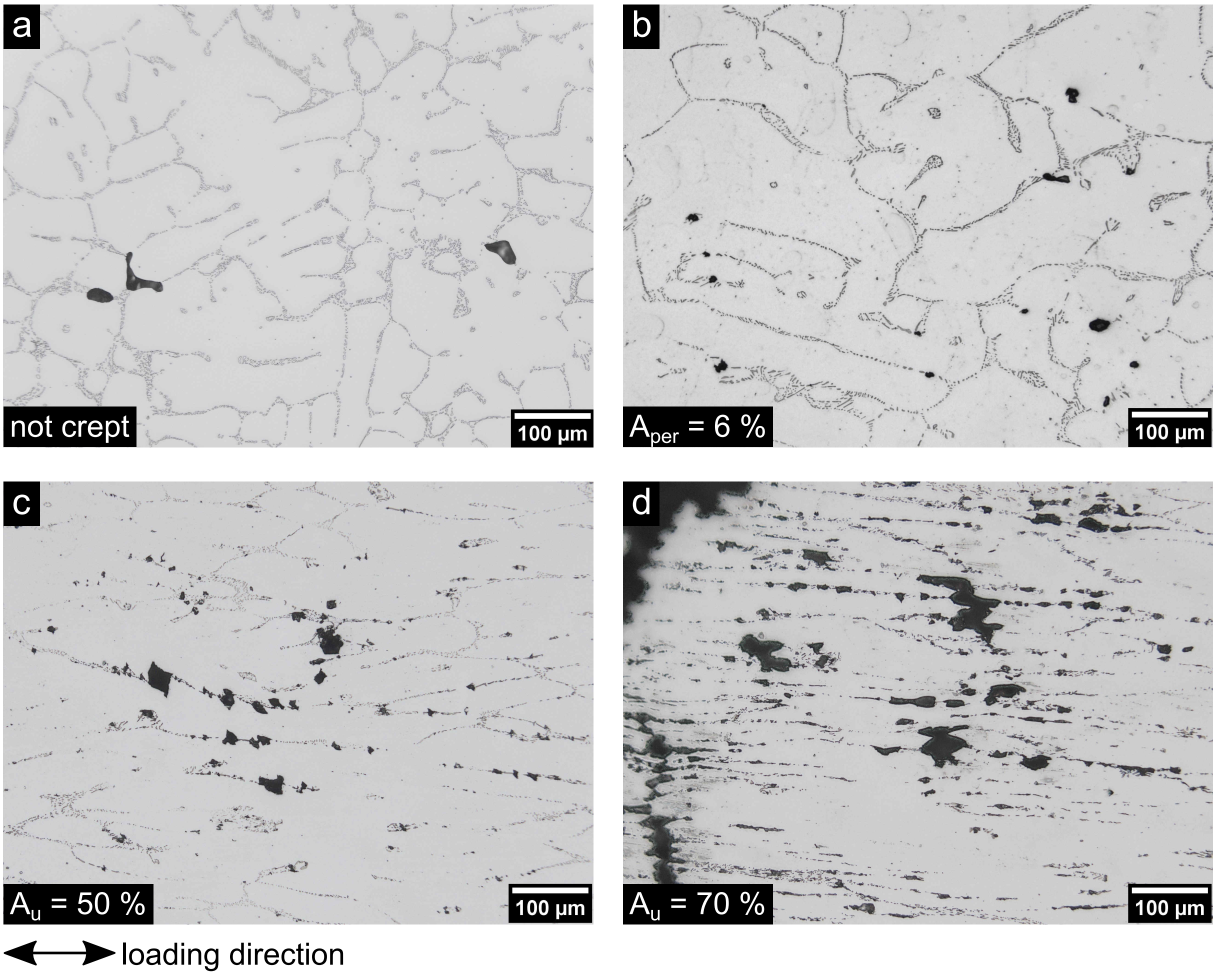

Figure 4.21.: Optical micrographs of pristine (a) and creep tested samples (b-d) from longitudinal cross-sections (loading direction is horizontal). (b) 600 °C/120 MPa, (c) 650 °C/200 MPa, (d) 700 °C/120 MPa.

of creep specimens with different creep elongations. Figures 4.21c and d are taken close to the fractured surface. The former loading direction corresponds to the horizontal axis. The original state of the homogenised microstructure before testing is given in Figure 4.21a for comparison. There, a few black pores are already visible which likely originate from the casting process. After creep tests at 600 °C/120 MPa without rupture and with low permanent creep elongation ($A_{per} = 6\%$ after 1000 h, Figure 4.21b), only minor cavitation is present. However, they are not easily distinguishable from casting pores. With increasing creep elongation (e.g. after creep rupture at 650 °C/200 MPa and 700 °C/120 MPa, Figures 4.21c and d), the number of cavities are markedly increasing, especially in the necking region (see also Figure 4.22 for a larger view of a longitudinal cross-section).

Cavitation is accompanied by increasing elongation of eutectic and matrix areas along the loading direction at ≥ 650 °C, mostly in consequence of the reduced cross-sectional area. Different

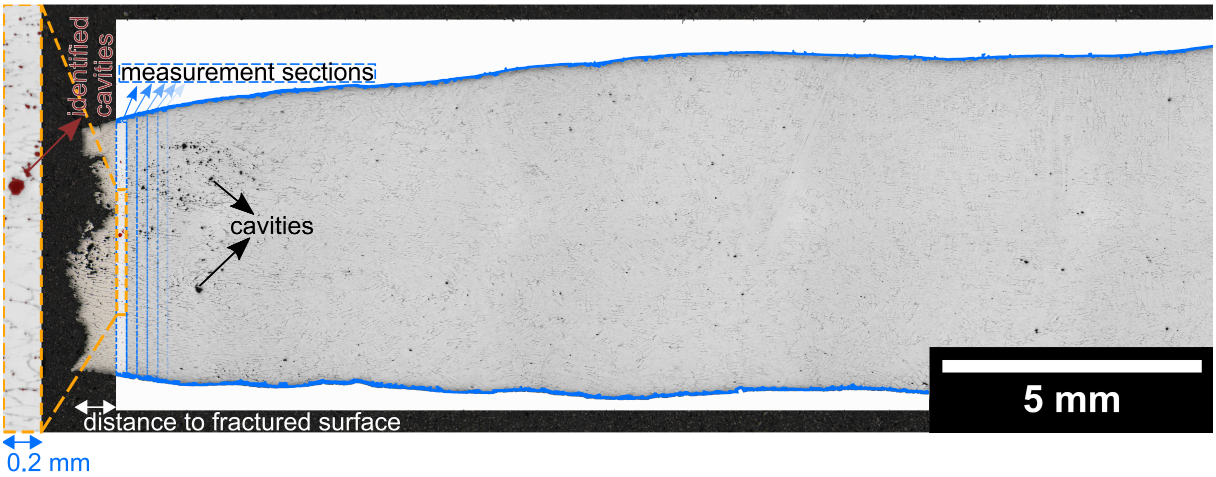

Figure 4.22.: Illustration of local creep cavitation quantification within Fe-25Al-3.7Al-0.4Ti-1B (shown example: 650 °C/200 MPa) dependent on the distance to the fractured surface by division of longitudinal macrosections into finite measurement sections. Cavities, as identified by segmentation, are exemplarily shown in a magnified view.

cavitation states can be observed, such as single wedge-type cavities, single cavities elongated in loading direction which develop a tip close to the maximum shear force direction (i.e. $> 45°$ to the loading direction, Figure 4.21c) and cavity chains which grow from single cavities along and perpendicular to the loading direction (Figure 4.21d). Most cavities have in common that they appear within or adjacent to eutectic areas. It might be therefore probable that cavities start forming at the phase boundary of eutectic particles. Nucleation could result from vacancy condensation at particle phase boundaries which could be enabled at higher temperatures in iron aluminide alloys due to increased vacancy mobility [101, 242]. It should be mentioned though that existing cavities (such as casting pores) could also largely contribute to nucleation or especially growth of cavities. Another factor, which could enhance cavity nucleation, is stress concentrations at grain boundaries which arise from grain boundary sliding processes and which are especially high in coarse grain microstructures [100, 101, 243]. Still, it is speculative to which extent grain boundary sliding is active in the investigated alloy.

It was already mentioned based on the example of Figure 4.22 that cavities tend to be more abundant in the necking region, but cavitation can be found in all parts of the specimen. To reliably quantify this trend, cavity parameters were locally examined by image thresholding dependent on the distance to the fracture surface (or the smallest cross-section if not ruptured). For this purpose, the longitudinal macrosection as displayed in Figure 4.22 (blue solid outline) was divided into measurement sections with a finite width of 0.2 mm (blue dashed upright rectangles) within

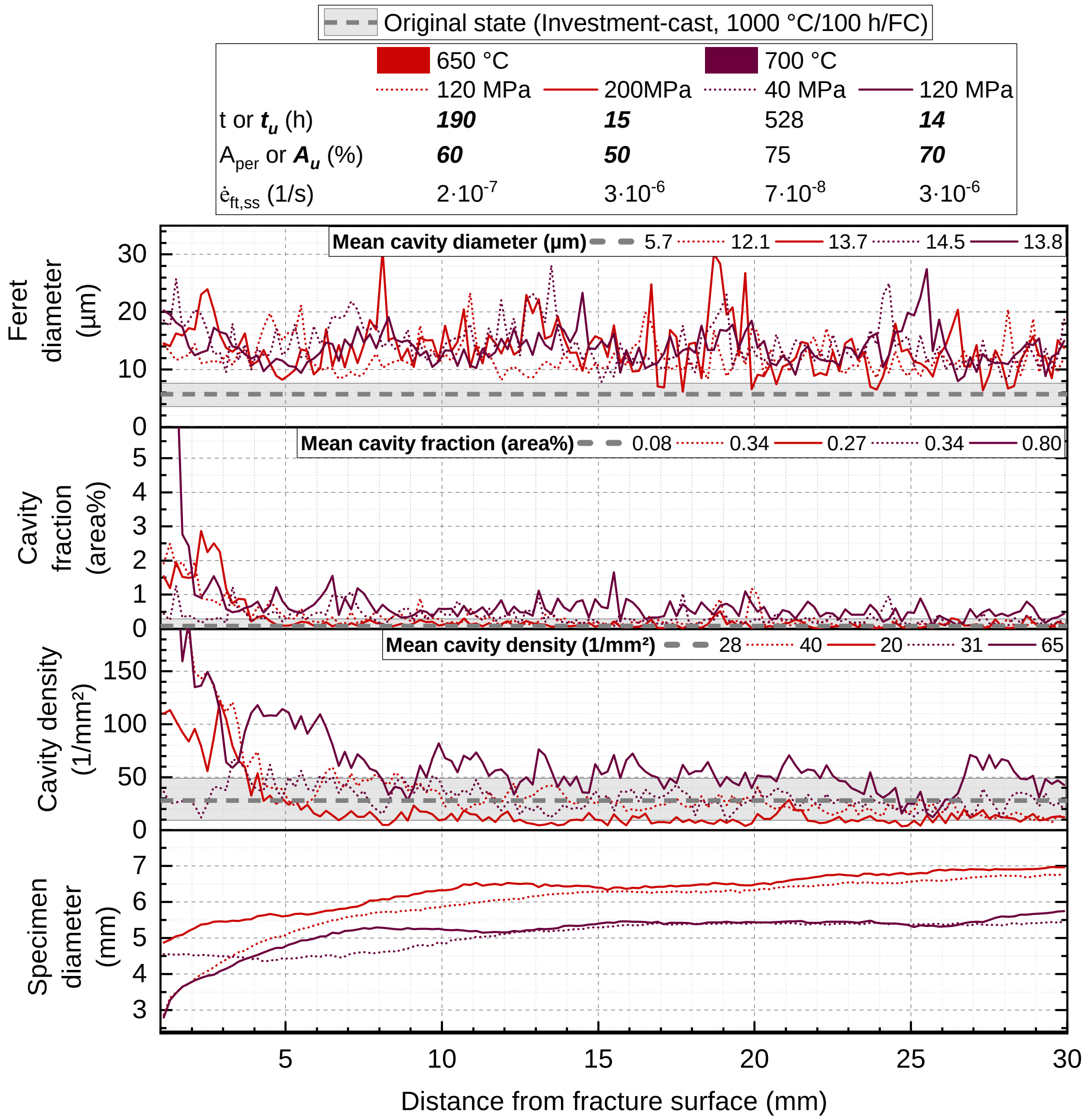

Figure 4.23.: Feret diameter of cavities, cavity fraction, cavity density and specimen diameter over distance from fracture surface of Fe-25Al-3.7Al-0.4Ti-1B creep tested at 650 and 700 °C and two initial stresses σ_0 each. Mean values and standard deviations of the original homogenised state are additionally displayed in the plots. Mean cavity parameters and given creep results of investigated specimens are given in the legends.

a distance of 1 to 30 mm from the fracture surface. Like this, the local cross-sectional width can be also taken into account. Cavities (highlighted by a red overlay) were segmented by Otsu auto thresholding as visualised in the magnified orange rectangle. Cavity parameters include cavity diameter (derived from Feret's maximum diameter), cavity area fraction and cavity density (i.e. the number of cavities per section area). Figure 4.23 displays the progression of cavity parameters including the specimen diameter at two temperatures (red: 650 °C, purple: 700 °C) and two stress levels (dotted line: lower stress, solid line: higher stress) each as a function of distance to the fracture surface. Further information on the creep performance of creep specimens is given in the top legend. The mean values (shown as grey dashed lines) and the standard deviation range (shown as grey area) of the original state after homogenisation are overlayed to assess the results against the background of casting pores. The mean values of creep-tested specimens were also derived from all investigated measurement sections and are given in the respective legend of each plot.

The necking region (i.e. section with a reduced specimen cross-section compared to the remaining gauge section) usually extends between 8–15 mm distance to the fracture surface. Only below a distance of 5-6 mm though, both local cavity fraction and local cavity density are markedly increased compared to the remaining part of the specimen. An exception is the specimen tested at 700 °C/40 MPa, which did not rupture during creep testing. Against this, the cavity diameter strongly varies across the complete gauge section in all specimens and is not particularly increased close to the fracture surface. Hence, the findings indicate that creep damage is concentrated in the necking region and mainly manifests by enhanced cavitation nucleation and only limited cavity growth.

In comparison to the original state, it can be concluded that both mean cavity diameters and mean cavity fractions are significantly increased in all creep-tested specimens. However, only the creep specimen tested at 700 °C/120 MPa shows a notably higher cavity fraction (0.8 area%) than the other creep-tested specimens, which are indistinguishable ($\sim$0.3 area%) despite different initial stresses and temperatures. Concerning the mean cavity density, only the specimen at 700 °C/120 MPa clearly exhibits more cavities per area than the original state. The reason why other creep-tested specimens show invariant cavity densities although mean cavity diameters and fractions are clearly increased compared to the original state, might be the simultaneous nucleation of new cavities and the coalescence of existing ones. Dyson et al. [244] reported that cavity density usually increases with creep strain. Still, many cavities might not be identified by OM as the critical nucleation size of cavities is between 2-5 nm [245]. Therefore, this theory cannot be unambiguously verified. Furthermore, the growth of casting pores could contribute more than expected to the increasing cavity diameter and fraction outside the necking region. In any case, creep testing at 700 °C/120 MPa markedly differs from the other cases as cavity nucleation and growth are enhanced throughout the complete gauge section.

This conclusion is also interesting concerning the question if different ordered states at 650 °C and 700 °C might have an impact on creep damaging. Although $\dot{\epsilon}_{ft,ss}$ and t_u are similar for creep tests at 650 °C/200 MPa and 700 °C/120 MPa, cavitation fraction and density differ notably. The difference in elongation after creep fracture A_u of around 20% could be a possible explanation for the different amounts of creep damage. Nevertheless, the creep specimen tested at 700 °C/40 MPa showed an even slightly higher permanent creep elongation with less creep damage compared to the creep test at 700 °C/120 MPa. It could be therefore hypothesized that the loss in order or the transition into a B2 structure might enhance creep damaging mechanisms. Still, this conclusion does not mean that the ability to accommodate creep deformation is reduced as A_u is still exceptionally high.

4.4. Tension-compression asymmetry

In sections 4.3.2 and 4.3.3, the reported results of both quasi-static tensile and tensile creep testing of Fe-25Al-3.7Mo-0.4Ti-1B were largely deviating from literature data. This applied to data on 0.2% proof strength $R_{p0.2}$ below the YSA (see Figure 4.13a) as well as to minimum true creep rates $\dot{\epsilon}_{ft,min}$ (see Figure 4.19). Besides differences in processing and post-processing of samples within this study and in literature [38], one potentially decisive difference consists in the loading direction. In numerous publications before, the differentiation between tension and compression under quasi-static and sustained loading has led to significantly different mechanical properties in superalloys and intermetallics [246–251]. The effect is mostly referred to as tension-compression asymmetry (TCA) in literature [252, 253]. Similar notions have also emerged such as the strength difference effect which was especially related to type II residual stresses induced by grain and phase boundaries [254, 255]. However, TCA has established as the more common description of this phenomenon. While TCA mostly describes differences in yield stress in quasi-static tests, the effect is also ascribed to different creep rates or different times to failure in creep tests [251, 256, 257]. The two loading scenarios, tension and compression, essentially create different stress states and many theories on the microstructural deformation mechanisms have evolved [252, 253, 256, 258, 259]. The effect has been specifically reported on bcc metals and ordered structure materials, including studies on iron aluminides. In binary and solid-solution Fe_3Al alloys, the effect of non-glide components from the applied stress on the core structure of screw dislocations is thought to be decisive [247, 248]. This was based on atomistic simulations which demonstrated a lower critically resolved shear stress under tension than under compression

[260]. Falat et al. [261] studied various particle-hardened Fe-26Al alloys and also witnessed significantly different yield stresses at room and elevated temperatures depending on loading direction. The authors explained the occurence especially in these alloys with internal stresses which develop during solidification between matrix and secondary phases due to different elastic moduli. Besides, they stated that the notch sensitivity of particles could also account for TCA.

In terms of detectable TCA within the creep tests of this study, investment-cast Fe-25Al-3.7Mo-0.4Ti-1B alloys exhibited minimum true creep rates $\dot{e}_{ft,min}$ which were approximately one order of magnitude higher under tensile loading than in die-cast alloys with similar composition under compressive loading [38]. A significant effect of test method and data acquisition (i.e. under stepwise increasing load) or other factors such as microstructural differences (i.e. grain size, Mo solute concentrations) could be excluded. Hence, it appears likely that tension and compression may induce different creep mechanisms in Fe-25Al-3.7Mo-0.4Ti-1B alloys. However, to the best of the author's knowledge, a TCA effect in creep testing has not yet been reported for any related Fe-Al alloy. It therefore remains open which deformation mechanisms could potentially contribute to higher creep rates.

With regard to quasi-static testing, quinary Fe-Al-Mo-Ti-B alloys are potentially relatable to the mechanisms proposed by Falat et al. [261]. Due to the presence of boride particles and their predominantly elongated shape which could enhance stress concentrations under tensile loading, these alloys might be equally or even more affected by TCA effects. This is also in line with the observed high susceptibility to cracking near boride phase boundaries found by fractography after tensile testing (see Figure 4.12a). To examine the applicability of this hypothesis to TiB_2 or Mo_2FeB_2-hardened Fe_3Al-alloys with different amounts of Mo solutes, available data on both tensile and compressive 0.2% proof strength was gathered and compared with each other. Figures 4.24a to d plot $R_{p0.2}$ and $R_{dp0.2}$ at ambient and higher temperatures for the investigated Fe-26Al-4Mo-0.5Ti-1B-type alloy [38] and related alloys (i.e. Fe_3Al-2Mo-TiB_2-type [38, 127], Fe_3Al-TiB_2-type [99, 131] and binary Fe_3Al [34, 88]).

Tensile data is depicted as inverse triangles with solid lines and compressive data as squares with dashed lines. Connecting lines shall be only understood as guide to the eye. As 0.2% proof strengths at distinct temperatures are not always given for both tensile and compressive loading, the TCA effect was only qualitatively assessed. Notably, below the respective T_{YSA} of all alloy types except for Fe_3Al-2Mo-TiB_2, compressive $R_{dp0.2}$ is generally larger than tensile $R_{p0.2}$. The lower difference between $R_{dp0.2}$ and $R_{p0.2}$ in Fe_3Al-2Mo-TiB_2 alloys (see Figures 4.24b) could be

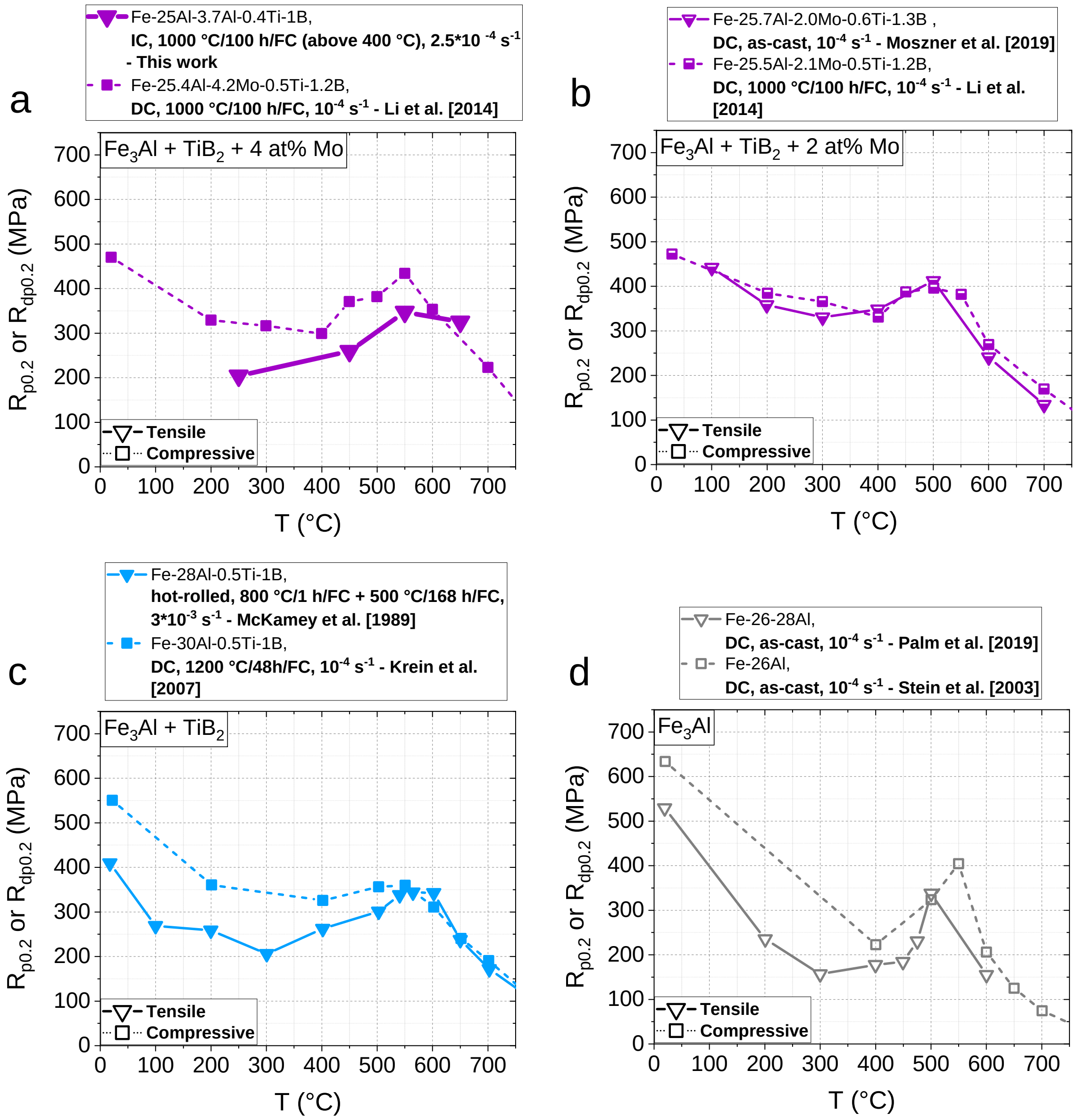

Figure 4.24.: $R_{p0.2}$ and $R_{dp0.2}$ as a function of T for different Fe-Al alloys: (a) Fe_3Al-4Mo-TiB_2-type [38], (b) Fe_3Al-2Mo-TiB_2-type [38, 127], (c) Fe_3Al-TiB_2-type [99, 131] and (d) binary Fe_3Al [34, 88].

induced by a missing homogenisation treatment of tensile specimens. Similar to investment-cast Fe-25Al-3.7Mo-0.4Ti-1B, the as-cast state should inherit higher strength than after HT2 (see Figure 4.9). Moreover, the TCA effect generally appears to decline above 300 °C with the onset of the YSA peak. At or above T_{YSA} at the latest, the TCA effect is only negligible or disappears. These observations slightly deviate from conclusions by Koeppe et al. [247] who already noted a disappearance of the TCA above 300 °C. When comparing binary and particle-strengthened Fe_3Al alloys, the TCA effect appears to be sustained at higher temperatures in boride-strengthened alloys. This trend could be associated to higher T_{YSA} in alloyed iron aluminides. Although it appears likely that a microstructure with secondary phase particles could be more affected by the TCA due to internal stresses and ease of notching, the TCA effect does not seem to be enhanced compared to binary Fe_3Al. Hence, the generally non-planar core structure of screw dislocations and their effect on glide might still be the key to the TCA effect in Fe-Al alloys.

One remaining uncertainty in this comparison of tensile and compressive data is the impact by processing and post-processing. Especially the immediate comparison of investment-cast data of Fe-25Al-3.7Mo-0.4Ti-1B to die-cast data from Li et al. [38] likely indicates a wrong level of TCA. To quantify the TCA effect at room temperature, the acquisition of tensile and compressive 0.2% proof strengths from a similar alloy batch was pursued. However, no $R_{p0.2}$ value could be determined with investment-cast specimens. Hence, die casting was alternatively employed to gain sufficient ductility for $R_{p0.2}$ determination. Die casting and post-processing of tensile specimens with standard geometry (see Figure A.5a) was complicated by more extensive cracking. To guarantee intact tensile specimens without cracks, smaller specimen dimensions with $L_c = 30$ mm (see Figure A.5b) were chosen and homogenisation treatment HT2 was additionally applied. To exclude size effects accompanied by the testing of smaller specimen volumes [262, 263], an investment-cast specimen was also manufactured with the new specimen dimensions and compared against as-cast IC specimens with standard geometry. The smaller specimen shows only slightly enhanced tensile strength R_m (278 MPa) compared to tensile specimens with standard geometry, but no difference in elongation after fracture A. Due to the comparability of mechanical properties of different specimen volumes, a size effect may be negligible. Figures 4.25a and b compare the compressive (blue line) and tensile curves (red line) of both homogenised DC and as-cast IC specimens at room temperature.

The onsets of plastic deformation of IC and DC specimens under tensile loading (red curves in Figures 4.25a and b) are very similar despite different grain sizes, thermal condition and different ductilities. Against this, the onsets of plastic deformation under compressive loading (blue curves) are clearly different and might be influenced by casting process and thermal condition. For this reason, special attention needs to be paid which processing and post-processing shall be selected for alloys if a conservative estimate of the TCA effect shall be made. A more thorough examination of die-cast alloys and an effect of solidification rate and heat treatment on microstructure and mechanical properties will be presented in chapter 7. As the as-cast state tends to overestimate the difference under tensile and compressive loading here, the homogenised state offers a more conservative evaluation of the TCA effect as illustrated in Figure 4.25a. The

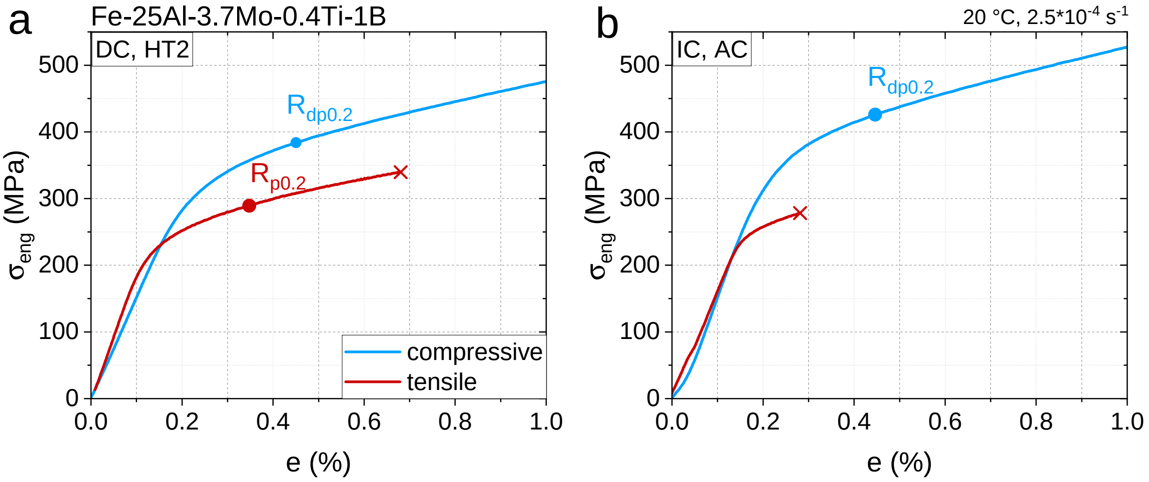

Figure 4.25.: Engineering stress-strain curves at room temperature under compressive and tensile loading for differently processed Fe-25Al-3.7Al-0.4Ti-1B alloys: (a) die-cast and homogenised (HT2), (b) investment-cast in as-cast state.

0.2% proof strengths under compressive loading ($R_{dp0.2}$ = 384 MPa) and under tensile loading ($R_{p0.2}$ = 290 MPa) yield a strength difference of 94 MPa at room temperature. This difference in strength is of a similar magnitude to that observed in the previously presented alloys at temperatures below 500 °C (see Figures 4.24b to d).

In conclusion, a considerable tension-compression asymmetry effect was assigned to the investigated Fe-25Al-3.7Mo-0.4Ti-1B alloy. This applied to quasi-static testing, which is a known phenomenon in other iron aluminides, as well as creep testing, which has never been reported for Fe-Al alloys. It was stressed that the TCA effect in quasi-static tests is largely dependent on processing parameters such as solidification rate and thermal condition as was demonstrated in Figure 4.25. An additional effect of boride particles was assumed to enhance TCA. However, no enhancing effect compared to binary Fe_3Al could be inferred from the data of this work or from the literature, regardless of boride species and/or Mo solute concentration. Due to the different processing histories found in the literature data, a systematic investigation of binary and various boride-strengthened alloys from comparable batches would be necessary to quantify a TCA effect induced by particles. Additionally, different homogenisation treatments are recommended to take different morphology and stress states of borides into account.

Chapter

5 Effect of alloy composition

The figures, tables, results and discussions of this chapter were reproduced and adapted from Abel et al. [191] under the CC BY 4.0 licence.

As thoroughly presented in chapter 4, the studied Fe-26Al-4Mo-0.5Ti-1B alloy with an actual composition of Fe-25Al-3.7Mo-0.4Ti-1B exhibits significant deficits in tensile performance, especially with respect to ductility at lower temperatures. Despite the positive effects of Mo alloying on the high-temperature mechanical properties, an increased brittleness and inclination to cracking was connected to its use [38, 131]. This was also apparent during production of casting specimens and the fracture behaviour after tensile testing (see Figures 3.2 and 4.12). Moreover, the low room-temperature ductility in Fe-25Al-3.7Mo-0.4Ti-1B alloys was partially attributed to the cracking sensitivity and limited cohesion of Mo_2FeB_2 phases (see Figure 4.12a). However, it is unknown how the variation of Mo and/or B concentration affects particle formation and brittleness. In addition, it is evident from multiple studies that strength, work hardening and YSA sensitively vary with Al concentration around the stoichiometric Fe_3Al composition of binary alloys [55, 56, 92]. In an attempt to optimise the alloying strategy for improved ductility and strength at ambient and higher temperatures, eight different alloy compositions were systematically investigated. Among those, two near-Fe_3Al alloys with hypostoichiometric and hyperstoichiometric composition (23.5 and 26 at%) were selected and varied with respect to Mo (2 and 4 at%) and B concentration (0.5 and 1 at%). With this choice, it was examined how the combined use of alloy additions affects microstructural evolution, phase stability and mechanical properties and if their effect varies below and above the stoichiometric composition. Hereby, microstructural parameters such as grain size, phase composition and secondary phase fractions were compared and correlations were drawn to phase transition temperatures, hardness and tensile properties at room temperature and 550 °C (i.e. near the YSA). A special focus was directed towards the effectiveness of solid-solution hardening by the combined use of Mo and Ti which will be discussed in section 5.3. To conserve the comparability to the base alloy, all samples were produced by centrifugal investment casting with a similar wall thickness. Nominal and actual compositions of Fe-xAl-yMo-0.5Ti-zB alloys (from here on denoted as x-y-z alloys) are summarised in Table 5.1.

Table 5.1.: Nominal and actual composition of as-cast Fe-xAl-yMo-0.5Ti-zB alloys (measured by XRF spectroscopy and S-OES*). Reproduced from Abel et al. [191] under the CC BY 4.0 licence.

Alloy x-y-z	Nominal composition (at%)					Actual composition (at%)				
	Fe	Al (x)	Mo (y)	Ti	B (z)	Fe	Al (x)	Mo (y)	Ti	B* (z)
26-4-1	68.5	26	4	0.5	1	69.0	26.0	3.5	0.5	1.0
26-4-0.5	69.0	26	4	0.5	0.5	69.2	26.3	3.6	0.5	0.5
26-2-1	70.5	26	2	0.5	1	69.8	26.8	1.8	0.5	1.1
26-2-0.5	71.0	26	2	0.5	0.5	70.8	26.4	1.8	0.5	0.5
23.5-4-1	71.0	23.5	4	0.5	1	71.1	23.9	3.5	0.5	1.0
23.5-4-0.5	71.5	23.5	4	0.5	0.5	71.5	24.1	3.5	0.5	0.5
23.5-2-1	68.5	23.5	2	0.5	1	72.0	24.6	1.8	0.5	1.1
23.5-2-0.5	68.5	23.5	2	0.5	0.5	72.6	24.6	1.8	0.5	0.5

5.1. Microstructure and phase evolution

As illustrated in Figure 4.5, grain sizes of Fe-25Al-3.7Mo-0.4Ti-1B varied significantly, ranging from several tens of microns to more than a few millimetres. This heterogeneous grain size distribution is mirrored in the measured average grain sizes and their scatter across all alloy variations. Table 5.2 lists the average grain diameters d_{gs} and the 95% CI of x-y-z alloys determined via Heyn lineal intercept counting. Due to irregular grain shapes, the confidence intervals of the measured average grain diameters are quite large. Average grain diameters stretch from 586 µm (alloy 23.5-4-0.5) to 876 µm (alloy 26-2-1). The formation of large grains is favoured by low heat transfer rates in insulated ceramic shell moulds, resulting in low cooling rates within the melt. Despite this, average grain sizes correspond well with other Fe-Al alloys produced by investment casting [264]. No systematic correlation between grain size and varying alloy composition could be established from the data.

Representative SEM-BSE images of all alloy compositions are compared for alloys with 26 at% Al in Figure 5.1 and for 23.5 at% Al in Figure 5.2. Table 5.3 additionally lists the WDS elemental compositions of the grey matrix phase and the bright secondary phase. Variation in nominal Mo content induces changes in solid-solution concentration. At 2 at% nominal concentration of Mo, Mo concentrations range between 1.2 to 1.3 at% in the Fe_3Al matrix, consistent with measurements by Li et al. [38] and McKamey et al. [131]. They observed that the amount of Mo forming a solid solution with Fe_3Al scales with the total Mo concentration in the alloy. Regard-

Table 5.2.: Average grain diameters d_{gs} and 95% confidence intervals of investment-cast Fe-xAl-yMo-0.5Ti-zB in as-cast condition according to Heyn lineal intercept method. Reproduced from Abel et al. [191] under the CC BY 4.0 licence.

Alloy x-y-z	d_{gs}
26-4-1	602 ± 121
26-4-0.5	740 ± 15
26-2-1	876 ± 167
26-2-0.5	696 ± 188
23.5-4-1	745 ± 117
23.5-4-0.5	586 ± 66
23.5-2-1	748 ± 152
23.5-2-0.5	715 ± 93

Table 5.3.: WDS elemental composition of Fe_3Al matrix and Mo_2FeB_2 secondary phase in investment-cast Fe-xAl-yMo-0.5Ti-zB alloys in as-cast condition. Reproduced from Abel et al. [191] under the CC BY 4.0 licence.

Alloy x-y-z	**Elemental composition (at%)**								
	Fe_3Al matrix				Mo_2FeB_2 secondary phase				
	Fe	Al	Mo	Ti	Fe	Al	Mo	Ti	B
26-4-1	70.3	26.6	2.4	0.7	23.7	1.4	29.7	6.7	38.5
26-4-0.5	69.9	26.7	2.6	0.8	23.8	2.0	28.2	6.4	39.6
26-2-1	71.5	26.9	1.2	0.4	23.9	0.5	27.1	9.7	38.9
26-2-0.5	71.3	26.7	1.3	0.7	25.7	2.0	25.1	8.6	38.6
23.5-4-1	72.7	24.1	2.5	0.7	24.7	1.2	30.2	6.8	37.1
23.5-4-0.5	72.4	24.1	2.7	0.8	24.3	1.5	29.7	6.6	37.9
23.5-2-1	74.0	24.2	1.2	0.6	24.0	0.8	26.9	9.5	38.9
23.5-2-0.5	73.5	24.5	1.2	0.7	23.5	0.3	26.9	10.4	38.9

ing boride composition, Ti concentrations generally increase as nominal Mo contents decrease. Furthermore, secondary phases tend to become more prevalent with reduced Mo content (see Figures 5.1 and 5.2).

In addition to the dark spherical particles already observed in 26-4-1 alloys, dark acicular particles formed after casting. Point analysis indicates similar compositions to spherical TiB_2-type particles (see section 4.1). Moszner et al. [127] observed similar findings in powder metallurgical Fe-25.3-2.0Mo-0.5Ti-1.4B, identifying Ti-rich borides and carbides. The increased fraction of TiB_2-type particles persisted with nominally lower B content. Generally, reduced B content

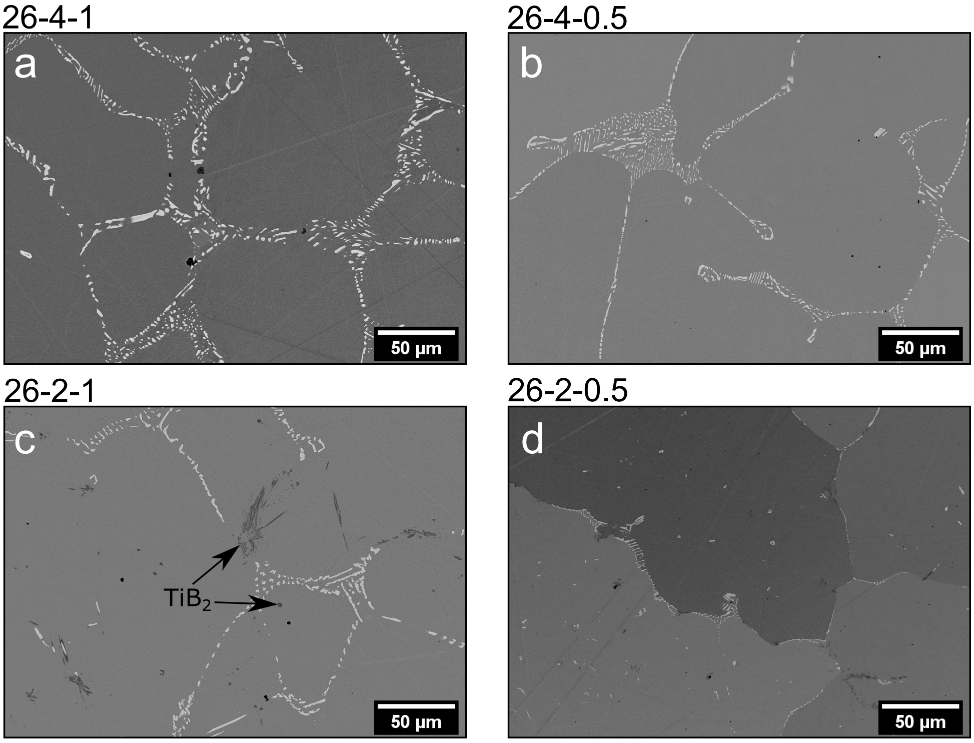
26-4-1
a
50 µm
26-4-0.5
b
50 µm
26-2-1
c
TiB$_2$
50 µm
26-2-0.5
d
50 µm

Figure 5.1.: SEM-BSE micrographs of as-cast Fe–26Al-yMo-0.5Ti-zB alloys (26-y-z). Reproduced from Abel et al. [191] under the CC BY 4.0 licence.

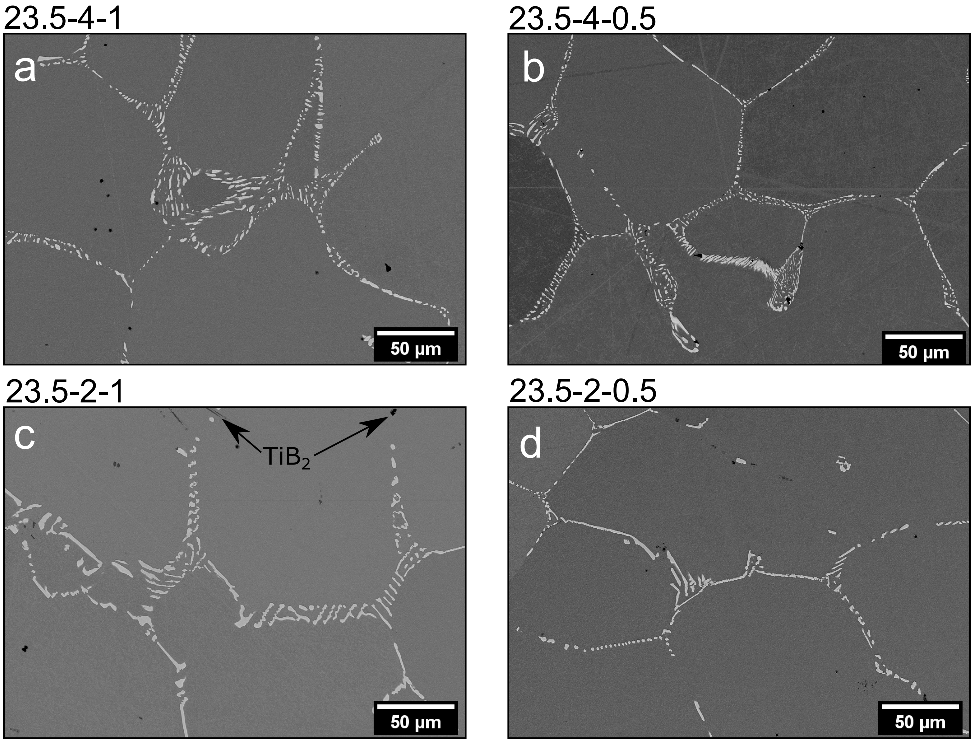
23.5-4-1
a
50 µm
23.5-4-0.5
b
50 µm
23.5-2-1
c
TiB$_2$
50 µm
23.5-2-0.5
d
50 µm

Figure 5.2.: SEM-BSE micrographs of as-cast Fe-23.5Al-yMo-0.5Ti-zB alloys (23.5-y-z). Reproduced from Abel et al. [191] under the CC BY 4.0 licence.

(0.5 at%) led to a refinement of the eutectic boride network (i.e. boride lamellae decreased in size and fraction). Only minor compositional changes of matrix and borides (< 10 rel%) occurred. Variation of nominal Al content mainly affected the concentration of Al in the matrix. 23.5-y-z alloys averaged to a matrix concentration of 24.2 at% Al opposed to 26-y-z alloys with 26.7 at% Al. Otherwise, elemental compositions of matrix and borides did not substantially differ between 23.5 and 26 at% Al.

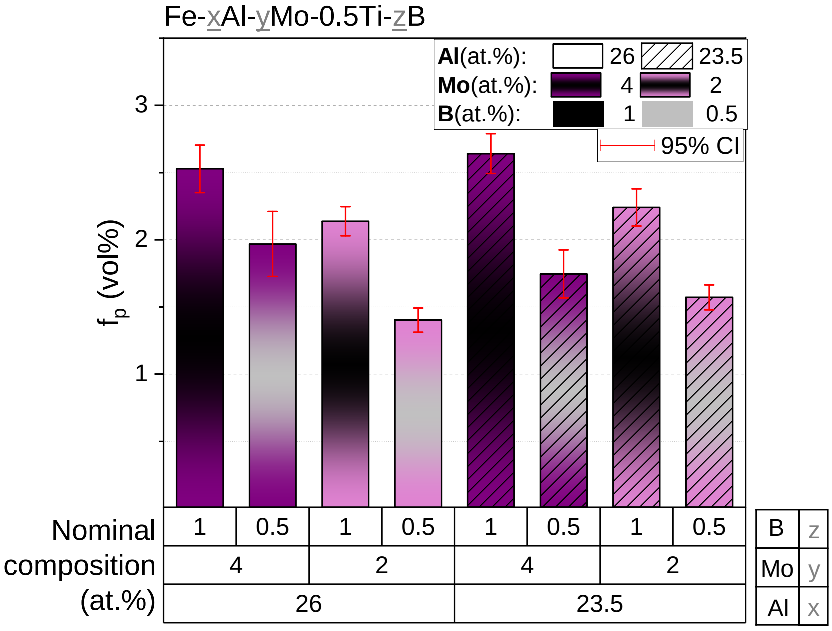

Figure 5.3.: Secondary phase fractions f_p including both Mo_2FeB_2 and TiB_2-type particles in as-cast Fe-xAl-yMo-0.5Ti-zB alloys. Adapted from Abel et al. [191] under the CC BY 4.0 licence.

Phase fractions of Mo_2FeB_2 and TiB_2-type particles in all alloys were quantified by OM and image processing. To enhance contrast and contouring of the matrix and secondary phases, metallographic surfaces were prepared with an alkaline etchant, which inhibited differentiation of Mo_2FeB_2 and TiB_2-type particles under OM. Therefore, the combined fraction of both secondary phases were acquired. Average secondary phase fractions f_p in all alloys are summarised in Figure 5.3. Area fractions were again assumed as volume fractions if secondary phases are randomly oriented [194]. Bars in the plot are sorted by descending nominal alloy concentrations for Al (x), Mo (y), and B (z). Secondary phase fractions range between 1.4 and 2.6 vol%. Note that values for 26-4-1 alloys (2.5 vol%) deviate from measurement results in Table 4.2 (4.1 vol%) due to the different etching strategies. The phase fractions in Fe-xAl-yMo-0.5Ti-zB alloys scale with increasing nominal Mo and B content. Thus, the refinement of eutectic borides in alloys x-y-0.5 with reduced B content (Figures 5.1b, d and Figures 5.2b, d) can be related to a general decrease in secondary phase fractions. Furthermore, lower nominal Mo content promotes the formation of TiB_2-type particles over eutectic borides, decreasing overall secondary phase fractions. These correlations apply for both hypostoichiometric and hyperstoichiometric Fe_3Al composition.

Differential thermal analysis was conducted to determine the phase transition temperatures with different alloy compositions. DTA heating curves of all alloy variants are shown in Figure 5.4, split into regions for solid-state transformations (Figure 5.4a) and melting transitions (Figure 5.4b). Detectable solid-state transformations of Fe_3Al in all alloys include the order-order transition $D0_3$ to B2 ($T_c^{D0_3 \leftrightarrow B2}$) and the order-disorder transition B2 to A2 ($T_c^{B2 \leftrightarrow A2}$). As explained in subsection 4.2.1, $T_{solidus}$ and $T_{liquidus}$ confine the melting interval of the eutectic and matrix phases, representing first-order transition temperatures. Liquidus temperatures in heating curves agree well with onset temperatures for solidification in the cooling curves. All transition temperatures are summarised in Table 5.4. Transition temperatures for two binary Fe_3Al alloys (i.e. Fe-25Al and Fe-27Al) are also included.

Compared to binary Fe-Al, $T_c^{D0_3 \leftrightarrow B2}$ and $T_c^{B2 \leftrightarrow A2}$ of all alloys shift to higher temperatures due to the addition of Mo and Ti [95, 131]. With varying Al and B additions, $T_c^{D0_3 \leftrightarrow B2}$ shifts between 54-78 K with 2 at% Mo or 110-130 K with 4 at% Mo. In alloys with lower B (i.e., x-y-0.5 alloys), the slightly higher solute concentrations of Mo in the matrix (see WDS results in Table 5.3) correlate well with the observed increases in $T_c^{D0_3 \leftrightarrow B2}$. Doubling the nominal Mo content (from 2 to 4 at%) results in an average increase of $T_c^{D0_3 \leftrightarrow B2}$ (58 K), which is greater than the average increase of $T_c^{B2 \leftrightarrow A2}$ (25 K). The absolute shift of $T_c^{B2 \leftrightarrow A2}$ is more influenced by Al content which is located between 784-823 °C for 23.5 at% Al and 888-921 °C for 26 at% Al. The reduction in the order-disorder transition temperature with lower Al content agrees well with binary alloys despite multiple alloying. Similarly, the order-order transition temperature ($D0_3 \leftrightarrow B2$) decreases by an average of 12 K when Al content is reduced from 26 to 23.5 at%. In binary $D0_3$ Fe_3Al, $T_c^{D0_3 \leftrightarrow B2}$ is nearly constant across the considered composition range (see Table 5.4). Thus, it can be speculated that solid-solution additions in $D0_3$ Fe_3Al increase the dependency of the phase transition temperature on Al concentration. For potential A2 phases in 23.5-x-y alloys, the presence of both $T_c^{D0_3 \leftrightarrow B2}$ and $T_c^{B2 \leftrightarrow A2}$ in alloys with nominal 23.5 at% Al confirms the absence of disordered A2 phases at room temperature.

Regarding first-order transitions, the melting interval of all alloys is broadened compared to bi-

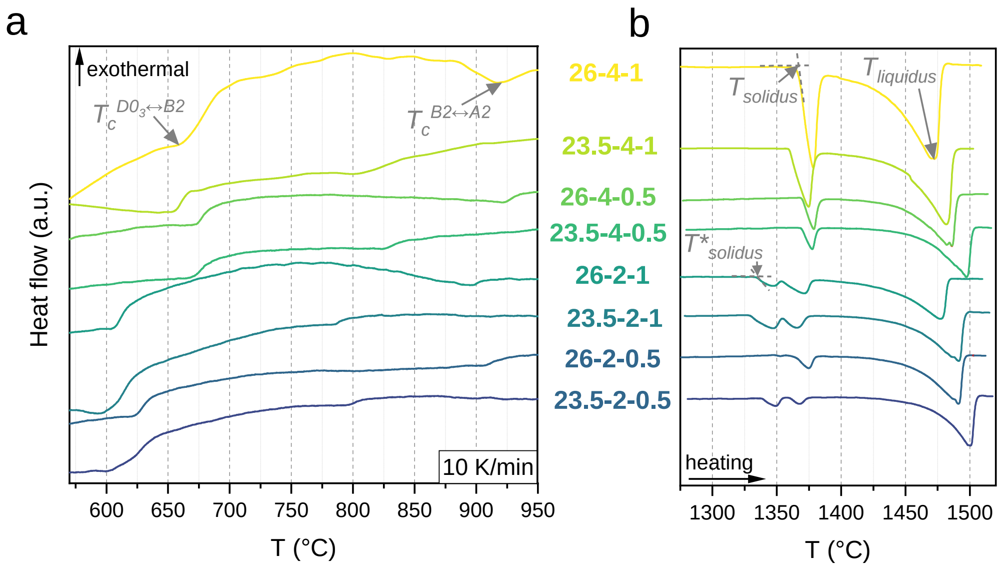

Figure 5.4.: DTA heating curves of as-cast Fe-xAl-yMo-0.5Ti-zB alloys with a constant heating rate of 10 K/min: (a) solid-state transformation range and (b) melting transition range. Reproduced from Abel et al. [191] under the CC BY 4.0 licence.

Table 5.4.: Phase transition temperatures of as-cast Fe-xAl-yMo-0.5Ti-zB alloys according to DTA analysis. Reproduced from Abel et al. [191] under the CC BY 4.0 licence.

Alloy x-y-z	$T_c^{D0_3\leftrightarrow B2}$ (°C)	$T_c^{B2\leftrightarrow A2}$ (°C)	$T^*_{solidus}$ (°C)	$T_{solidus}$ (°C)	$T_{liquidus}$ (°C)
26-4-1	662	917	-	1367	1473
23.5-4-1	652	812	-	1360	1482
26-4-0.5	673	921	-	1370	1486
23.5-4-0.5	665	823	-	1369	1497
26-2-1	604	888	1334	1353	1477
23.5-2-1	596	784	1326	1354	1491
26-2-0.5	621	907	1349	1362	1491
23.5-2-0.5	601	794	1339	1355	1500
Fe-27Al	543	868	-	1482	1500
Fe-25Al	542	753	-	-	-

nary alloys due to the additional melting of eutectic borides. Notably, alloys x-4-z and x-2-z differ in the number of endothermic peaks during melting. Alloys x-4-z have two peaks, while alloys x-2-z exhibit an additional third reaction at T^*_{solidus} (see Figure 5.4). For alloys with 2 at% Mo, T^*_{solidus} ranges from 1326 to 1349 °C and $T_{solidus}$ from 1353 to 1362 °C. For alloys with 4 at% Mo, the onset of melting $T_{solidus}$ ranges between 1360-1370 °C. Additionally, the enthalpies of the melting peaks at $T_{solidus}$ decrease with reduced B and Mo contents. This decrease in enthalpy correlates with the apparent decrease in eutectic boride phase fractions in Figures 5.1 and 5.2, suggesting that this temperature range corresponds to the melting of the eutectic phase. The occurrence of T^*_{solidus} in x-2-z alloys may be associated with the dissolution of TiB_2-type particles, which increase in apparent fraction at lower Mo contents.

5.2. Hardness and tensile properties

Figure 5.5a compares the HV10 macrohardness of all eight alloys. With Vickers indent diagonals over 200 µm, hardness effectively probes the combined microstructure of the Fe_3Al matrix and borides. Macrohardness ranges from 281 to 344 HV10 depending on alloy composition. For 26-y-z alloys, macrohardness varies between 281 and 296 HV10. Literature values state a hardness of 299 HV5 for binary, $D0_3$-structured Fe-27.9Al produced by vacuum induction melting [265].

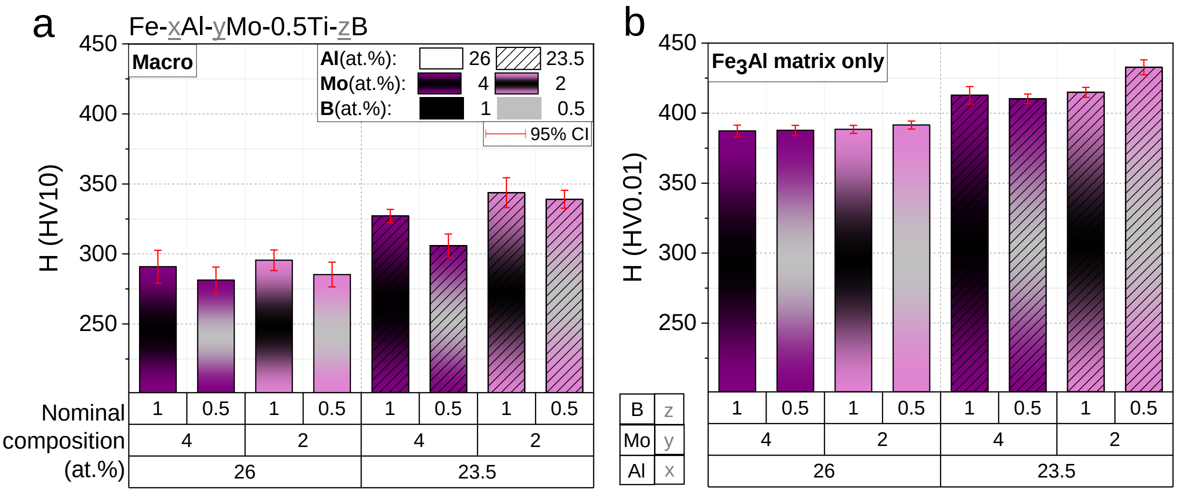

Figure 5.5.: Mean HV10 macrohardness (a) and mean HV0.01 microhardness in the Fe_3Al matrix phase (b) of as-cast Fe-xAl-yMo-0.5Ti-zB alloys. Adapted from Abel et al. [191] under the CC BY 4.0 licence.

All alloys with nominal 23.5 at% Al show increased hardness compared to those with nominal 26 at% Al. Alloys with 23.5 at% Al have on average 14% higher macrohardness than their 26 at% Al counterparts. To further investigate this hardness difference without potential effects by grain boundary hardening and particle hardening, the microhardness within the Fe_3Al matrix was compared.

Figure 5.5b compares the HV0.01 values of x-y-z alloys. Absolute HV0.01 values are higher than HV10 values due to the indentation size effect [211, 266]. Changing Mo or B contents shows less variation for microhardness compared to macrohardness. Alloys with 23.5 at% Al (417 ± 10 HV0.01) have higher average microhardness than 26-y-z alloys (389 ± 2 HV0.01), suggesting higher strength in 23.5-y-z alloys. The presented data match the Al-dependent yield strengths of binary alloys near Fe_3Al stoichiometry found in experiments [56, 267]. For binary alloys below 25 at% Al, there is a local maximum of yield strength. Around this maximum, yield strengths at lower Al concentrations decrease less than at higher concentrations. Thus, 23.5-y-z alloys likely belong to the higher yield strength regime. This alignment of yield strength relations in binary and alloyed Fe_3Al suggests that solid-solution additions do not affect yield strength evolution with Al concentration.

Regarding other alloy additions, macrohardness tends to increase with higher nominal B content, correlating with the increase in secondary phase fractions (i.e. eutectic phase fraction) in Figure 5.3. Microhardness measurements within the eutectic phase region in alloy 26-4-1 (not shown here) indicated a 50% higher hardness compared to the Fe_3Al matrix. Thus, a refinement of the eutectic phase and a reduction of borides likely decreases hardness. As no B incorporation into the Fe_3Al matrix was found according to WDS, a change in matrix hardness with different B contents was not expected and is generally not observed. The unexpected rise in matrix hardness in alloy 23-2-0.5 remained unexplained. Surprisingly, variations in Mo content did not affect the microhardness of Fe_3Al. This agrees well with macrohardness values, which remained constant or were even slightly increased with less Mo (alloy 23.5-2-1).

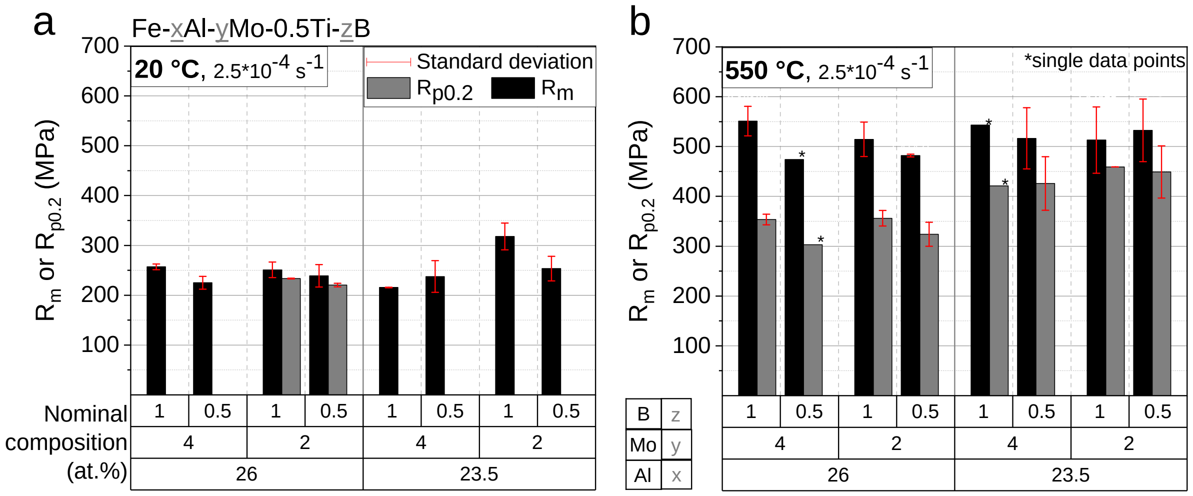

Figure 5.6.: Average 0.2% proof strength $R_{p0.2}$ and ultimate tensile strength R_m at room temperature (a) and 550 °C (b) in Fe-xAl-yMo-0.5Ti-zB alloys. Specimens at 550 °C were homogenised at HT2 before testing. Adapted from Abel et al. [191] under the CC BY 4.0 licence.

To verify the effect of alloy elements on mechanical properties, tensile tests at room and elevated temperature were conducted. The elevated test temperature was chosen to 550 °C, the temperature of the base alloy's YSA as determined in subsection 4.3.2. The respective YSA temperatures of other alloys may shift slightly due to different alloying contents [18]. Figures 5.6a and b display average 0.2% proof strengths $R_{p0.2}$ and ultimate tensile strengths R_m of all alloys at the respective temperatures. Standard deviations are shown as red error bars if mean values are displayed.

R_m of all alloy variants span from 216 MPa (alloy 23.5-4-1) to 318 MPa (alloy 23.5-2-1) at room temperature. Correlations of strength and alloy composition agree well with previous hardness measurements. Most alloys failed before reaching 0.2% plastic deformation, except for the 26-2-z alloys. They achieved $R_{p0.2}$ values of 234 MPa (alloy 26-2-1) and 221 MPa (alloy 26-2-0.5), reaching the highest elongations after fracture A with 0.4% and 0.3% respectively.

For comparison, A of cast binary Fe_3Al is given as 0.7% [115]. Thus, reducing Mo effectively reduces brittleness and recovers ductility in boride-strengthened, solid-solution hardened Fe-26Al-xMo-0.5Ti-zB. As secondary phase fractions and solute concentrations decreased when Mo content was reduced from 4 to 2 at%, one or both factors may contribute to reduced embrittlement. However, secondary phase fractions also decreased with reduced B, which did not increase ductility. This supports the major role of Mo solute concentration in the Fe_3Al matrix to govern ductility. It also matches the fracture behaviour of all alloys after room temperature testing (not shown here), which commonly featured transgranular cleavage. Fracture surfaces mainly featured cracks propagating through the matrix and detouring borides, indicating the matrix as the weakest link under tensile loading. Similar statements were given by McKamey and Horton [131] reporting ductility to continuously decrease above 0.5 at% Mo. Against this, reducing Mo in 23.5-y-z alloys did not recover ductility but only increased strength. This observation highlights that embrittlement at room temperature by Mo sensitively depends on Al concentration around Fe_3Al stoichiometry.

Mean values of $R_{p0.2}$ and R_m at 550 °C are depicted in Figure 5.6b. The 0.2% proof strengths show similar trends as seen from R_m and HV10 values at room temperature. The average $R_{p0.2}$ of all 23.5-y-z alloys is approximately 100 MPa higher than that of all 26-y-z alloys. For individual 23.5 at% Al alloys, mean values range between 421 MPa (alloy 23.5-4-1) and 459 MPa (alloy 23.5-2-1), while 26 at% Al alloys range between 303 MPa (alloy 26-4-0.5) and 356 MPa (alloy 26-2-1). Higher B contents increase the strength in 26-y-z alloys, likely due to higher secondary phase fractions. Surprisingly, 26-y-z alloys with only 2 at% Mo have similar strength to those with 4 at% Mo. In 23.5-y-z alloys, $R_{p0.2}$ is even higher with lower Mo concentration. The observations cast doubts on the effect of solid-solution hardening, which will be discussed in the next section. Ultimate tensile strengths R_m at 550 °C range from 474 MPa (alloy 26-4-0.5) to 551 MPa (alloy 26-4-1) for Fe-26Al alloys, and from 513 MPa (alloy 23.5-2-1) to 543 MPa (alloy 23.5-4-1) for Fe-23.5Al alloys. In 26-y-z alloys, reduced B content and lower secondary phase fractions decrease strength as was seen before. However, R_m in 23.5-y-z alloys varies inconsistently with alloy composition. A final conclusion is difficult as specimens among 23.5-y-z alloys exhibited fundamentally different plastic deformation behaviour at 550 °C which is reflected by clearly larger standard deviations of $R_{p0.2}$ and R_m. This issue is further investigated and discussed in chapter 6.

5.3. Solid-solution hardening by Mo in near-Fe_3Al alloys

The results indicate that no strength increase was induced by higher Mo incorporation beyond 2 at%. The observations on hardness and tensile strength up to elevated temperatures match reported data on comparable boride-strengthened alloys with Mo concentrations between 0.5 and 4 at% [38, 131]. However, the results cast doubts on the solid-solution hardening (SSH) effect in Fe-Al-Mo-Ti-B alloys, especially in the investigated base alloy for which a high contribution was attributed under tensile and creep loading (see subsections 4.3.2 and 4.3.3). It also contradicts the accepted and often observed linear dependency of SSH on solute concentration [268]. Feltham's nucleation model is recognized for describing SSH in common f.c.c., b.c.c. and h.c.p. crystal systems [269]. It describes a power-law dependency of the critical resolved shear stress ($CRSS$) on solute concentration c as $CRSS \propto c^r$, with the exponent r usually located between 0.5 and 1. However, explaining SSH in ordered intermetallics is difficult due to stoichiometry effects [270], which alter vacancy and anti-site defect concentrations based on solute atom positions. Accordingly, the mechanical behaviour in intermetallic solid solutions may be different than expected. First-principle calculations also showed that the electronic structure of host-solute pairings is critical for the effective misfit parameters for SSH [271]. Experimental studies verified this and demonstrated that different solute elements follow different power laws in intermetallic iron aluminides [59, 272]. Reports on the effect of Mo additions is available for higher temperatures. Palm [34] studied compressive 0.2% proof strengths of ternary Fe-26Al-xMo alloys with up to 5 at% Mo between 600 and 800 °C. He found nearly linear correlations of solute Mo concentration with 0.2% proof strength, though the gradient decreased with temperature. This agrees with the nucleation model's prediction that SSH weakens at higher temperatures [268]. It also implies that SSH at lower temperatures should be as strong as at 600 °C. At this temperature, a jump of nearly 100 MPa in 0.2% proof strength was reported when Mo increased from 2 to 4 at%. These observations contrast with the strength relations in tensile tests at 550 °C presented here. $R_{p0.2}$ in 26-2-z and 26-4-z alloys (on average 1.2 and 2.5 at% Mo solute concentration, respectively) were similar for equal B content, showing no additional SSH effect with increased Mo. Similarly, strength in alloys with different Mo contents was comparable at room temperature according to microhardness and tensile strength.

Due to the complexity of the alloy design, other hardening mechanisms might superimpose SSH and change with alloy composition. Grain boundary hardening effects can be excluded due to very large grains in all alloys. The particle hardening effect probably varies with alloy composition regarding the depletion and enrichment of different secondary phase particles. However, variation of B content suggested that lower secondary phase fractions generally lead to decreased strength. Therefore, strength in alloys with lower Mo concentration, which also contained lower secondary phase fractions, is expected to further decrease instead of compensating for a loss in SSH. To fully evaluate hardening by secondary phases, factors such as particle size, shape, and distance, as well as modulus difference contributions, must be considered [273]. However, as already explained in subsection 4.3.3, quantification of particle hardening is complicated due to the inhomogeneous distribution of secondary phases, making a thorough consideration of particle hardening out of scope. Another hardening contribution especially connected to Fe-Al alloys could originate from thermal vacancies. With respect to alloying additions, it is unclear how the ability to freeze in thermal vacancies in Fe-Al alloys varies with different solute concentrations or solute ratios. Medvedeva et al. [271] found that different solute species with different site preference energies can in fact change vacancy concentrations. Still, the interaction effect of two solutes (i.e. Mo and Ti) on total vacancy concentration remains unclear. For now, it seems unlikely that equally processed Fe-Al alloys with different alloying concentrations but equal Al content would have fundamentally different thermal vacancy concentrations in this study. A more thorough study of thermal vacancy hardening is given later in section 7.2.

In conclusion, solid-solution hardening by Mo may saturate below 1.2 at% in near-Fe_3Al alloys with small Ti additions, contradicting the linear power-law relationship with Mo concentration.

Conventional SSH laws might not apply due to the impact of additional Ti alloying. No further hardening with increasing Mo concentration might be due to softening effects. Phenomenological models for softening suggest local elastic modulus changes [274] or decreased Peierls stress [275] with increasing solute additions.

Chapter 6

Casting-induced microstructural variations: Implications for tensile properties

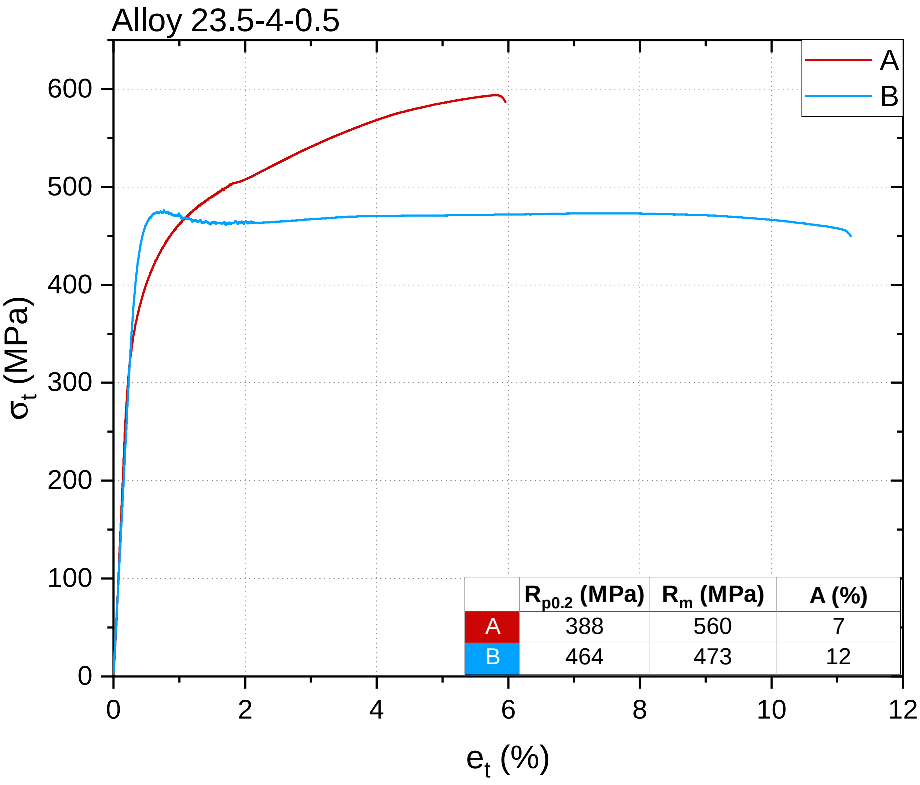

	$R_{p0.2}$ (MPa)	R_m (MPa)	A (%)
A	388	560	7
B	464	473	12

Figure 6.1.: True stress-strain curves of two investment-cast Fe-23.5Al-4Mo-0.5Ti-0.5B specimens at 550 °C with equal processing conditions and test parameters.

The tensile tests at 550 °C of three Fe-23.5Al-yMo-0.5Ti-zB alloys (i.e. alloys 23.5-4-0.5, 23.5-2-1, 23.5-2-0.5) were accompanied by a large scatter of $R_{p0.2}$ and R_m as depicted in Figure 5.6b. With regard to the tensile curves, it turned out that comparable Fe-23.5Al-yMo-0.5Ti-zB specimens exhibited both different yielding points and different work hardening behaviour. An example is given for alloy 23.5-4-0.5 in Figure 6.1. True tensile stresses are plotted against true strain to reveal the plastic behaviour. Specimen A (red solid line) shows continuous work hardening during plastic deformation until failure. Against this, ultimate tensile strength (473 MPa) in specimen B (blue solid line) is just reached after passing $R_{p0.2}$ and is clearly lower than in specimen A (560 MPa). After a short drop in true stress which is accompanied by frequent stress serrations, the flow curve B shows nearly ideal plastic behaviour without work hardening. Consequently, elongation after fracture of specimen B is higher (12%) than specimen A (7%).

As the two specimens of each alloy variant were extracted from different positions within the investment castings (see Figure A.2), one being in the back (specimen A) and one being in the front (specimen B) with respect to the centrifugal direction, the microstructures of both specimens potentially differ. Simulations of form filling and solidification behaviour indicated differences for specimens A and B (not shown here). To elucidate an impact of microstructure on the deformation behaviour, EBSD studies on both 23.5-4-0.5 specimens were carried out. These comprised investigations of texture, grain size evolution and misorientation evolution. It was differentiated between longitudinal cross-sections at gauge sections (close to the fractured surface) and at threading sections which serve as an undeformed reference.

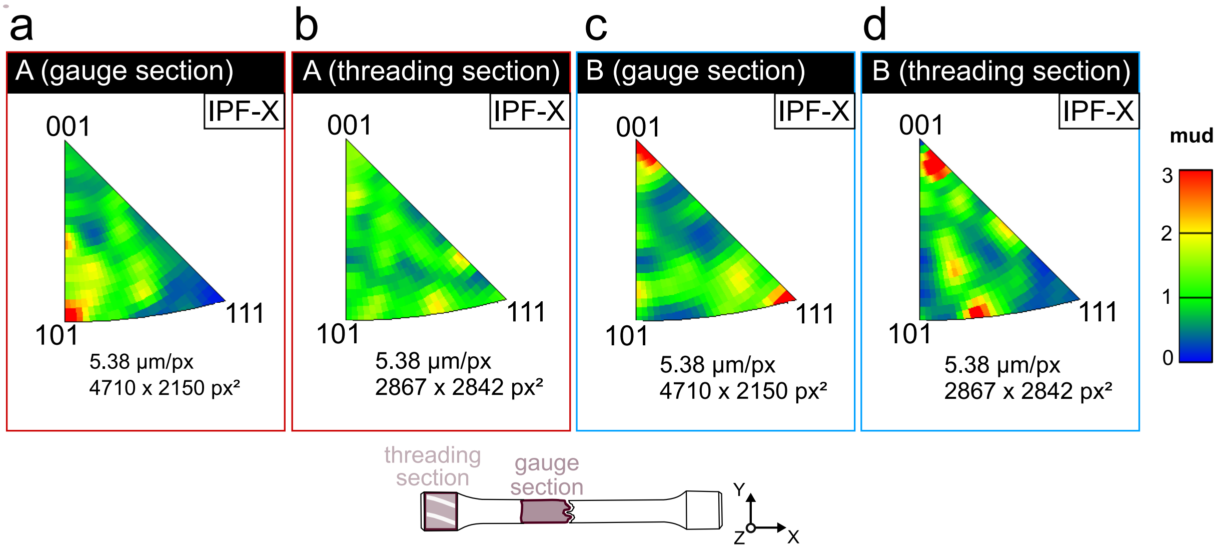

Figure 6.2.: Inverse pole figures measured by EBSD along the tensile axis (X-direction) of investment-cast 23.5-4-0.5 alloys in HT2 state after tensile testing at 550 °C: Comparison of gauge sections (a,c) and threading sections (b,d) in specimens A and B respectively.

Figure 6.2 displays contour plots of the inverse pole figures (IPF) along the tensile axis (X) of all investigated cross-sections. Intensities are given as multiples of uniform density (mud), with 1 indicating randomly oriented grains. Apparently, threading sections of specimens A and B (Figures 6.2b and d) exhibit clearly different textures. Whereas specimen A shows a nearly random distribution of grains, specimen B comprises a few more abundant orientations. Speaking about a fibre texture along specific crystallographic directions would be misleading as a few large grains oriented in these directions also contribute to the increased densities. EBSD pole figures with respect to the crystallographic main axes (not shown here) also did not hint at any specific texture. One more abundant orientation which is situated on the zone between (101) and (111) coincides with the maximum Schmid factor of the {112}<111> slip system [276, 277]. The {112} planes were reported as possible cross-slip planes in Fe_3Al alloys [278, 279]. In sum, the comparison of IPF-X figures of both threading sections indicates that different initial microstructural states were present. Accordingly, IPF-X figures at deformed gauges sections of specimens A and B (Figure 6.2a and c) differ in their deformation textures. During tensile loading, an alignment of specific crystallographic axes with the loading direction is common and also visible in both IPF-X figures [175]. However, specimen A develops one preferred orientation of <101>-grains, whereas specimen B with higher ductility shows two preferred orientations of grains along <001>- and <111>-directions. The former is usually seen in b.c.c. metals, the latter in f.c.c. metals [175]. More in-depth investigations of how these deformation textures could have evolved is out of scope of this thesis, but it illustrates that the initial microstructure might significantly affect the deformation capabilities. One potential hint which could explain the higher deformability in specimen B is the favourable orientation and high abundance of {112} planes which could facilitate cross-slip of {110}<111> screw dislocations.

For grain detection, a minimum grain boundary angle of 10° was chosen. Additionally, an option for grain boundary completion down to 5° was opted if incomplete grain boundaries arose. Both choices aimed for reliable detection of newly formed grains, which might appear due to recrystallisation phenomena, while differentiation of HAGBs and LAGBs was not pursued. Figure 6.3 displays the relative grain size distributions as bar plots within gauge sections (solid interior) and threading sections (hatched interior) of specimens A (red) and B (blue). The grain size was calculated as circle equivalent diameter of grains. The illustration of distributions is limited to below 300 µm as only smaller grains might significantly change ductility and are therefore of interest. However, statistics were calculated for the complete sample size. The average grain sizes of all samples range between 425 µm (specimen A) and 472 µm (specimen B) and are below the 95% CI of previous measurements (586 ± 66 µm, see Table 5.2). The difference most probably stems from different measurement techniques. More suitable for comparison is the me-

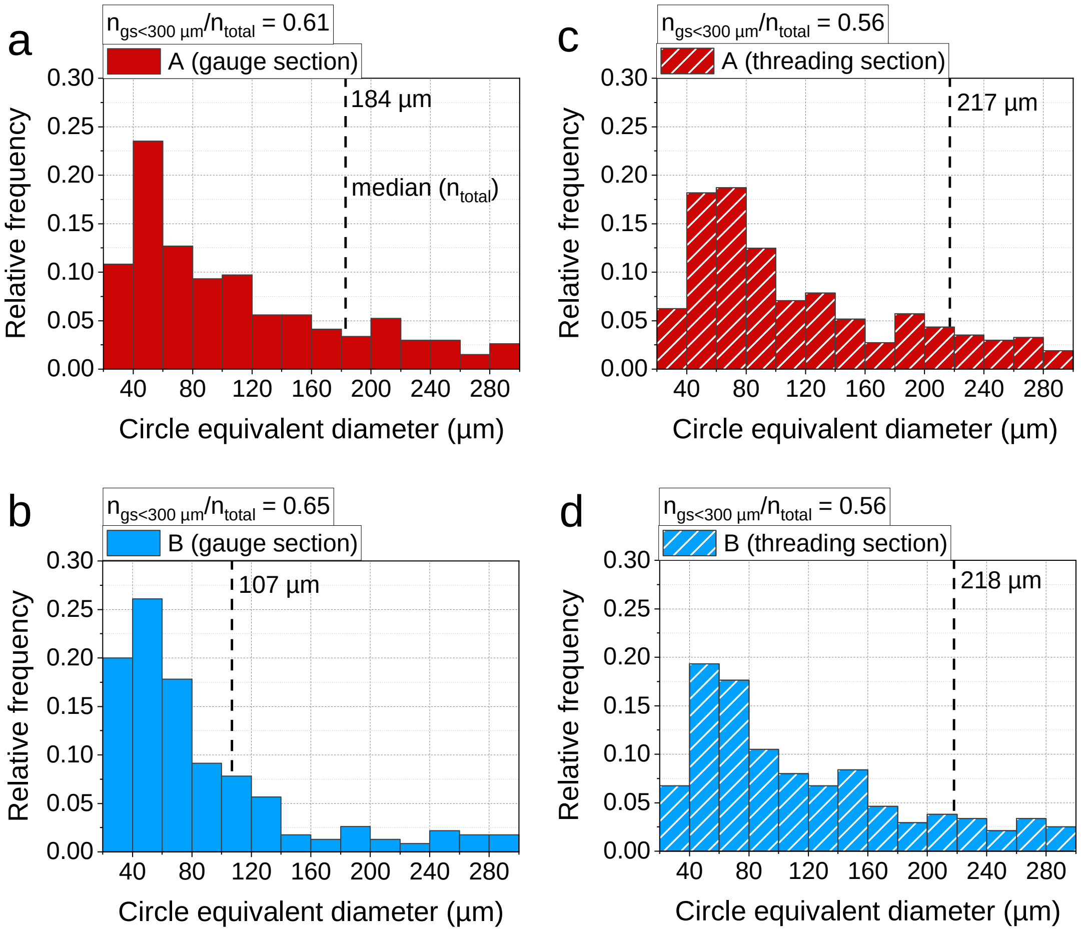

Figure 6.3.: EBSD grain size distributions of investment-cast 23.5-4-0.5 alloys in HT2 state after tensile testing at 550 °C: Comparison of gauge sections (a,b) and threading sections (c,d) in specimens A and B respectively.

dian of distributions which is better reflecting the surplus of small grains. The median values in threading sections are equivalent (217 and 218 μm). Against this, median values in both deformed gauge sections are lower than in undeformed threading sections, but significantly differ from each other (specimen A: 184 μm, specimen B: 107 μm). Similarly, the ratio of grains below 300 μm ($n_{gs<300\ m}$) versus all identified grains (n_{total}) is higher in gauge section B (0.65) compared to gauge section A (0.61) and both threading sections (0.56). An excess amount of small grains below 80 μm in gauge section B might potentially originate from discontinuous dynamic recrystallisation (dDRX). This mechanism also matches the true flow progression of specimen B shown in Figure 6.1 as expected for materials with recrystallised microstructure [175, 280]. A single round peak before steady-state flow is especially common for large initial grain sizes [280], which is the case in the investigated Fe-23.5Al-yMo-0.5Ti-zB specimens. The constant stress deformation would then be mainly driven by a dynamic equilibrium between strain hardening (i. e. grain boundary migration) and strain softening (i. e. formation of new grains). dDRX was both reported for B2 ordered FeAl [281, 282] and $D0_3$ ordered Fe_3Al [283] at temperatures of $T > 0.5T_{liquidus}$. Although our test temperature is at around $0.46T_{liquidus}$, the given circumstances may still support dynamic recrystallisation events.

Further evidence was sought by local misorientation maps below 5° which are summarised in Figure 6.4. They are especially suitable in highlighting regions of higher deformation. Histograms plotting the normalised frequencies of local misorientations are added as quantitative measure for orientation changes. Figures 6.4c and d depict the threading sections of both specimens. They show a comparable state of low local misorientation with mean values below 0.35°. Against this, gauge sections (Figures 6.4a and b) have a higher spread of local misorientations following a log-normal distribution. This is visualised as local grain areas with higher misorientations (in green). Hence, deformation is not homogeneous, but is concentrated in specific grains. No systematic correlation of specific grain orientation and higher local misorientation could be deduced though. At higher magnifications (see Figure 6.4e), it becomes apparent that large misorientations are localised adjacent to non-indexed areas (in black). These usually represent boride phase boundaries, but also sometimes depict cracking surfaces (see top left in Figure 6.4b). The localisation of misorientation changes to boride phase boundaries can be expected as the acicular morphology of borides and the incoherence of phase boundaries induce higher stress concentrations. Note that specimen B exhibits significantly more areas of large local misorientation than in specimen A. In consequence, specimen B shows a higher abundance of misorientations $> 2°$ with a mean value of $0.8 \pm 0.58°$ compared to specimen A with $0.58 \pm 0.24°$. The values might correlate with elongations after fracture A in specimen B (12%) and specimen A (7%). As for strains, the cause of different misorientation evolution could be the lacking comparability of initial microstructures and grain orientations. These primarily govern deformation processes and can therefore induce higher stress concentrations at phase boundaries if higher strain is given. The measured local misorientations are lower than reported values by Lin et al. [284] who connected continuous recrystallisation processes to increasing misorientations between 3 and 6° in large-grained Fe_3Al. Therefore, there is likely no strong manifestation of recrystallisation in both specimens, but the increased quantity of small grains in specimen B could indicate that low amounts of localised recrystallisation might have occured.

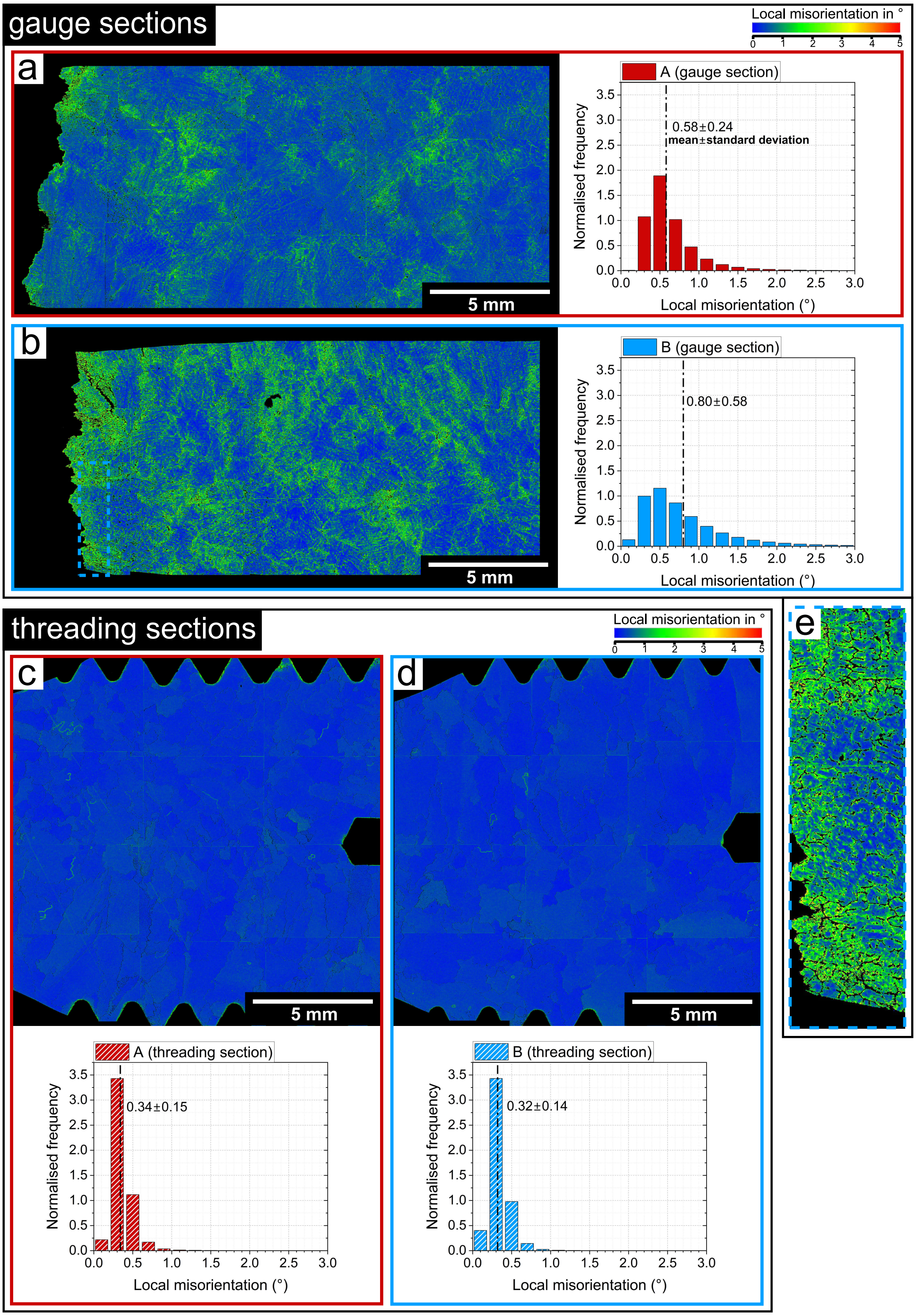

Figure 6.4.: EBSD local misorientation maps and normalised frequency distributions below <5° in investment-cast 23.5-4-0.5 alloys in HT2 state after tensile testing at 550 °C: Comparison of gauge sections (a,b) and threading sections (c,d) in specimens A and B respectively, (e) magnification of local misorientation map close to the fracture surface of specimen B.

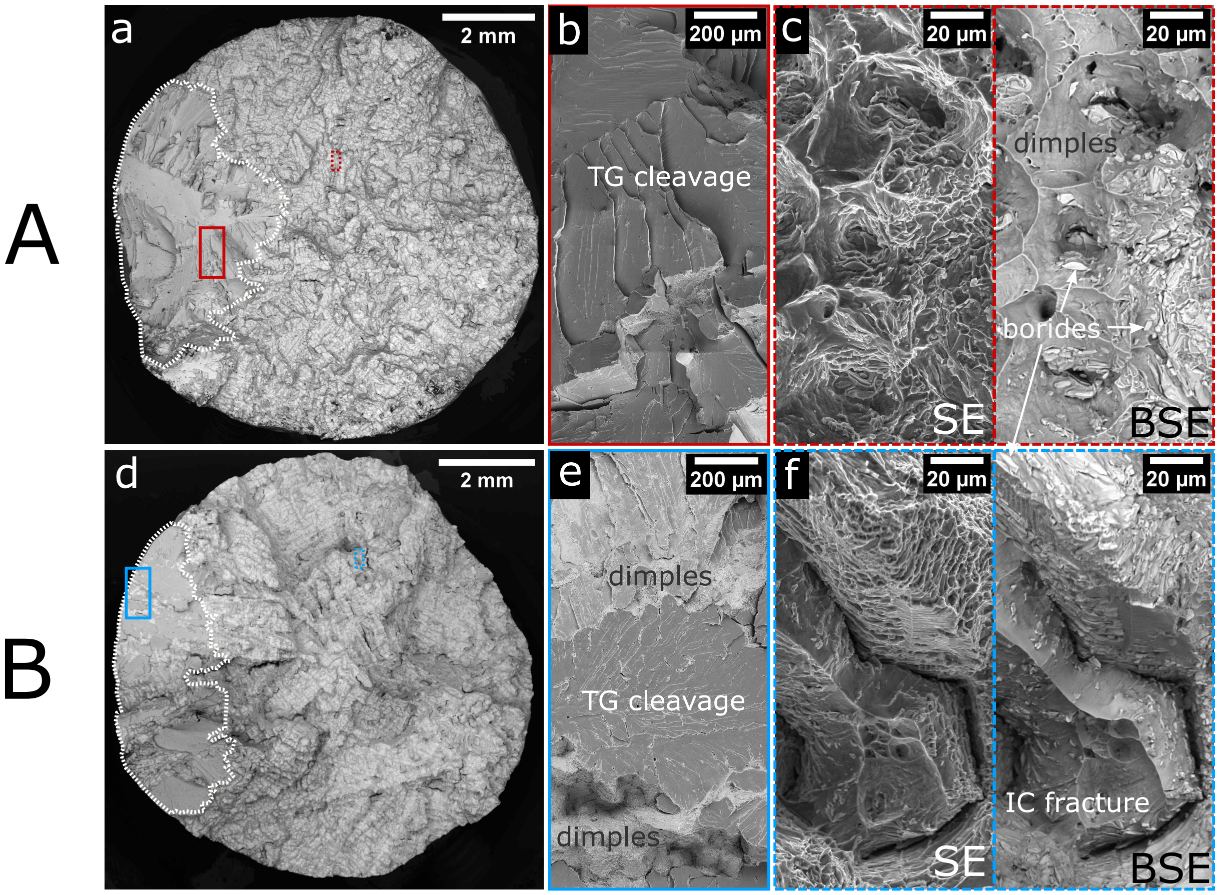

Figure 6.5.: Overview and magnified SEM images of the fracture surfaces of specimens A (a-c) and B (d-f) in investment-cast 23.5-4-0.5 alloys in HT2 state after tensile testing at 550 °C.

Another reason for constant stress deformation or softening as was seen with specimen B may be related to cracking. Yang and Baker [70] suggested that with increasing thermal vacancy concentration, more cracking was observed which led to a lowering of work hardening rate in Fe-40Al polycrystals. The cracking susceptibility and ease of propagation in ordered intermetallics is a known problem which is associated with its high work hardening rates [63]. To verify this hypothesis, images of fractured surfaces after failure were gathered. They are displayed in Figure 6.5. SEM overview images (Figures 6.5 a, d) reveal that both specimens mainly deformed in a ductile way. This is confirmed at higher magnifications (Figures 6.5 c, f) where mostly deformation areas containing dimples are identified. Also note that signs of intergranular fracture appear (Figure 6.5 f), which contrast with the predominantly transgranular fracture mode of all Fe-Al-Mo-Ti-B alloys tested at room temperature (not shown here). Nevertheless, dimple evolution in specimen B appears significantly finer than in specimen A, most probably due to larger elongations after fracture. Both specimens feature a confined, less deformed fracture area on the left in Figures 6.5a and d (encircled by a white outline). They are mostly composed of transgranular (TG) cleavage areas (see magnifications in Figures 6.5b and e). Still, the cleavage areas in specimen B with higher elongation after fracture are permeated by scattered ductile regions suggesting a higher deformability in specimen B. Concerning cracking, overview images in Figures 6.5a and d reveal that secondary cracking was present at least on the fracture surface. It also appears that more cracking occurred in specimen B than in specimen A.

Besides recrystallisation or cracking as explicit cause for the deformation behaviour in specimen B, the differences in both specimens might be related to the sensitivity of work hardening behaviour on temperature and Al concentration. Although the comparability of the tensile tests of both specimens (see Figure 6.1) was guaranteed by prior homogenisation treatment and precise control of test conditions (i.e. temperature and strain rate), the work hardening curves significantly differed from each other. Notably, the work hardening rates at 0.05%, 0.1% and 0.2% proof strength levels were usually higher in specimen A. Against this, stresses at low plastic strains $< 1\%$ are usually higher in specimen B. Both aspects speak for fundamentally different dislocation nucleation and migration behaviours in the early stage of plastic deformation. On the one hand, T_{YSA} depicts a sensitive tipping point for the activation of multiple strengthening and softening phenomena as described in subsection 2.3.1. On the other hand, it is surprising that different work hardening behaviour was only observed in most 23.5-y-z alloys and never in 26-y-z alloys within this study. Hence, effects related to Al matrix concentration might be decisive here, too. A high elastic anisotropy increases the likelihood of dislocation instabilities for specific orientation ranges of dislocation lines and therefore might affect the deformation mechanisms during yielding and work hardening [285]. As elastic anisotropy was shown to have a narrow peak at stoichiometric Fe_3Al composition [56], it can be assumed that elastic anisotropy is larger in 23.5-y-z alloys with 24–25 at% Al than in 26-y-z alloys with 26-27 at% Al. Another reason might be the Al concentration dependency of the slip vector transition from <111> to <100> at temperatures near the YSA [286, 287]. The presence or absence of slip in <100> could alter the general mobility of dislocations and influence the likelihood for dislocation climb processes. To summarise, the initial microstructure differences might depict the primary reason for the observed plasticity differences. Besides, the sensitivity of slip vector transition temperature and elastic anisotropy to Al concentration might not only explain the absence in 26-y-z alloys, but also amplify variations of work hardening behaviour. It illustrates that the casting process, especially the centrifugal casting method, and the location for extracting test specimens could clearly affect the derived mechanical properties. It is therefore imperative to exercise caution when determining and interpreting mechanical properties around T_{YSA} in Fe-Al-Mo-Ti-B alloys with a matrix concentration of 24–25 at% Al.

Chapter 7

Effect of cooling rate and heat treatments on room temperature properties

7.1. Processing-microstructure-property correlation

Parts of the results of this section were first reported in Abel et al. [288].

After revealing the side effects of centrifugal casting on microstructure and hot tensile properties in chapter 6, it became clear that the microstructural evolution is essential for predictable mechanical properties. In turn, the key parameter to control microstructure is the cooling rate and solidification rate during casting. Two different strategies were chosen to modify cooling rates: i) changing mould material and ii) changing wall thickness of castings. The study was also utilized to analyse the impact of average grain size on mechanical properties in the Fe-26Al-4Mo-0.5Ti-1B base alloy. Higher average grain diameters in investment castings (IC) were dealt as possible argument for lower 0.2% proof strengths in comparison to literature data in subsection 4.3.2. As alternative to IC, die casting (DC) with copper dies as mould material was chosen. Copper dies possess a fundamentally higher thermal conductivity than insulated ceramic shell moulds enabling a faster removal of internal heat. For varying wall thickness, a step sample geometry was designed (see Figure A.4) comprising wall thicknesses of 2.5, 5, 10, 15 and 20 mm in one casting. Optical micrographs with grain area contrast of as-cast castings from DC and IC and all wall thicknesses are compared in Figures 7.1a and b respectively. They show the transversal microstructures with respect to the original melt flow direction ranging from edge to centre within the cast steps.

The microsections of die casting and investment casting reveal notable distinctions in both grain size and morphology. Analogous to the description in section 4.1, the IC microstructure of all wall thicknesses (Figure 7.1b) is characterised by an uniform distribution of grains of varying sizes

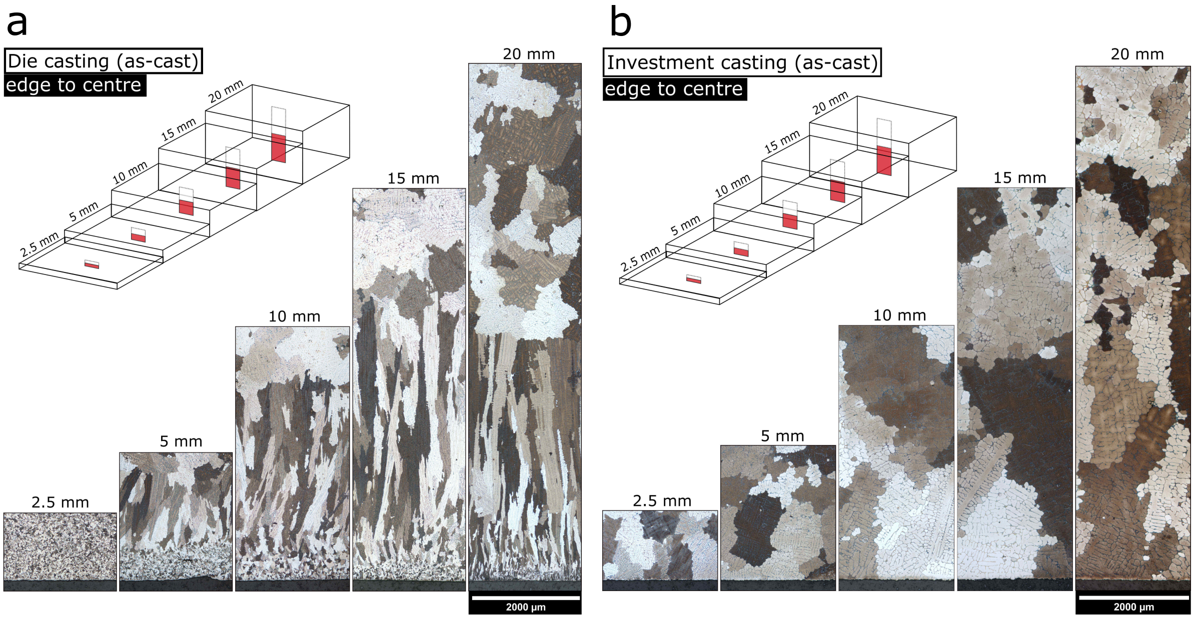

Figure 7.1.: Optical microsections from edge to centre of Fe-25Al-3.7Mo-0.4Ti-1B step samples after die casting (a) and investment casting (b) as a function of wall thickness. Reproduced from [143].

across the entire cross-section. In contrast, die-cast microstructures except for 2.5 mm (Figure 7.1a) exhibit distinct microstructural zones which are indicative of constitutional supercooling. The zones comprise an area of fine equiaxed grains near the edge, coarse globular grains in the centre and columnar grains in-between. The thickness of the central coarse globular zone increases with increasing wall thickness. The constitutional supercooling is likely a result of the solidification rate achieved with die casting and the eutectic reaction involved [289, 290].

To investigate how processing, microstructure and mechanical properties correlate with each other within the as-cast base alloy, the average grain diameter d_{gs} as well as the mean HV10 macrohardness H were plotted over the solidification rate dT/dt in a common plot in Figure 7.2. The solidification rate of each wall thickness was derived from simulations of temperature during cooling in the centre of cast steps by MAGMASOFT®. A linear gradient of the temperature was determined over the solidification range of Fe-25Al-3.7Mo-0.4Ti-1B (between 1473 °C and 1367 °C according to DTA, see Figure 4.6) and equalized as dT/dt. Likewise, average grain diameters according to Heyn lineal intercept method (in red) and macrohardness (in blue) were only measured in coarse globular grain zones or in the centre region of cast steps. d_{gs} appears to follow an inverse relationship with dT/dt. This corresponds to suggested correlations of cooling rate and grain size based on experimental data in general single-phase polycrystals [291, 292]. An inverse regression (displayed as red dashed line) is shown for a qualitative fit of the data. Grain size itself often correlates well with hardness as grain refinement provides additional strengthening. The correlation of grain size and strength is known as the Hall-Petch relationship and is usually described by equation 7.1 [293, 294],

$$\sigma_y = \sigma_{lattice} + \frac{k}{d_{gs}^{0.5}} \tag{7.1}$$

with σ_y as the yield stress, $\sigma_{lattice}$ as the lattice resistance and k as the Hall-Petch constant. The yield stress σ_y, similar to $R_{p0.2}$, can be substituted by the hardness if the lattice resistance is not to be determined [295]. Under the assumption that hardness values follow a Hall-Petch relationship with grain sizes which corresponds to $H \propto d_{gs}^{-0.5}$, hardness and solidification rate should follow a $H \propto (dT/dt)^{0.5}$ law. Despite some deviating data points, the data set roughly follows this relationship as the regression line (blue dashed line) suggests.

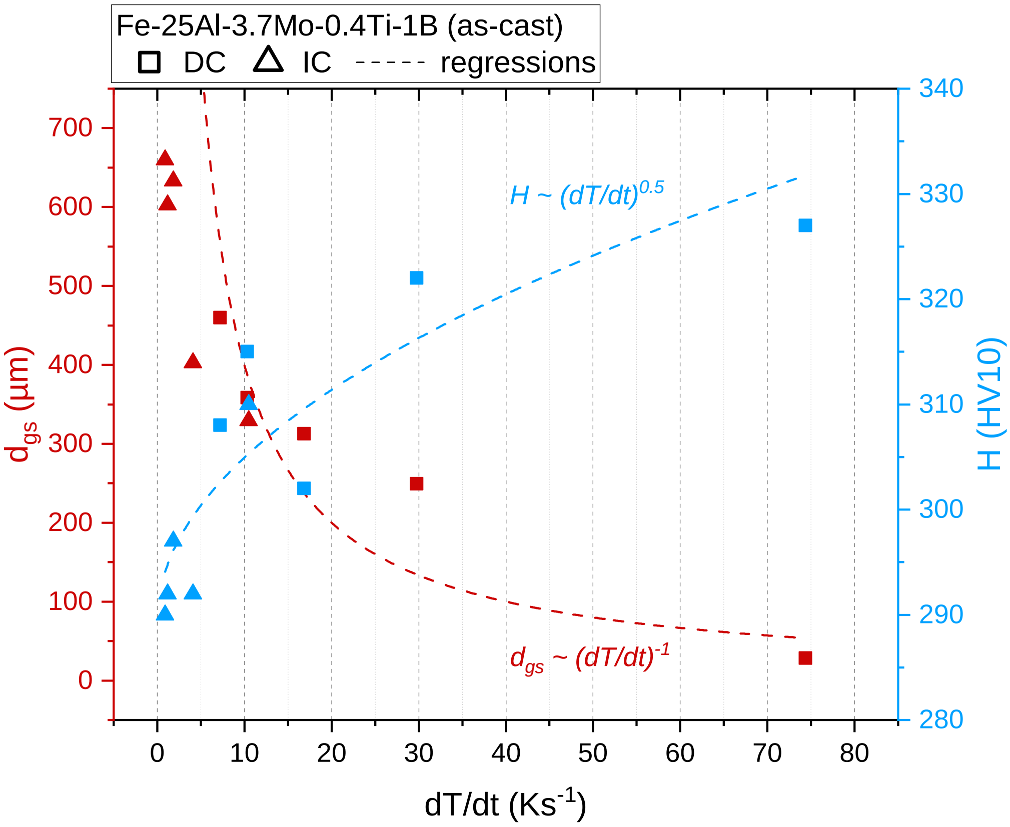

Figure 7.2.: Average grain diameter d_{gs} and mean Vickers macrohardness H of die-cast and investment-cast samples of as-cast Fe-25Al-3.7Mo-0.4Ti-1B over solidification rate dT/dt. Regression lines of both datasets are displayed as dashed lines. Reproduced and adapted from [143].

Higher solidification rates also directly affected the evolution of the eutectic phase. Figure 7.3a depicts the as-cast microstructure of die-cast Fe-25Al-3.7Mo-0.4Ti-1B with a wall thickness of 20 mm. In contrast to investment casting (see Figure 4.1), a much finer morphology of boride lamellae is observable after die casting. Consequently, the homogenisation treatment HT2 (1000 °C /100 h/FC) after die casting (see Figure 7.3b) led to a more pronounced modification of the eutectic structure than after investment casting. Boride lamellae grew in size and reshaped to a rounder morphology in accordance to Li et al. [38]. The inherent mechanism might be connected to coalescence of multiple boride particles. Measurements of secondary phase fraction area (see also Figure 7.5a) also revealed partial dissolution of the boride phase as f_p significantly decreased from 4.4 ± 0.4 vol% (as-cast, AC) to 3.3 ± 0.2 vol% (HT2). This observation illustrates that the incorporation of the secondary boride phase in Fe_3Al alloys can be controlled by the solidification rate during casting, but may be subject to thermal changes and could require subsequent homogenisation treatments to stabilize their shape.

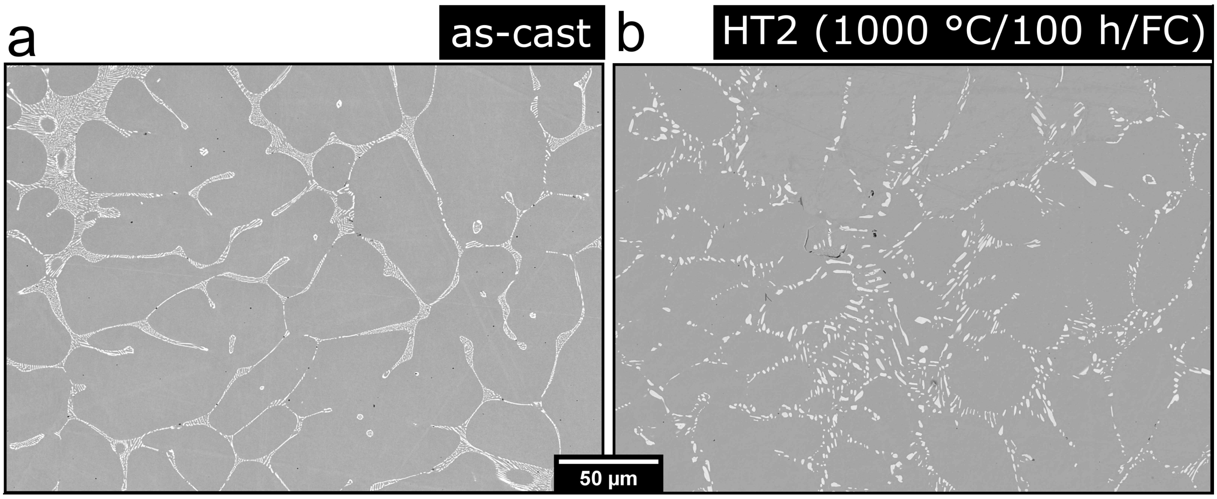

Figure 7.3.: SEM microsections of die-cast Fe-25Al-3.7Mo-0.4Ti-1B: (a) as-cast condition, (b) after homogenisation treatment HT2 (1000 °C/100 h/FC). Adapted from [143].

Besides an effect of solidification rate on the eutectic phase evolution, one must also consider a potential effect of thermal vacancies inside the Fe-Al matrix on mechanical properties. As pointed out in subsection 2.3.1, the concentration of thermal vacancies in iron aluminides mainly varies with Al concentration, temperature and cooling rate after solidification [69, 73]. To verify how strength may be tuned by faster cooling rates during processing and vacancy hardening in quinary Fe_3Al-Mo-Ti-B alloys, step samples annealed at 400 °C for 168 h followed by slow furnace cooling (from here on denoted as HT1) were additionally prepared. Heat treatment is considered to reset

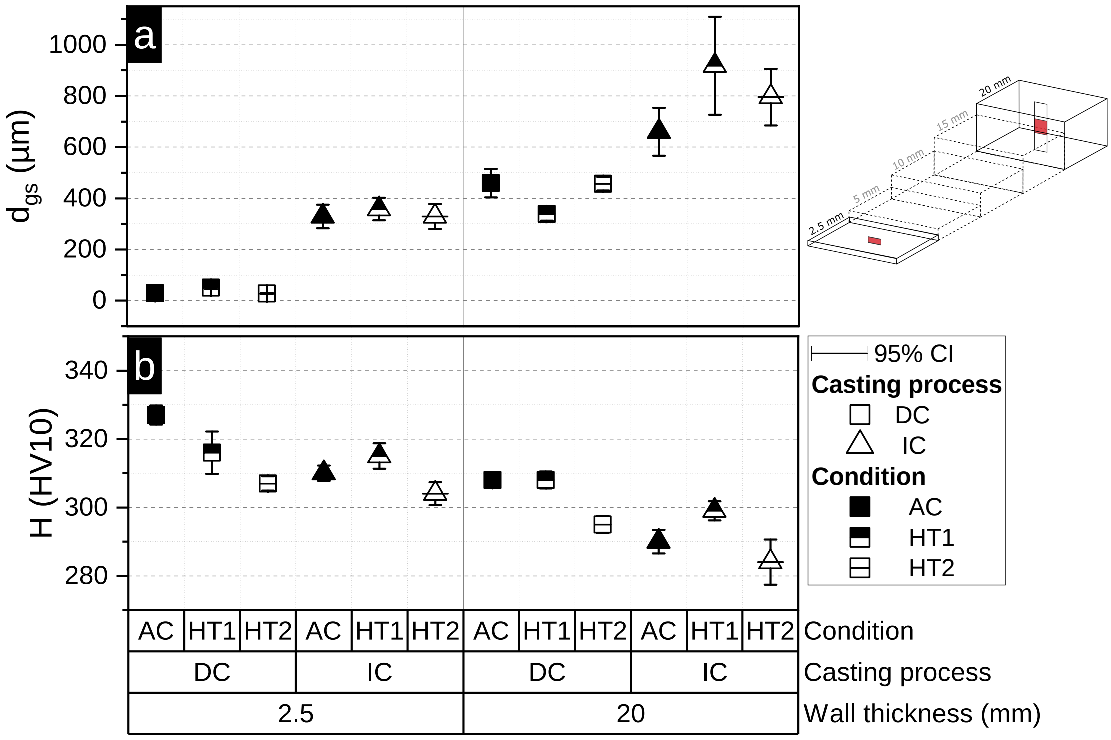

Figure 7.4.: Comparison of average grain diameters d_{gs} (a) and mean macrohardness H (b) of Fe-25Al-3.7Mo-0.4Ti-1B step samples with different wall thicknesses (2.5/20 mm), casting methods (DC/IC) and heat treatments (AC/HT1/HT2). (b) adapted from [143].

any state of frozen-in thermal vacancies after casting. Besides the measurement of macrohardness H, average grain diameters were examined as before to monitor contributions by Hall-Petch strengthening. By comparison of H after HT1 and after casting (AC), hardening contributions by thermal vacancies can be assessed. To reduce the set of parameters for comparison, only minimum (2.5 mm) and maximum (20 mm) wall thickness were considered. The results for IC (squares) and DC (triangles) samples after casting (AC, solid interior), HT1 (half-solid) and HT2 (open) are depicted in Figure 7.4.

With respect to grain sizes, the correlations according to solidification rate can now be easier recognised: with the use of lower wall thicknesses or copper dies, pronounced decreases in average grain diameter d_{gs} may be achieved. By choosing DC, grain sizes in samples with 20 mm wall thickness as were investigated in sections 4.3.2 and 4.3.3 can be lowered to 460 ± 56 µm. By the use of both DC and low wall thickness (2.5 mm) which resulted in a completely fine globular microstructure (see Figure 7.1a), d_{gs} may be even decreased to 28 ± 2 µm. As expected, grain sizes were not affected by both heat treatments and only varied at higher wall thicknesses due to the variability between different castings. Against this, macrohardness values of the set of samples scattered in a limited range of 284 ± 7 HV10 (IC, HT2, 20 mm) and 327 ± 3 HV10 (DC, AC, 2.5 mm). However, analogous to grain sizes, hardness values significantly increased after die casting or within lower wall thicknesses. Hall-Petch strengthening is therefore likely responsible for the observed hardness differences. After HT2, in contrast to prior conclusions for IC, hardness of DC samples decreases compared to the as-cast state by on average 5 rel%. Based on microstructural observations, the hardness decrease may be linked to a reduction of the harder Mo_2FeB_2 phase fraction as Figure 7.5a illustrates. This correlation only applies though if the microhardness of the eutectic phase is more or less constant. Microhardness in the eutectic phase area usually strongly scatters due to the difficulty of probing a dual-phase region with Vickers microindents (see grey data points in the plot and exemplary microsections of Vickers indents in Figure 7.5b). Nevertheless, no significant change of the eutectic phase hardness appears across different sample states. Thus, macrohardness likely scales with the present secondary phase fraction.

After HT1, no comprehensible trend can be drawn from the macrohardness evolution in comparison to the as-cast condition. Mean hardness values across all sample states span a lower range, from 299 ± 3 HV10 (IC, HT1, 20 mm) to 316 ± 6 HV10 (DC, HT1, 2.5 mm), than after casting. To exclude any effect of the eutectic phase on the analysis and because this heat treatment is mainly aimed at controlling matrix properties, HV0.01 microhardness was additionally measured in the Fe_3Al matrix regions. Mean values (in black) are compared in Figure 7.5b.

Here, values scatter between 369 ± 5 HV10 (IC, HT1, 2.5 mm) and 393 ± 4 HV10 (IC, HT1, 20 mm). In comparison to the as-cast condition, two cases are observable: i) at low wall thickness (2.5 mm), microhardness slightly decreases after HT1 (from 388 HV0.01 to 372 HV0.01 on average) as expected by potential removal of thermal vacancies, ii) at high wall thicknesses (20 mm), microhardness increases after HT1 (from 369 HV0.01 to 392 HV0.01 on average). A reason why case ii) is deviating from expectations is not fully trivial. Hence, the hardening contribution by thermal vacancies, which was primarily expected to govern hardness, requires more in-depth investigations. In the following section 7.2, further cross-correlative studies are presented to qualitatively assess the contribution of thermal vacancy hardening in these alloys.

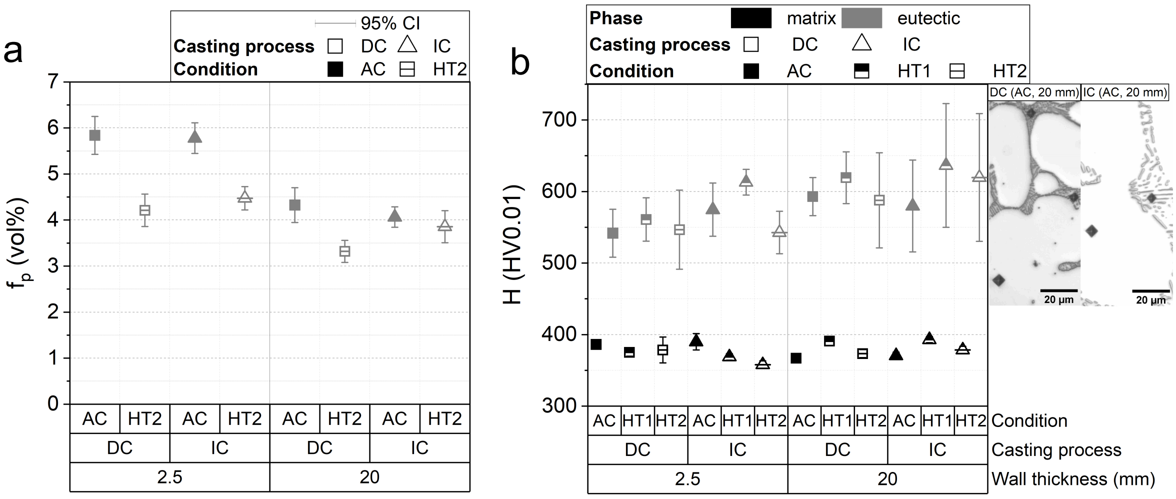

Figure 7.5.: Comparison of average secondary phase fractions f_p of Mo_2FeB_2 particles (a) and mean HV0.01 microhardness H of matrix and eutectic phase (b) in Fe-25Al-3.7Mo-0.4Ti-1B step samples with different wall thicknesses (2.5/20 mm), casting methods (DC/IC) and heat treatments (AC/HT2 in (a) or AC/HT1/HT2 in (b)). (a) adapted from [143].

7.2. Vacancy hardening in quinary and binary Fe-Al alloys

In a first series of experiments, the effectiveness of heat treatment HT1 (400 °C/168 h/FC) to remove thermal vacancies was studied on as-cast Fe-25Al-3.7Mo-0.4Ti-1B alloys from investment and die castings with 20 mm wall thickness. This was done by time-dependent or isothermal dilatometry at 400 °C in air (see Figure 3.3c). Like this, relative length changes $\Delta L/L_0$ as they might appear during annihilation of thermal vacancies can be monitored during thermal conditions similar to HT1. To compare the results to a benchmark, two quasi-binary alloys, Fe-27Al and Fe-37Al, which were oil-quenched (OQ) after sufficiently long annealing at elevated temperatures (OQ1: 700 °C for 100 h, OQ2: 1000 °C for 100 h), were also investigated. Quenching experiments are the most effective option to preserve thermal vacancies at room temperature which might evolve at elevated temperatures. Chemical analysis on quasi-binary alloys by XRF (see Table B.1 in the annex) revealed that small additions of Nb (0.4 at%) and Zr (0.1 at%) are present. This sporadically led to carbide precipitation in both alloys as optical microscopy images confirmed (see Figures B.4a-d in the annex), hence their denotion as quasi-binary alloys. However, minor precipitation should only have a marginal effect on dilatometry as was explained in subsection 4.2.2, so it is fair to deal with both alloys as binary alloys. The dilatometric measurement curves (solid lines) within the first 24 h are displayed in Figure 7.6.

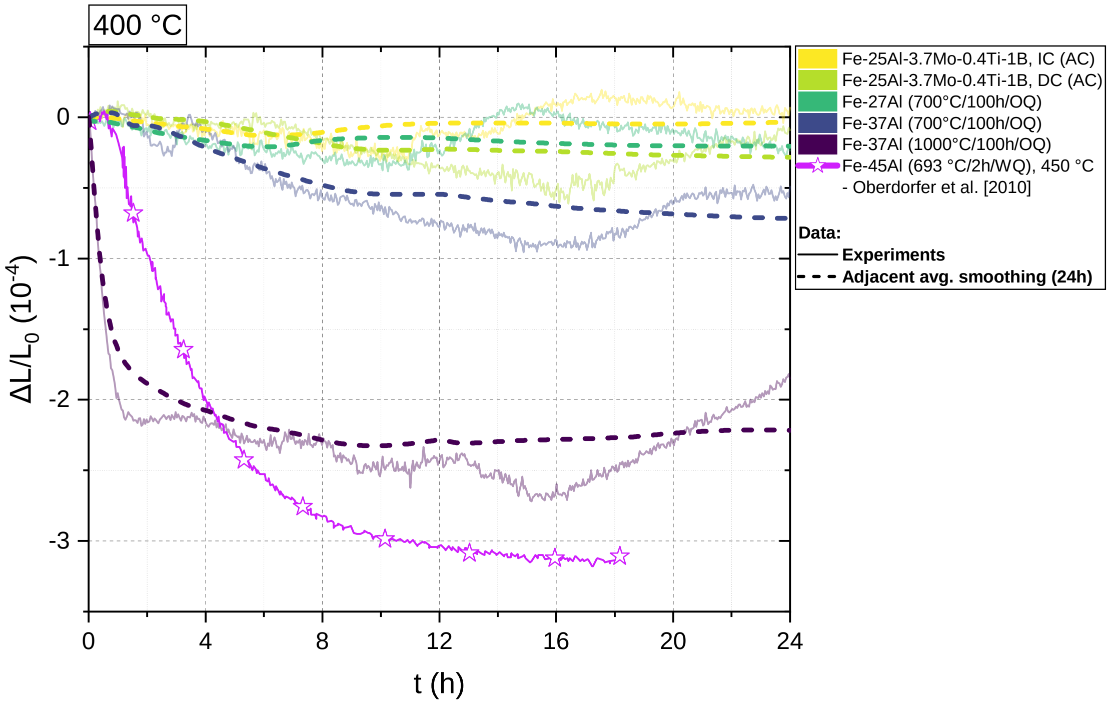

Figure 7.6.: Relative length changes $\Delta L/L_0$ measured at an annealing temperature of 400 °C over time for various quinary and binary alloys with different prior processing history. Experimental and smoothed curves are displayed. Literature data on a water-quenched Fe-45Al alloy is given for comparison [296].

Note that after a usual decline of $\Delta L/L_0$ within the first hours, $\Delta L/L_0$ tends to increase after at least 10 h in all experimental curves. It corresponds to day-dependent increases of the laboratory temperature which also affected the test setup as nearby installed thermocouples verified (data not shown here). As $\Delta L/L_0$ was monitored beyond 24 h, adjacent-average smoothing (dashed lines) was performed on data points within a 24 h window to reveal the general trend of measurement curves. Literature data of Fe-45Al at 450 °C (magenta line with open stars) which was water-quenched after annealing at 693 °C for 2 h is additionally shown for comparison [296]. It gives a baseline for observable relative length changes in iron aluminides amounting here to $-3{\cdot}10^{-4}$ within 10 h. Against this, as-cast Fe-25Al-3.7Mo-0.4Ti-1B alloys (IC: yellow lines, DC: light green lines) only show marginal $\Delta L/L_0$ of clearly less than $-0.5{\cdot}10^{-4}$ which is in the range of induced $\Delta L/L_0$ by laboratory temperature changes. It appears that cooling rates representative of casting processes do not retain significant amounts of thermal vacancies in quinary alloys. However, dilatometric measurements of quasi-binary Fe-27Al (dark green lines) indicate no further gain of thermal vacancies even after oil-quenching from 700 °C. Only for Fe-37Al alloys, signif-

icant relative length changes $\Delta L/L_0$ are observed after oil-quenching. Those amount to nearly -1·10^{-4} after quenching from 700 °C (OQ1, dark blue lines) and -2.5·10^{-4} from 1000 °C (OQ2, dark brown lines). Interestingly, $\Delta L/L_0$ changes more rapidly after OQ2 than OQ1 suggesting a shorter time constant for equilibration at higher quenching temperatures.
In order to analyse the general ability of Fe-25Al-3.7Mo-0.4Ti-1B alloys to retain thermal vacancies at room temperature, measurement methods were extended and only focussed on quenched sample conditions. Due to the setup's susceptibility to laboratory temperature fluctuations, differential dilatometry was employed as a more robust procedure (see Figures 3.3a and b). By the use of a fixed temperature programme with a constant heat rate, external temperature changes do not affect the measurement accuracy anymore. For maximum thermal vacancy concentrations, only quenched sample conditions (OQ1 and/or OQ2) were investigated in both quinary and binary alloys. In comparison to as-cast samples, oil-quenching of thin dilatometer samples with a wall thickness of 5 mm ensured an even higher cooling rate. Both IC and DC samples were prepared according to OQ1 treatment and analysed to also consider different prior processing routes among quinary alloys. The same quenching treatments were chosen for binary alloys. Measurements of $\Delta L/L_0$ in quenched samples during heating and cooling cycles were compared against vacancy-annealed reference conditions (OQ+HT1). To compare and substantiate the results from differential dilatometry, density measurements were additionally performed. Furthermore, the impact by thermal vacancy hardening was assessed by HV0.1 microhardness measurements in Fe-Al matrix phases. Figure 7.7 summarises and contrasts the experimental results of the three analysis techniques.

Differential dilatometry curves of heating cycles up to 700 °C are depicted in Figures 7.7a to d in the top two thirds of each plot. Relative length changes $\Delta L/L_0$ during the first and second heating cycle (black and grey lines respectively) are vertically shifted by a constant value to facilitate the visual distinction between curves of oil-quenched state (solid line with solid triangles) and vacancy-annealed state as a reference (dash-dotted line with open triangles). Additionally, the calculated difference between both curves, $\Delta(\Delta L/L_0) = (\Delta L/L_0)_{OQ+HT1}$ - $(\Delta L/L_0)_{(OQ)}$ (dotted line), is depicted in the lower one third of the plot. A negative value of $\Delta L/L_0$ or a negative gradient represents contraction and a potential loss of thermal vacancies. With respect to DC and IC Fe-25Al-3.7Mo-0.4Ti-1B alloys (Figures 7.7a and b), the progression of oil-quenched (OQ1) and vacancy-annealed (OQ1+HT1) condition during both heating cycles is very similar. The relative length change $\Delta L/L_0$ is continuously increasing as a direct cause of thermal expansion of

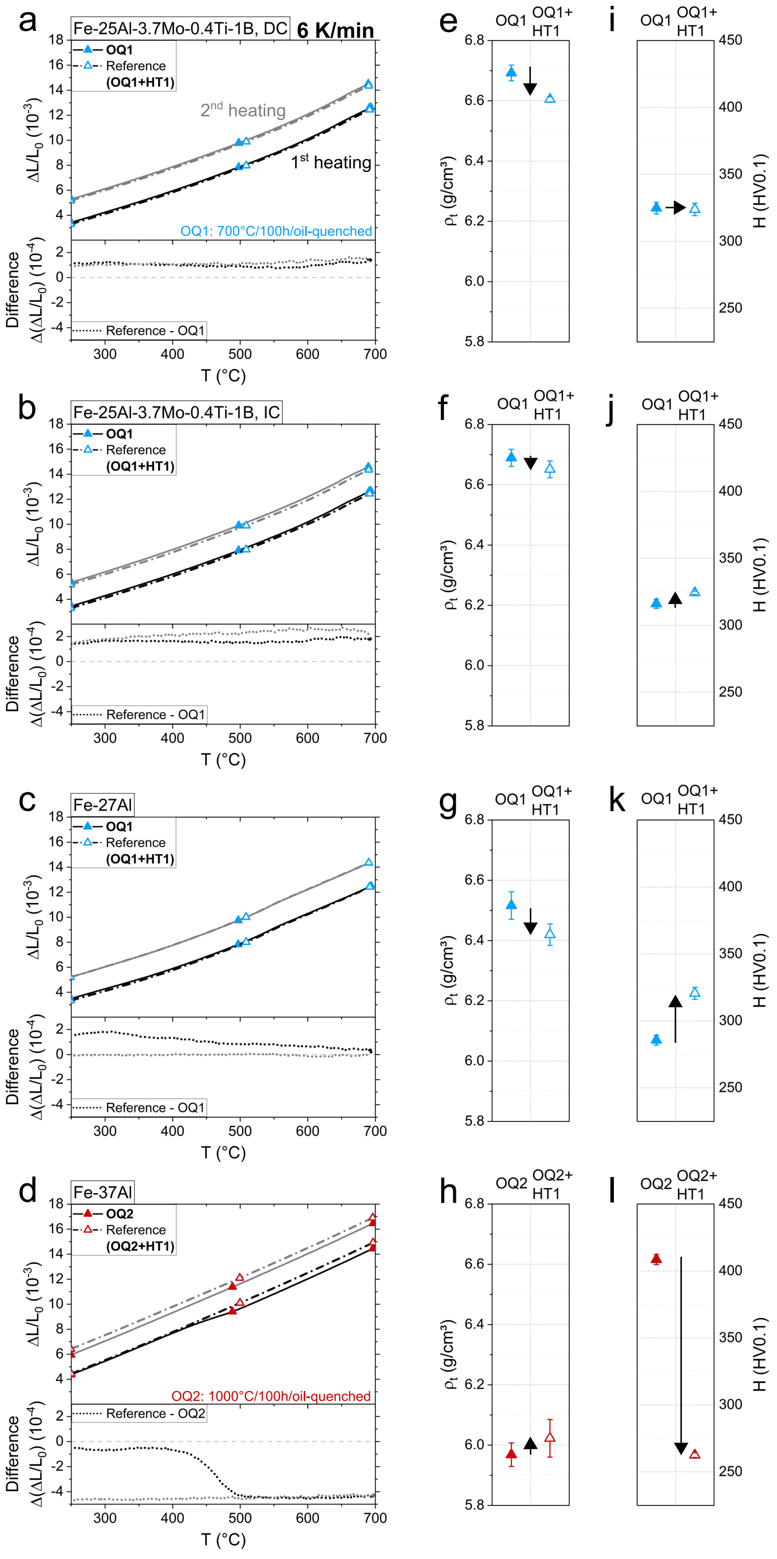

Figure 7.7.: Juxtaposition of three different methods to investigate retained thermal vacancies in various quinary (i.e. die-cast (a,e,i) and investment-cast (b,f,j) Fe-25Al-3.7Mo-0.4Ti-1B) and binary alloys (i.e. Fe-27Al (c,g,k) and Fe-37Al (d,h,l)) after quenching from 700 (OQ1) or 1000 °C (OQ2) and after subsequent vacancy annealing (HT1: 400 °C/168 h/FC): (a-d) differential dilatometry recording the relative length changes $\Delta L/L_0$ over temperature during two heating cycles at 6 Kmin^{-1}, (e-h) true density ρ_t measurements, (i-l) HV0.1 microhardness H measured in the Fe_3Al matrix.

dilatometer samples. Hence, neither negative values, nor a negative gradient of $\Delta(\Delta L/L_0)$ during the first heating cycle nor a change against the second cycle can be recognized. Binary Fe-27Al alloys (see Figure 7.7c) do not show obvious contraction either according to $\Delta(\Delta L/L_0)$, but it is remarkable that the first and second heating cycle deviate. Up to 300 °C, during the first heating cycle, the oil-quenched state has a higher expansion than the vacancy-annealed state, which is followed by a continuous decrease of $\Delta(\Delta L/L_0)$ until maximum test temperature. In contrast, the second cycle is nearly identical for both sample conditions. There is no clear explanation to the observations at lower temperatures. Furthermore, a change of trend for $\Delta(\Delta L/L_0)$ at 300 °C is too low to be reasoned by mobile thermal vacancies [125]. Only binary Fe-37Al (see Figure 7.7d) which was oil-quenched from 1000 °C (OQ2) exhibits a pronounced inflection point at around 480 °C. This corresponds to an irreversible contraction of $\Delta(\Delta L/L_0) = -4{\cdot}10^{-4}$ during the first heating cycle, which is not altered during the second cycle. It therefore reproduces a similar expansion behaviour as was first reported by Schneibel and Munroe [169]. The onset for contraction potentially represents the thermal activation and annihilation of vacancies which remained in the B2 Fe-Al matrix after quenching. The latter experiment also verifies both the validity of the test setup and a potentially higher concentration of thermal vacancies at increased Al concentrations and in B2 Fe-Al alloys.

To further validate the experimental findings, true density measurements were taken after quenching and after vacancy annealing as before. An increased density ρ_t after annealing at higher temperatures signals a removal of thermal vacancies. Results of ρ_t are depicted in Figures 7.7e-h. Interestingly, die-cast Fe-25Al-3.7Mo-0.4Ti-1B (OQ1: 6.69 ± 0.03 gcm^{-3}, OQ1+HT1: 6.60 ± 0.01 gcm^{-3}) and Fe-27Al alloys (OQ1: 6.52 ± 0.05 gcm^{-3}, OQ1+HT1: 6.42 ± 0.04 gcm^{-3}) indicate a decreasing true density after OQ1+HT1. The true density of investment-cast Fe-25Al-3.7Mo-0.4Ti-1B (OQ1: 6.69 ± 0.03 gcm^{-3}, OQ1+HT1: 6.65 ± 0.03 gcm^{-3}) is rather constant. Only ρ_t of Fe-37Al (OQ2: 5.97 ± 0.02 gcm^{-3}, OQ2+HT1: 6.02 ± 0.06 gcm^{-3}), in accordance to conclusions from dilatometry, tends to increase after vacancy annealing (OQ2+HT1), but the difference is within the statistical deviation of measured values.

Before further interpretation, the consideration of microhardness results is worthwhile. They are depicted in Figures 7.7i-l. A decrease of microhardness after HT1 is potentially connected to a loss of thermal vacancy hardening induced by quenching from higher temperatures. In case of Fe-25Al-3.7Mo-0.4Ti-1B alloys, microhardness is nearly unchanged for die-cast samples (OQ1: 325 ± 4 HV0.1, OQ1+HT1: 324 ± 5 HV0.1) or slightly increased for investment-cast samples

(OQ1: 316 ± 3 HV0.1, OQ1+HT1: 324 ± 1 HV0.1) after vacancy annealing. An even larger increase is registered for Fe-27Al alloys after quenching from 700 °C followed by vacancy annealing (OQ1: 286 ± 4 HV0.1, OQ1+HT1: 321 ± 4 HV0.1). Again, only Fe-37Al conforms to the analogy of thermal vacancy hardening and shows a drastic decrease of microhardness after vacancy annealing (OQ2: 409 ± 4 HV0.1, OQ1+HT1: 263 ± 2 HV0.1).

Especially in contrast to Fe-37Al alloys, the three methods cast doubt on a significant contribution by thermal vacancy hardening in Fe-25Al-3.7Mo-0.4Ti-1B alloys. While the results of differential dilatometry and microhardness measurements show no clear difference between the quenched state and the vacancy-annealed state, results of density appear misleading, e.g. true densities of die-cast Fe-25Al-3.7Mo-0.4Ti-1B (see Figure 7.7e) even decrease after vacancy annealing. This observation does not correspond to a plausible correlation with how thermal vacancy concentrations evolve after annealing at 400 °C. Generally speaking, no significant increases of density were observed in any of the investigated alloys although some alloys (i.e. Fe-37Al) experience considerable changes in microhardness. It is well known that bulk density measurements are prone to uncertainty due to cracking or residual porosity, which was partially observed after casting and induction melting [75, 297]. Even though density samples in OQ and OQ+HT1 state were extracted adjacent to each other from initial samples, variances in processing quality may contribute to the observed differences. These effects should have a lesser impact on the other two methods.

However, it shall be noted that quenching experiments from 1000 °C which were also conducted on all alloys generally indicate larger microhardness values compared to a quenching temperature of 700 °C. Both conditions can be compared as solid blue (OQ1) and red (OQ2) triangles in Figure 7.8 (see Table B.2 in the appendix for all values). This is in line with quenching experiments from Hasemann et al. [298] as well as Morris et al. [299] on Fe-Al alloys with similar Al concentrations. This correlation was usually explained that higher thermal vacancy concentrations exist at higher temperatures. Yet, the achievable hardness of Fe-25Al-3.7Mo-0.4Ti-1B (339 HV0.1) and Fe-27Al alloys (327 HV0.1) after quenching from 1000 °C is far less than in Fe-37Al alloys (409 HV0.1). Furthermore, microhardness of Fe-25Al-3.7Mo-0.4Ti-1B and Fe-27Al alloys is mostly unchanged and sometimes even increased after subsequent vacancy annealing. This is contrary to the usually expected decrease of strength which depicts a necessary criterion for the original presence of thermal vacancies. This was demonstrated for Fe-37Al alloys after both quenching temperatures. If at least minor amounts of thermal vacancies are present in Fe-

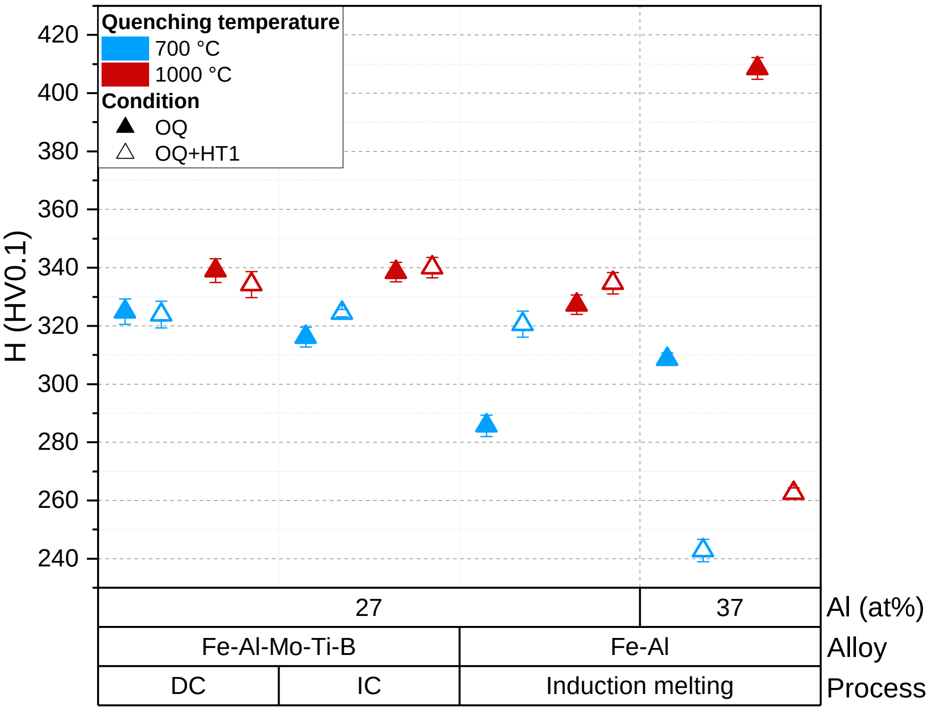

Figure 7.8.: HV0.1 microhardness and 95% CI measured in the Fe_3Al matrix of quinary and binary alloys after quenching from 700 °C (OQ1) or 1000 °C (OQ2) and after subsequent vacancy annealing (HT1: 400 °C/168 h/FC).

25Al-3.7Mo-0.4Ti-1B alloys, two aspects might affect the ambiguous experimental findings: i) the interaction of thermal vacancies with solutes in the Fe_3Al matrix, ii) overlapping hardening mechanisms influenced by thermal treatments.

With respect to solute elements, only few studies were published on the interaction of transition metal elements with thermal vacancies in iron aluminides and mainly targeted near-FeAl alloys [79–81]. For ternary additions of Ni, multiple researchers found a decreasing influence of thermal treatments on equilibrium hardness as it is reached after similar low-temperature annealing as HT1. This was explained by a strong attraction of vacancies to Ni solutes. These form solute-vacancy complexes which can trap further thermal vacancies and build less temperature-sensitive agglomerated voids. High concentrations of other transition metal solutes such as Cu, Co and Cr also yielded a reduced susceptibility to thermal vacancy hardening [81]. Hence, a similar mechanism could exist in quinary alloys with especially high concentrations of Mo solutes in the Fe_3Al matrix. This could be explained based on the binding energies between solute atoms and vacancies. Binding energies within pairings of different transition metal elements and vacancies were computed by Kuriplach et al. [300] in Fe b.c.c. lattices with ab-initio calculations. They found generally high attractive binding energies of various solutes and no difference between Mo and Ni solutes. Vacancies on Fe sublattices should also be the most probable vacancy type here as their formation energies are usually lower than on Al sublattices, independent of ordered structure [301, 302]. Mo-vacancy complexes could therefore explain the similarity of OQ and OQ + HT1 states in dilatometric and hardness measurements. However, no experimental proof of the formation of transition metal solute-vacancy complexes was given in iron aluminides so far.

Still, the exceedance of quenched hardness after low-temperature annealing HT1 as it was observed for as-cast Fe-25Al-3.7Mo-0.4Ti-1B alloys in prior HV0.01 microhardness measurements in section 7.1 cannot be solely justified by solute-vacancy interactions. Instead, multiple strengthening contributions may be affected by cooling conditions and heat treatments, especially for iron aluminides close to Fe_3Al stoichiometry [298]. Samples with different cooling rates might produce different anti-phase domain (APD) sizes which build during ordering reactions at $T_c^{B2 \leftrightarrow A2}$ and $T_c^{D0_3 \leftrightarrow B2}$. In turn, these can cause different amounts of domain hardening [303]. Accordingly, rapidly cooled samples with 2.5 mm wall thickness should develop a finer APD network after casting and a higher strength than slowly cooled samples with 20 mm wall thickness. As this conclusion applies, domain hardening might be a complementary approach to the hardness difference of as-cast samples with different cooling rates apart from vacancy hardening. However, domain hardening alone cannot explain why hardness values of samples with different wall thicknesses are nearly reversed after HT1. Annealing at 400 °C for sufficiently long times should equally revoke domain hardening effects for both wall thicknesses as APDs are growing, which is usually accompanied by decreasing strength [49, 62]. Therefore, the effect of long-range order (LRO) on strength could play a decisive role here. It was demonstrated that an annealing temperature of 400 °C was most effective in regenerating LRO in Fe-24.8Al after quenching [304]. This effect alone does not reason the observed differences, but a combination with the related effect of "thermal memory" in Fe-Al alloys could substantiate the LRO effect. It was first reported by Lawley and Cahn in Fe-(23-27)Al alloys [304]. They basically ascribed different abilities of alloys to establish LRO on their thermal history. They reported lower achievable degrees of order at room temperature when alloys were rapidly cooled below $T_c^{D0_3 \leftrightarrow B2}$ compared to being slowly cooled (less than 3 Kmin^{-1}). This was still true when alloys were re-annealed just above $T_c^{D0_3 \leftrightarrow B2}$, held for a few hours and slowly cooled to room temperature, therefore keeping a thermal memory.

Transferred to the alloys investigated here, samples with lower wall thickness and rapid cooling could establish a lower LRO after HT1 than alloys with higher wall thickness and slow cooling. The implications of this difference are not straight forward, but may be explained as follows: Lower LRO or a lower degree of $D0_3$ order may imply a higher degree of B2 order [55]. This has a decisive consequence on the ease of superdislocation motion. Despite the dominance of $D0_3$ order, it was shown by several authors that perfect $D0_3$ superdislocations are nearly absent in $D0_3$ superlattices at room temperature due to insufficient thermal activation [54, 305]. Instead, imperfect $D0_3$ superdislocations which correspond to perfect B2 superdislocations were found in hyperstoichiometric Fe_3Al [54]. The ease of movement during deformation is essentially dependent on the superlattice type. While B2 superdislocations move under low stresses through a B2 superlattice, they trail an APB in $D0_3$ superlattices, which requires higher stresses [50]. Considering all aspects together, a higher fraction of B2 order or lower LRO which is assumed for samples with 2.5 mm wall thickness due to thermal memory effects may result in a lower strength than for samples with 20 mm wall thickness and a higher LRO. Hence, both the reduction of domain hardening and the LRO build-up during annealing as well as thermal memory effects from different casting methods may be responsible for the hardness reversal after HT1.

In summary, the thermal vacancy hardening effect in quinary Fe-25Al-3.7Mo-0.4Ti-1B alloys may be less developed than in binary Fe-Al alloys with higher Al concentrations but, in turn, appears less temperature-sensitive due to its solute additions. Consequently, the investigated alloys can be easily exposed to low-temperature heat treatments without expecting major decreases in strength if thermal post-processing is required.

7.3. Effects of grain refinement on tensile behaviour

The potential of the immediate correlation between solidification rate, grain diameter and hardness derived from Figure 7.2 in section 7.1 is close at hand: casting strategies with higher cooling rates can minimize the average grain size and thereby improve mechanical properties. The underlying strengthening mechanism known as Hall-Petch strengthening could positively affect both strength and ductility at room temperature [295, 306, 307]. Grain refinement usually achieves higher strengths by two causes: the pile-up length for dislocations decreases and the accommodation process of neighbouring grains is hampered as more glide systems need to be activated for deformation [308]. In effect, both increase the required stress to induce plastic flow. Its advantage is that ductility is usually not negatively affected, but can be even enhanced by an increasing strain rate sensitivity [307]. Both room temperature strength and ductility are critical parameters of the investigated quinary Fe-25Al-3.7Mo-0.4Ti-1B alloys which were lacking in performance under tensile loading (see Table 4.5). Therefore, it is fundamental to understand how far grain refinement can overcome the alloy's attested brittleness at ambient conditions. For this goal, the mechanical performance of Fe-25Al-3.7Mo-0.4Ti-1B alloys with different average grain sizes was compared under tensile loading at room temperature.

Tensile specimens with the lowest grain size achieved in prior processing (i.e. DC, AC, 2.5 mm wall thickness: 28 µm) were produced to examine the reach of strength and ductility increase. For this goal, a shift to miniature specimens with rectangular cross-section was necessary (see Figure A.5c). Furthermore, the use of digital image correlation (DIC) allowed a more thorough investigation of localized strains to gain insights into the alloy's macroscopic deformation behaviour at room temperature. As the actual strain rate cannot be controlled by DIC, a constant crosshead speed was applied. Crosshead speed was iterated in trials to achieve a target strain rate of $2.5{\cdot}10^{-4}$ s^{-1} (±10%) after yielding in accordance to other tensile tests. For calculation of specimen elongation e after mechanical testing, a virtual extensometer with an original gauge length of $L_0 = 10$ mm was centered along the flat side of the specimen. The chosen value of L_0 was below the minimum standard value [183], which affects the uncertainty of elongations after fracture A. To gain more statistical significance, five tests were conducted with this geometry.

The stress-strain curves of miniature tensile specimens were compared against tensile test data of as-cast IC and homogenised DC specimens with lower dimensions representing larger average grain diameters d_{gs} (previously presented in Figure 4.25). Figure 7.9 contrasts them in a line graph. The average values for $R_{p0.2}$, R_m and A including 95% CIs if applicable are summarised in Table 7.1.

As-cast IC specimens with the largest average grain size ($d_{gs} = 660$ µm, black line) exhibit the lowest mechanical performance with negligible ductility. Although the die-cast homogenised specimen with lower average grain size ($d_{gs} = 457$ µm, blue line) exhibits a comparable onset of yielding as the as-cast IC specimen, it continues to deform up to $A = 0.5\%$. Accordingly, mechanical strength ($R_{p0.2} = 290$ MPa, $R_m = 340$ MPa) is clearly increased. With respect to as-cast DC miniature tensile specimens with a more than ten times lower grain size ($d_{gs} = 28$ µm, red line), no further gain in ductility is noticed ($A = 0.3 \pm 0.1\%$). However, both $R_{p0.2}$ (+35%) and R_m (at least +18%) are even more increased compared to homogenised DC specimens. The selected specimen design was proven to be reliable as the mean values gathered from five samples ($R_{p0.2} = 392 \pm 3$ MPa, $R_m = 401 \pm 28$ MPa) only scatter marginally. With respect to strength under tensile loading, it can be concluded that higher solidification rates and grain refinement can positively tune mechanical properties of quinary alloys. It also agrees with the correlation of lower average grain sizes and higher HV10 macrohardness as was shown in Figure 7.4. Consequently, clear signs of Hall-Petch strengthening are visible.

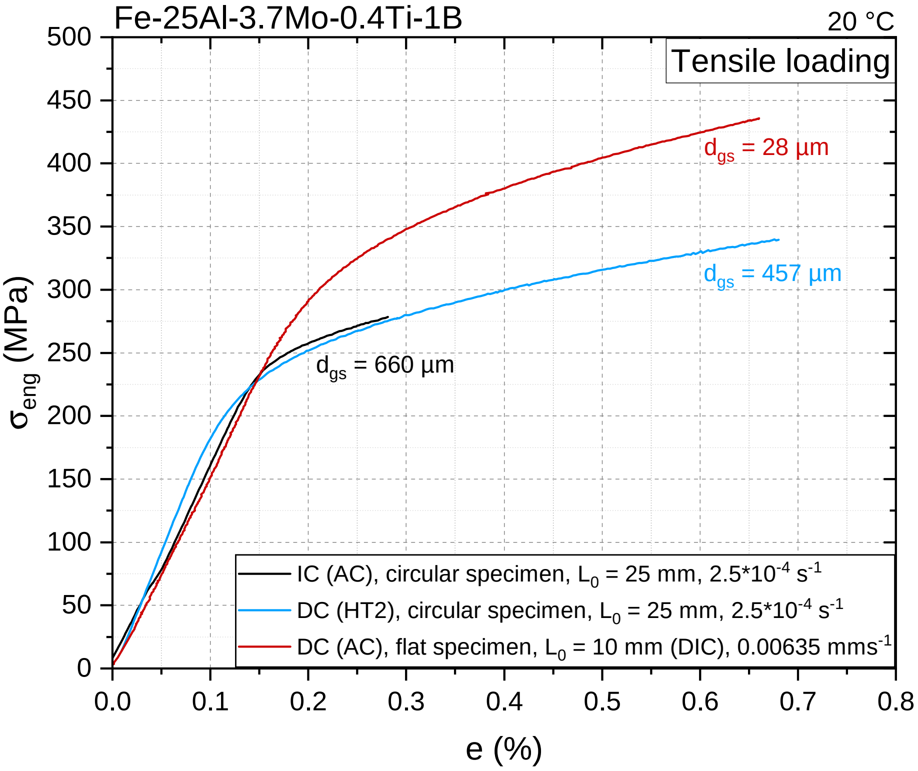

Figure 7.9.: Engineering stress-strain curves of small and miniature tensile specimens of Fe-25Al-3.7Mo-0.4Ti-1B with different average grain diameters d_{gs} at room temperature. Information on processing condition, specimen specification and strain rate during testing is given in the legend.

To get an understanding of the scale of Hall-Petch strengthening in the investigated alloy, the Hall-Petch coefficient k from equation (7.1) can serve as a comparative value as it describes the scaling of hardness with grain size. For the determination of k, other strengthening contributions need to be kept constant. Yet, they might fluctuate as a result of different cooling rates which were needed to generate different grain sizes. Strength differences by thermal vacancy hardening were only marginal (see sections 7.1 and 7.2). Against this, hardness values mostly changed after

Table 7.1.: Mean tensile properties and 95% CI (if applicable) at room temperature of several Fe-25Al-3.7Mo-0.4Ti-1B alloys with different average grain diameters d_{gs}.

Tensile sample specification	Sample count	d_{gs} (µm)	$R_{p0.2}$ (MPa)	R_m (MPa)	A (%)
IC (AC), circular, $L_0 = 50\,\mathrm{mm}$, $d_0 = 10\,\mathrm{mm}$	5	660	-	252 ± 14	0.10 ± 0.04
IC (AC), circular, $L_0 = 25\,\mathrm{mm}$, $d_0 = 5\,\mathrm{mm}$	1	660	-	278	0.1
DC (HT2), circular, $L_0 = 25\,\mathrm{mm}$, $d_0 = 5\,\mathrm{mm}$	1	457	290	340	0.5
DC (AC), flat, $L_0 = 10\,\mathrm{mm}$, $S_0 = 1\,\mathrm{x}\,2.5\,\mathrm{mm}^2$	5	28	392 ± 3	401 ± 28	0.3 ± 0.1

homogenisation treatment HT2 (see Figure 7.4). As the average grain size was almost constant after annealing, the Hall-Petch relationship can be estimated from hardness values of homogenised samples. A regression of the hardness data can be found in Figure B.5 in the appendix. A Hall-Petch constant of $k = 811$ MPa·µm$^{0.5}$ could be determined from the slope. This value compares well with previous studies on B2 Fe-34Al, which stated a constant of 620 MPa·µm$^{0.5}$. Unfortunately, the available data from tensile tests in Table 7.1 is not sufficient to derive a reliable value of k, but a regression of $R_{p0.2}$-d_{gs} value pairs from die-cast tensile specimens (not shown here) points towards a similar order of magnitude. TEM investigations to examine dislocation structures and pile-ups in different grain sizes would be necessary to verify the mechanism, but were out of scope for this study.

It shall be emphasized that it may be also possible that the positive effect by grain refinement is also overlapped by a more favourite arrangement of borides. As conclusions from fractography of tensile-tested IC specimens suggested (see Figure 4.12a), boride phase boundaries may pose easy paths for crack propagation or even crack initiation sites. Hence, the higher solidification rate of die casting and the subsequent homogenisation treatment may create a more ductile design and arrangement of secondary phase particles, which are smaller in size and rounder in shape. This morphology could induce less stress concentrations at phase boundaries and reduce the brittle response under tensile loading with consequently higher ultimate tensile strengths. In sum, the positive impact by processing with higher solidification rate is unambiguous and can clearly enhance the mechanical performance of the investigated Fe-25Al-3.7Mo-0.4Ti-1B alloy at ambient conditions. Yet, the required wall thickness to achieve the lowest average grain size with casting strategies and the higher cracking probability with higher solidification rates raises questions to which extent this strengthening mechanism can be exploited in practical applications.

With regard to the achievable plasticity however, the effectiveness of grain refinement is rather poor. The investigation of miniature tensile specimens with DIC allowed more thorough insights into why deformation may be limited. With the aid of full-field analysis by DIC, local strains across the flat side of the gauge section were monitored during tensile loading. Figure 7.10 displays the stress-strain curve from before (Figure 7.10a) along with two illustrations of local strain data (note that the local strain e_x usually depicts the strain along the specimen or loading direction). One is resolving e_x on a line, which is situated on the flat side of the gauge section and is adjacent to one of the outer edges (see Figure 7.10b). The level of e_x can be derived from the colour bar. The local strain e_x is also synchronized to the applied strain e from the tensile curve measuring the total specimen strain. Like this, local changes of e_x on the line can be directly assigned to the deformation stage in the stress-strain curve. The second illustration displays 2D strain maps of the flat side of the gauge section at distinct stages of applied strain e (see Figure 7.10c). The same colour coding of e_x is applicable as before. After only $e = 0.2\%$, wavy strain lines already spread across the full gauge section surface as 2D maps show. At a few spots, local strain concentrations are visible within the gauge centre. With increasing e, they only grow marginally in size, but rather increase in strain level (up to ~1.5% until rupture). Yet, even higher strain concentrations appear starting from the left edge. They all form after the onset of plastic deformation and almost instantly grow a few mm into the centre. The first one already develops after the onset of yielding at x = ~2.5 mm (see Figure 7.10b) and reaches a local strain e_x of more than 5%. Magnifications of the 2D mapped area around the maximum strain peak (see orange dashed circles in 7.10c) indicate that it built from a sharp surface defect which was already present during initial loading. Although the strain concentration with strain levels of more than 2% stays confined, it radially affects the strain lines and condenses the surrounding strain field. Surprisingly, the specimen failed near the bore holes and not at the maximum strain peak. Figures 7.11a and b depict OM images of the sample before and after tensile testing. Presumably, a defect on the bottom edge of the right fixture might have caused premature failure. Still, as the gauge section remained intact, post-investigation could be conducted on the maximum strain peak. Figure 7.11c is an SEM image with an inclined view on the edge close to the strain concentration determined by DIC. Note that the two adjacent surfaces, the flat side and the on-edge side, show different profiles: the on-edge side was removed from EDM wire cutting and the flat side was ground to target thickness

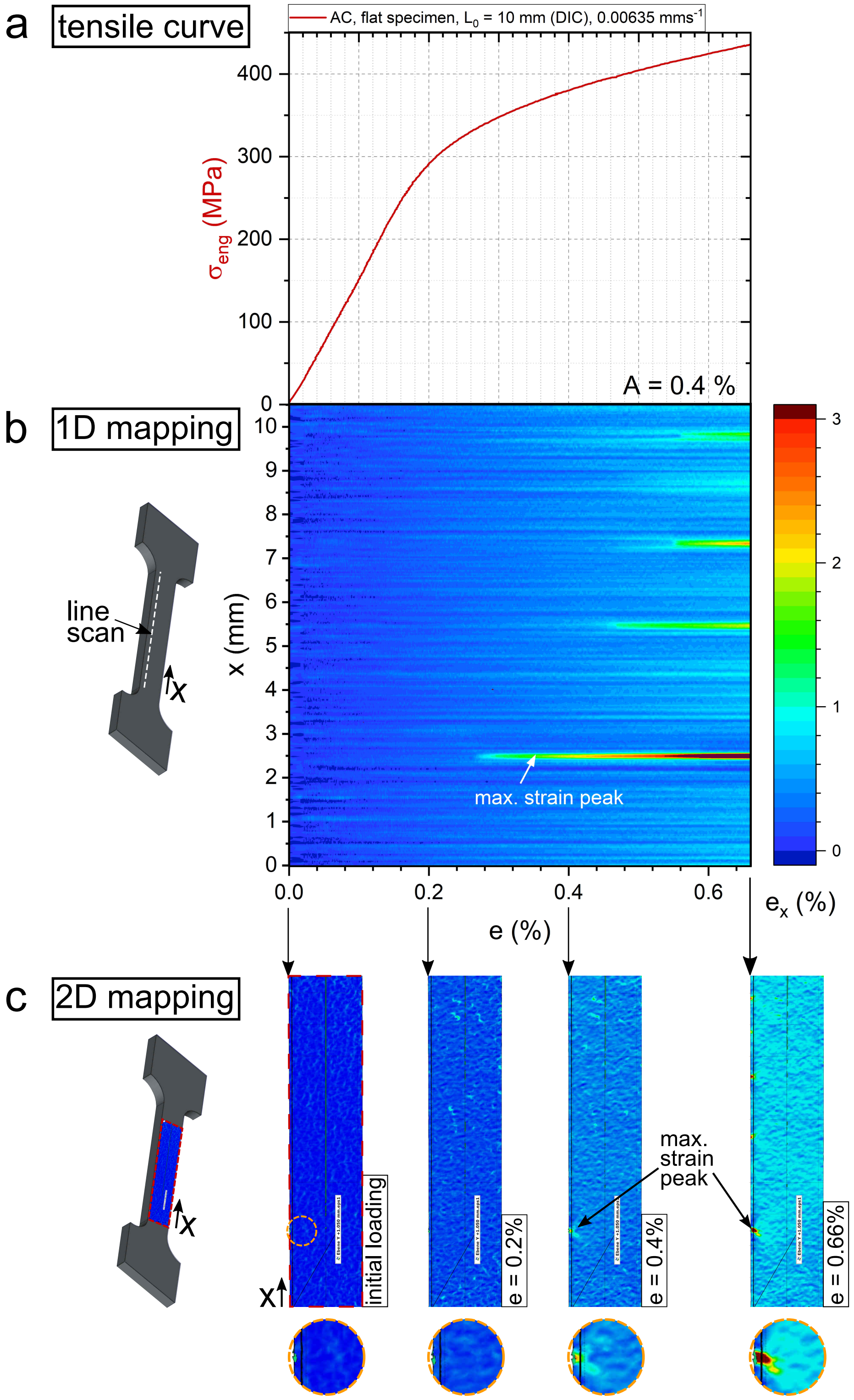

Figure 7.10.: (a) Stress-strain curve of an as-cast Fe-25Al-3.7Mo-0.4Ti-1B miniature tensile specimen, (b) 2D colour plot of local strain e_x measured and analysed by DIC line scanning on the flat gauge section as a function of line position x and the applied strain e, (c) DIC 2D maps of the flat gauge section and magnifications of the maximum strain peak at x = ~2.5 mm at distinct applied strains e.

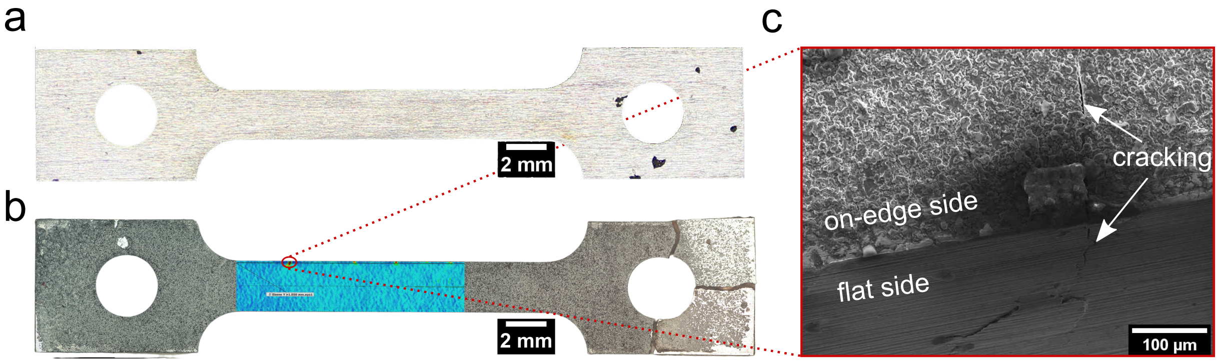

Figure 7.11.: Optical images of the die-cast Fe-25Al-3.7Mo-0.4Ti-1B miniature tensile specimen (a) before tensile testing and (b) after fracture, (c) inclined view and magnification of the maximum strain peak at x = ~2.5 mm after fracture by SEM.

after blade cutting. Clearly, a crack can be recognized running on both sides. Dye penetrant inspection did not indicate any prior cracking at this location. It potentially originated from the mentioned edge defect which appears here as a surface elevation. No further investigation was conducted to determine the origin of the defect. Still, the occurence of a crack explains the high local strain levels measured by DIC 1D mapping. Similar investigations on other samples revealed that these strain concentrations (and presumably evolving cracks) can grow even larger and lead to fracture (not shown here). The cracking behaviour is certainly influenced by the rectangular tensile specimen design as edges pose locations of stress concentrations, which need to be avoided in brittle materials if possible. Yet, the case also highlights the alloy's sensitivity to surface defects and environmental embrittlement. This is connected to the conclusions from early works by Liu and Stoloff [110, 111] that air and humid conditions negatively affect the ductility of iron aluminides at room temperature. Additional alloying with Mo and Ti in the investigated quinary alloy might enhance the ease of crack propagation if cracks have already formed. The immediacy of crack evolution indicated by DIC measurements and the predominantly transgranular cleavage mode (see Figure 4.12a) support this theory. In accordance to conclusions from chapter 5, a reduction of solute alloying content would be necessary to significantly enhance ductility.

Chapter

8 Conclusions and outlook

The goal of this work was to examine the potential of an investment-cast Fe-26Al-4Mo-0.5Ti-1B alloy for use in high-temperature applications. Therefore, the investigations mainly aimed at exploring the alloy's mechanical performance under quasi-static tensile and creep loading, which are critical scenarios to verify a material's safe employment under these conditions. A comprehensive dataset of mechanical properties up to 700 °C was generated, which was complemented by characterisation of microstructural characteristics and thermophysical properties. This complete alloy characterisation both enabled a holistic and coherent portrayal of properties achieved by an industrially relevant casting method (i.e. centrifugal investment casting) and a deeper understanding of the alloy's limitations and areas for improvement. With a focus on alloy development, multiple studies of alloy composition, casting strategies and thermal treatments were followed-up to identify effective variables along the process chain to tweak mechanical properties. The investigations also aimed at putting strengthening contributions such as solid-solution hardening, grain refinement as well as thermal vacancy hardening into context. The main conclusions on the investigated alloy system are broken down below before giving a final comparison to P92 steel as a benchmark and an outlook on further research topics.

Characterisation of investment-cast Fe-25Al-3.7Mo-0.4Ti-1B

Microstructure

The Fe-25Al-3.7Mo-0.4Ti-1B alloy, produced by centrifugal investment casting with a 20 mm wall thickness, has a two-phase microstructure. It consists of a $D0_3$ Fe_3Al matrix and a tetragonal Mo_2FeB_2 secondary phase with a volume fraction of $f_p = 4$ vol%. The matrix is a hyperstoichiometric Fe-27Al solid solution with Mo (2.4 at%) and Ti (0.4 at%) solutes, while the secondary phase indicated compositional fluctuations of the main elements and additions of Ti and Al. The microstructure features a dendritic solidification structure with interdendritic eutectic areas containing lamellar µm-sized particles. The average grain diameter d_{gs} is 660 µm, with a log-normal distribution ranging from a few µm to 3 mm and a median value of 188 µm.

Mechanical properties

- **Quasi-static tensile properties:** At room temperature, Fe-25Al-3.7Mo-0.4Ti-1B shows a brittle behaviour only reaching low average tensile strengths of $R_m = 252$ MPa with poor ductility, failing before reaching the 0.2% proof strength. Transgranular cleavage fracture and occasional cracking within eutectic phase areas is observed to dominate up to 550 °C. The presence of Mo and Ti solutes in the matrix was suggested to be mainly responsible for the brittleness at low and intermediate temperatures although the large grain sizes and eutectic borides as cracking sites can also contribute to the fracture mode.

  At 650°C, fracture behaviour shifts to a mixed fracture mode with transgranular cleavage and predominantly ductile fracture which is accompanied by large elongations of $A > 30\%$ and extensive necking. Accordingly, the brittle-to-ductile transition temperature was estimated to be $T_{BDT} > 550$ °C, although the conventional definition by $A > 3\%$ was already found between 450–550 °C. The yield stress anomaly with a maximum 0.2% proof strength of $R_{p0.2} = 347$ MPa occurs at $T_{YSA} = 550$ °C.

  In comparison to alloys with lower solute concentrations, the quinary alloy can maintain higher $R_{p0.2}$ values above T_{YSA}. Below T_{YSA}, a considerable tension-compression asymmetry (TCA) was observed which explained the strength difference to a similar alloy composition from literature. Own data on compressive and tensile 0.2% proof strengths indicated a minimum strength difference of nearly 100 MPa at room temperature, which was similarly found in other iron aluminide alloys.

- **Creep properties:** The creep behaviour of Fe-25Al-3.7Mo-0.4Ti-1B alloy was investigated under constant load and temperature. The three investigated temperatures (600 °C, 650 °C, 700 °C) covered a homologous temperature range of $0.5–0.56 T_{liquidus}$ across the order-order reaction temperature $T_c^{D0_3 \leftrightarrow B2}$, whereas applied loads (40—240 MPa) yielded a σ_0/G ratio range of $9 \cdot 10^{-4}$ to $5 \cdot 10^{-3}$.

  The alloy only showed a short primary creep stage of $e_{ft} < 1.5\%$ or $t < 50$ h presumably due to prior homogenisation treatment at 1000 °C. Most of them exhibited a local minimum creep rate $\dot{e}_{ft,min}$ representative for inverse transient creep behaviour. The secondary creep stage did not evolve into steady-state creep, but a limited regime of constant creep rate $\dot{e}_{ft,ss}$ of a few hours to less than 200 h. An activation energy of creep Q_c of 362 ± 24 kJ·mol^{-1} was determined at $\sigma_0 = 120$ MPa which was comparable to near-Fe_3Al alloys and Fe-Al solid solutions with Mo in literature.

At most temperatures and stresses, the alloy indicates class A (alloy-type) creep behaviour, which was proven by inverse transient behaviour during primary creep and Norton stress exponents of $n \leq 4.1$. A power law breakdown was hypothesised for 600 °C ≥ 240 MPa and for 650 °C ≥ 200 MPa indicated by normal transient behaviour during primary creep and a slightly deviating progression from Norton law.

Creep rates at 650 °C were almost an order of magnitude higher than a similar alloy reported from compressive creep tests. The difference was also attributed to a TCA effect, which has never been reported for Fe-Al alloys. No sharp increase of creep rates was noticed upon increasing temperatures above $T_c^{D0_3 \leftrightarrow B2}$. As stress exponents n only slightly vary, a change of creep mechanism may not be evident. However, an effect of Mo and Ti solutes stabilising fractions of $D0_3$ ordered domains above $T_c^{D0_3 \leftrightarrow B2}$ has been suggested. Comparison to similar binary and alloyed Fe_3Al alloys with TiB_2 and with or without Mo additions from literature allowed the conclusion that creep resistance is both enhanced by solid-solution hardening and particle hardening. Particles might have a lesser impact due to large particle sizes and distances though, which was estimated by calculations for Orowan strengthening.

Creep failure was dominated by ductile transgranular fracture with extensive necking, but also showed clear signs of cavity chain formation. Different shapes and states of cavities were often found adjacent to eutectic borides. It was concluded that borides could act as main cracking sites during creep. Position-resolved and mean values of cavity diameter, cavity fraction and cavity density were gathered from OM image analysis of longitudinal macrosections. In general, cavity nucleation and growth was highest within the necking region, but cavity growth was also present in the rest of the gauge sections. Creep tests at 700 °C/120 MPa exhibited a significantly higher creep damage although tests at 650 °C/200 MPa yielded similar constant creep rates and elongations after creep fracture. It was speculated that B2 ordering might enhance creep damaging mechanisms in Fe-25Al-3.7Mo-0.4Ti-1B alloys.

Alloy development of Fe-Al-Mo-Ti-B alloys

Effect of alloy composition

Different alloy compositions were explored after investment casting. For that, nominal alloy concentrations of Mo (2 and 4 at%) and B (0.5 and 1 at%) were changed for two quinary Fe-Al-Mo-Ti-B alloys with hyperstoichiometric (27 at%) and hypostoichiometric (24 at%) Fe_3Al matrix composition. The microstructures of all alloys is comparable to the investigated base alloy in that it mainly consists of a near-Fe_3Al dendritic matrix and mainly Mo_2FeB_2 secondary phase particles arranged in eutectic phase seams. Average grain sizes stayed at a large level (586–876 µm) and were assumed to rather vary with casting process than by varying Al, Mo, and B concentrations. However, phase compositions and fractions correlated in a comprehensible way with nominal alloy additions. The elemental phase compositions vary similarly below and above ideal Fe_3Al stoichiometry when Mo and B concentrations are adjusted. The Mo solute concentration in the Fe_3Al matrix and the volume fractions of secondary phases scale with nominal Mo concentration. Moreover, lower Mo additions lead to Ti enrichment in Mo_2FeB_2 particles, regardless of B content. As the Mo content decreases, the volume fraction of the minor TiB_2-type phase, partially with acicular morphologies, increases, but below significant amounts (< 1 vol%). A reduction in B content decreases the secondary phase fractions, causing slight increases in the Mo and Ti solute concentrations in the matrix. Correlations of alloy concentrations and phase transitions were derived by DTA. The known principle of increasing order-order $T_c^{D0_3 \leftrightarrow B2}$ and order-disorder $T_c^{B2 \leftrightarrow A2}$ transition temperature with increasing Mo and/or Ti solute concentration was confirmed, even for marginal concentration changes. Furthermore, $T_c^{D0_3 \leftrightarrow B2}$ of quinary alloys with equal Mo and B content were shown to more sensitively change with Al matrix concentration compared to binary alloys.

Mechanical properties were assessed by macrohardness tests at ambient conditions and tensile tests at 20 °C and 550°C. All hypostoichiometric alloys exhibit increased strength at room and elevated temperatures. Microhardness measurements suggest an increased matrix hardness to be responsible in accordance to literature data. Reducing B content (i.e. decreased secondary phase fractions) tends to lower strength, invariant of test temperature, without reducing brittleness at room temperature. Lower Mo content slightly increased room temperature ductility in hyperstoichiometric, but not in hypostoichiometric alloys. Concerning strength, $R_{p0.2}$ at 550 °C was invariant or slightly higher with lower Mo concentration, which is contrary to reported solid-solution hardening correlations in ternary Fe–Al-Mo alloys. It is hypothesised that the combined use of Mo and Ti as solutes may either saturate solid-solution hardening or cause softening in a certain concentration range.

Effect of solidifaction rate and heat treatments on room temperature properties

Experimental data on average grain size and corresponding HV10 macrohardness of Fe-25Al-3.7Mo-0.4Ti-1B were correlated to simulated solidification rates dT/dt changing as a result of different heat transfer rates by the selection of different mould material (DC: copper dies, IC: ceramic moulds) and casting wall thickness (2.5–20 mm). An inverse relationship of grain size and dT/dt in the centre of samples as well as a square root dependency of macrohardness on dT/dt was qualitatively suggested. By the use of die casting and minimum wall thickness, d_{gs} could be reduced to 28 µm and macrohardness H increased to 327 HV10. This was also accompanied by a refinement of Mo_2FeB_2 particles and increased volume fractions. The exposure to homogenisation treatments at 1000 °C (HT2) generally indicated no grain coarsening, potentially inhibited by Mo_2FeB_2 particles on grain boundaries. However, borides were found to be less thermodynamically stable if solidification rates during casting increased. Consequently, homogenisation led to more particle coarsening and reshaping and decreasing f_p in these castings. Both findings corroborate the causal correlation of decreasing d_{gs} and increasing f_p with increasing macrohardness.

Room temperature tensile tests of die-cast miniature specimens with minimum d_{gs} (28 µm) supported a beneficial effect of higher solidification rate on mechanical strength, with a 35% higher $R_{p0.2}$-value than for specimens with considerably larger grain size (457 µm). The strength increase was mainly attributed to Hall-Petch strengthening, with a similar Hall-Petch constant as reported for other Fe-Al alloys, although an influence by particle refinement was also considered possible. However, ductility was limited to $A = 0.5\%$ despite higher solidification rates with grain and particle refinement. DIC analysis and post-investigations identified localized strain concentrations in the investigated alloy which were related to crack formation and fracture. The origin was confined to surface defects and geometry-related stress concentrations. The findings indicate a decisive role of the surface and the surface condition in the found behaviour at ambient tensile loading.

Apart from grain and particle refinement, the effect of different solidification rates on thermal vacancy hardening was investigated in as-cast and quenched Fe-25Al-3.7Mo-0.4Ti-1B alloys.

Isothermal dilatometry of as-cast alloys at 400 °C did not yield any significant relative length changes, comparable to measurements of quenched binary Fe-27Al alloys with D0$_3$ order, but opposing to quenched Fe-37Al with B2 order which exhibited a notable contraction over time. Differential dilatometry on quinary alloys quenched from 700 °C with supposedly higher retained thermal vacancies confirmed the prior results and did not show clear signs of contraction compared to a vacancy-annealed state (HT1: 400 °C/168 h/FC). Cross-correlation to results on true density ρ_t and HV0.1 microhardness H gave a more complex impression: While densities appeared inconclusive due to the alleged presence of cracks and pores, microhardness was almost unchanged or even increased after HT1 agreeing with the observations from dilatometric measurements. The lacking sensitivity of microhardness to thermal treatments was interpreted to be imposed by the presence of Mo solutes. These may decrease the mobility of thermal vacancies at higher temperatures by forming stable solute-vacancy complexes. Nevertheless, microhardness measurements of castings with higher solidification rates as well as quenching from higher temperatures (i.e. 1000 °C) demonstrated slight, but evident increases as expected by higher retained thermal vacancy concentrations. In addition to small changes of thermal vacancy concentration, a complex interplay of anti-phase domain (APD) hardening, thermal memory effects and long-range order (LRO) was explained to contribute to the resulting strength after annealing at 400 °C. Overall, the quinary alloys demonstrate a less pronounced but more stable thermal vacancy hardening effect than B2 Fe-Al alloys, allowing them to withstand low-temperature heat treatments without significant loss of strength.

Comparison with P92 steel for high-temperature applications

In immediate comparison to P92 grade ferritic-martensitic steels, the quasi-static tensile properties of investment-cast Fe-25Al-3.7Mo-0.4Ti-1B alloy are especially competitive or even superior at high temperatures above 500 °C. However, mechanical performance at intermediate or low temperatures clearly falls behind P92 steels. Although grain and particle refinement was effective in increasing $R_{p0.2}$ at room temperature, P92 steel still has a higher strength (> 440 MPa) and the lack of ductility until temperatures as high as T_{YSA} is a major bottleneck for applications. Similar conclusions can be drawn on creep properties at 650 °C. As Norton plots demonstrated, quinary Fe-25Al-3.7Mo-0.4Ti-1B alloys are more creep-resistant than P92 steels in high-stress conditions (above 170 MPa), but have clearly higher creep rates at lower load levels which are more relevant in material design for standard applications. Hence, long-term aging at high temperatures which is a particularly strong asset in P92 steels with a reliable database would be inevitably accelerated in the investigated iron aluminide alloy. For instance, the creep rupture strength of P92 steel for a service hour of 10,000 h at 650 °C is 88 MPa. A comparable stress (80 MPa) applied to Fe-25Al-3.7Mo-0.4Ti-1B resulted in creep fracture after only 580 h. Even the prospective properties of cast quinary alloys which are optimised according to the conclusions for alloy composition, solidification rate and thermal treatment, might be out of range to meet the requirements in supercritical CO_2 power plants or steam generators. In conclusion, the quinary Fe-Al-Mo-Ti-B alloy system may not be able to substitute for P92 steels.

Outlook

Measures for improvement of mechanical strength at high temperatures and especially room temperature ductility could include other manufacturing methods which are able to produce fine-grained (1–10 µm) or ultrafine-grained (< 1 µm) microstructures, such as additive manufacturing, powder metallurgy or severe plastic deformation routes. The fixing of grain boundaries by borides and the low tendency to grain coarsening are ideal characteristics to maintain microstructures up to high temperatures. Furthermore, Cr additions could especially help increase ambient ductility without expected strength decreases.

However, the quinary Fe-Al-Mo-Ti-B alloy system still revealed many open research questions. This is especially owed to the multiplicity of deformation and hardening mechanisms involved in binary near-Fe_3Al alloys and the ambiguity to interpret them. These do not allow easy answers due to the complex interaction of dislocations, anti-phase boundaries and vacancies in ordered structures with partially mixed long-range order and different site preferences. Therefore, adding solutes and secondary phase particles to an alloy system will inevitably require re-evaluation of these mechanisms. A few examples based on the performed investigations are:

- With respect to creep testing results, true constant creep rates $\dot{e}_{ft,ss}$ expectedly varied with temperature, but were not specifically affected by the solid-state transformation from $D0_3$ to B2 order. Ergo, further investigations of creep specimens tested below and above the order-order reaction $T_c^{D0_3 \leftrightarrow B2}$ would be necessary to understand whether Mo and Ti solute additions have an effect on the transition of long-range order. These could include post-mortem TEM investigations of APB relaxation and dislocation structures and/or in-situ XRD studies to determine the order parameters during creep loading.

- Mo solute-vacancy complexes were argued to reduce the sensitivity of thermal treatments to equilibrium hardness, however without experimental proof. The formation of solute-vacancy complexes could be investigated by positron annihiliation spectroscopy and coincidence Doppler broadening spectroscopy, which was already successfully demonstrated on diluted alloys [300, 309, 310].
- The Hall-Petch strengthening is still a matter of research nowadays and was only lightly covered for a few binary Fe-Al alloys, but not for those near ideal Fe_3Al composition. Hence, further TEM investigations would be necessary to examine dislocation structures and pile-up formation in different grain sizes in order to comprehend and rank the Hall-Petch strengthening mechanism in higher-order Fe-Al alloys with multiple strengthening mechanisms in place.
- With respect to tension-compression asymmetry, a systematic investigation of tensile and compressive strength of binary and various boride-strengthened alloys from comparable batches would be necessary to reliably quantify the TCA effect in quinary Fe-Al-Mo-Ti-B alloys as a function of temperature. Additionally, different homogenisation treatments are recommended to take different morphology and stress states of borides into account.

Appendices

pendix

A Drawings

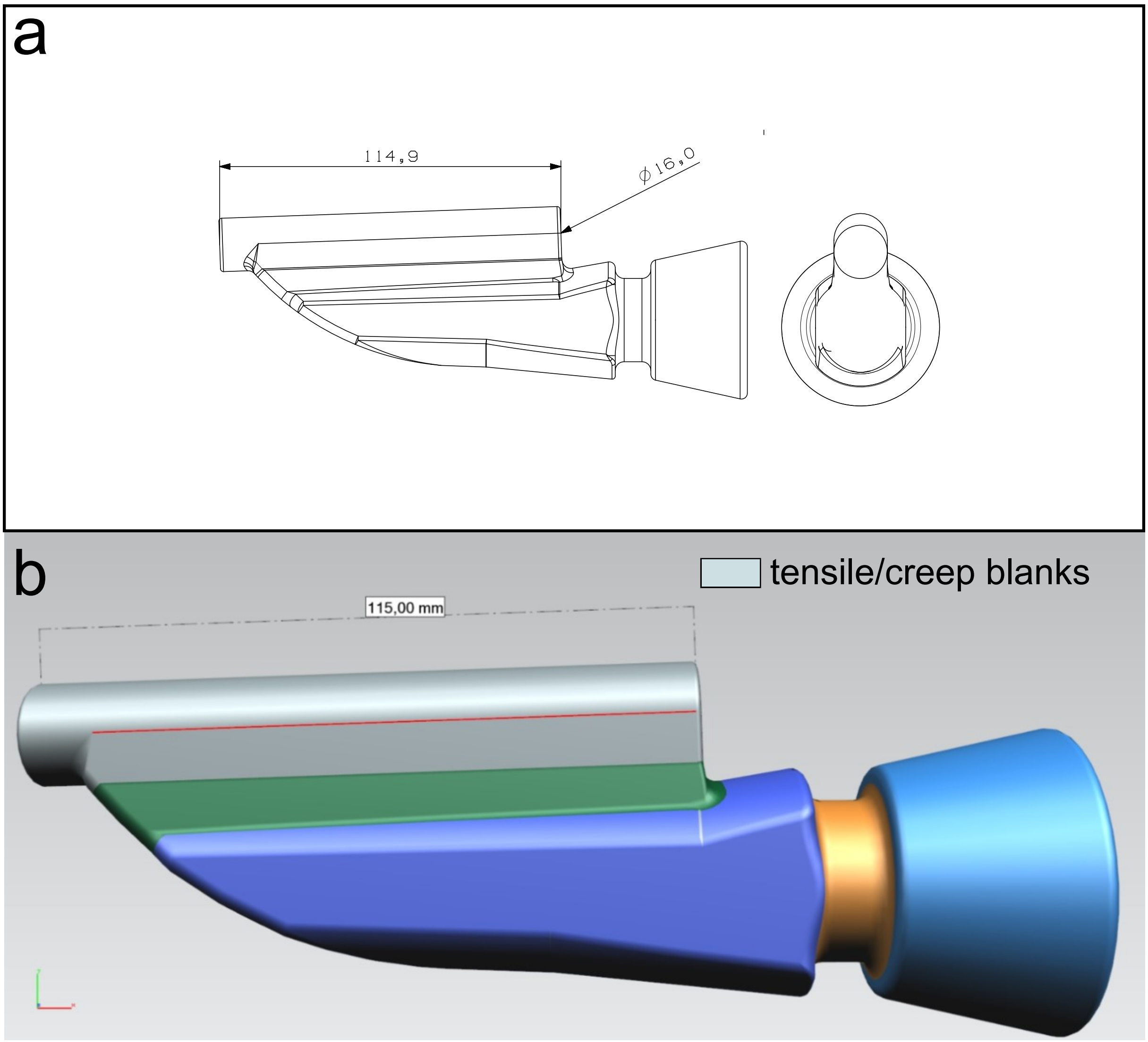
a
114,9
ϕ16,0
b
tensile/creep blanks
115,00 mm

Figure A.1.: Drawing (a) and 3D rendering (b) of Fe-26Al-4Mo-0.5Ti-1B investment castings for the processing of tensile and creep specimens (extraction location indicated in grey). Adapted from [143].

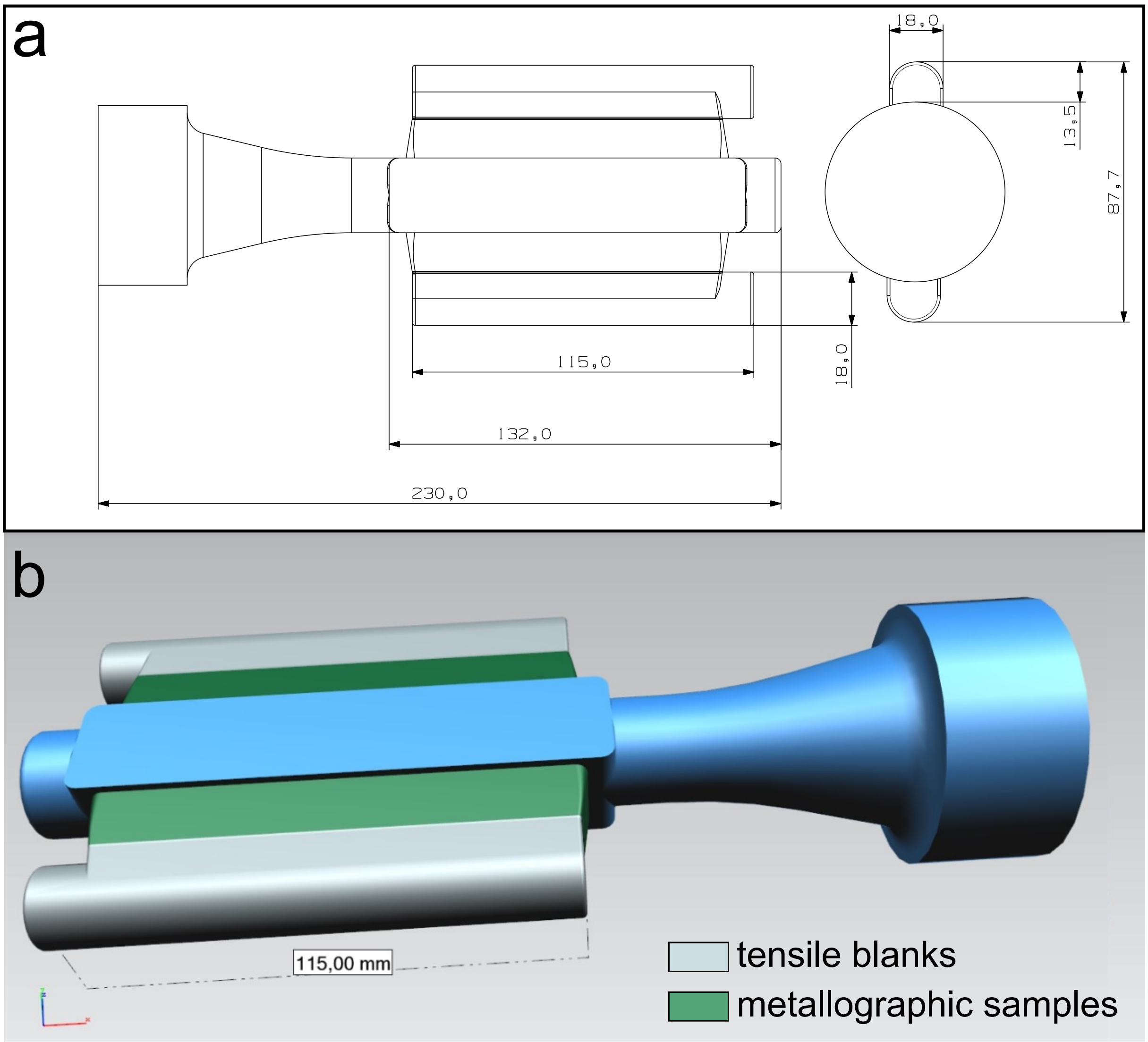
a
18,0
13,5
87,7
18,0
115,0
132,0
230,0
b
115,00 mm
tensile blanks
metallographic samples

Figure A.2.: Drawing (a) and 3D rendering (b) of Fe-xAl-yMo-Ti-zB investment castings with different alloy concentrations. Locations for extraction of tensile blanks (grey) and metallographic samples (green) are indicated by colours. Adapted from [143].

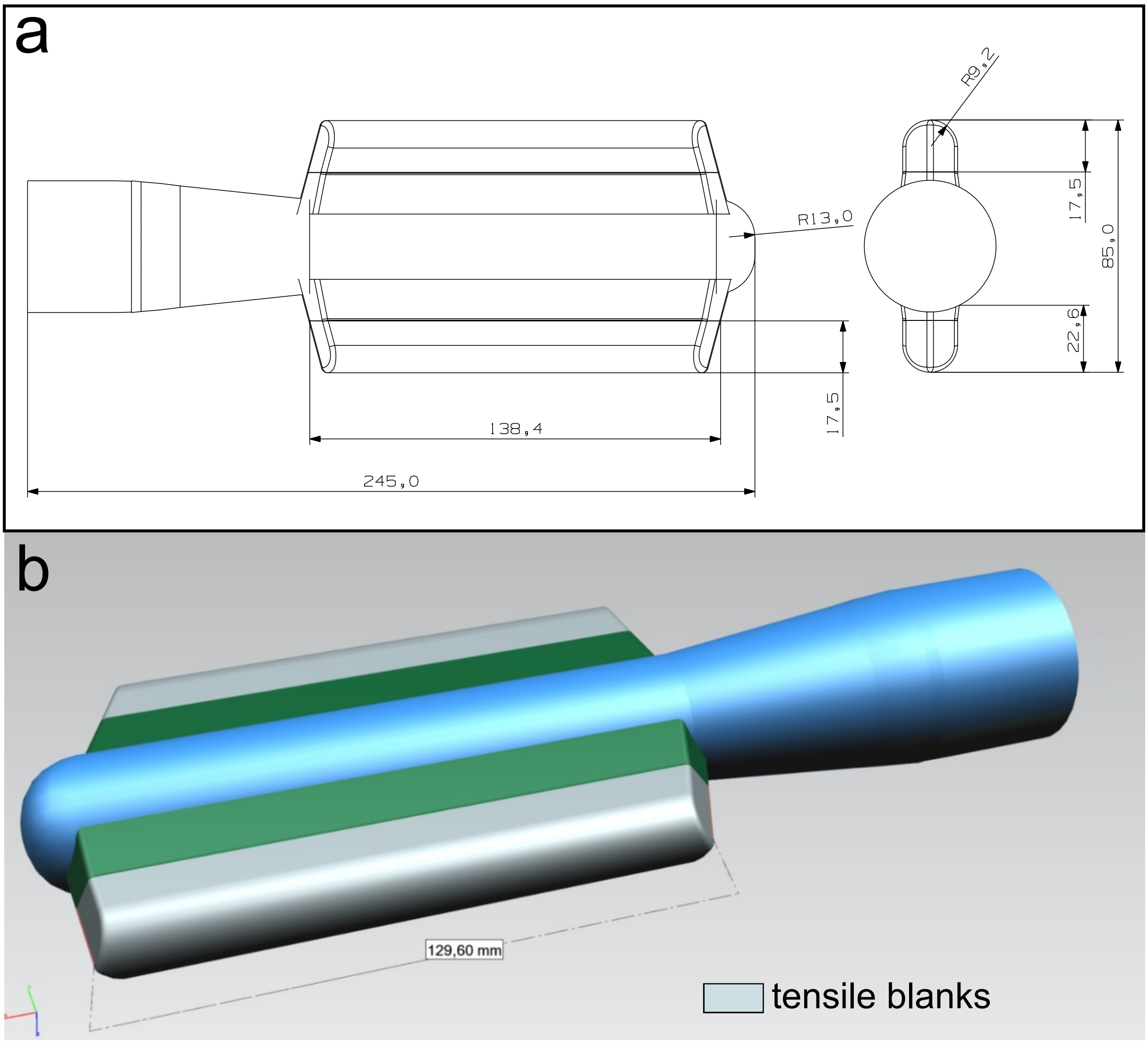
a
R9,2
R13,0
17,5
85,0
22,6
17,5
138,4
245,0
b
129,60 mm
tensile blanks

Figure A.3.: Drawing (a) and 3D rendering (b) of Fe-26AlMo-0.5Ti-1B die castings for the processing of tensile specimens (extraction location indicated in grey). Adapted from [143].

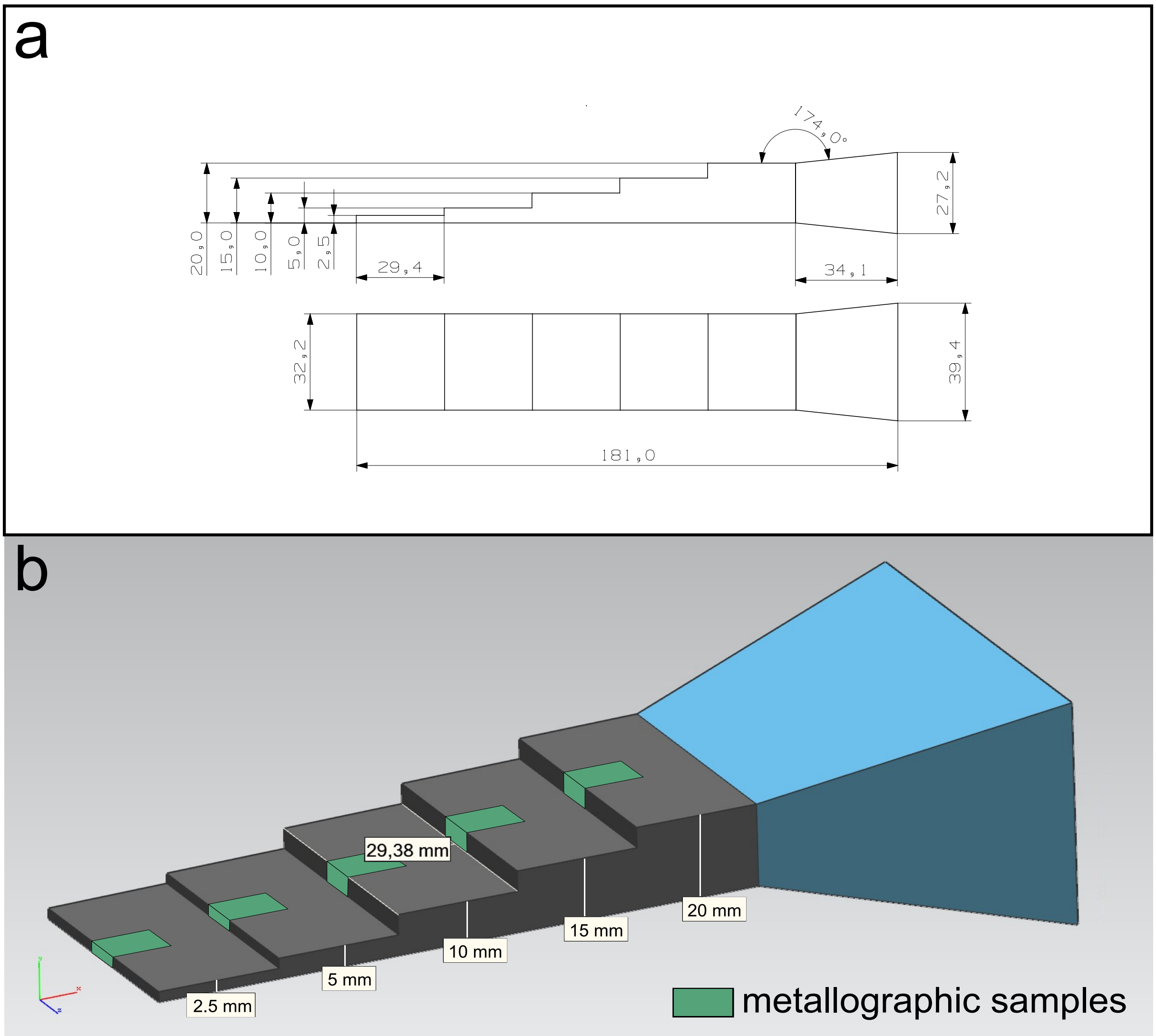
a
174,0°
27,2
20,0
15,0
10,0
5,0
2,5
29,4
34,1
32,2
39,4
181,0
b
29,38 mm
2.5 mm
5 mm
10 mm
15 mm
20 mm
🟩 metallographic samples

Figure A.4.: Drawing (a) and 3D rendering (b) of Fe-26Al-4Mo-0.5Ti-1B step samples cast into both copper dies and ceramic moulds. Locations for extraction of metallographic samples at different wall thicknesses are indicated in green. Adapted from [143].

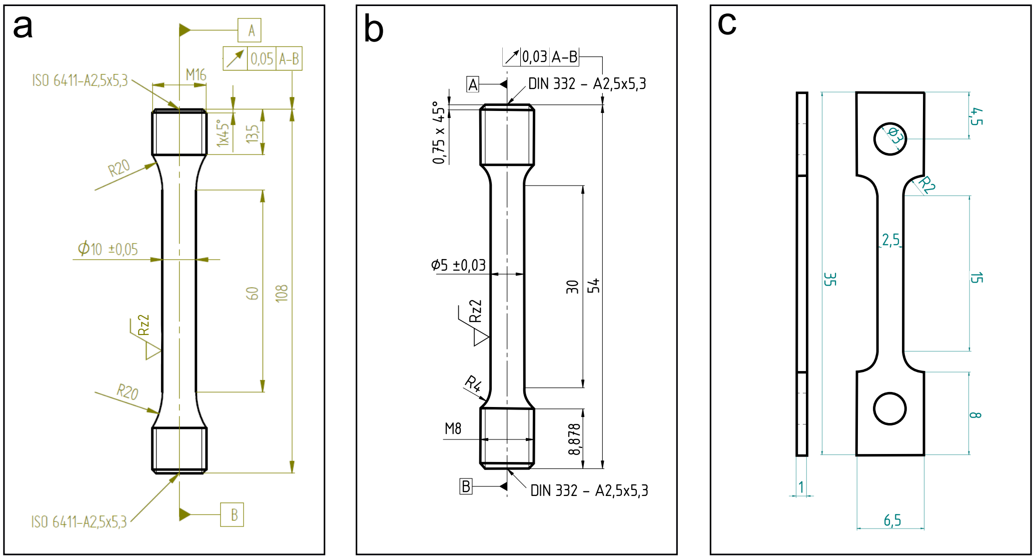
a
A
0,05 A–B
ISO 6411-A2,5x5,3
M16
1x45°
13,5
R20
Φ10 ±0,05
Rz2
60
108
R20
ISO 6411-A2,5x5,3
B
b
0,03 A–B
A
DIN 332 – A2,5x5,3
0,75 x 45°
Φ5 ±0,03
Rz2
30
54
R4
M8
8,878
B
DIN 332 – A2,5x5,3
c
4,5
Φ3
R2
2,5
35
15
8
1
6,5

Figure A.5.: Drawings of tensile specimen geometries: (a) standard geometry with cylindrical gauge section, a diameter of 10 mm and $L_c = 60$ mm [143], (b) reduced cylindrical gauge section, a diameter of 5 mm and $L_c = 30$ mm, (c) miniature geometry with flat gauge section, a thickness of 1 mm thickness, a width of 2.5 mm and $L_c = 15$ mm.

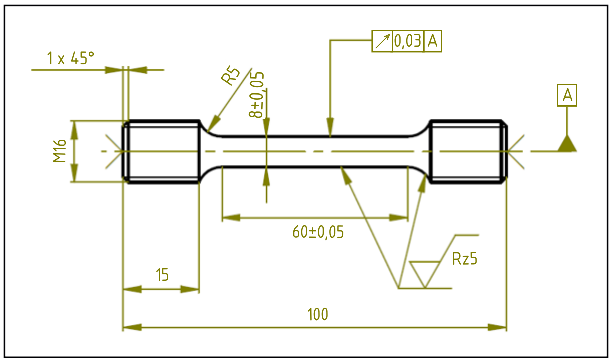
1 x 45°
R5
8±0,05
0,03 A
A
M16
60±0,05
Rz5
15
100

Figure A.6.: Drawing of creep specimen geometry with cylindrical gauge section, a diameter of 8 mm and $L_c = 60$ mm [143].

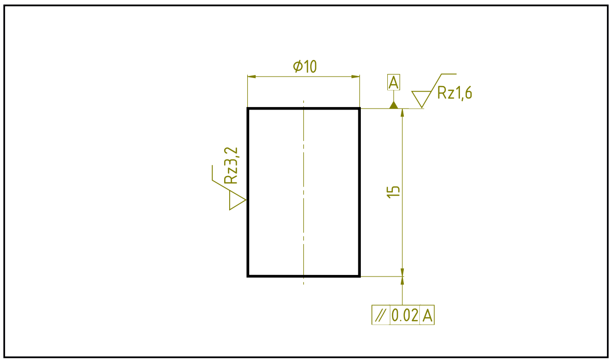
Φ10
A
Rz1,6
Rz3,2
15
// 0.02 A

Figure A.7.: Drawing of compression specimen geometry with cylindrical gauge section and a diameter of 10 mm.

pendix

B Further investigations

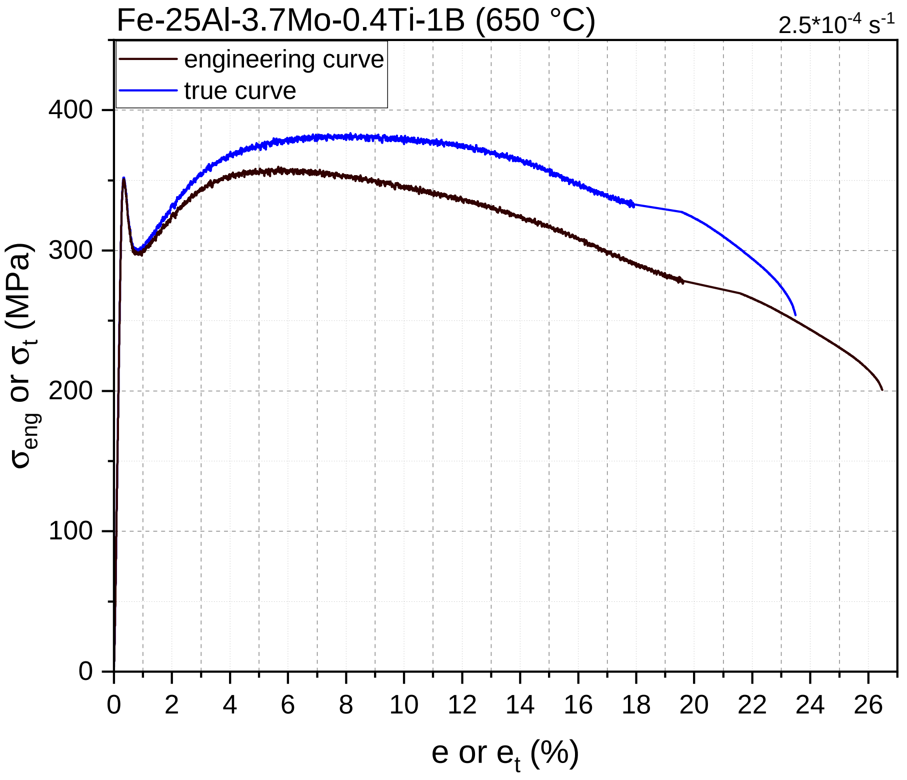

Figure B.1.: Engineering and true stress-strain curves of investment-cast Fe-25Al-3.7Al-0.4Ti-1B homogenised at HT2 during tensile testing at 650 °C.

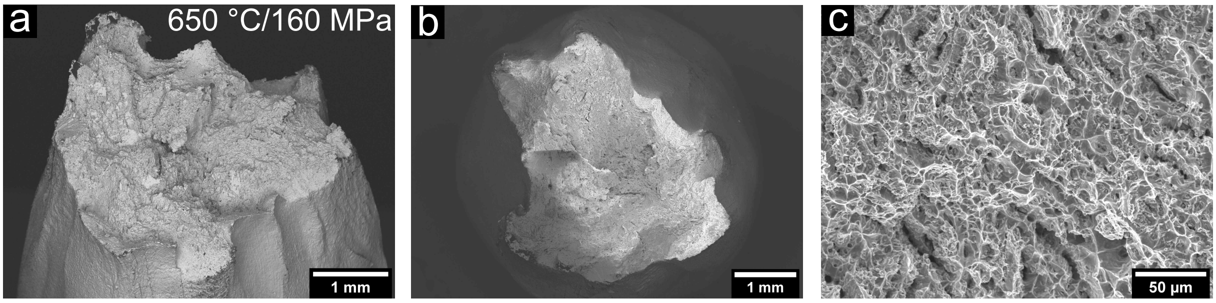

Figure B.2.: SEM images of fracture surfaces of Fe-25Al-3.7Mo-0.4Ti-1B after creep testing at 650 °C/160 MPa.

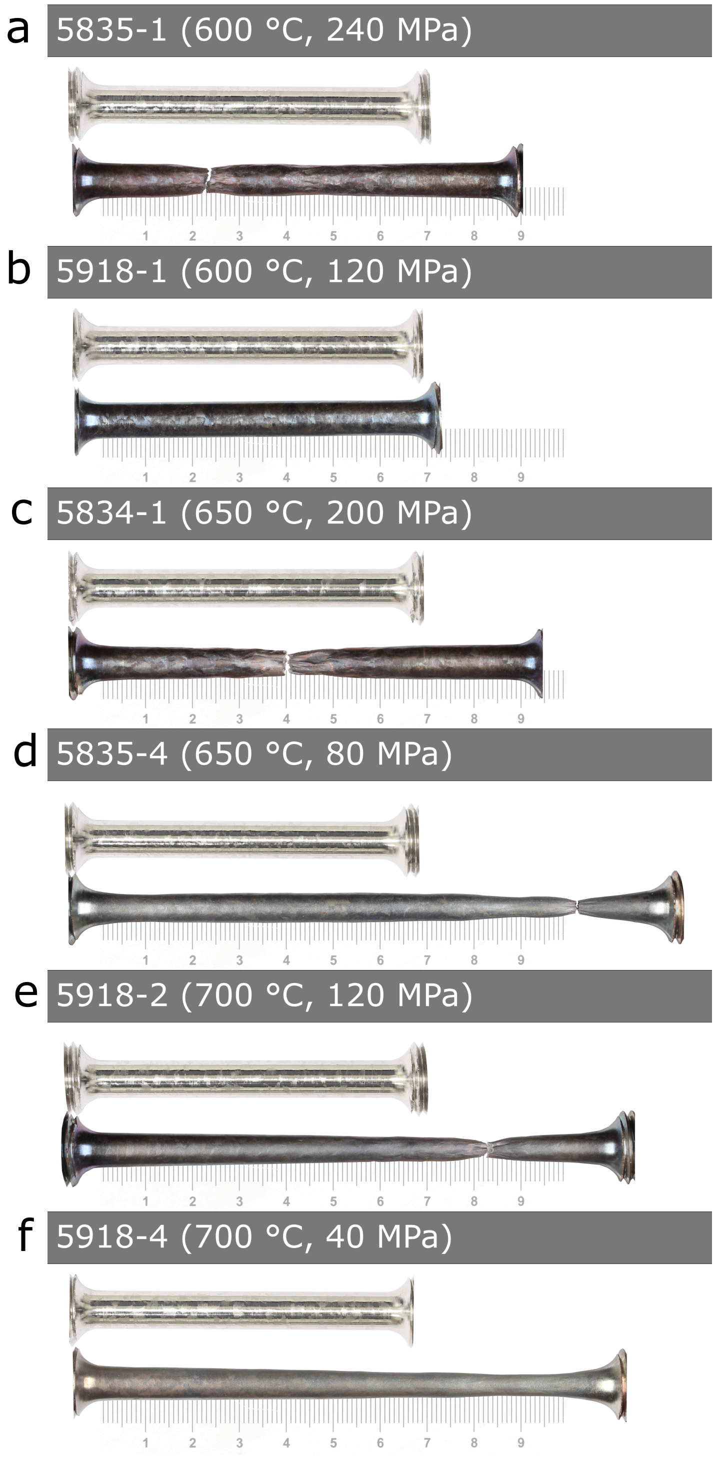
a
5835-1 (600 °C, 240 MPa)
1 2 3 4 5 6 7 8 9
b
5918-1 (600 °C, 120 MPa)
1 2 3 4 5 6 7 8 9
c
5834-1 (650 °C, 200 MPa)
1 2 3 4 5 6 7 8 9
d
5835-4 (650 °C, 80 MPa)
1 2 3 4 5 6 7 8 9
e
5918-2 (700 °C, 120 MPa)
1 2 3 4 5 6 7 8 9
f
5918-4 (700 °C, 40 MPa)
1 2 3 4 5 6 7 8 9

Figure B.3.: Comparison of the creep specimen geometry before and after the creep test of Fe-25Al-3.7Mo-0.4Ti-1B [143]. The images compare the maximum and minimum stress levels tested at the three test temperatures 600 °C (a,b), 650 °C (c,d) and 700 °C (e,f).

Table B.1.: XRF compositions of quasi-binary Fe-Al alloys after induction melting.

	Measured composition (at%)			
Alloy	Fe	Al	Nb	Zr
Fe-27Al	72.4	27.1	0.4	0.1
Fe-37Al	62.2.	37.3	0.4	0.1

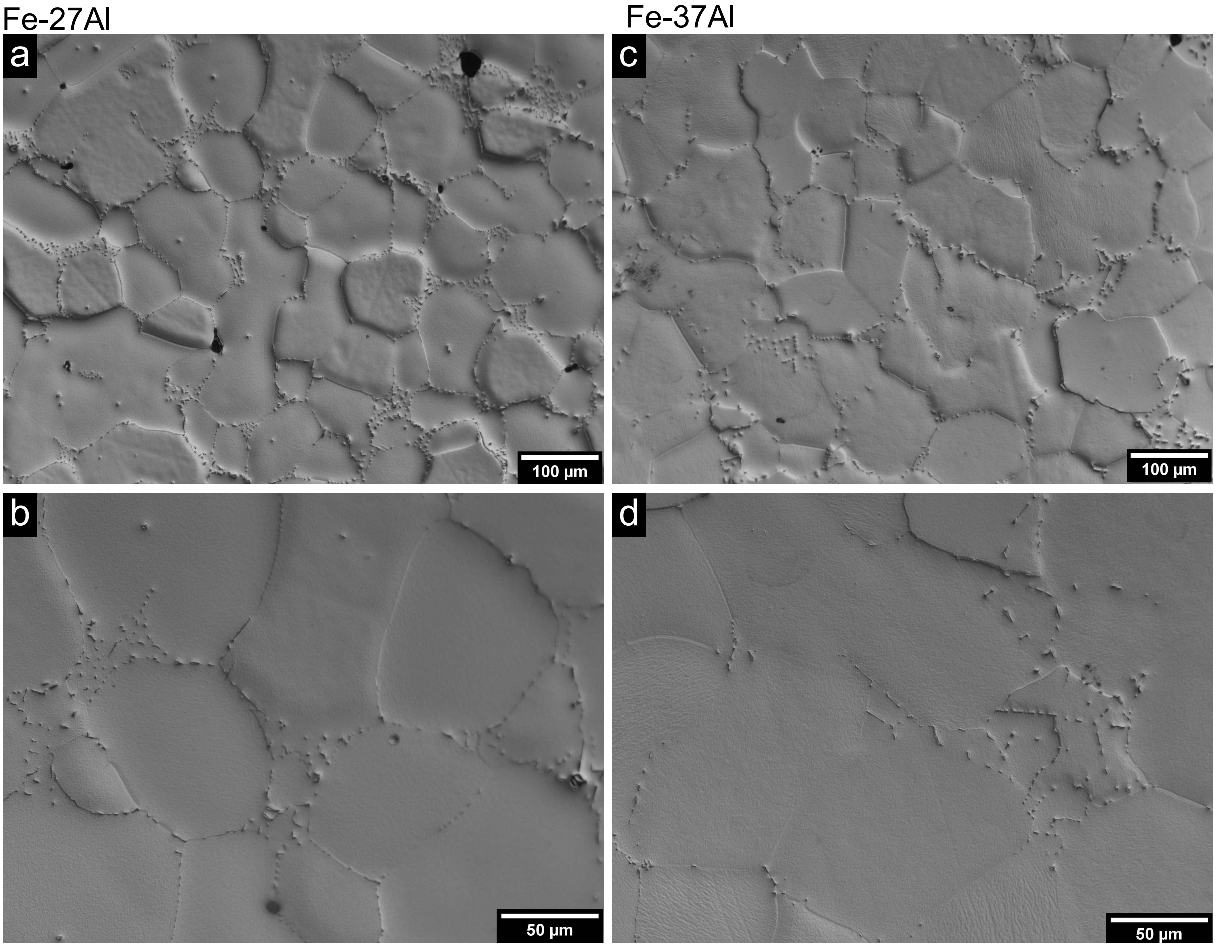
Fe-27Al
Fe-37Al
a
100 µm
c
100 µm
b
50 µm
d
50 µm

Figure B.4.: Optical microsections of cross-sectional areas of Fe-27Al (a,b) and Fe-37Al (c,d) at two magnifications. Images were taken after oil-quenching from 700 °C followed by HT1.

Table B.2.: Mean microhardness HV0.1 and 95% CI of Fe_3Al phase in Fe-25Al-3.7Mo-0.4Ti-1B, Fe-27Al and Fe-37Al alloys after oil-quenching (OQ) from different temperatures (OQ1: 700 °C/100 h/OQ, OQ2: 1000 °C/100 h/OQ) as well as after subsequent vacancy annealing at HT1 (400 °C/168 h/FC).

	Microhardness (HV0.1)			
Alloy	OQ1	OQ1+HT1	OQ2	OQ2+HT1
Fe-25Al-3.7Mo-0.4Ti-1B (DC)	325 ± 4	324 ± 5	339 ± 4	334 ± 5
Fe-25Al-3.7Mo-0.4Ti-1B (IC)	316 ± 3	324 ± 1	338 ± 3	340 ± 3
Fe-27Al	286 ± 4	321 ± 4	327 ± 3	335 ± 4
Fe-37Al	309 ± 2	243 ± 4	409 ± 4	263 ± 2

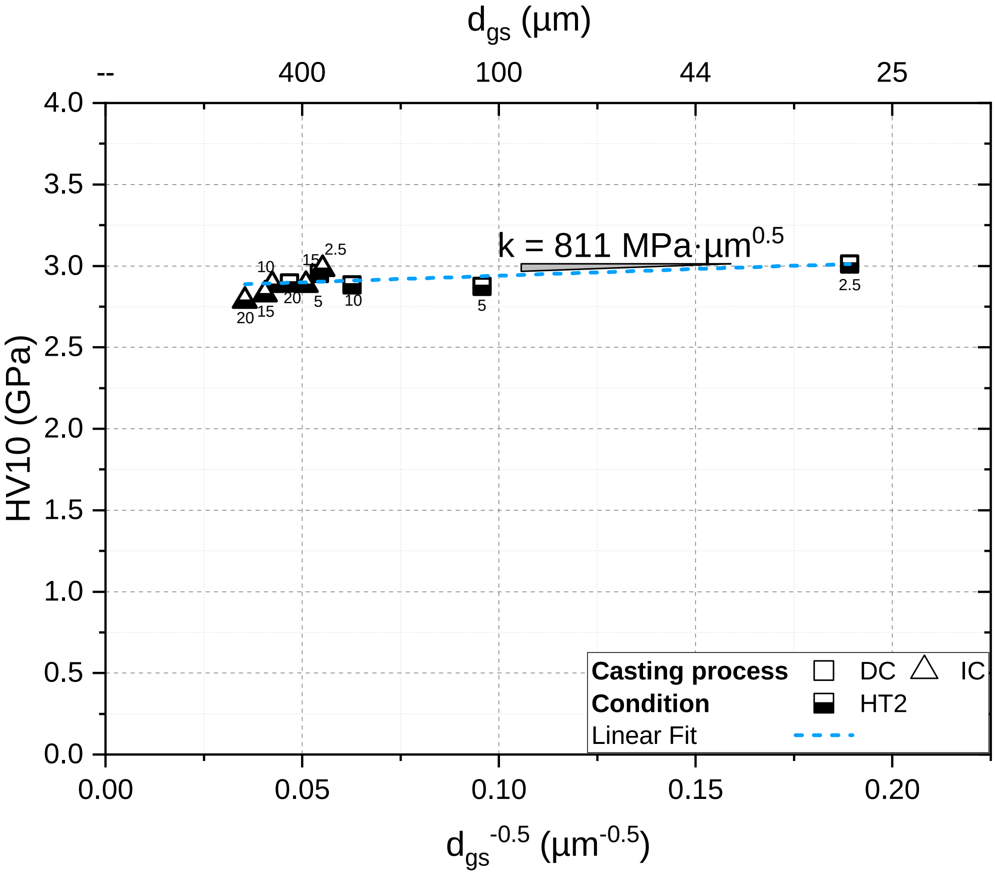

Figure B.5.: Hall-Petch regression applied to macrohardness HV10 over $d_{gs}^{-1/2}$ of Fe-25Al-3.7Mo-0.4Ti-1B step samples. Only die-cast and investment-cast samples with different wall thicknesses and subsequent homogenisation treatment (HT2) were considered.

References

[1] IEA, *Renewables 2023: Analysis and forecast to 2028*, International Energy Agency, 2024.

[2] M. Joos, I. Staffell, “Short-term integration costs of variable renewable energy: Wind curtailment and balancing in Britain and Germany”, Renewable and Sustainable Energy Reviews 86 (2018) 45–65.

[3] H. L. Ferreira, R. Garde, G. Fulli, W. Kling, J. P. Lopes, “Characterisation of electrical energy storage technologies”, Energy 53 (2013) 288–298.

[4] M. T. White, G. Bianchi, L. Chai, S. A. Tassou, A. I. Sayma, “Review of supercritical CO2 technologies and systems for power generation”, Applied Thermal Engineering 185 (2021) 116447.

[5] D. Hilberg, H. Knittel, T. Polklas, A. Wiedermann, B. Witzel, F. di Mare, V. Gümmer, R. Mönig, D. Vogt, *The role of turbomachinery in the energy transition*, AG Turbo, 2023.

[6] W.-D. Steinmann, “Thermo-mechanical concepts for bulk energy storage”, Renewable and Sustainable Energy Reviews 75 (2017) 205–219.

[7] T. M. Gür, “Review of electrical energy storage technologies, materials and systems: challenges and prospects for large-scale grid storage”, Energy & Environmental Science 11 (2018) 2696–2767.

[8] M. Zapf, *Stromspeicher und Power-to-Gas im deutschen Energiesystem: Rahmenbedingungen, Bedarf und Einsatzmöglichkeiten*, Springer Fachmedien, Wiesbaden, 2022.

[9] Z. Xu, Y. Yang, S. Mao, W. Wu, Q. Yang, “Review on corrosion of alloys for application in supercritical carbon dioxide brayton cycle”, Heliyon 9 (2023) e22169.

[10] D. Fleming, A. Kruizenga, J. Pasch, T. Conboy, M. Carlson, *Corrosion and Erosion Behavior in Supercritical* CO_2 *Power Cycles*, SAND2014-0602C, Springfield, VA: Sandia National Laboratories, 2014.

[11] P. J. Ennis, A. Czyrska-Filemonowicz, “Recent advances in creep-resistant steels for power plant applications”, Sadhana 28 (2003) 709–730.

[12] *ASTM A335/A335M-23 Specification for Seamless Ferritic Alloy-Steel Pipe for High-Temperature Service*, ASTM International.

[13] *DIN EN 10216-2:2020-04, Seamless steel tubes for pressure purposes - Technical delivery conditions - Part 2: Non-alloy and alloy steel tubes with specified elevated temperature properties; German version EN 10216-2:2013+A1:2019*, DIN Media GmbH.

[14] H. Cerjak, P. Hofer, B. Schaffernak, "The Influence of Microstructural Aspects on the Service Behaviour of Advanced Power Plant Steels." ISIJ International 39 (1999) 874–888.

[15] P. Duan, Z. Liu, B. Li, J. Li, X. Tao, "Study on microstructure and mechanical properties of P92 steel after high-temperature long-term aging at 650°C", High Temperature Materials and Processes 39 (2020) 545–555.

[16] K. Yin, S. Qiu, R. Tang, Q. Zhang, L. Zhang, "Corrosion behavior of ferritic/martensitic steel P92 in supercritical water", The Journal of Supercritical Fluids 50 (2009) 235–239.

[17] C. G. McKamey, *Iron Aluminides*, in: *Physical metallurgy and processing of intermetallic compounds*, ed. by N. S. Stoloff, V. K. Sikka, Springer, Boston, MA, 1996: 351–391.

[18] M. Palm, F. Stein, G. Dehm, "Iron Aluminides", Annual Review of Materials Research 49 (2019) 297–326.

[19] G. C. Culbertson, C. S. Kortovich, *Development of iron aluminides*, Report AFWAL-TR-85-4155, AF Wright Aeronautical Laboratories, 1986.

[20] M. Palm, "Fe–Al materials for structural applications at high temperatures: Current research at MPIE", International Journal of Materials Research 100 (2009) 277–287.

[21] P. Kratochvíl, I. Schindler, P. Hanus, "Conditions for hot rolling of Fe_3Al - type aluminide", Kovové materiály - Metallic Materials 44 (2006) 321–326.

[22] V. Sikka, D. Wilkening, J. Liebetrau, B. Mackey, "Melting and casting of FeAl-based cast alloy", Materials Science and Engineering: A 258 (1998) 229–235.

[23] V. Seetharaman, S. Semiatin, *Powder Metallurgy*, in: *Intermetallic Compounds: Principles and Practice*, 3rd ed. John Wiley & Sons, Chichester, UK, 2002: 643–662.

[24] G. Rolink, S. Vogt, L. Senčekova, A. Weisheit, R. Poprawe, M. Palm, "Laser metal deposition and selective laser melting of Fe–28 at.% Al", Journal of Materials Research 29 (2014) 2036–2043.

[25] P. J. Maziasz, G. M. Goodwin, D. J. Alexander, S. Viswanathan, *Alloy Development and Processing of FeAl: An overview*, in: International Conference on Nickel and Iron Aluminides: Processing, Properties, and Applications, ASM International, 1996.

[26] S. Deevi, V. Sikka, "Nickel and iron aluminides: an overview on properties, processing, and applications", Intermetallics 4 (1996) 357–375.

[27] R. R. Judkins, U. S. Rao, "Fossil energy applications of intermetallic alloys", Intermetallics 8 (2000) 1347–1354.

[28] V. K. Sikka, R. W. Swindeman, I. G. Wright, R. R. Judkins, R. Johnson, *Fabrication of Test Tubes for Coal Ash Corrosion Testing*, in: *Oak Ridge National Lab (ORNL)*, Fossil Energy Conference, Knoxville, TN, 1999: 1–7.

[29] P. Kratochvíl, "The history of the search and use of heat resistant Pyroferal© alloys based on FeAl", Intermetallics 16 (2008) 587–591.

[30] J. Cebulski, "Application of FeAl intermetallic phase matrix based alloys in the turbine components of a turbocharger", Metalurgija 54 (2015) 154–156.

[31] D. J. Gaydosh, M. V. Nathal, "Influence of testing environment on the room temperature ductility of FeAl alloys", Scripta Metallurgica et Materialia 24 (1990) 1281–1284.

[32] D. G. Morris, M. A. Muñoz-Morris, J. Chao, "Development of high strength, high ductility and high creep resistant iron aluminide", Intermetallics 12 (2004) 821–826.

[33] A. Bahadur, "Enhancement of high temperature strength and room temperature ductility of iron aluminides by alloying", Materials science and technology 19 (2003) 1627–1634.

[34] M. Palm, "Concepts derived from phase diagram studies for the strengthening of Fe–Al-based alloys", Intermetallics 13 (2005) 1286–1295.

[35] D. G. Morris, M. A. Muñoz-Morris, "Development of creep-resistant iron aluminides", Materials Science and Engineering: A 462 (2007) 45–52.

[36] D. D. Risanti, G. Sauthoff, "Strengthening of iron aluminide alloys by atomic ordering and Laves phase precipitation for high-temperature applications", Intermetallics 13 (2005) 1313–1321.

[37] C. S. Tiwary, P. Pandey, S. Sarkar, R. Das, S. Samal, K. Biswas, K. Chattopadhyay, "Five decades of research on the development of eutectic as engineering materials", Progress in Materials Science 123 (2022) 100793.

[38] X. Li, P. Prokopčáková, M. Palm, "Microstructure and mechanical properties of Fe–Al–Ti–B alloys with additions of Mo and W", Materials Science and Engineering: A 611 (2014) 234–241.

[39] W. J. Keep, "Aluminum in cast iron", Transactions of the Metallurgical Society of AIME 18 (1890) 102–122.

[40] {European Commission}, *Advanced Materials for Industrial Leadership*, COM(2024) 98 final, 2024.

[41] S. C. Deevi, "Advanced intermetallic iron aluminide coatings for high temperature applications", Progress in Materials Science 118 (2021) 100769.

[42] M. Palm, F. Stein, *Iron-Based Intermetallics*, in: *High-Performance Ferrous Alloys*, ed. by R. Rana, Springer International Publishing, Cham, 2021: 423–458.

[43] M. Zamanzade, A. Barnoush, C. Motz, "A Review on the Properties of Iron Aluminide Intermetallics", Crystals 6 (2016) 10.

[44] K. Momma, F. Izumi, "*VESTA 3* for three-dimensional visualization of crystal, volumetric and morphology data", Journal of Applied Crystallography 44 (2011) 1272–1276.

[45] A. R. Paul, M. Mukherjee, D. Singh, "A Critical Review on the Properties of Intermetallic Compounds and Their Application in the Modern Manufacturing", Crystal Research and Technology 57 (2022) 2100159.

[46] R. Kuentzler, "Ordering effects in the Fe-Al system", Journal de Physique 44 (1983) 1167–1178.

[47] A. Taylor, R. Jones, "Constitution and magnetic properties of iron-rich iron-aluminum alloys", Journal of Physics and Chemistry of Solids 6 (1958) 16–37.

[48] M. J. Marcinkowski, N. Brown, "Direct Observation of Antiphase Boundaries in the Fe_3Al Superlattice", Journal of Applied Physics 33 (1962) 537–552.

[49] A. Lawley, E. Vidoz, R. Cahn, "The dependence of the flow stress of Fe_3Al on crystallographic order", Acta Metallurgica 9 (1961) 287–296.

[50] H. J. Leamy, F. X. Kayser, M. J. Marcinkowski, "The plastic deformation behaviour of long-range ordered iron-aluminium alloys: I. Single crystal deformation experiments", Philosophical Magazine 20 (1969) 763–777.

[51] H. J. Leamy, F. X. Kayser, M. J. Marcinkowski, "The plastic deformation behaviour of long-range ordered iron-aluminium alloys: II. Transmission electron microscopical observations", Philosophical Magazine 20 (1969) 779–798.

[52] R. C. Crawford, I. L. F. Ray, "Antiphase boundary energies in iron-aluminium alloys", Philosophical Magazine 35 (1977) 549–565.

[53] M. Marcinkowski, N. Brown, R. Fisher, "Dislocation configurations in $AuCu_3$ and AuCu type superlattices", Acta Metallurgica 9 (1961) 129–137.

[54] T. Saburi, I. Yamauchi, S. Nenno, "Electron Microscope Observation of Dislocations and Antiphase Boundaries in Iron-Aluminum Alloys", Journal of the Physical Society of Japan 32 (1972) 694–701.

[55] J.-W. Park, "Anomalous yield behavior of hypo- and hyper-stoichiometric Fe_3Al intermetallic compounds", Intermetallics 10 (2002) 683–691.

[56] D. G. Morris, M. A. Muñoz-Morris, L. M. Requejo, "Work hardening in Fe–Al alloys", Materials Science and Engineering: A 460–461 (2007) 163–173.

[57] C. T. Liu, K. S. Kumar, "Ordered Intermetallic Alloys, Part I: Nickel and Iron Aluminides", Journal of The Minerals, Metals & Materials Society 38 (1993) 38–44.

[58] W. Köster, T. Gödecke, "Physikalische Messungen an Eisen-Aluminium-Legierungen mit 10 bis 50 At.-% Al: IV. Der Elastizitätsmodul der Legierungen", International Journal of Materials Research 73 (1982) 111–114.

[59] M. Friák, J. Deges, R. Krein, G. Frommeyer, J. Neugebauer, "Combined ab initio and experimental study of structural and elastic properties of Fe_3Al-based ternaries", Intermetallics 18 (2010) 1310–1315.

[60] W. Köster, T. Gödecke, "Physikalische Messungen an Eisen-Aluminium-Legierungen mit 10 bis 50 At.-% Al Il. Die Ausdehnungskoeffizienten der Legierungen mit 10 bis 35 At.-% Al", International Journal of Materials Research 72 (1981) 569–574.

[61] E. Zintl, "Intermetallische Verbindungen", Angewandte Chemie 52 (1939) 1–6.

[62] N. Stoloff, R. Davies, "The mechanical properties of ordered alloys", Progress in Materials Science 13 (1968) 1–84.

[63] M. J. Marcinkowski, „Strengthening of alloys by atomic order“, physica status solidi (a) 90 (1985) 621–630.

[64] P. McQuay, V. Sikka, Y. Khalfalla, K. Benyounis, *Casting of Intermetallics*, in: *Reference Module in Materials Science and Materials Engineering*, Elsevier, 2016.

[65] G. W. Meetham, M. H. Van De Voorde, *Materials for High Temperature Engineering Applications*, Engineering Materials, Springer Berlin Heidelberg, Berlin, Heidelberg, 2000.

[66] C. G. McKamey, J. H. Devan, P. F. Tortorelli, V. K. Sikka, "A review of recent developments in Fe_3Al-based alloys", Journal of Materials Research 6 (1991) 1779–1805.

[67] S. Ko, R. Gnanamoorthy, S. Hanada, "Effect of environment on tensile ductility and fracture toughness of iron aluminides", Materials Science and Engineering: A 222 (1997) 133–139.

[68] P. Nagpal, I. Baker, "Effect of Cooling Rate on Hardness of FeAI and NiAI", Metallurgical Transactions A 21A (1990) 2281–2282.

[69] Y. A. Chang, L. M. Pike, C. T. Liu, A. R. Bilbrey, D. S. Stone, "Correlation of the hardness and vacancy concentration in FeAl", Intermetallics 1 (1993) 107–115.

[70] Y. Yang, I. Baker, "The influence of vacancy concentration on the mechanical behavior of Fe-40Al", Intermetallics 6 (1998) 167–175.

[71] G. Hasemann, J. H. Schneibel, E. P. George, "Dependence of the yield stress of Fe_3Al on heat treatment", Intermetallics 21 (2012) 56–61.

[72] M. Doyama, "Vacancy-solute interactions in metals", Journal of Nuclear Materials 69–70 (1978) 350–361.

[73] J. L. Jordan, S. C. Deevi, "Vacancy formation and effects in FeAl", Intermetallics 11 (2003) 507–528.

[74] J. Čížek, F. Lukáč, O. Melikhova, I. Procházka, R. Kužel, "Thermal vacancies in Fe_3Al studied by positron annihilation", Acta Materialia 59 (2011) 4068–4078.

[75] J. H. Schneibel, L. M. Pike, "A technique for measuring thermal vacancy concentrations in stoichiometric FeAl", Intermetallics 12 (2004) 85–90.

[76] R. Feder, A. S. Nowick, "Use of Thermal Expansion Measurements to Detect Lattice Vacancies near the Melting Point of Pure Lead and Aluminum", Physical Review 109 (1958) 1959–1963.

[77] H.-E. Schaefer, K. Frenner, R. Würschum, "Time-Differential Length Change Measurements for Thermal Defect Investigations: Intermetallic B2-FeAl and B2-NiAl Compounds, a Case Study", Physical Review Letters 82 (1999) 948–951.

[78] H.-E. Schaefer, R. Würschum, M. Sŏb, T. Zák, W. Z. Yu, W. Eckert, F. Banhart, "Thermal vacancies and positron-lifetime measurements in Fe 76.3 Al 23.7", Physical Review B 41 (1990) 11869–11874.

[79] P. Munroe, "The effect of nickel on vacancy hardening in iron-rich FeAl", Intermetallics 4 (1996) 5–11.

[80] J. H. Schneibel, "Strengthening of iron aluminides by vacancies and/or nickel", Materials Science and Engineering: A 258 (1998) 181–186.

[81] C. Kong, P. Munroe, "The effect of ternary additions on the vacancy hardening of FeAl", Scripta Metallurgica et Materialia 30 (1994) 1079–1083.

[82] L. Umakoshi, M. Lamaguchi, L. Namba, K. Murakami, "The effect of crystal orientation on the strength anomaly in β Culn at around 200 °C", Acta Metallurgica 24 (1976) 89–93.

[83] H. Saka, Y. M. Zhu, "Climb dissociation of ⟨111⟩ superdislocations in β-CuZn", Philosophical Magazine A 51 (1985) 629–637.

[84] M. Yoo, J. Horton, C. Liu, "Micromechanisms of yield and flow in ordered intermetallic alloys", Acta Metallurgica 36 (1988) 2935–2946.

[85] K. Yoshimi, S. Hanada, M. Yoo, "Yielding and plastic flow behavior of B2-type Fe-39.5 mol.% A1 single crystals in compression", Acta Metallurgica et Materialia 43 (1995) 4141–4151.

[86] E. P. George, I. Baker, "A model for the yield strength anomaly of Fe—Al", Philosophical Magazine A 77 (1998) 737–750.

[87] D. G. Morris, "A Dislocation Constriction, Pinning Point Model for the Flow Stress Anomaly in Iron Aluminides", MRS Proceedings 552 (1998) 431.

[88] F. Stein, A. Schneider, G. Frommeyer, "Flow stress anomaly and order–disorder transitions in Fe3Al-based Fe–Al–Ti–X alloys with X=V, Cr, Nb, or Mo", Intermetallics 11 (2003) 71–82.

[89] I. Baker, Y. Yang, "On the yield stress anomaly in stoichiometric FeAl", Materials Science and Engineering: A 239–240 (1997) 109–117.

[90] D. Weber, M. Meurtin, D. Paris, A. Fourdeux, P. Lesbats, "Vacancy elimination in FeAl alloys with B2 structure", Le Journal de Physique Colloques 38 (1977) 332–336.

[91] Y. Umakoshi, M. Yamaguchi, "Deformation of FeAl single crystals at high temperatures", Philosophical Magazine A 41 (1980) 573–588.

[92] O. Ikeda, I. Ohnuma, R. Kainuma, K. Ishida, "Phase equilibria and stability of ordered BCC phases in the Fe-rich portion of the Fe–Al system", Intermetallics 9 (2001) 755–761.

[93] A. Lawley, J. A. Coll, R. W. Cahn, "Influence of crystallographic order on creep of iron-aluminum solid solutions", Transactions of the Metallurgical Society of AIME 218 (1960) 166–176.

[94] R. T. Fortnum, D. E. Mikkola, "Effects of molybdenum, titanium and silicon additions on the $D0_3 \rightleftarrows B2$ transition temperature for alloys near Fe_3Al", Materials Science and Engineering 91 (1987) 223–231.

[95] M. G. Mendiratta, S. K. Ehlers, H. A. Lipsitt, "$D0_3$-B2-α Phase Relations in Fe-Al-Ti Alloys", Metallurgical Transactions A 18A (1987) 509–518.

[96] I. Baker, P. Nagpal, F. Liu, P. R. Munroe, "The effect of grain size on the yield strength of FeAl and NiAl", Acta Metallurgica & Materialia 39 (1991) 1637–1644.

[97] D. G. Morris, M. A. Morris-Muñoz, "The influence of microstructure on the ductility of iron aluminides", Intermetallics 7 (1999) 1121–1129.

[98] T. Doucakis, K. S. Kumar, "Formation and stability of refractory metal diborides in an Fe3Al matrix", Intermetallics 7 (1999) 765–777.

[99] R. Krein, A. Schneider, G. Sauthoff, G. Frommeyer, "Microstructure and mechanical properties of Fe3Al-based alloys with strengthening boride precipitates", Intermetallics 15 (2007) 1172–1182.

[100] H. J. Maier, T. Niendorf, R. Bürgel, *Handbuch Hochtemperatur-Werkstofftechnik*, 5th ed., Springer Vieweg, Wiesbaden, 2015.

[101] M. E. Kassner, *Fundamentals of creep in metals and alloys*, 3rd ed., Elsevier, Amsterdam, 2015.

[102] M.-T. Perez-Prado, M. Kassner, *Creep of Intermetallics*, in: *Fundamentals of Creep in Metals and Alloys*, Elsevier, 2015: 189–232.

[103] W. Blum, P. Eisenlohr, "Dislocation mechanics of creep", Materials Science and Engineering: A 510–511 (2009) 7–13.

[104] J. C. M. Li, J. Weertman, “An Experimental relation defining the stress dependence of minimun creep rate in metals”, Transactions of the Metallurgical Society of AIME 227 (1963) 1475–1476.

[105] *Quantitative relation between properties and microstructure*, in: ed. by D. G. Brandon, A. Rosen, Israel Universities Press, Haifa, Israel, 1969.

[106] J. Weertman, “Creep of indium, lead, and some of their alloys with various metals”, Transactions of the Metallurgical Society of AIME 218 (1960) 207–218.

[107] H. Riedel, *Fracture at High Temperatures*, Springer, Berlin, Heidelberg, 1987.

[108] J. Phillips, G. Eggeler, B. Ilschner, E. Batawi, “On the influence of crystal structure on creep in a Fe_3Al -based alloy”, Scripta Materialia 36 (1997) 693–698.

[109] D. G. Morris, M. A. Muñoz-Morris, *High-Temperature Creep of Iron Aluminide Intermetallics*, in: *Encyclopedia of Thermal Stresses*, ed. by R. B. Hetnarski, Springer Netherlands, Dordrecht, 2014: 2226–2236.

[110] C. T. Liu, E. H. Lee, C. G. McKamey, “An environmental effect as the major cause for room-temperature embrittlement in FeAl”, Scripta Metallurgica 23 (1989) 875–880.

[111] N. S. Stoloff, C. T. Liu, “Environmental embrittlement of iron aluminides”, Intermetallics 2 (1994) 75–87.

[112] C. Liu, C. McKamey, E. Lee, “Environmental effects on room-temperature ductility and fracture in Fe_3Al”, Scripta Metallurgica et Materialia 24 (1990) 385–389.

[113] M. Zamanzade, A. Barnoush, “An Overview of the Hydrogen Embrittlement of Iron Aluminides”, Procedia Materials Science 3 (2014) 2016–2023.

[114] G. F. Fuchs, N. S. Stoloff, “Effects of temperature, ordering and composition on high cycle fatigue of polycrystalline Fe_3Al”, Acta Metallurgica 36 (1988) 1381–1387.

[115] D. Risanti, J. Deges, L. Falat, S. Kobayashi, J. Konrad, M. Palm, B. Pöter, A. Schneider, C. Stallybrass, F. Stein, “Dependence of the brittle-to-ductile transition temperature (BDTT) on the Al content of Fe–Al alloys”, Intermetallics 13 (2005) 1337–1342.

[116] E. M. Schulson, *Brittle Fracture and Toughening*, in: *Physical Metallurgy and processing of Intermetallic Compounds*, ed. by N. S. Stoloff, V. K. Sikka, Springer US, Boston, MA, 1996: 56–94.

[117] Y. Kimura, D. P. Pope, “Ductility and toughness in intermetallics”, Intermetallics 6 (1998) 567–571.

[118] S. Nizamoglu, K.-H. Lang, S. Guth, M. Heilmaier, “A New Method for Determining the Brittle-to-Ductile Transition Temperature of a TiAl Intermetallic”, Metals 10 (2020) 1550.

[119] M. Zamanzade, H. Vehoff, A. Barnoush, “Cr effect on hydrogen embrittlement of Fe3Al-based iron aluminide intermetallics: Surface or bulk effect”, Acta Materialia 69 (2014) 210–223.

[120] M. A. Crimp, K. Vedula, “Effect of boron on the tensile properties of B2 FeAl”, Materials Science and Engineering 78 (1986) 193–200.

[121] W. R. Kerr, “Fracture of Fe_3Al”, Metallurgical Transactions A 17 (1986) 2298–2300.

[122] J. Herrmann, G. Inden, G. Sauthoff, “Deformation behaviour of iron-rich iron-aluminum alloys at low temperatures”, Acta Materialia 51 (2003) 2847–2857.

[123] O. Klein, I. Baker, “Effect of heat-treatment on the tensile behavior of iron-rich FeAl and FeAl + B”, Scripta Metallurgica et Materialia 30 (1994) 627–632.

[124] D. Gaydosh, S. Draper, R. Noebe, M. Nathal, “Room temperature flow and fracture of Fe-40at.%Al alloys”, Materials Science and Engineering: A 150 (1992) 7–20.

[125] I. Baker, P. R. Munroe, “Mechanical properties of FeAl”, International Materials Reviews 42 (1997) 181–205.

[126] A. Michalcová, L. Senčekova, G. Rolink, A. Weisheit, J. Pešička, M. Stobik, M. Palm, “Laser additive manufacturing of iron aluminides strengthened by ordering, borides or coherent Heusler phase”, Materials and Design 116 (2017) 481–494.

[127] F. Moszner, J. Peng, J. Suutala, U. Jasnau, M. Damani, M. Palm, “Application of Iron Aluminides in the Combustion Chamber of Large Bore 2-Stroke Marine Engines”, Metals 9 (2019) 847.

[128] J. G. Kim, R. A. Buchanan, “Pitting and Crevice Corrosion of Iron Aluminides in a Mild Acid-Chloride Solution”, Corrosion 50 (1994) 658–668.

[129] H. C. Choe, H. S. Kim, D. C. Choi, K. H. Kim, “Effects of alloying elements on the electrochemical characteristics of iron aluminides”, Journal of Materials Science 32 (1997) 1221–1227.

[130] J. F. Nachman, W. J. Buehler, “Fe-Al-Mo alloys for high-temperature use”, Metallurgical Programme 70 (1956) 107–110.

[131] C. G. McKamey, J. A. Horton, “The effect of molybdenum addition on properties of iron aluminides”, Metallurgical Transactions A 20 (1989) 751–757.

[132] L. Anthony, B. Fultz, “Effects of early transition metal solutes on the D03-B2 critical temperature of Fe_3Al”, Acta Materialia 43 (1995) 3885–3891.

[133] Z. Sun, W. Yang, L. Shen, Y. Huang, B. Zhang, J. Yang, “Neutron diffraction study on site occupation of substitutional elements at sub lattices in Fe3 Al intermetallics”, Materials Science and Engineering: A 258 (1998) 69–74.

[134] Y. Nishino, B. J. Inkson, T. Ogawa, C. J. Humphreys, “Effect of molybdenum substitution on phase stability and high-temperature strength of Fe_3Al alloys”, Philosophical Magazine Letters 78 (1998) 97–103.

[135] C. T. Liu, C. L. White, J. A. Horton, “Effect of boron on grain-boundaries in Ni_3Al”, Acta Metallurgica 33 (1985) 213–229.

[136] C. T. Liu, E. P. George, “Environmental embrittlement in boron-free and boron-doped FeAl (40 at. % Al) alloys”, Scripta Metallurgica et Materialia 24 (1990) 1285–1290.

[137] S. Pattnaik, D. B. Karunakar, P. Jha, “Developments in investment casting process—A review”, Journal of Materials Processing Technology 212 (2012) 2332–2348.

[138] R. Prasad, *Progress in Investment Castings*, in: *Science and Technology of Casting Processes*, ed. by M. Srinivasan, InTech, 2012.

[139] G. Chirita, D. Soares, F. S. Silva, “Advantages of the centrifugal casting technique for the production of structural components with Al–Si alloys”, Materials & Design 29 (2008) 20–27.

[140] K. Ho, R. D. Pehlke, “Metal-Mold interfacial heat transfer”, Metallurgical Transactions B 16 (1985) 585–594.

[141] V. Kolarik, H. Fietzek, W. Engel, B. Eltester, H. J. Grabke, “High Temperature Oxidation of Fe-Al Alloys Studied by In Situ X-Ray Diffraction”, Materials Science Forum 251–254 (1997) 251–258.

[142] X. F. Zhang, K. Thaidigsmann, J. Ager, P. Y. Hou, “Al_2O_3 scale development on iron aluminides”, Journal of Materials Research 21 (2006) 1409–1419.

[143] P. Zapala, A. Abel, H. Michels, B. Skrotzki, *Werkstoffanwendung FeAl (WAFEAL)*, FVV final report, Frankfurt a. M., 2023.

[144] D. Janda, H. Fietzek, M. Galetz, M. Heilmaier, “The effect of micro-alloying with Zr and Nb on the oxidation behavior of Fe_3Al and FeAl alloys”, Intermetallics 41 (2013) 51–57.

[145] D. Janda, H. Ghassemi-Armaki, E. Bruder, M. Hockauf, M. Heilmaier, K. Kumar, “Effect of strain-rate on the deformation response of D03-ordered Fe_3Al”, Acta Materialia 103 (2016) 909–918.

[146] D. Janda, *Mechanical properties and oxidation behavior of micro-alloyed iron aluminides*, PhD thesis, Karlsruhe: Karlsruhe Institute of Technology, 2015.

[147] Y. Natarajan, P. K. Murugesan, M. Mohan, S. A. Liyakath Ali Khan, “Abrasive Water Jet Machining process: A state of art of review”, Journal of Manufacturing Processes 49 (2020) 271–322.

[148] *DIN EN ISO 4287:2010-07, Geometrical Product Specifications (GPS) - Surface texture: Profile method - Terms, definitions and surface texture parameters (ISO 4287:1997 + Cor 1:1998 + Cor 2:2005 + Amd 1:2009); German version EN ISO 4287:1998 + AC:2008 + A1:2009*, Beuth Verlag GmbH.

[149] *DIN EN ISO 4288:1998-04, Geometrical Product Specifications (GPS) - Surface texture: Profile method - Rules and procedures for the assessment of surface texture (ISO 4288:1996); German version EN ISO 4288:1997*, Beuth Verlag GmbH.

[150] E. Jameson, *Electrical Discharge Machining*, Society of Manufacturing Engineers, Dearborn, Michigan, 2001.

[151] *DIN EN ISO 3452-1:2014-09, Non-destructive testing - Penetrant testing - Part 1: General principles (ISO 3452-1:2021); German version EN ISO 3452-1:2021*, Beuth Verlag GmbH.

[152] M. C. Marker, B. Skolyszewska-Kühberger, H. S. Effenberger, C. Schmetterer, K. W. Richter, “Phase equilibria and structural investigations in the system Al–Fe–Si”, Intermetallics 19 (2011) 1919–1929.

[153] M. Švec, V. Vodičková, P. Hanus, P. Pazourková Prokopčáková, L. Čamek, J. Moravec, “Effect of Higher Silicon Content and Heat Treatment on Structure Evolution and High-Temperature Behaviour of Fe-28Al-15Si-2Mo Alloy”, Materials 14 (2021) 3031.

[154] M. Zamanzade, A. Barnoush, "Effect of chromium on the electrochemical properties of iron aluminide intermetallics", Corrosion Science 78 (2014) 223–232.

[155] B. J. Schlothmann, *Manual for the Iron Works Laboratory, Part 2 Analysis of Metals, Part 2 New Methods*, 3rd ed., Stahleisen GmbH, Düsseldorf, 2018.

[156] C. B. Boss, K. J. Fredeen, *Concepts, Instrumentation and Techniques in Inductively Coupled Plasma Optical Emission Spectrometry*, 3rd ed., PerkinElmer Life and Analytical Sciences, Shelton, CT, 2004.

[157] J. Nölte, *ICP emission spectrometry: A practical guide*, 2nd ed., Wiley-VCH, Weinheim, 2021.

[158] *DIN EN ISO 4829-2:2016-08, Steels - Determination of total silicon contents - Reduced molybdosilicate spectrophotometric method - Part 2: Silicon contents between 0.01 % and 0.05 % (ISO 4829-2:2016); German version EN ISO 4829-2:2016*, Beuth Verlag GmbH.

[159] *DIN EN ISO 9556:2002-04, Steel and iron - Determination of total carbon content - Infrared absorption method after combustion in an induction furnace (ISO 9556:1989); German version EN ISO 9556:2001*, Beuth Verlag GmbH.

[160] *Determination of the Hydrogen Content in Steel*, in: *Manual for the Iron Works Laboratory, Part 2 Analysis of Metals, Part 2 New Methods*, 2nd ed., Stahleisen GmbH, Düsseldorf, 1998: 235–239.

[161] F. Mbingeneeko, A. Wanke, S. Lohmeier, S. Abraham, *Analytical capability of the Thermo Scientific™ Niton™ XL3t GOLDD+ XRF analyzer*, in: *1st International Conference Mineral Resources for Future Generations*, AIMS 2020, RWTH Aachen University, Aachen, 2020: Poster–019.

[162] B. Beckhoff, ed., *Handbook of practical X-ray fluorescence analysis*, 1st ed., Springer, Berlin, Heidelberg, 2006.

[163] *DIN 66137-2:2019-03, Determination of solid state density - Part 1: Principles*, Beuth Verlag GmbH.

[164] *DIN EN 820-5:2009-10, Advanced technical ceramics - Thermomechanical properties of monolithic ceramics - Part 5: Determination of elastic moduli at elevated temperatures; German version EN 820-5:2009*, Beuth Verlag GmbH.

[165] *ASTM E1875-13 Test Method for Dynamic Youngs Modulus, Shear Modulus, and Poissons Ratio by Sonic Resonance*, ASTM International.

[166] *DIN EN 843-2:2007-03, Advanced technical ceramics - Mechanical properties of monolithic ceramics at room temperature - Part 2: Determination of Young's modulus, shear modulus and Poisson's ratio; German version EN 843-2:2006*, Beuth Verlag GmbH.

[167] *DIN 51007:2019-04, Thermal analysis - Differential thermal analysis (DTA) and differential scanning calorimetry (DSC) - General Principles*, Beuth Verlag GmbH.

[168] *DIN 51045-1:2005-08, Determination of the thermal expansion of solids - Part 1: Basic rules*, Beuth Verlag GmbH.

[169] J. H. Schneibel, P. R. Munroe, "On the path dependence of the thermal vacancy concentration in stoichiometric FeAl", Intermetallics 12 (2004) 111–115.

[170] W. Kraus, G. Nolze, "POWDER CELL – a program for the representation and manipulation of crystal structures and calculation of the resulting X-ray powder patterns", Journal of Applied Crystallography 29 (1996) 301–303.

[171] *ASTM E112-96 Test Methods for Determining Average Grain Size*, ASTM International.

[172] *ASTM E1382-97 Test Methods for Determining Average Grain Size Using Semiautomatic and Automatic Image Analysis*, ASTM International.

[173] C. A. Schneider, W. S. Rasband, K. W. Eliceiri, "NIH Image to ImageJ: 25 years of image analysis", Nature Methods 9 (2012) 671–675.

[174] A. J. Schwartz, M. Kumar, B. L. Adams, D. P. Field, eds., *Electron Backscatter Diffraction in Materials Science*, Springer US, Boston, MA, 2009.

[175] F. J. Humphreys, M. Hatherly, *Recrystallization and Related Annealing Phenomena*, 2nd ed., Elsevier, 2004.

[176] X. Llovet, A. Moy, P. T. Pinard, J. H. Fournelle, "Electron probe microanalysis: A review of recent developments and applications in materials science and engineering", Progress in Materials Science 116 (2021) 100673.

[177] D. B. Williams, C. B. Carter, *Transmission Electron Microscopy: A Textbook for Materials Science*, 2nd ed., Springer, New York, 2008.

[178] J. Kopeček, P. Kratochvíl, D. Rafaja, D. Plischke, "Ordering in the sublattices of Fe_3Al during the phase transformation B2 ↔ $D0_3$", Intermetallics 7 (1999) 1367–1372.

[179] P. Stadelmann, “EMS - a software package for electron diffraction analysis and HREM image simulation in materials science”, Ultramicroscopy 21 (1987) 131–145.

[180] C. C. Ahn, O. L. Krivanek, R. P. Burgner, M. M. Disko, P. R. Swann, *EELS atlas: A reference collection of electron energy loss spectra covering all stable elements*, Gatan, Inc., Warrendale, PA, 1983.

[181] *DIN EN ISO 6507-1:2018-07, Metallic materials - Vickers hardness test - Part 1: Test method (ISO 6507-1:2018); German version EN ISO 6507-1:2018*, Beuth Verlag GmbH.

[182] *DIN 50106:2016-11, Testing of metallic materials - Compression test at room temperature*, Beuth Verlag GmbH.

[183] *DIN EN ISO 6892-1:2020-06, Metallic materials - Tensile testing - Part 1: Method of test at room temperature (ISO 6892-1:2019); German version EN ISO 6892-1:2019*, Beuth Verlag GmbH: 1–96.

[184] *DIN EN ISO 6892-2:2018-09, Metallic materials - Tensile testing - Part 2: Method of test at elevated temperature (ISO 6892-2:2018); German version EN ISO 6892-2:2018*, Beuth Verlag GmbH: 1–31.

[185] T. Connolley, P. E. Mchugh, M. Bruzzi, “A review of deformation and fatigue of metals at small size scales”, Fatigue & Fracture of Engineering Materials & Structures 28 (2005) 1119–1152.

[186] P. Lorenzino, A. Navarro, “Influence of the ratio between specimen thickness and grain size on the fatigue and tensile properties of plain and notched aluminium plate specimens”, International Journal of Fatigue 164 (2022) 107149.

[187] M. Sutton, W. Wolters, W. Peters, W. Ranson, S. McNeill, “Determination of displacements using an improved digital correlation method”, Image and Vision Computing 1 (1983) 133–139.

[188] H. A. Bruck, S. R. McNeill, M. A. Sutton, W. H. Peters, “Digital image correlation using Newton-Raphson method of partial differential correction”, Experimental Mechanics 29 (1989) 261–267.

[189] *DIN EN ISO 204:2019-04, Metallic materials - Uniaxial creep testing in tension - Method of test (ISO 204:2018); German version EN ISO 204:2018*, Beuth Verlag GmbH.

[190] *DIN EN ISO 7500-2:2007-04, Metallic materials - Verification of static uniaxial testing machines - Part 2: Tension creep testing machines - Verification of the applied force (ISO 7500-2:2006); German version EN ISO 7500-2:2006*, Beuth Verlag GmbH.

[191] A. Abel, J. M. Rosalie, S. Reinsch, P. Zapala, H. Michels, B. Skrotzki, "Influence of Mo and B additions in intermetallic near-Fe_3Al alloys on microstructure and mechanical properties", Intermetallics 163 (2023) 108074.

[192] J. Herrmann, G. Inden, G. Sauthoff, "Microstructure and Deformation Behaviour of Iron-Rich Iron-Aluminium Alloys with Ternary Carbon and Silicon Additions", steel research international 75 (2004) 343–352.

[193] H. P. Longworth, D. E. Mikkola, "Effects of alloying additions of titanium, molybdenum, silicon, hafnium and tantalum on the microstructure of iron aluminides near Fe_3Al", Materials Science and Engineering 96 (1987) 213–229.

[194] P. Mouton, *Principles and Practices of Unbiased Stereology: An Introduction for Bioscientists*, Principles and Practices of Unbiased Stereology, Johns Hopkins University Press, Baltimore, 2002.

[195] E. I. Gladyshevskii, T. F. Fedorov, Y. B. Kuz'ma, R. V. Skolozdra, "Isothermal section of the molybdenum-iron-boron system", Poroshkovaya Metallurgiya 5 (1966) 305–309.

[196] E. Popiel, M. Tuszyński, W. Zarek, T. Rendecki, "Investigation of $Fe_{3-x}V_xAl$ alloys with DO_3 type structure by X-ray, magnetostatic and Mössbauer effect methods", Journal of the Less Common Metals 146 (1989) 127–135.

[197] F. Stein, M. Palm, "Re-determination of transition temperatures in the Fe–Al system by differential thermal analysis", International Journal of Materials Research 98 (2007) 580–588.

[198] E. Hornbogen, H. Warlimont, B. Skrotzki, *Strukturelle Phasenumwandlungen*, in: *Metalle*, 7th ed., Springer Vieweg, Berlin, Heidelberg, 2019: 181–210.

[199] M. Švec, E. Macajová, *The coefficient of thermal expansion of Fe_3Al and FeAl-type iron aluminides*, in: *Proceedings 24th International Conference on Metallurgy and Materials*, Brno, CZ, 2015: 1657–1661.

[200] W. Köster, T. Gödecke, "Physikalische Messungen an Eisen-Aluminium-Legierungen mit 10 bis 50 At.-% Al Ill. Die Ausdehnungskoeffizienten der Legierungen mit 20 bis 50 At.-% Al", International Journal of Materials Research 72 (1981) 707–711.

[201] N. K. Sharma, R. Misra, S. Sharma, "Modeling of thermal expansion behavior of densely packed Al/SiC composites", International Journal of Solids and Structures 102–103 (2016) 77–88.

[202] P. S. Turner, "Thermal-expansion stresses in reinforced plastics", Journal of Research of the National Bureau of Standards 37 (1946) 239–250.

[203] H. Leamy, E. Gibson, F. Kayser, "The elastic stiffness coefficients of iron-aluminum alloys—I experimental results and thermodynamic analysis", Acta Metallurgica 15 (1967) 1827–1838.

[204] B. Wang, Y. Liu, J.-W. Ye, J. Wang, "Electronic, magnetic and elastic properties of Mo_2FeB_2: First-principles calculations", Computational Materials Science 70 (2013) 133–139.

[205] K.-I. Takagi, "Development and application of high strength ternary boride base cermets", Journal of Solid State Chemistry 179 (2006) 2809–2818.

[206] M. Švec, P. Kejzlar, "The influence of ternary alloying element in iron aluminides on coefficient of thermal expansion", Metallic Materials 54 (2016) 83–89.

[207] D. H. Chung, W. R. Buessem, "The Voigt-Reuss-Hill Approximation and Elastic Moduli of Polycrystalline MgO, CaF2, β-ZnS, ZnSe, and CdTe", Journal of Applied Physics 38 (1967) 2535–2540.

[208] G. V. Jagadeesh, S. Gangi Setti, "A review on micromechanical methods for evaluation of mechanical behavior of particulate reinforced metal matrix composites", Journal of Materials Science 55 (2020) 9848–9882.

[209] Y. Luo, "An Accuracy Comparison of Micromechanics Models of Particulate Composites against Microstructure-Free Finite Element Modeling", Materials 15 (2022) 4021.

[210] P. Malinovskis, S. Fritze, J. Palisaitis, E. Lewin, J. Patscheider, P. O. A. Persson, U. Jansson, "Synthesis and Characterisation of Nanocomposite Mo-Fe-B Thin Films Deposited by Magnetron Sputtering", Materials 14 (2021) 1739.

[211] W. D. Nix, H. Gao, "Indentation size effects in crystalline materials: A law for strain gradient plasticity", Journal of the Mechanics and Physics of Solids 46 (1998) 411–425.

[212] H. Ledbetter, "Dynamic vs. static Young's moduli: a case study", Materials Science and Engineering: A 165 (1993) L9–L10.

[213] R. Horiuchi, H. Yoshinaga, "Mechanism of the High Temperature Yield Point Phenomenon in Some Aluminium Alloys", Transactions of the Japan Institute of Metals 6 (1965) 131–138.

[214] A. H. Cottrell, M. A. Jaswon, "Distribution of solute atoms round a slow dislocation", Proceedings of the Royal Society of London. Series A. Mathematical and Physical Sciences 199 (1949) 104–114.

[215] D. G. Morris, J. C. Joye, M. Leboeuf, "Hardening and strain-ageing by vacancies and their aggregates in FeAl", Philosophical Magazine A 69 (1994) 961–980.

[216] A. Portevin, F. Le Chatelier, "Sur un phénomène observé lors de l'essai de traction d'alliages en cours de transformation", Comptes Rendus de l'Académie des Sciences Paris 176 (1923) 507–510.

[217] A. Yilmaz, "The Portevin–Le Chatelier effect: a review of experimental findings", Science and Technology of Advanced Materials 12 (2011) 063001.

[218] VDEh, *The appearance of cracks and fractures in metallic materials*, 2nd ed., Verlag Stahleisen GmbH, Düsseldorf, 1996.

[219] M. J. Marcinkowski, M. E. Taylor, F. X. Kayser, "Relationship between atomic ordering and fracture in Fe-Al alloys", Journal of Materials Science 10 (1975) 406–414.

[220] U. Prakash, R. Buckley, H. Jones, "Effect of molybdenum substitution on B2 antiphase domain formation in rapidly solidified Fe-Al-Mo alloys", Materials Science and Engineering: A 133 (1991) 588–591.

[221] U. Prakash, R. A. Buckley, H. Jones, G. W. Greenwood, "The role of antiphase boundary energy in influencing intergranular failure in iron aluminides", Philosophical Magazine Letters 65 (1992) 129–132.

[222] L. T. Eleno, L. A. Errico, P. G. Gonzales-Ormeño, H. M. Petrilli, C. G. Schön, "Ordering phase relationships in ternary iron aluminides", Calphad 44 (2014) 70–80.

[223] A. H. Cottrell, "Theory of brittle facture in steel and similar metals", Transactions of the Metallurgical Society of AIME 212 (1958).

[224] J. Datsko, C. T. Yang, "Correlation of Bendability of Materials With Their Tensile Properties", Journal of Engineering for Industry 82 (1960) 309–313.

[225] C. Iacono, J. Sinke, R. Benedictus, "Prediction of Minimum Bending Ratio of Aluminum Sheets From Tensile Material Properties", Journal of Manufacturing Science and Engineering 132 (2010) 021001.

[226] A. Nádai, *Theory of flow and fracture of solids*, vol. 1, McGraw-Hill, New York, 1950.

[227] R. A. Mayville, I. Finnie, "Uniaxial stress-strain curves from a bending test: A single bending specimen can be used to generate both the tension and compression stress-strain curves of a material", Experimental Mechanics 22 (1982) 197–201.

[228] S. Naseem, E. S. Perdahcıoğlu, H. J. M. Geijselaers, A. H. Van Den Boogaard, "A New in-Plane Bending Test to Determine Flow Curves for Materials with Low Uniform Elongation", Experimental Mechanics 60 (2020) 1225–1238.

[229] W. Blum, P. Eisenlohr, F. Breutinger, "Understanding creep—a review", Metallurgical and Materials Transactions A 33 (2002) 291–303.

[230] R. Sandström, *Basic Modeling and Theory of Creep of Metallic Materials*, 1st ed., Springer Series in Materials Science, Springer Nature Switzerland, Cham, 2024.

[231] J. Weertman, "Steady-State Creep through Dislocation Climb", Journal of Applied Physics 28 (1957) 362–364.

[232] O. D. Sherby, P. M. Burke, "Mechanical behavior of crystalline solids at elevated temperature", Progress in Materials Science 13 (1968) 323–390.

[233] G. Gottstein, *Mechanische Eigenschaften*, in: *Physikalische Grundlagen der Materialkunde*, Springer, Berlin, Heidelberg, 2007: 197–301.

[234] C. G. McKamey, P. J. Maziasz, J. W. Jones, "Effect of addition of molybdenum or niobium on creep-rupture properties of Fe_3Al", Journal of Materials Research 7 (1992) 2089–2106.

[235] L. N. Larikov, V. V. Geichenko, V. M. Fal'chenko, *Diffusion Processes in Ordered Alloys*, Amerind Publishing Company, New Dehli, 1981, 111-117.

[236] M. Eggersmann, H. Mehrer, "Diffusion in intermetallic phases of the Fe-Al system", Philosophical Magazine A 80 (2000) 1219–1244.

[237] R. W. Cahn, "How does long-range order affect creep of alloys?", Materials Science and Engineering: A 324 (2002) 1–4.

[238] D. G. Morris, M. Leboeuf, S. Gunther, M. Nazmy, "Disordering behaviour of alloys based on Fe_3Al", Philosophical Magazine A 70 (1994) 1067–1090.

[239] D. G. Morris, *Grown-In and Shear-Produced APB Faults in Ordered Intermetallics*, in: *Ordered Intermetallics — Physical Metallurgy and Mechanical Behaviour*, ed. by C. T. Liu, R. W. Cahn, G. Sauthoff, Springer Netherlands, Dordrecht, 1992: 123–142.

[240] L. Brown, R. Ham, *Dislocation-particle interactions*, in: *Strengthening methods in crystals*, ed. by A. Kelly, R. Nicholson, Halstead Press Division, Wiley, New York, 1971: 9–70.

[241] R. S. Sundar, T. R. G. Kutty, D. H. Sastry, "Hot hardness and creep of Fe_3Al-based alloys", Intermetallics 8 (2000) 427–437.

[242] H. Mehrer, M. Eggersmann, A. Gude, M. Salamon, B. Sepiol, "Diffusion in intermetallic phases of the Fe–Al and Fe–Si systems", Materials Science and Engineering: A 239–240 (1997) 889–898.

[243] J. S. Waddington, "On the conditions affecting the mechanism of fracture at high temperatures", The Philosophical Magazine: A Journal of Theoretical Experimental and Applied Physics 17 (1968) 51–59.

[244] B. Dyson, "Continuous cavity nucleation and creep fracture", Scripta Metallurgica 17 (1983) 31–37.

[245] J. Čadek, *Creep in metallic materials*, 2nd ed., Elsevier, Amsterdam, 1988.

[246] K. Kakehi, "Tension/compression asymmetry in creep behavior of a Ni-based superalloy", Scripta Materialia 41 (1999) 461–465.

[247] M. Koeppe, Ch. Hartig, H. Mecking, "Anomalies of the plastic yield stress in the intermetallic compound Fe–30 at.% Al", Intermetallics 7 (1999) 415–422.

[248] W. Bang, H. Tae Lim, T. Kwon Ha, Y. W. Chang, "Anomalous temperature dependence and tension–compression asymmetry of Fe $_3$ Al intermetallics—an internal variable approach", International Journal of Mechanical Sciences 45 (2003) 1661–1670.

[249] N. Tsuno, S. Shimabayashi, K. Kakehi, C. Rae, R. Reed, *Tension/compression asymmetry in yield and creep strengths of Ni-based superalloys*, in: *Proceedings of the International Symposium on Superalloys*, TMS, New Orleans, 2008: 433–442.

[250] L. Chen, W. Wen, H. Cui, H. Zhang, Y. Xu, "Yield anisotropy and tension/compression asymmetry of a Ni_3Al based intermetallic alloy", Chinese Journal of Aeronautics 26 (2013) 801–806.

[251] M. Lenz, Y. M. Eggeler, J. Müller, C. H. Zenk, N. Volz, P. Wollgramm, G. Eggeler, S. Neumeier, M. Göken, E. Spiecker, "Tension/Compression asymmetry of a creep deformed single crystal Co-base superalloy", Acta Materialia 166 (2019) 597–610.

[252] S. Copley, B. Kear, "The dependence of the width of a dissociated dislocation on dislocation velocity", Acta Metallurgica 16 (1968) 227–231.

[253] S. S. Ezz, D. Pope, V. Paidar, "The tension/compression flow stress asymmetry in Ni_3(Al,Nb) Single crystals", Acta Metallurgica 30 (1982) 921–926.

[254] W. C. Leslie, R. J. Sober, "The strength of ferrite and of martensite as functions of composition, temperature, and strain rate", Transactions ASM 60 (1968) 459–484.

[255] S. Wiederhorn, R. Fields, S. Low, G.-W. Bahng, A. Wehrstedt, J. Hahn, Y. Tomota, T. Miyata, H. Lin, B. Freeman, S. Aihara, Y. Hagihara, T. Tagawa, *Mechanical Properties*, in: *Handbook of Materials Measurement Methods*, ed. by H. Czichos, T. Saito, L. Smith, Springer, Berlin, Heidelberg, 2006: 283–397.

[256] S. Takeuchi, E. Kuramoto, "Temperature and orientation dependence of the yield stress in Ni_3Ga single crystals", Acta Metallurgica 21 (1973) 415–425.

[257] A. H. Sully, G. N. Cale, G. Willoughby, "Creep of Metals Subjected to Compression Stress", Nature 162 (1948) 411–412.

[258] C. Lall, S. Chin, D. P. Pope, "The orientation and temperature dependence of the yield stress of Ni_3 (Al, Nb) single crystals", Metallurgical Transactions A 10 (1979) 1323–1332.

[259] V. Paidar, D. Pope, V. Vitek, "A theory of the anomalous yield behavior in $L1_2$ ordered alloys", Acta Metallurgica 32 (1984) 435–448.

[260] V. Vitek, "Computer simulation of the screw dislocation motion in b. c. c. metals under the effect of the external shear and uniaxial stresses", Proceedings of the Royal Society of London. A. Mathematical and Physical Sciences 352 (1976) 109–124.

[261] L. Falat, A. Schneider, G. Sauthoff, G. Frommeyer, "Mechanical properties of Fe–Al–M–C (M=Ti, V, Nb, Ta) alloys with strengthening carbides and Laves phase", Intermetallics 13 (2005) 1256–1262.

[262] T. Tsuchiya, O. Tabata, J. Sakata, Y. Taga, "Specimen size effect on tensile strength of surface-micromachined polycrystalline silicon thin films", Journal of Microelectromechanical Systems 7 (1998) 106–113.

[263] A. Sergueeva, J. Zhou, B. Meacham, D. Branagan, "Gage length and sample size effect on measured properties during tensile testing", Materials Science and Engineering: A 526 (2009) 79–83.

[264] A. Emdadi, S. Weiß, "A Comparative Study of Microstructure and Hot Deformability of a Fe–Al–Ta Iron Aluminide Prepared via Additive Manufacturing and Conventional Casting", Crystals 12 (2022) 1709.

[265] Ewelina Bernstock-Kopaczyńska, M. Jabłońska, "Study of Defects Structure in Fe-Al Alloys", Solid State Phenomena 203–204 (2013) 411–416.

[266] E. Broitman, "Indentation Hardness Measurements at Macro-, Micro-, and Nanoscale: A Critical Overview", Tribology Letters 65 (2017) 23.

[267] P. Morgand, P. Mouturat, G. Sainfort, « Structure and mechanical properties of iron-aluminium alloys », Acta Metallurgica 16 (1968) 867-875.

[268] M. Z. Butt, P. Feltham, "Solid-solution hardening", Journal of Materials Science 28 (1993) 2557–2576.

[269] P. Feltham, "Solid solution hardening of metal crystals", Journal of Physics D: Applied Physics 1 (1968) 303–308.

[270] C. Fu, J. Zou, "Site preference of ternary alloying additions in FeAl and NiAl by first-principles calculations", Acta Materialia 44 (1996) 1471–1478.

[271] N. Medvedeva, Y. Gornostyrev, D. Novikov, O. Mryasov, A. Freeman, "Ternary site preference energies, size misfits and solid solution hardening in NiAl and FeAl", Acta Materialia 46 (1998) 3433–3442.

[272] J. Schneibel, E. Specht, W. Simpson, "Solid solution strengthening in ternary B2 iron aluminides containing 3d transition elements", Intermetallics 4 (1996) 581–583.

[273] A. J. Ardell, "Precipitation hardening", Metallurgical Transactions A 16 (1985) 2131–2165.

[274] S. Takeuchi, "On the shear modulus parameter in the theory of solid-solution hardening", Scripta Metallurgica 2 (1968) 481–483.

[275] R. Arsenault, “The double-kink model for low-temperature deformation of B.C.C. metals and solid solutions”, Acta Metallurgica 15 (1967) 501–511.

[276] W. F. Hosford, *The mechanics of crystals and textured polycrystals*, Oxford engineering science series, Oxford University Press, New York Oxford, 1993.

[277] J.-F. Croteau, *Single crystal and polycrystalline niobium and OFE copper for SRF cavities applications: Mechanical characterization at low to high strain rates and microstructural investigations*, PhD thesis, ENSTA Bretagne, 2021.

[278] S. Hanada, S. Watanabe, T. Sato, O. Izumi, “Deformation of Fe_3Al single crystals at high temperatures”, Scripta Metallurgica 15 (1981) 1345–1348.

[279] W. Schröer, C. Hartig, H. Mecking, “Plasticity of DO_3-ordered Fe-Al and Fe-Al-Si single-erystals”, International Journal of Materials Research 84 (1993) 294–300.

[280] T. Sakai, A. Belyakov, R. Kaibyshev, H. Miura, J. J. Jonas, “Dynamic and post-dynamic recrystallization under hot, cold and severe plastic deformation conditions”, Progress in Materials Science 60 (2014) 130–207.

[281] I. Baker, D. Gaydosh, “Dynamic recrystallization and grain boundary migration in B2 FeAl”, Metallography 20 (1987) 347–357.

[282] M. Kupka, M. Prewendowski, “Dynamic recrystallization in a Fe–40at.% Al alloy”, Journal of Alloys and Compounds 437 (2007) 367–372.

[283] B. Kad, S. Schoenfeld, R. Asaro, C. Mckamey, V. Sikka, “Deformation textures in Fe3Al alloys: An assessment of dominant slip system activity in the 900–1325 K temperature range of hot working”, Acta Materialia 45 (1997) 1333–1350.

[284] D. Lin, Y. Liu, “An electron back-scattered diffraction study on the microstructural evolution in large-grained iron aluminides during superplastic deformation”, Materials Science and Engineering: A 329–331 (2002) 863–871.

[285] M. Yoo, K. Yoshimi, S. Hanada, “Dislocation stability and deformation mechanisms of iron aluminides and silicide”, Acta Materialia 47 (1999) 3579–3588.

[286] Y. Umakoshi, M. Yamaguchi, “The effect of compositional deviations from stoichiometry on the transition in slip directions from (111) to (001) in FeAl at high temperatures”, Philosophical Magazine A 44 (1981) 711–715.

[287] M. G. Mendiratta, H.-M. Kim, H. A. Lipsitt, “Slip Directions in B2 Fe-Al Alloys”, Metallurgical Transactions A 15 (1984) 395–399.

[288] A. Abel, P. Zapala, H. Michels, B. Skrotzki, *Microstructure-Property-Correlation of a Mo-Ti-B alloyed iron aluminide*, in: *Proceedings Intermetallics*, ed. by M. Heilmaier, M. Krüger, M. Palm, F. Stein, Conventus Congressmanagement & Marketing GmbH, Jena, 2021: 119–120.

[289] L. Hogan, *Crystals, Dendritic Solidification of*, in: *Encyclopedia of Materials: Science and Technology*, Elsevier, 2001: 1913–1918.

[290] R. Elliott, *Eutectic Solidification*, in: *Encyclopedia of Materials: Science and Technology*, Elsevier, 2001: 2816–2821.

[291] W. Kim, B. Cantor, “The variation of grain size with cooling rate during melt spinning”, Scripta Metallurgica et Materialia 24 (1990) 633–637.

[292] B. Cantor, K. O’Reilly, *Solidification and casting*, 1st ed., CRC Press, Boca Raton, 2003.

[293] E. O. Hall, “The Deformation and Ageing of Mild Steel: III Discussion of Results”, Proceedings of the Physical Society. Section B 64 (1951) 747–753.

[294] N. J. Petch, “The cleavage strength of polycrystals”, Journal of the Iron and Steel Institute 174 (1953) 25–28.

[295] E. O. Hall, “Variation of Hardness of Metals with Grain Size”, Nature 173 (1954) 948–949.

[296] B. Oberdorfer, B. Lorenzoni, K. Unger, W. Sprengel, M. Zehetbauer, R. Pippan, R. Wurschum, “Absolute concentration of free volume-type defects in ultrafine-grained Fe prepared by high-pressure torsion”, Scripta Materialia 63 (2010) 452–455.

[297] L. M. Pike, Y. A. Chang, C. T. Liu, “Point defect concentrations and hardening in binary B2 intermetallics”, Acta Materialia 45 (1997) 3709–3719.

[298] G. Hasemann, J. H. Schneibel, M. Krüger, E. P. George, “Vacancy strengthening in Fe_3Al iron aluminides”, Intermetallics 54 (2014) 95–103.

[299] M. Morris, O. George, D. Morris, “Vacancies, vacancy aggregates and hardening in FeAl”, Materials Science and Engineering: A 258 (1998) 99–107.

[300] J. Kuriplach, O. Melikhova, C. Domain, C. Becquart, D. Kulikov, L. Malerba, M. Hou, A. Almazouzi, C. Duque, A. Morales, "Vacancy-solute complexes and their clusters in iron", Applied Surface Science 252 (2006) 3303–3308.

[301] J. Mayer, B. Meyer, J. Oehrens, G. Bester, N. Börnsen, M. Fähnle, "Effective formation energies of atomic defects in $D0_3$ Fe3Al: an ab-initio study", Intermetallics 5 (1997) 597–600.

[302] M. Fähnle, J. Mayer, B. Meyer, "Theory of atomic defects and diffusion in ordered compounds, and application to B2-FeAl", Intermetallics 7 (1999) 315–323.

[303] H. J. Leamy, F. X. Kayser, "The Compressive Deformation Behavior of Long Range Ordered Polycrystalline iron—aluminum Alloys", physica status solidi (b) 34 (1969) 765–780.

[304] A. Lawley, R. Cahn, "A high temperature X-ray study of ordering in iron-aluminium alloys", Journal of Physics and Chemistry of Solids 20 (1961) 204–221.

[305] M. J. Marcinkowski, H. J. Leamy, "Analysis of Dislocation Loops in Superlattices", physica status solidi (b) 24 (1967) 149–162.

[306] Z. C. Cordero, B. E. Knight, C. A. Schuh, "Six decades of the Hall–Petch effect – a survey of grain-size strengthening studies on pure metals", International Materials Reviews 61 (2016) 495–512.

[307] R. B. Figueiredo, M. Kawasaki, T. G. Langdon, "Seventy years of Hall-Petch, ninety years of superplasticity and a generalized approach to the effect of grain size on flow stress", Progress in Materials Science 137 (2023) 101131.

[308] J. Rösler, H. Harders, M. Bäker, *Mechanisches Verhalten der Werkstoffe*, Springer Fachmedien, Wiesbaden, 2019.

[309] M. A. Van Huis, A. Van Veen, H. Schut, C. V. Falub, S. W. H. Eijt, P. E. Mijnarends, J. Kuriplach, "Positron confinement in embedded lithium nanoclusters", Physical Review B 65 (2002) 085416.

[310] M. Elsayed, T. E. Staab, J. Čížek, R. Krause-Rehberg, "On the interaction of solute atoms with vacancies in diluted Al-alloys: A paradigmatic experimental and ab-initio study on indium and tin", Acta Materialia 219 (2021) 117228.